Wireless Communications and Mobile Computing

Wireless Internet of Things: Enabling Future Generation Connectivity and Communications

Lead Guest Editor: Mingbo (Michael) Niu
Guest Editors: Francois Chan, Hongzhi Guo, Changqing Wang, Salari Soheil, and Chaoyun Song

Wireless Internet of Things: Enabling Future Generation Connectivity and Communications

Wireless Communications and Mobile Computing

Wireless Internet of Things: Enabling Future Generation Connectivity and Communications

Lead Guest Editor: Mingbo (Michael) Niu
Guest Editors: Francois Chan, Hongzhi Guo, Changqing Wang, Salari Soheil, and Chaoyun Song

Contents

Hindawi
Wireless Communications and Mobile Computing
Volume 2022, Article ID 8885240, 12 pages
https://doi.org/10.1155/2022/8885240

Research Article

Multi-Tag Selection in Cognitive Ambient Backscatter Communications for Next-Generation IoT Networks

Mi Ji Kim, Junsu Kim, and Su Min Kim

Department of Electronics Engineering, Korea Polytechnic University, Siheung 15073, Republic of Korea

Correspondence should be addressed to Su Min Kim; suminkim@kpu.ac.kr

Received 18 September 2020; Revised 14 August 2021; Accepted 27 December 2021; Published 31 January 2022

Academic Editor: Francois Chan

In this paper, we propose multi-tag selection schemes to improve achievable rate of a secondary ambient backscatter communication (ABC) system with multiple tags and a single power beacon in cognitive radio (CR) environments. Using the secondary power beacon, which plays a role as radio frequency (RF) source when there is no ambient RF source signals, with spectrum sensing capability, the secondary ABC system determines operation modes according to activity of the licensed primary system. When the primary system is active, a tag is randomly selected due to a lack of channel information, while when it is inactive, the best tag maximizing achievable rate is selected using the secondary power beacon. Moreover, we apply a successive interference cancellation (SIC) technique when the secondary power beacon is able to work. The performance of the proposed multi-tag selection schemes is mathematically analyzed in terms of bit error rate (BER) and achievable rate. Finally, the performance of the proposed schemes is evaluated through simulations in terms of BER and achievable rate. It is shown that our approach can significantly outperform a conventional ABC system in CR environments, especially under a low-active primary system regime.

1. Introduction

As Internet of things (IoT) era is coming, the number of wireless devices constructing IoT networks is explosively increasing. This causes a serious shortage in spectrum resource which is necessarily required for wireless connectivity. In order to solve this problem, many researchers have been conducting studies to improve spectral efficiency for large-scale wireless communications.

Recently, an ambient backscatter communication (ABC) system exploiting existing radio frequency (RF) signals such as TV, FM radio, and Wi-Fi was proposed [1]. It is a very promising IoT technology to solve the spectrum shortage problem as it does not require additional spectrum for communications [2]. Moreover, it enables wireless transmissions with very low power since ABC devices do not require an RF transceiver at transmitter side. Therefore, it is also promising to solve a battery problem of wireless IoT devices with combination of energy harvesting technologies [3–7].

In the ABC system, a tag, a passive transmitter that is not equipped with an RF transceiver, can modulate and transmit wireless signals by adjusting antenna impedance. That is, if it adjusts the impedance to absorb or reflect the ambient RF signals, a bit "0" or "1" is modulated, respectively. More specifically, in reflecting state, the tag maximally reflects the ambient signals so that the received power level is high at the receiver, where it is regarded as bit "1." On the contrary, in absorbing state, the tag absorbs the ambient signals as much as possible so that the received power level at the receiver is low, which leads to decide bit "0."

So far, there have been many studies on the ABC systems with various ambient RF signals such as FM radio [1], Wi-Fi [8–10], Bluetooth [11], ultra-wideband (UWB) [12], OFDM signals [13], and so on. For a variety of ambient signals, many researchers have been studying on signal modulation and coding [13, 14], semi-coherent [15] and non-coherent [16] detections, and performance analysis and approximation [17–19]. Thereafter, they are extended to multi-antenna systems [20, 21], cooperative

communications [22, 23], and multi-tag environments [24–30].

So far, there have been several studies on multi-tag ABC systems. In [24], a location-based tag-reader paring scheme was proposed to enhance bit error rate (BER) performance of the proposed ABC system. In [25], employing a multiple-input multiple-output (MIMO) reader, a least-squares-based channel estimation protocol and a low complexity algorithm were proposed in order to obtain the optimal transceiver designs to maximize backscattered throughput among multiple single-antenna tags. To exploit a multi-user diversity gain, several tag selection schemes have been proposed. In [19], a tag selection scheme was proposed to maximize BER at the receiver and its BER performance is mathematically analyzed. In [27, 28], tag selection schemes were proposed to improve secrecy outage and data rate in a wire-tap channel with a single eavesdropper. In [29, 30], artificial noise-aided tag scheduling schemes were proposed in order to maximize the secrecy rate. These studies mainly focus on performance improvements in the perspective of physical layer security in wire-tap channels.

On the other hand, cognitive radio (CR) communication, which allows unlicensed systems to share and utilize the spectrum bands of the licensed primary system when it is idle, is another promising technology to solve the spectrum shortage problem [31, 32]. There have been many studies on resource allocation and management in CR networks [33]. Among them, medium access control (MAC) protocols are designed and proposed for multi-user environments in both centralized and distributed manners [34–37]. In CR networks, sensing the primary system and reporting the sensing results to a secondary fusion node are important issues. Accordingly, there are several studies on the performance improvements in primary sensing [38] and reporting [39]. Recently, there are also a few studies on ABC systems under CR environments [40–42]. In these studies, the ABC system plays a role as an unlicensed secondary system under CR restrictions, where the secondary system is able to access the primary channel when it is only allowed by the primary system.

More specifically, in [40], an adaptive harvest-then-transmit protocol was proposed for an RF-powered cognitive radio network. In the proposed protocol, backscattering, harvesting, and transmitting modes are adaptively controlled to enhance transmission rate. In [41], error-floor-free detectors were proposed to tackle direct link interference using a multi-antenna receive beamforming technique in a cognitive ABC network which consists of a single tag and a single receiver as a secondary ABC system in a CR environment. Most recently, in [42], a novel spectrum sharing system was proposed to maximize data rate of secondary backscatter transmission subject to a minimum rate requirement of the primary system by jointly optimizing the time sharing and power allocation parameters. The previous work considers a new paradigm for IoT networks as cognitive backscatter communications where the secondary system exploits existing RF signals transmitted from the primary system. However, its performance can be limited by activity of the primary system since if there is no RF source signals, no backscatter information can be transmitted. Moreover, in previous work, only a single tag is considered although a basic feature of IoT networks is to require massive number of IoT devices in the network.

In this paper, we consider a secondary ABC system with multiple tags and a single power beacon, which can opportunistically access wireless channel of the licensed primary system under CR requirements. In this concept, according to the activity of the primary system, we propose adaptive multi-tag selection schemes to improve the performance of the secondary ABC system in terms of bit error rate (BER) and achievable rate. Therefore, the proposed schemes can significantly improve the performance of the secondary ABC system, especially under a low-active primary system regime. The contributions of this paper are summarized as follows:

(i) Employing a power beacon in the secondary CR system, a novel multi-tag selection scheme is proposed in order to improve the achievable rate of the secondary system in overlay CR environments.

(ii) The performance of the proposed multi-tag selection scheme is mathematically analyzed in terms of BER and achievable rate of the secondary system.

(iii) Through extensive simulations, the performance of the proposed multi-tag selection scheme is evaluated. It is shown that the proposed scheme can obtain additional spectral efficiency by improving average BER and activity of the secondary system.

The rest of this paper is organized as follows. In Section 2, the system model considered is illustrated. The proposed multi-tag selection schemes are presented in Section 3, and their performance analysis is provided in Section 4. In Section 5, numerical results for performance evaluation are shown. Finally, we conclude this paper in Section 6.

2. System Model

Figure 1 shows a secondary ABC system in a CR environment where primary and secondary systems coexist. The licensed primary system consists of a single transmitter generating RF signals and a single receiver. The secondary system consists of a single power beacon that transmits additional RF signals, K tags, and a single receiver. The activity of the primary system, which is a ratio of busy and idle states, is denoted by $\nu \in [0, 1]$. In the secondary ABC system, there are two operation modes according to the primary activity. If the primary system is active, the secondary ABC system modulates backscatter bits using the RF signals sent from the primary transmitter, while if the primary system is idle, it modulates backscatter bits using the RF signals generated by the secondary power beacon.

By employing a new power beacon as a part of the secondary ABC system, the secondary tags are still able to modulate and transmit their information to the secondary receiver by using the RF signals from the secondary power beacon, even if the primary system is idle. To this end, the secondary power beacon is capable to sense the primary channel and it generates

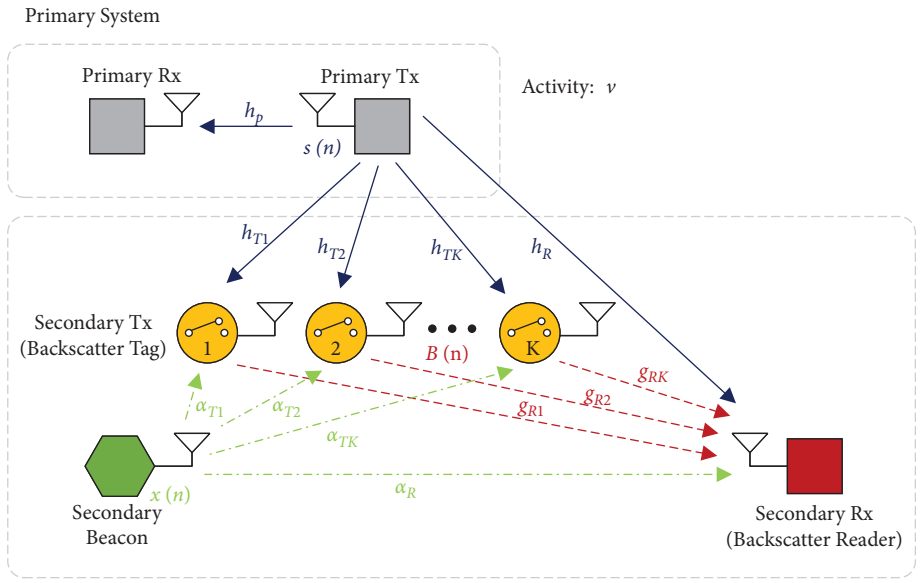

FIGURE 1: A cognitive ambient backscatter communication system with multiple tags and a single power beacon.

and transmits its own RF signals when the primary channel is decided as idle. Since the secondary power beacon is a part of the secondary system, the channel gains can be estimated at the secondary receiver using pilot signals, while it is impossible for the primary channel. Thus, we assume known channel information for the secondary power beacon and unknown channel information for the primary channel in this paper. It is worth noting that known channel information enables to apply for interference cancellation techniques.

In this system model, h_P, h_{T_i}, and h_R denote the channel gains between the primary transmitter and the primary receiver, the i-th tag, and the secondary receiver, respectively, α_{T_i} and α_R denote the channel gains between the secondary beacon and the i-th tag and the secondary receiver, respectively, and g_{R_i} denotes the channel gain between the i-th tag and the secondary receiver. We assume that all the channels suffer from i.i.d. block Rayleigh fading, i.e., $h_x \sim \mathcal{CN}(0, \sigma_{h_x}^2)$, $\alpha_x \sim \mathcal{CN}(0, \sigma_{\alpha_x}^2)$, $g_x \sim \mathcal{CN}(0, \sigma_{g_x}^2)$, $x \in \{R, T_i, R_i\}$, and $i \in \{1, 2, \ldots, K\}$, as in [26].

Figure 2 shows the frame structure of the secondary ABC system. In the training period, a preamble signal is transmitted to determine bit decision threshold values, Φ_0 and Φ_1, which imply the average received power values at the receiver when $B(n) = 0$ and $B(n) = 1$. That is, we consider a binary phase shift keying (BPSK) modulation for the secondary ABC system. A data frame consists of sensing, channel estimation, tag selection, and data transmission periods. In the sensing period, the secondary power beacon senses the primary channel using an energy detector (in this paper, we assume perfect sensing at the secondary power beacon; therefore, the performance of the proposed multi-tag selection scheme evaluated in this paper corresponds to the upper bound). Based on this, the primary activity is determined as either busy or idle. The channel gains h_x and α_x are estimated in the channel estimation period [43]. In the tag selection period, a single tag to transmit is scheduled. The channel estimation and tag selection are performed at the secondary receiver, and it is imformed to tags during the tag selection period. Finally, data transmission and detection are performed in the data transmission period. Note that since the secondary ABC system operates based on sensing at the secondary beacon, the secondary ABC system does not require synchronization with the primary system. However, the synchronization among the secondary beacon, multiple tags, and the secondary receiver is possible based on the frame structure in Figure 2.

3. Proposed Multi-Tag Selection Schemes

In this section, we propose multi-tag selection schemes to maximize achievable rate of the secondary ABC system considering the primary activity.

3.1. Tag Selection Schemes according to the Primary Activity

3.1.1. Status of the Primary System Is Busy. When the primary system is busy, the received signal at the secondary ABC receiver for the i-th tag and the n-th sample is given by

$$y(n) = h_R s(n) + \eta g_{R_i} h_{T_i} s(n) B(n) + \omega(n) = \begin{cases} h_R s(n) + \omega(n), & \text{if } B(n) = 0, \\ \left(h_R + \eta g_{R_i} h_{T_i}\right) s(n) + \omega(n), & \text{if } B(n) = 1, \end{cases} \quad (1)$$

where $s(n)$ denotes the primary RF signal, η denotes the antenna efficiency factor, $B(n)$ denotes the secondary backscatter bit, and $\omega(n)$ denotes the additive white Gaussian noise (AWGN) with zero mean and unit variance, i.e., $\omega(n) \sim \mathcal{CN}(0, \sigma_\omega^2)$. For this case, the channel estimation is impossible since the primary signal $s(n)$ is unknown at the secondary system. Thus, we randomly select a tag as follows:

$$i^* = \text{Uniform}(\{1, \ldots, K\}). \quad (2)$$

3.1.2. Status of the Primary System Is Idle. When the primary system is idle, we operate the secondary power beacon to

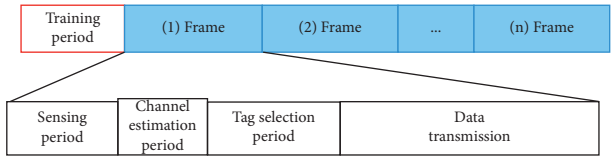

FIGURE 2: Frame structure of the secondary ABC system.

generate ambient RF signals artificially. Thus, the received signal at the secondary receiver for the i-th tag and the n-th sample is rewritten by

$$y(n) = \alpha_R x(n) + \eta g_{R_i} \alpha_{T_i} x(n) B(n) + \omega(n) = \begin{cases} \alpha_R x(n) + \omega(n), & \text{if } B(n) = 0, \\ \left(\alpha_R + \eta g_{R_i} \alpha_{T_i}\right) x(n) + \omega(n), & \text{if } B(n) = 1, \end{cases} \quad (3)$$

where $x(n)$ denotes the RF signal transmitted by the secondary power beacon.

Since the secondary power beacon is a part of the secondary system, the channel gains can be estimated for this case and we can employ a successive interference cancellation (SIC) technique at the secondary receiver. In the following, we present the proposed multi-tag selection schemes for both SIC-disabled and SIC-enabled cases.

(i) Tag selection without SIC: for this case, we apply a tag selection scheme maximizing BER proposed in [19]. Then, the selected tag is determined by

$$i^* = \arg\max_{i \in \{1,\ldots,K\}} \left| \left| \alpha_R + \eta \alpha_{T_i} g_{R_i} \right|^2 - \left| \alpha_R \right|^2 \right|. \quad (4)$$

(ii) Tag selection with SIC: for known $x(n)$, we can eliminate the interference term from the secondary power beacon based on the channel estimation [44]. This is possible since the power beacon is a part of the secondary system. Additionally, we assume the perfect channel estimation in order to investigate the performance upper bound. Then, the received signal for the i-th tag can be rewritten by

$$z(n) = y(n) - \widehat{\alpha}_R x(n) = \eta g_{R_i} \alpha_{T_i} x(n) B(n) + \omega(n) = \begin{cases} \omega(n), & \text{if } B(n) = 0, \\ \eta g_{R_i} \alpha_{T_i} x(n) + \omega(n), & \text{if } B(n) = 1, \end{cases} \quad (5)$$

where $\widehat{\alpha}_R$ is the estimated channel gain and with the perfect estimation, $\widehat{\alpha}_R = \alpha_R$. For this case, the best tag maximizing achievable rate is selected as follows:

$$i^* = \arg\max_{i \in \{1,\ldots,K\}} \left| \eta \alpha_{T_i} g_{R_i} \right|^2. \quad (6)$$

3.2. Detection Mechanism

3.2.1. Status of the Primary System Is Busy. When the primary system is busy, the decision thresholds, average received power levels during training period, for the i-th tag are determined by

$$\Phi_{0,i} = \frac{1}{N_0} \sum_{n=1}^{N_0} \left[\left| h_R \right|^2 P_s + \sigma_\omega^2 + 2 h_R s(n) \omega(n) \right], \quad (7)$$

$$\Phi_{1,i} = \frac{1}{N_0} \sum_{n=1}^{N_0} \left[\left| \mu_i \right|^2 P_s + \sigma_\omega^2 + 2 \mu_i s(n) \omega(n) \right], \quad (8)$$

where N_0 is the number of transmitted samples for a single backscatter bit during the training period, P_s is the average transmit power of the RF source signal $s(n)$, σ_ω^2 is the noise variance, and $\mu_i \triangleq h_R + \eta g_{R_i} h_{T_i}$. In the data transmission period, the selected i^*-th tag modulates and transmits a backscatter bit $B(n)$, and then the received signal at the secondary receiver is written by

$$y(n) = h_R s(n) + \eta g_{R_{i^*}} h_{T_{i^*}} s(n) B(n) + \omega(n). \quad (9)$$

The average received power at the secondary receiver during data transmission period can be calculated as

$$\Phi_B = \frac{1}{N_B} \sum_{n=1}^{N_B} |y(n)|^2 = \begin{cases} \left| h_R \right|^2 P_s + \sigma_\omega^2 + \Omega_{B_0}, & \text{if } B(n) = 0, \\ \left| \mu_{i^*} \right|^2 P_s + \sigma_\omega^2 + \Omega_{B_1}, & \text{if } B(n) = 1, \end{cases} \quad (10)$$

where

$$\Omega_{B_0} = \frac{2}{N_B} \sum_{n=1}^{N_B} \Re\left\{ h_R s(n) \omega(n)^H \right\}, \quad (11)$$

$$\Omega_{B_1} = \frac{2}{N_B} \sum_{n=1}^{N_B} \Re\left\{ \mu_{i^*} s(n) \omega(n)^H \right\}, \quad (12)$$

where N_B denotes the number of samples while transmitting a backscatter bit $B(n)$, $\Re(\cdot)$ denotes the real part of a complex number, and $(\cdot)^H$ is the conjugate and transpose operation. Note that the cross-correlation terms in (7), (8), (11), and (12) can be negligible for sufficiently large N_0 and N_B since $s(n)$ and $\omega(n)$ are statistically uncorrelated.

Finally, the backscattered bit $B(n)$ can be decoded at the secondary receiver with a comparison between the instantaneous average received power, Φ_B, and the threshold values, Φ_0 and Φ_1, as follows [17]:

$$\widehat{B}(n) = \begin{cases} 0, & \text{if } \left| \Phi_B - \Phi_{0,i^*} \right| \le \left| \Phi_B - \Phi_{1,i^*} \right|, \\ 1, & \text{if } \left| \Phi_B - \Phi_{0,i^*} \right| > \left| \Phi_B - \Phi_{1,i^*} \right|, \end{cases} = \begin{cases} 0, & \text{if } \Phi_B \le \xi, \\ 1, & \text{if } \Phi_B > \xi. \end{cases} \quad (13)$$

where $\xi = |h_R|^2 + |\mu_{i^*}|^2 / 2P_s$.

3.2.2. Status of the Primary System Is Idle. If the primary system is idle, the secondary power beacon is able to be active. Without SIC, the decision thresholds for the i-th tag are predetermined by

$$\Phi_{0,i} = \frac{1}{N_0}\sum_{n=1}^{N_0}\left[\left|\alpha_R\right|^2 P_x + \sigma_\omega^2 + 2\alpha_R x(n)\omega(n)\right],$$
$$\Phi_{1,i} = \frac{1}{N_0}\sum_{n=1}^{N_0}\left[\left|\varepsilon_i\right|^2 P_x + \sigma_\omega^2 + 2\varepsilon_i x(n)\omega(n)\right], \quad (14)$$

where P_x is the average transmit power of the secondary beacon signal $x(n)$, σ_ω^2 is the noise variance, and $\varepsilon_i \triangleq \alpha_R + \eta g_{R_i} h_{T_i}$. In the data transmission period, the received signal at the secondary receiver for the selected i^*-th tag is expressed as

$$y(n) = \alpha_R x(n) + \eta g_{R_{i^*}} \alpha_{T_{i^*}} x(n) B(n) + \omega(n). \quad (15)$$

Then, the average received power at the secondary receiver during data transmission period is calculated by

$$\Phi_B == \begin{cases} \left|\alpha_R\right|^2 P_x + \sigma_\omega^2 + \Omega'_{B0}, & \text{if } B(n) = 0, \\ \left|\varepsilon_{i^*}\right|^2 P_x + \sigma_\omega^2 + \Omega'_{B1}, & \text{if } B(n) = 1, \end{cases} \quad (16)$$

where

$$\Omega'_{B0} = \frac{2}{N_B}\sum_{n=1}^{N_B}\Re\left\{\alpha_R x(n)\omega(n)^H\right\},$$
$$\Omega'_{B1} = \frac{2}{N_B}\sum_{n=1}^{N_B}\Re\left\{\varepsilon_{i^*} x(n)\omega(n)^H\right\}. \quad (17)$$

Finally, the backscattered bit $B(n)$ can be decoded at the secondary receiver as follows:

$$\widehat{B}(n) = \begin{cases} 0, & \text{if } \Phi_B \le \xi', \\ 1, & \text{if } \Phi_B > \xi', \end{cases} \quad (18)$$

where $\xi' = |\alpha_R|^2 + |\varepsilon_{i^*}|^2/2P_x$.

With SIC, the decision thresholds for the i-th tag can be simplified as

$$\Phi_{0,i} = \frac{1}{N_0}\sum_{n=1}^{N_0}|\omega(n)|^2,$$
$$\Phi_{1,i} = \frac{1}{N_0}\sum_{n=1}^{N_0}\left|\eta g_{R_i}\alpha_{T_i} x(n) + \omega(n)\right|^2. \quad (19)$$

In the data transmission period, the received signal at the secondary receiver for the selected i^*-th tag is expressed as

$$y(n) = \eta g_{R_{i^*}} \alpha_{T_{i^*}} x(n) B(n) + \omega(n). \quad (20)$$

The average received power at the secondary receiver during data transmission period is rewritten by

$$\Phi_B = \begin{cases} \sigma_\omega^2, & \text{if } B(n) = 0, \\ \left|\rho_{i^*}\right|^2 P_x + \sigma_\omega^2 + \Omega''_{B1}, & \text{if } B(n) = 1, \end{cases} \quad (21)$$

where $\rho_i \triangleq \eta g_{R_i}\alpha_{T_i}$ and

$$\Omega''_{B_1} = \frac{2}{N_B}\sum_{n=1}^{N_B}\Re\left\{\rho_i x(n)\omega(n)^H\right\}. \quad (22)$$

Finally, the backscattered bit $B(n)$ can be decoded at the secondary receiver as follows:

$$\widehat{B}(n) = \begin{cases} 0, & \text{if } \Phi_B \le \xi'', \\ 1, & \text{if } \Phi_B > \xi'', \end{cases} \quad (23)$$

where $\xi'' = |\rho_{i^*}^2|/2P_x$.

4. Performance Analysis

In this section, we mathematically analyze the performance of the proposed multi-tag selection schemes in terms of BER and achievable rate. For analytical tractability, it is assumed that the channel between the selected tag and the secondary receiver, g_R, is line of sight and regarded as a constant as in [19]. This is reasonable since the distance between a tag and the secondary receiver is usually close in ABC networks.

4.1. Average BER. In this paper, BER is defined as a probability that the transmitted and estimated backscatter bits are not the same at the receiver. Thus, the BER for a single slot is expressed as

$$\begin{aligned} P_b &= \Pr\left(\widehat{B}(n) \ne B(n)\right) \\ &= \Pr\left(\widehat{B}(n) = 0 | B(n) = 1\right)\Pr\left(B(n) = 1\right) \\ &\quad + \Pr\left(\widehat{B}(n) = 1 | B(n) = 0\right)\Pr\left(B(n) = 0\right), \forall n. \end{aligned} \quad (24)$$

Note that bit "0" or "1" can be designed as equally probable in practice, and therefore $\Pr(B(n) = 0) = \Pr(B(n) = 1) = 0.5$ without loss of generality.

Hence, the average BER for a single frame which consists of multiple slots is given by

$$\begin{aligned} \overline{P}_b &= \mathbb{E}\left[P_b\right] = \mathbb{E}\left[\Pr\left(\widehat{B}(n) \ne B(n)\right)\right], \forall n, \\ &= \nu\overline{P}_b^{\text{busy}} + (1-\nu)\overline{P}_b^{\text{idle}}, \end{aligned} \quad (25)$$

where ν is the primary activity, $\overline{P}_b^{\text{busy}}$ is the average BER when the primary system is busy, and $\overline{P}_b^{\text{idle}}$ is the average BER when the primary system is idle.

In the following, we derive BER for a single slot and average BER when the primary system is either busy or idle. When it is idle, the secondary beacon is active in order to provide source RF signals. For this case, we also consider to employ the SIC technique in order to further improve the BER performance at the secondary receiver.

4.1.1. Random Tag Selection When the Primary System Is Busy. Let us recall $\mu_i \triangleq h_R + \eta g_{R_i} h_{T_i}$ and $\widetilde{\Phi}_B \triangleq \Phi_B - \sigma_\omega^2$. Similar to [19], for the selected i^*-th tag, if $|\mu_{i^*}|^2 > |h_R|^2$, conditional bit error probabilities of the energy detection are derived as

$$\begin{aligned}\Pr(\widehat{B}(n)=0|B(n)=1)&=\Pr\left(\widetilde{\Phi}_B<\xi|B(n)=1\right)\\&=\Pr\left(\Omega_{B_1}<-\frac{\left|\mu_{i^*}^2\right|-\left|h_R^2\right|}{2}P_s\right)\\&=Q\left(\frac{\left|\mu_{i^*}\right|^2-\left|h_R\right|^2}{\left|\mu_{i^*}\right|}\beta_s\right),\\\Pr(\widehat{B}(n)=1|B(n)=0)&=\Pr\left(\widetilde{\Phi}_B>\xi|B(n)=0\right)\\&=\Pr\left(\Omega_{B_0}>-\frac{\left|\mu_{i^*}\right|^2-\left|h_R\right|^2}{2}P_s\right)\\&=Q\left(\frac{\left|\mu_{i^*}\right|^2-\left|h_R\right|^2}{\left|h_R\right|}\beta_s\right),\end{aligned}\tag{26}$$

where $\xi=|h_R|^2+|\mu_{i^*}|^2/2P_s$ and $\beta_s=\sqrt{8\sigma_\omega^2/N_BP_s}$.

If $|\mu_{i^*}|^2<|h_R|^2$, they are rewritten, respectively, by

$$\begin{aligned}\Pr(\widehat{B}(n)=0|B(n)=1)&=Q\left(-\frac{\left|\mu_{i^*}\right|^2-\left|h_R\right|^2}{\left|\mu_{i^*}\right|}\beta_s\right),\\\Pr(\widehat{B}(n)=1|B(n)=0)&=Q\left(-\frac{\left|\mu_{i^*}\right|^2-\left|h_R\right|^2}{\left|h_R\right|}\beta_s\right).\end{aligned}\tag{27}$$

Substituting (32)–(35) into (24) and assuming $\Pr(B(n)=1)=\Pr(B(n)=0)=0.5$, BER for a single slot can be derived as

$$P_b^{\text{busy}}=\frac{1}{2}\left[Q\left(\frac{\left|\left|\mu_{i^*}\right|^2-\left|h_R\right|^2\right|}{\left|\mu_{i^*}\right|}\beta_s\right)+Q\left(\frac{\left|\left|\mu_{i^*}\right|^2-\left|h_R\right|^2\right|}{\left|h_R\right|}\beta_s\right)\right].\tag{28}$$

Thus, average BER over all slots is obtained as

$$\begin{aligned}\overline{P}_b^{\text{busy}}&=\mathbb{E}\left[P_b^{\text{busy}}\right]\\&=\frac{1}{2}\left[\int_0^\infty Q(\beta_s m)f_{M_1}(m)\,\mathrm{d}m+\int_0^\infty Q(\beta_s n)f_{N_1}(n)\,\mathrm{d}n\right],\end{aligned}\tag{29}$$

where $M_1=||\mu_{i^*}|^2-|h_R|^2|/|\mu_{i^*}|$ and $N_1=||\mu_{i^*}|^2-|h_R|^2|/|h_R|$.

Unfortunately, since the channel gains are not known exactly, it is hard to find the exact PDFs of M_1 and N_1. However, the average BER can be approximated as [19]

$$\overline{P}_b^{\text{busy}}\approx\frac{1}{2}\int_0^\infty\left[Q(\beta_1 z)+Q(\beta_2 z)\right]f_{|Y_{i^*}|}(z)\,\mathrm{d}z,\tag{30}$$

where $\beta_{s,1}=\beta_s/C_1\sigma_{\mu_{i^*}}$, $\beta_{s,2}=\beta/C_2\sigma_{h_R}$, $\beta_s=\sqrt{8\sigma_\omega^2/N_BP_s}$, and C_1 and C_2 are constants that are determined by the number of tags and channel variances. Here, since we select a tag randomly, assuming i.i.d. block Rayleigh fading, the PDF of $|Y_{i^*}|$ is obtained by

$$f_{|Y_{i^*}|}(y)=\frac{1}{\sigma_{\mu_{i^*}}^2+\sigma_{h_R}^2}\left(e^{-1/\sigma_{\mu_{i^*}}^2y}+e^{-1/\sigma_{h_R}^2y}\right),\quad y>0,\tag{31}$$

where $Y_{i^*}\triangleq|\mu_{i^*}|^2-|h_R|^2$.

4.1.2. Tag Selection without SIC When the Primary System Is Idle. Hereafter, we derive average BER without employing the SIC technique when the primary system is inactive.

Let us recall $\varepsilon_i\triangleq\alpha_R+\eta g_{R_i}\alpha_{T_i}$ and $\widetilde{\Phi}_B\triangleq\Phi_B-\sigma_\omega^2$. Similar to the BER derivation when the primary system is busy, for the selected i^*-th tag, if $|\varepsilon_{i^*}|^2>|\alpha_R|^2$, conditional bit error probabilities of the energy detection are derived as

$$\Pr(\widehat{B}(n)=0|B(n)=1)=Q\left(\frac{\left|\varepsilon_{i^*}\right|^2-\left|\alpha_R\right|^2}{\left|\varepsilon_{i^*}\right|}\beta_x\right),\tag{32}$$

$$\Pr(\widehat{B}(n)=1|B(n)=0)=Q\left(\frac{\left|\varepsilon_{i^*}\right|^2-\left|\alpha_R\right|^2}{\left|\alpha_R\right|}\beta_x\right),\tag{33}$$

where $\xi'=|\alpha_R|^2+|\varepsilon_{i^*}|^2/2P_x$ and $\beta_x=\sqrt{8\sigma_\omega^2/N_BP_x}$.

If $|\varepsilon_{i^*}|^2<|\alpha_R|^2$, they are rewritten, respectively, by

$$\Pr(\widehat{B}(n)=0|B(n)=1)=Q\left(-\frac{\left|\varepsilon_{i^*}\right|^2-\left|\alpha_R\right|^2}{\left|\varepsilon_{i^*}\right|}\beta_x\right),\tag{34}$$

$$\Pr(\widehat{B}(n)=1|B(n)=0)=Q\left(-\frac{\left|\varepsilon_{i^*}\right|^2-\left|\alpha_R\right|^2}{\left|\alpha_R\right|}\beta_x\right).\tag{35}$$

Substituting (32)–(35) into (24) and assuming $\Pr(B(n)=1)=\Pr(B(n)=0)=0.5$, BER for a single slot can be derived as

$$P_b^{\text{idle}}=\frac{1}{2}\left[Q\left(\frac{\left|\left|\varepsilon_{i^*}\right|^2-\left|\alpha_R\right|^2\right|}{\left|\varepsilon_{i^*}\right|}\beta_x\right)+Q\left(\frac{\left|\left|\varepsilon_{i^*}\right|^2-\left|\alpha_R\right|^2\right|}{\left|\alpha_R\right|}\beta_x\right)\right].\tag{36}$$

Thus, average BER over all slots is obtained as

$$\overline{P}_b^{\text{idle}}=\mathbb{E}\left[P_b^{\text{idle}}\right]=\frac{1}{2}\left[\int_0^\infty Q(\beta_x m)f_{M_2}(m)\,\mathrm{d}m+\int_0^\infty Q(\beta_x n)f_{N_2}(n)\,\mathrm{d}n\right],\tag{37}$$

where $M_2 = ||\varepsilon_{i^*}|^2 - |\alpha_R|^2|/|\varepsilon_{i^*}|$ and $N_2 = ||\varepsilon_{i^*}|^2 - |\alpha_R|^2|/|\alpha_R|$.

Since it is hard to find the exact PDFs of M_2 and N_2, using Theorem 1 in [19], the average BER can be approximated as

$$\overline{P}_b^{\text{idle}} \approx \frac{1}{2}\int_0^{\infty}\left[Q\left(\beta_{x,1}z\right) + Q\left(\beta_{x,2}z\right)\right] f_{|Z_{i^*}|}(z)\,\mathrm{d}z, \tag{38}$$

where $Z_{i^*} \triangleq |\varepsilon_{i^*}|^2 - |\alpha_R|^2$, $\beta_{x,1} = \beta_x/D_1\sigma_{\varepsilon_{i^*}}$, $\beta_{x,2} = \beta_x/D_2\sigma_{\alpha_R}$, $\beta_x = \sqrt{8\sigma_\omega^2/N_B P_s}$, and D_1 and D_2 are constants that are determined by the number of tags and channel variances. For this case, since the best tag i^* is selected according to (6), the PDF of $|Z_{i^*}|$ is obtained by [19]

$$f_{|Z_{i^*}|}(z) = \frac{K}{\sigma_{\varepsilon_{i^*}}^2 + \sigma_{\alpha_R}^2}\left(e^{-1/\sigma_{\varepsilon_{i^*}}^2 z} + e^{-1/\sigma_R^2 z}\right)$$

$$\cdot\left(1 - \frac{\sigma_{\varepsilon_{i^*}}^2}{\sigma_{\varepsilon_{i^*}}^2 + \sigma_{\alpha_R}^2}e^{-1/\sigma_{\varepsilon_{i^*}}^2 z} - \frac{\sigma_{\alpha_R}^2}{\sigma_{\varepsilon_{i^*}}^2 + \sigma_{\alpha_R}^2}e^{-1/\sigma_{\alpha_R}^2 z}\right)^{K-1}, \quad z > 0, \tag{39}$$

where K denotes the number of tags.

4.1.3. Tag Selection with SIC When the Primary System Is Idle. When SIC is employed, since the interference from the RF source is eliminated, the analysis can be simplified. Similar to the case without SIC, we first define $\rho_i \triangleq \eta g_{R_i}\alpha_{T_i}$ and $\widetilde{\Phi}_B \triangleq \Phi_B - \sigma_\omega^2$. Since $|\rho_i|^2 > 0$, the BER for a single slot can be obtained as

$$\begin{aligned}\Pr\left(\widehat{B}(n) = 0 | B(n) = 1\right) &= \Pr\left(\widetilde{\Phi}_B < \xi'' | B(n) = 1\right)\\ &= \Pr\left(\Omega_{B_1}'' < -\frac{|\rho_{i^*}|^2}{2}P_x\right)\\ &= Q\left(|\rho_{i^*}|\beta\right),\end{aligned} \tag{40}$$

$$\begin{aligned}\Pr\left(\widehat{B}(n) = 1 | B(n) = 0\right) &= \Pr\left(\widetilde{\Phi}_B > \xi'' | B(n) = 0\right)\\ &= \Pr\left(\Omega_{B_0}'' > -\frac{|\rho_{i^*}|^2}{2}P_x\right) = 0,\end{aligned} \tag{41}$$

where $\beta_x = \sqrt{8\sigma_\omega^2/N_B P_x}$.

Substituting (40) and (41) into (24) and assuming $\Pr(B(n) = 1) = \Pr(B(n) = 0) = 0.5$, BER for a single slot can be simplified as

$$P_b^{\text{idle}} = \frac{1}{2}Q\left(|\rho_{i^*}|\beta_x\right). \tag{42}$$

Finally, the average BER for all slots is obtained as

$$\overline{P}_b^{\text{idle}} = \mathbb{E}\left[P_b^{\text{idle}}\right] = \frac{1}{2}\int_0^{\infty} Q\left(|\rho_{i^*}|\beta_x\right) f_{|\rho_{i^*}|}(z)\,\mathrm{d}z, \tag{43}$$

where

$$f_{|\rho_{i^*}|}(z) = \frac{1}{\sigma_{\rho_{i^*}}^2}\left(e^{-1/\sigma_{\rho_{i^*}}^2 z}\right)\left(1 - e^{-1/\sigma_{\rho_{i^*}}^2 z}\right)^{K-1}, \quad z > 0, \tag{44}$$

and $\sigma_{\rho_{i^*}}^2 = \eta^2\sigma_{\alpha_{T_{i^*}}}^2\sigma_{g_{R_{i^*}}}^2$ and K is the number of tags.

4.2. Average Achievable Rate. Based on the obtained BERs, average achievable rate of the secondary ABC system is expressed as

$$\overline{R}_B^x = R_s\frac{N_B\left(1 - \overline{P}_b^x\right)}{N_{\text{tot}}}, \; x \in \{\text{busy, idle}\}, \tag{45}$$

where R_s is the source data rate of the primary signal $s(n)$, N_B is the number of backscattered bits, and N_{tot} is the total number of transmitted bits. $\overline{P}_b^x$ are obtained in (30), (38), and (43).

Finally, the average achievable rate of the proposed secondary ABC systems is expressed as

$$\overline{R}_B = \nu\overline{R}_B^{\text{busy}} + (1 - \nu)\overline{R}_B^{\text{idle}}, \tag{46}$$

where ν is the primary activity.

5. Numerical Results

In this section, we evaluate the performance of the proposed multi-tag selection schemes in terms of BER and average achievable rate of the secondary ABC system through simulations. Throughout the simulations, we set unit i.i.d. channel gains for all the links, i.e., $\sigma_{h_x}^2 = \sigma_{\alpha_x}^2 = \sigma_{R_x}^2 = 1$, $i \in \{1, 2, \ldots, K\}$.

Figures 3 and 4 show the BER and the average achievable rate of the secondary ABC system for varying primary activity when the number of tags $K = 8$ and SNR = 15 dB. When the primary system is always busy, i.e., $\nu = 1$, all the schemes obtain the same BER and achievable rate. However, as shown in Figure 4, as the primary activity decreases, the achievable rate of the conventional scheme significantly degrades due to absence of ambient RF source signals, while those of the proposed multi-tag selection schemes are kept or even improved with SIC. Especially, for the proposed multi-tag selection scheme with SIC, the BER is further improved as the primary activity is decreased, while the BERs of both the proposed multi-tag selection scheme without SIC and the conventional scheme are almost maintained as the primary activity is getting low as shown in Figure 3. As a result, the proposed cognitive ABC system with multi-tag selection schemes can provide significantly improved achievable rate even under limited spectrum resource.

Figures 5 and 6 show the BER and the average achievable rate of the secondary ABC system for varying SNR when $\nu = 0.1$. In Figure 5, it is shown that the BERs of the proposed multi-tag selection schemes with and without SIC are reduced, as the number of tags increases due to a selection diversity gain, while that of the conventional scheme is invariant. In addition, the proposed multi-tag selection scheme with SIC significantly outperforms that without SIC in high SNR regime. On the other hand, as shown in Figure 6, the achievable rate of the conventional scheme is very small with low primary activity, regardless of SNR and the number of tags. On the contrary, the proposed multi-tag selection schemes provide sufficient achievable rates in the whole range of SNRs. Furthermore, they can obtain a selection diversity gain, and thus their achievable rates

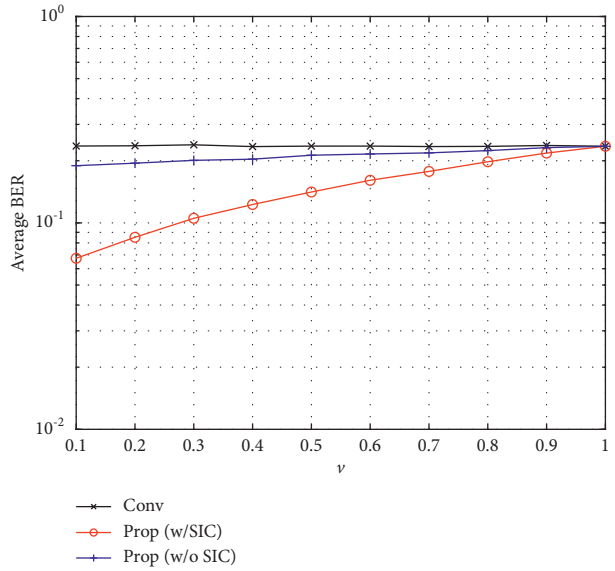

Figure 3: Average BER of the secondary ABC system for varying primary activity (K = 8 and SNR = 15 dB).

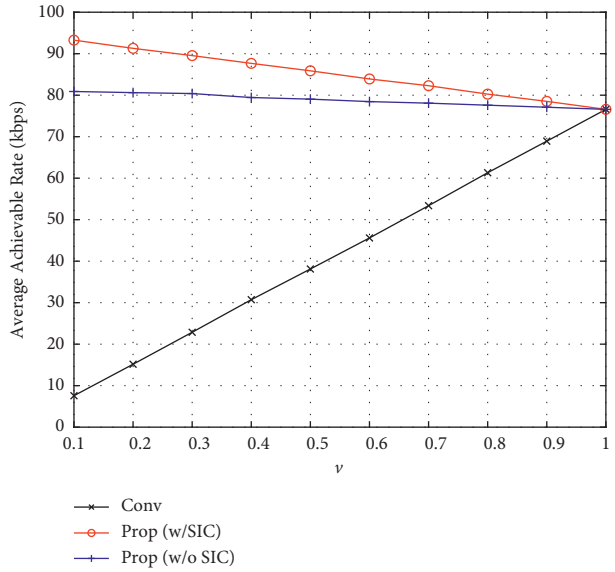

Figure 4: Average achievable rate of the secondary ABC system for varying primary activity (K = 8 and SNR = 15 dB).

increase as the number of tags increases, regardless of the primary activity. Additionally, the proposed multi-tag selection scheme with SIC always outperforms that without SIC thanks to the improved BER performance.

Figures 7 and 8 show the BER and the average achievable rate of the secondary ABC system for varying the number of tags when ν = 0.3 and SNR = 15 dB. In the figures, it is shown that the BERs and the achievable rates of the proposed multi-tag selection schemes are almost converged to the best performance when the number of tags is more than five. This implies that only a small number of tags are enough to achieve sufficiently good performance. On the contrary, the BER of the conventional scheme is not affected by the number of tags and its average rate is significantly low, compared to those of the proposed multi-tag selection schemes with and without SIC. This is because in the conventional scheme, the secondary ABC system cannot operate during idle period of the primary system due to absence of the ambient RF source signal. However, in the proposed multi-tag selection-based cognitive ABC system, a power beacon with spectrum sensing capability for the primary channel can provide the ambient RF source signal to the tags, although the primary system is silent.

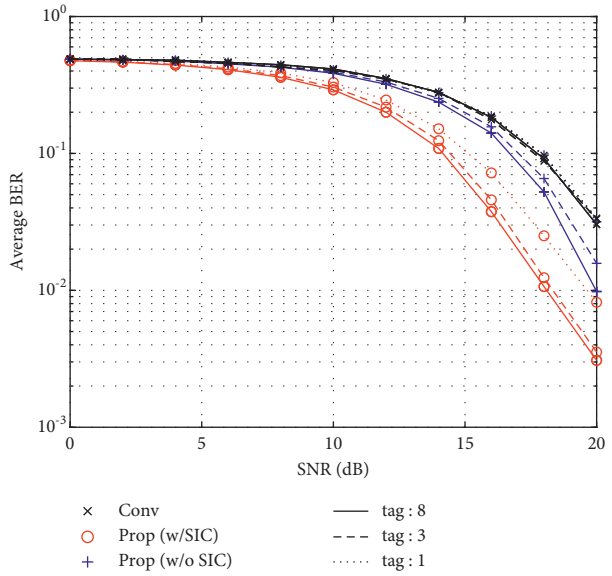

Figure 5: Average BER of the secondary ABC system for varying SNR ($\nu = 0.1$).

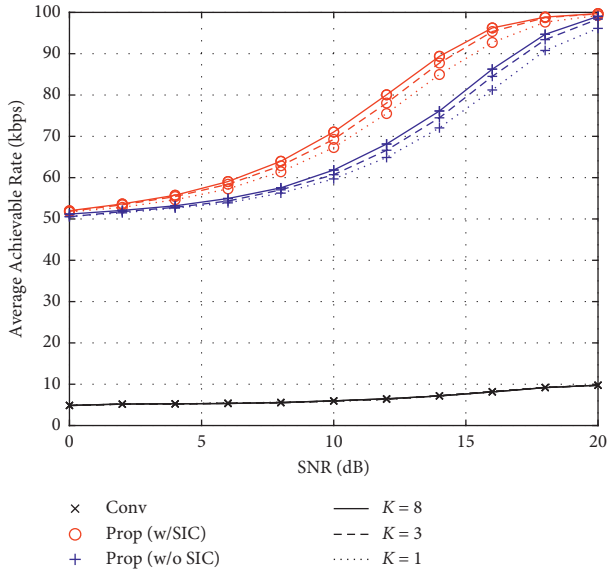

Figure 6: Average achievable rate of the secondary ABC system for varying SNR ($\nu = 0.1$).

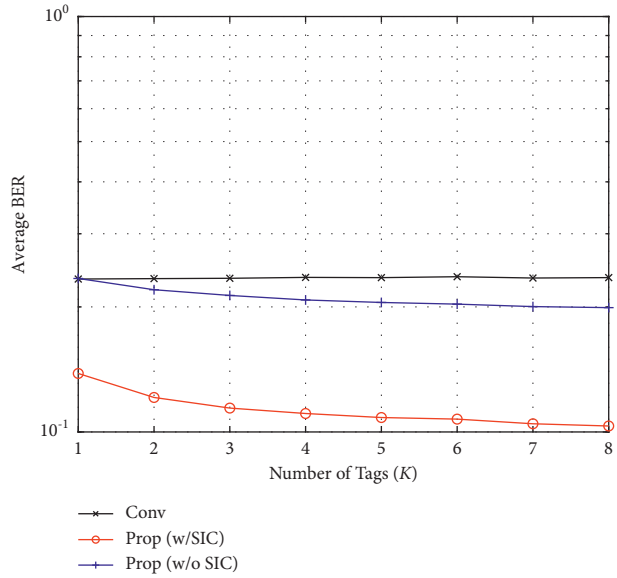

Figure 7: Average BER of the secondary ABC system for varying number of tags ($\nu = 0.3$ and SNR = 15 dB).

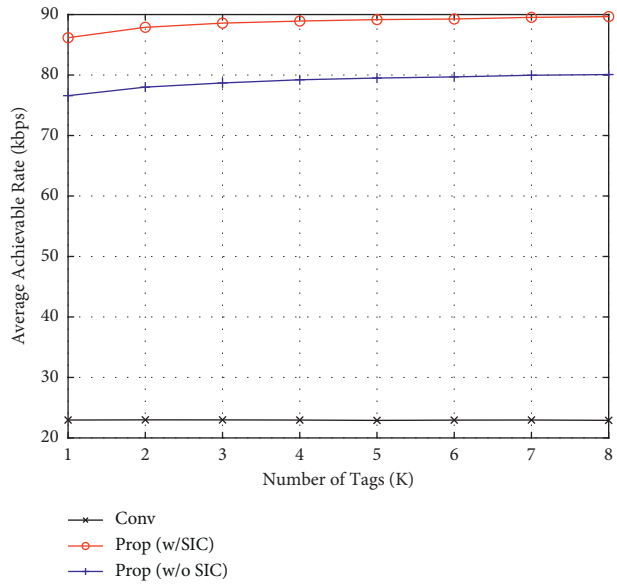

Figure 8: Average achievable rate of the secondary ABC system for varying number of tags ($\nu = 0.3$ and SNR = 15 dB).

6. Conclusion

In this paper, we proposed multi-tag selection schemes to improve the achievable rate of a secondary ABC system under CR environments. The performance of the proposed schemes was mathematically derived and evaluated through simulations. It is shown that the proposed multi-tag selection scheme without SIC can significantly improve the performance, compared to the conventional scheme, thanks to additional secondary power beacon and selection diversity gain. By applying SIC, it is further enhanced with reduced BER performance obtained from an interference cancellation technique. Further work will allow the power beacon to control the transmit power level and optimize it under given power constraint in order to design an energy-efficient secondary ABC system. In addition, incorporation of energy harvesting or conservation strategies for the secondary power beacon can be also considered. Furthermore, the impact of imperfect sensing at the secondary power beacon and machine learning-based detecting approaches for imperfect channel information conditions can be another research topic.

Data Availability

The data used to support the finding of this study are included within the article.

Conflicts of Interest

The authors declare that they have no conflicts of interest.

Acknowledgments

This study was supported in part by the MSIT, Korea, under the ITRC Support Program (IITP-2021-2018-0-01 426) supervised by the IITP and in part by the National Research Foundation of Korea (NRF) grant funded by the Korean Government (MSIT) (no. 2019R1F1A1059125).

References

[1] V. Liu, A. N. Parks, V. Talla, S. Gollakota, D. Wetherall, and J. R. Smith, "Ambient backscatter: wireless communication out of thin air," in *Proceedings of the ACM Special Interest Group on Data Communication (SIGCOMM)*, Hong Kong, China, August 2013.

[2] N. Van Huynh, D. T. Hoang, X. Lu, D. Niyato, P. Wang, and D. I. Kim, "Ambient backscatter communications: a contemporary survey," *IEEE Communications Surveys & Tutorials*, vol. 20, no. 4, pp. 2889–2922, 2018.

[3] X. Lu, P. Wang, D. Niyato, D. I. Kim, and Z. Han, "Wireless networks with RF energy harvesting: a contemporary survey," *IEEE Communications Surveys & Tutorials*, vol. 17, no. 2, pp. 757–789, 2015.

[4] P. Kamalinejad, C. Mahapatra, Z. Sheng, S. Mirabbasi, V. C. M. Leung, and Y. L. Guan, "Wireless energy harvesting for the internet of things," *IEEE Communications Magazine*, vol. 53, no. 6, pp. 102–108, 2015.

[5] I. Bang, S. M. Kim, and D. K. Sung, "Adaptive multiuser scheduling for simultaneous wireless information and power transfer in a multicell environment," *IEEE Transactions on Wireless Communications*, vol. 16, no. 11, pp. 7460–7474, 2017.

[6] K. Han and K. Huang, "Wirelessly powered backscatter communication networks: modeling, coverage, and capacity," *IEEE Transactions on Wireless Communications*, vol. 16, no. 4, pp. 2548–2561, 2017.

[7] A. N. Parks, A. Liu, S. Gollakota, and J. R. Smith, "Turbocharging ambient backscatter communication," *ACM Special Interest Group on Data Communication (SIGCOMM)*, vol. 444, 2014.

[8] B. Kellogg, A. Parks, S. Gollakota, J. R. Smith, and D. Wetherall, "Wi-Fi backscatter: internet connectivity for RF-powered devices," *ACM Special Interest Group on Data Communication (SIGCOMM)*, vol. 44, no. 4, 2014.

[9] D. Bharadia, K. R. Joshi, M. Kotaru, and S. Katti, "BackFi: high throughput WiFi backscatter," *ACM Special Interest Group on Data Communication (SIGCOMM)*, vol. 45, no. 4, 2015.

[10] B. Kellogg, V. Talla, S. Gollakota, and J. R. Smith, "Passive wi-fi: bringing low power to wi-fi transmissions," *USENIX Symposium on Networked Systems Design and Implementation (NSDI)*, vol. 20, no. 3, 2016.

[11] V. L. V. Talla, B. Kellogg, S. Gollakota, and J. R. Smith, "Inter-technology backscatter: towards Internet connectivity for implanted devices," in *Proceedings of the ACM Special Interest Group on Data Communication (SIGCOMM)*, Hong Kong, China, August 2016.

[12] C. Yang, J. Gummeson, and A. Sample, "Riding the airways: ultra-wideband Ambient backscatter via commercial broadcast systems," in *Proceedings of the IEEE International Conference on Computer Communications (INFOCOM)*, Atlanta, GA, USA, May 2017.

[13] G. Yang, Y.-C. Liang, R. Zhang, and Y. Pei, "Modulation in the air: backscatter communication over ambient OFDM carrier," *IEEE Transactions on Communications*, vol. 66, no. 3, pp. 1219–1233, 2018.

[14] Y. Liu, G. Wang, Z. Dou, and Z. Zhong, "Coding and detection schemes for ambient backscatter communication systems," *IEEE Access*, vol. 5, pp. 4947–4953, 2017.

[15] J. Qian, F. Gao, G. Wang, S. Jin, and H. Zhu, "Semi-coherent detection and performance analysis for ambient backscatter system," *IEEE Transactions on Communications*, vol. 65, no. 12, pp. 5266–5279, 2017.

[16] J. Qian, F. Gao, G. Wang, S. Jin, and H. Zhu, "Noncoherent detections for ambient backscatter system," *IEEE Transactions on Wireless Communications*, vol. 16, no. 3, pp. 1412–1422, 2017.

[17] G. Wang, F. Gao, R. Fan, and C. Tellambura, "Ambient backscatter communication systems: detection and performance analysis," *IEEE Transactions on Communications*, vol. 64, no. 11, pp. 4836–4846, 2016.

[18] W. Zhao, G. Wang, R. Fan, L.-S. Fan, and S. Atapattu, "Ambient backscatter communication systems: capacity and outage performance analysis," *IEEE Access*, vol. 6, pp. 22695–22704, 2018.

[19] X. Zhou, G. Wang, Y. Wang, and J. Cheng, "An approximate BER analysis for ambient backscatter communication systems with tag selection," *IEEE Access*, vol. 5, pp. 22552–22558, 2017.

[20] H. Guo, Q. Zhang, S. Xiao, and Y.-C. Liang, "Exploiting multiple antennas for cognitive ambient backscatter communication," *IEEE Internet of Things Journal*, vol. 6, no. 1, pp. 765–775, 2019.

[21] R. Long, G. Yang, Y. Pei, and R. Zhang, "Transmit beamforming for cooperative ambient backscatter communication

systems," in *Proceedings of the IEEE Global Communications Conference (Globecom)*, Singapore, December 2017.

[22] G. Yang, Q. Zhang, and Y. C. Liang, "Cooperative ambient backscatter communications for green internet-of-things," *IEEE Internet of Things Journal*, vol. 5, no. 2, pp. 1116–1130, 2018.

[23] G. Yang, Y. C. Liang, and Q. Zhang, "Cooperative receiver for ambient backscatter communications with multiple antennas," in *Proceedings of the IEEE International Conference on Communications (ICC)*, Paris, France, May 2017.

[24] K. H. Jang, S. M. Kim, and J. Kim, "Performance analysis of multi-tag multi-reader ambient backscatter communication systems," in *Proceedings of the IEEE International Conference on Ubiquitous and Future Networks (ICUFN)*, Zagreb, Croatia, July 2019.

[25] D. Mishra and E. G. Larsson, "Multi-tag backscattering to MIMO reader: channel estimation and throughput fairness," *IEEE Transactions on Wireless Communications*, vol. 18, no. 12, pp. 5584–5599, 2019.

[26] Y. Zhang, F. Gao, L. Fan, X. Lei, and G. K. Karagiannidis, "Secure communications for multi-tag backscatter systems," *IEEE Wireless Communications Letters*, vol. 8, no. 4, pp. 1146–1149, 2019.

[27] Y. Liu, Y. Ye, and R. Q. Hu, "Secrecy outage probability in backscatter communication systems with tag selection," *IEEE Communications Letters*, vol. 10, no. 10, 2021.

[28] Y. Jia, W. Gongpu, and Z. Zhangdui, "Physical layer security enhancing transmission protocol against eavesdropping for ambient backscatter communication system," in *Proceedings of the IET International Conference on Wireless, Mobile, and Multimedia Networks (ICWMMN)*, Beijing, China, April 2015.

[29] J. Y. Han, J. Kim, and S. M. Kim, "Physical layer security improvement using artificial noise-aided tag scheduling in ambient backscatter communication systems," in *Proceedings of the IEEE International Conference on Ubiquitous and Future Networks (ICUFN)*, Zagreb, Croatia, July 2019.

[30] J. Y. Han, M. J. Kim, J. Kim, and S. M. Kim, "Physical layer security in multi-tag ambient backscatter communications—jamming vs. coooperation," in *Proceedings of the IEEE Wireless Communications and Networking Conference (WCNC)*, Seoul, South Korea, May 2020.

[31] J. Mitola and G. Q. Maguire, "Cognitive radio: making software radios more personal," *IEEE Personal Communications*, vol. 6, no. 4, pp. 13–18, 1999.

[32] S. Haykin, "Cognitive radio: brain-empowered wireless communications," *IEEE Journal on Selected Areas in Communications*, vol. 23, no. 2, pp. 201–220, 2005.

[33] A. Ahmad, S. Ahmad, M. H. Rehmani, and N. U. Hassan, "A survey on radio resource allocation in cognitive radio sensor networks," *IEEE Communications Surveys & Tutorials*, vol. 17, no. 2, pp. 888–917, 2015.

[34] A. De Domenico, E. Calvanese Strinati, and M.-G. Di Benedetto, "A survey on MAC strategies for cognitive radio networks," *IEEE Communications Surveys & Tutorials*, vol. 14, no. 1, pp. 21–44, 2012.

[35] S. Jha, M. Rashid, V. Bhargava, and C. Despins, "Medium access control in distributed cognitive radio networks," *IEEE Wireless Communications*, vol. 18, no. 4, pp. 41–51, 2011.

[36] L. T. Tan and L. B. Le, "Distributed MAC protocol for cognitive radio networks: design, analysis, and optimization," *IEEE Transactions on Vehicular Technology*, vol. 60, no. 8, pp. 3990–4003, 2011.

[37] S. M. Kim and J. Kim, "Adaptive sensing period based distributed medium access control for cognitive radio networks," *IEICE—Transactions on Communications*, vol. E97-B, no. 11, pp. 2502–2511, 2014.

[38] N. Gul, M. S. Khan, J. Kim, and S. M. Kim, "Robust spectrum sensing via double-sided neighbor distance based on genetic algorithm in cognitive radio networks," *"Mobile Information Systems*, vol. 2020, Article ID 8876824, 10 pages, 2020.

[39] M. S. Khan, J. Kim, E. H. Lee, and S. M. Kim, "An efficient contention-window based reporting for Internet of things features in cognitive radio networks," *Wireless Communications and Mobile Computing*, vol. 20199 pages, 2019.

[40] D. T. Hoang, D. Niyato, P. Wang, D. I. Kim, and Z. Han, "Ambient backscatter: a new approach to improve network performance for RF-powered cognitive radio networks," *IEEE Transactions on Communications*, vol. 65, no. 9, pp. 3659–3674, 2017.

[41] H. Guo, Q. Zhang, S. Xiao, and Y.-C. Liang, "Multi-antenna beamforming receiver for cognitive ambient backscatter communications," in *Proceedings of the IEEE Global Communications Conference (Globecom)*, Abu Dhabi, United Arab Emirates, December 2018.

[42] H. Guo, R. Long, and Y.-C. Liang, "Cognitive backscatter network: a spectrum sharing paradigm for passive IoT," *IEEE Wireless Communications Letters*, vol. 8, no. 5, 2019.

[43] T. Taesang Yoo and A. Goldsmith, "Capacity and power allocation for fading MIMO channels with channel estimation error," *IEEE Transactions on Information Theory*, vol. 52, no. 5, pp. 2203–2214, 2006.

[44] X. Kang, H. F. Chong, Y.-K. Chia, and S. Sun, "Ergodic sum-rate maximization for fading cognitive multiple-access channels without successive interference cancelation," *IEEE Transactions on Vehicular Technology*, vol. 64, no. 9, pp. 4009–4018, 2015.

Hindawi
Wireless Communications and Mobile Computing
Volume 2021, Article ID 8847008, 11 pages
https://doi.org/10.1155/2021/8847008

Research Article

The Design of a Class of Nonlinear Networked System

Biao Wang, Xing Zhao, Changbo Li, Ji Ke, Yude Qin, Hao Wu, and Hang Yang

College of Electronic & Control Engineering Chang'an University, Xi'an, China

Correspondence should be addressed to Biao Wang; wangbiao@chd.edu.cn

Received 15 September 2020; Revised 29 January 2021; Accepted 18 February 2021; Published 11 March 2021

Academic Editor: Changqing Wang

A class of nonlinear networked systems with external interference is designed in this paper. Currently, we have witnessed that networked control technology has played a key role in the Internet of Things (IoT). However, the amount of big data in the Internet of Things will cause network congestion in the data transmission of the network control system. In order to solve this problem, event-driven control scheme can effectively save the network resources of the network control system. But when there is interference in the system, the conventional constant threshold parameter is difficult to achieve the expected energy-saving effect. In order to solve this challenge, this paper proposes a design with a continuously variable threshold. After each trigger to transmit data, the threshold gets changed accordingly, and the sliding mode approach rate is changed simultaneously. Compared with the constant threshold event drive, the number of transmissions in this design can be greatly reduced, while sliding mode jitter is suppressed. The simulation results show that the scheme can achieve higher resource utilization efficiency and better robustness.

1. Introduction

In recent years, we have witnessed the rapid development of the Internet of Things (IoT). By 2020, the surge in mobile devices is expected to exceed 50 billion. NCS research plays a key role in this field. At present, networked-control systems (NCSs), including multiloop NCSs, are extensively used. Their systems have the advantages of high reliability, high system flexibility, and low installation and maintenance costs [1–6]. Network control systems are used in many fields, such as mobile sensor networks [7], intelligent transportation systems [8], remote network control technologies [9], and theoretical results in [2, 3, 10] and other applications. In general, for the control of IoT, the collection and processing of data are very important. Note that with the emergence of IoT, the captured data will increase significantly. In the network control system (NCS), when the network is congested, phenomena such as jitter, packet loss, and transmission delay are particularly prone to occur [11–13], leading to poor performance of the network control system. Therefore, it is urgent to design a reasonable control scheme to reduce data transmission on the network. This solution should ensure that the network control system still has satisfactory performance even in the presence of uncertainty and delayed transmission.

In the past few decades, scientific literature has proposed several control schemes to save communication network transmission resources [14–16]. Event driving (ED) is one of the widely recognized and effective methods [17–24]. In traditional time-driven control schemes, data is transmitted periodically. Unlike the traditional implementation of time-driven control, the ED control scheme allows communication between the controlled object and the controller (feedback path) and between the controller and the actuator (direct path) only when certain trigger conditions are met. Therefore, the ED control method can significantly reduce data transmissions and avoid network congestion and its possible unavailability. In [25], the authors propose a decentralized event-driven implementation of a centralized nonlinear controller on a sensor-actuator network. In [26], Wang and Lemmon assumed that the control system was composed of weakly coupled subsystems and proposed a

distributed event-driven control method. In [27], the authors developed an event-driven transmission strategy based on state estimation. Designing event-driven algorithms based on changes in the Lyapunov function and selection of input variables to be updated is given in [28]. The threshold value of the event driving condition may greatly affect the execution of the control task. In recent years, a common design method for the feedback control gain of the system and the parameters of the event driving condition has been studied, such as [29–32] and references in the text.

The aforementioned event driving scheme (EDS) has a common feature that the threshold value of the event driving condition is known in advance. Since the threshold value is a preset constant, it is difficult to adapt to changes in the system; that is, the designed event driving parameters cannot adapt to external disturbances. To overcome this shortcoming, event trigger parameters need to be optimized online to achieve adaptation to external disturbances. But so far, there are few researches on the variable threshold under the event-driven condition of nonlinear systems in the public literature. Increasing the anti-interference ability of the event-driven system is a factor that must be considered in the design of high-performance event-driven control systems. Increasing the anti-interference ability of the event-driven system is a factor that must be considered in the design of high-performance event-driven control systems. Sliding mode control (SMC) is a well-known robust control method, which is especially suitable for models subject to modeling uncertainty and external interference control system [33, 34]. Due to its robustness, sliding mode control is also an effective control method based on the arrival law, which greatly improved the fast convergence of the sliding mode surface under the excessive strategy for networked control systems [35, 36]. Asifa Yesmin et al. proposed an event-driven sliding mode control jitter and gave designers greater freedom to design parameters to achieve: the expected steady state in the absence of disturbance uncertainty [37]. An event-driven sliding mode controller with a fuzzy variable threshold is designed for a nonlinear continuous time-varying MIMO system. The fuzzy control is used to variablely adjust the event trigger condition threshold of the nonlinear system to make the system more flexible.

The main contributions of this paper include the following: (1) designing event-driven control with fuzzy control for nonlinear continuous time-varying MIMO systems based on sliding mode control; (2) designing a novel variable event driving condition for nonlinear systems, in order to promote system stability and speed, while reducing network data transmission; and (3) the formula which is used to prove and simulate the closed-loop stability of the system.

The content of this article is arranged as follows: the second part introduces the system description and continuous-time sliding mode control, the third part introduces the event-driven sliding mode controller design, and then the fourth part introduces the fuzzy control and event driven control (EDC) variable design. The numerical example simulation in Section 5 validates the analysis results. Finally, conclusions are drawn in Section 6.

2. System Description and Sliding Mode Control

2.1. System Description. First, we consider a MIMO nonlinear system, as shown below:

$$\dot{\mathbf{x}} = \mathbf{f}(\mathbf{x}) + \mathbf{B}u + \mathbf{B}d. \tag{1}$$

Here, $\mathbf{x} = [x_1, x_2] \in R^{2n}$, $\mathbf{f}(\mathbf{x}) = [f_1(x_1), f_2(x_1, x_2)]$, $\mathrm{B} \in R^{2n}$, x_1, and $x_2 \in R^n$ represent the system's state variables. $\mathrm{u} \in R^n$ is the control input vector of the system, and d is the external disturbance affecting the system. It is assumed that the disturbance is bounded, i.e., $\sup_{t\geq 0}|d(t)| \leq d_0 < \infty$, and it satisfies the matching condition with respect to the control input.

For the nonlinear functions $f_1(\bullet)$ and $f_2(\bullet, \bullet)$, we make the following assumptions.

Assumption 1. The function $f_1(x_1)$ has a unique equilibrium point without loss of generality, and we assume $f_1(0)=0$. In addition, the system can be represented by both linear and nonlinear terms, such as $f_1(x_1)=A_1x_1 + \gamma(x_1)$, A_1 is a linearized system at the equilibrium point, and $\gamma(x_1)$ is the nonlinear components of higher-order terms.

Assumption 2. In the compact domain $D \in R^{2n}$, the functions $f_1(\bullet)$ and $f_2(\bullet, \bullet)$ are Lipschitz functions. For any vector z_1, z_2 in D, which are satisfied, $\|f(z_1) - f(z_2)\| \leq L\|z_1 - z_2\|$.

$$\begin{aligned} ||f(\xi_1) - f(\xi_2)|| &= ||f(z_1, y_1) - f(z_2, y_2)|| \\ &\leq \|f_1(z_1) - f_1(z_2)\| + ||B_1(y_1 - y_2)|| \\ &\quad + |f_2(z_1, y_1) - f_2(z_2, y_2)| \leq L_1||z_1 - z_2|| \\ &\quad + \|B_1\||y_1 - y_2| + |f_2(z_1, y_1) - f_2(z_2, y_2)| \\ &= (L_1 + L_2)||z_1 - z_2|| + (||B_1|| + L_2)|y_1 - y_2| \\ &\leq (L_1 + L_2)\|\xi_1 - \xi_2\| + (||B_1|| + L_2)\|\xi_1 - \xi_2\| \\ &= (L_1 + 2L_2 + ||B_1||)\|\xi_1 - \xi_2| = L\|\xi_1 - \xi_2\| \end{aligned} \tag{2}$$

2.2. Design of Sliding Mode Controller. Considering the nonlinear MIMO system given above, here, we choose $s = \mathbf{c}^T\mathbf{x}$ as the sliding mode surface of the system, where $\mathbf{c} \in R^n$.

$$S = \left\{\mathbf{x} \in R^n : s = \mathbf{c}^T\mathbf{x} = 0\right\}, \tag{3}$$

where $\boldsymbol{c} = [c_1^T \bullet 1]^T$ and $c_1 \in R^{n-1}$, $\boldsymbol{x} = [x_1^T \bullet x_2]^T$. Differentiating $s = \boldsymbol{c}^T\boldsymbol{x}$ with respect to time, we obtain:

$$\begin{aligned} \dot{s} = c_1^T\dot{x}_1 + \dot{x}_2 &= c_1^T f_1(x_1) + c_1^T\mathbf{B}_1x_2 + f_2(x_1, x_2) \\ &\quad + \mathbf{B}_2u + \mathbf{B}_2d = c^T f(\mathbf{x}) + \mathbf{B}_2u + \mathbf{B}_2d. \end{aligned} \tag{4}$$

The SMC design must ensure that the system trajectory converges to the sliding manifold, so the system trajectory must be converged to the equilibrium point within a limited time. Here, we design the control rate u as shown below:

$$u = -\mathbf{B}_2^{-1}\left(c^T f(\mathbf{x}) + K \operatorname{sign} s\right). \tag{5}$$

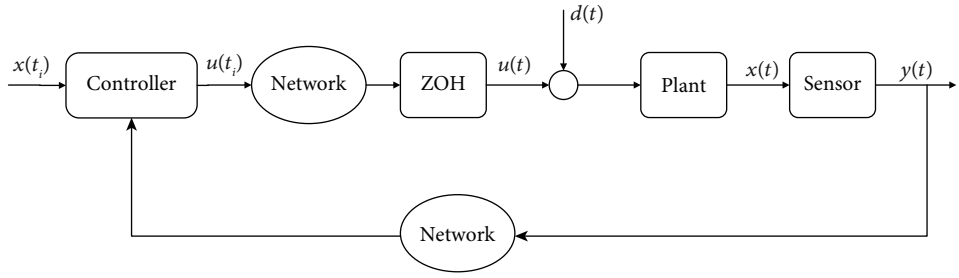

Figure 1: ED-SMC network controller architecture.

In the above formula, the gain K is a bounded constant and satisfies $K > |\mathbf{B}_2|d_0$. Therefore, the reaching law of sliding mode can be expressed as

$$\dot{s} = -K \text{ sign } s + \mathbf{B}_2 u. \tag{6}$$

The design of the control law and the approach law of the sliding mode controller ensures that the system can reach an equilibrium state in a finite lime. This chapter mainly analyzes the implementation of the SMC in the normal state. In the following content, we mainly analyze the implementation of the SMC in the event-driven state and consider the threshold of the ED-SMC trigger condition to design a variable event-driven sliding mode controller that meets the control performance.

3. Event-Driven Sliding Mode Controller

At present, there are few studies on SMC discretization of nonlinear systems. Similar to a linear system, the implementation of a discrete SMC, in this case, will never produce an accurate sliding mode, which is $s = 0$. Therefore, for discrete cases, the sliding trajectory does not remain on the switching manifold but remains near the sliding surface. In the SMC periodic operation, the final limit depends on the sampling interval and the perturbation limit. As the sampling interval decreases, the system performance improves accordingly. On the other hand, the steady-state boundary is designed in advance for the implementation of event driving, so performance can be improved as desired.

In order to make the system reach the tracking target in a limited time and keep the tracking error within a certain limit, the following content mainly studies the sliding mode controller with an event trigger. For example, in the LTI system, the trajectory of a nonlinear system simply depends on the design of some parameters to keep it within a certain range. In the following, the standard definition of the sliding mode of nonlinear systems based on the event-driven mechanism is given, and an event-driven sliding mode controller that meets the performance indicators is designed.

3.1. Design of Event-Driven Sliding Mode Controller. For the LTI system, the trajectory of the system stays constant within a certain range has nothing to do with the sampling interval. We can use the event trigger strategy to make the sliding mode motion reach any ideal stable state. This control will be kept constant until the next trigger Time is coming. $\{t_i\}_{i-=0}^{\infty}$ is a series of driving moments for control updates. Here, $T_i = t_{i+1} - t_i$ is used to represent the time of internal events. In Figure 1, the role of the zero-order retainer is to keep the data at the time $t \in [t_i, t_{i+1})$, so once the control is updated, the controller will continue to the next time t_{i+1}, before that the control signal has been $u(t) = u(t_i)$. We define $\mathbf{e}(t) = \mathbf{x}(t_i) - \mathbf{x}(t)$ as the systematic error. The error e here plays a very important role in the implementation of event-driven control. The main performance is by constantly observing the change of e until it reaches a preset threshold and then using this to determine the next time t_{i+1}. The event trigger mechanism has the advantage of reducing network signal transmission, saving network resources, and saving energy consumption. Moreover, this strategy will determine the state evolution and disturbance steady-state boundary in advance no matter what.

The design of the event-driven sliding mode controller here should also be divided into two steps: First, we need to design this sliding variable $s(t) = \mathbf{cx}(t) = x_1(t) + x_2(t)$, $\boldsymbol{c} = [1\ 1] \otimes I_{nn} \in R^{2n}$, and define this sliding mode surface as follows:

$$S = \{\mathbf{x} \in R^n : \|s\| = \|\mathbf{cx}\| \le u\}. \tag{7}$$

In the above formula, $u > 0$, because S here means "the practical sliding surface" [21].

In the second step, in order to enable the system trajectory to reach the sliding die surface, we should also design appropriate driving rules and control laws. The design of driving rules and control laws is given below.

Since the control signal remains constant in the time interval (t_i, t_{i+1}) between two consecutive driving moments, the control law can be written as follows:

$$u(t) = -\mathbf{B}_2{}^{-1}\left(\mathbf{c}^T f(\mathrm{x}(t_i)) + K \text{ sign } s(t_i)\right). \tag{8}$$

The purpose here is to design the switching gain so that the stability of the system trajectory remains for a limited time.

Theorem 3. *Considering the above nonlinear system and the given control law, let $\alpha > 0$, and give the following trigger conditions:*

$$L||\mathbf{c}||||e(t)|| < \alpha. \tag{9}$$

All time $t > 0$ here, if the gain K is selected as follows, the

actual sliding mode will appear in the system.

$$K > |\mathbf{B}_2|d_0 + \alpha. \tag{10}$$

Proof. Consider the Lyapunov function $V = 1/2S^2$. Differentiating V with respect to time $t \in [t_i, t_{i+1})$, we obtain the following:

$$\dot{V}(s) = s\dot{s} = s\left(\mathbf{c}^T f(\mathbf{x}) + \mathbf{B}_2 u + \mathbf{B}_2 d\right). \tag{11}$$

Taking the control law u (8) into the above formula, we get the following:

$$\begin{aligned}\dot{V}(s(t)) &= s(t)\left(\mathbf{c}^T f(\mathbf{x}(t))\mathbf{c}^T f(\mathbf{x}(t)) - c^T f(\mathbf{x}(t_i))\right.\\ &\quad - K \text{ sign } s(t_i) + \mathbf{B}_2 d \le -s(t)K \text{ sign } s(t_i)\\ &\quad + |s(t)|\left|\left|\mathbf{c}^T f(\mathbf{x}(t)) - \mathbf{c}^T f(\mathbf{x}(t_i))\right|\right| + |s(t)||\mathbf{B}_2|d_0\\ &\le -s(t)K \text{ sign } s(t_i) + |s(t)|||\mathbf{c}||||f(\mathbf{x}(t)) - f(\mathbf{x}(t_i))||\\ &\quad + |s(t)||\mathbf{B}_2|d_0 \le -s(t)K \text{ sign } s(t_i)\\ &\quad + |s(t)|L||\mathbf{c}||||\mathbf{x}(t) - \mathbf{x}(t_i)|| + |s(t)||\mathbf{B}_2|d_0.\end{aligned} \tag{12}$$

Until this trajectory reaches the sliding surface, the sign of the sliding variable will not change, and sign $s(t_i)$ = sign $s(t)$; we can write it as $-K \mid s(t) \mid$ And by taking equations (9) and (10) into (12), we can get

$$\begin{aligned}\dot{V}(s(t)) &\le -\mid s(t)|K + |s(t)|\alpha + |s(t)||\mathbf{B}_2|\mathrm{d}_0\\ &= -|s(t)|(K - \alpha - |\mathbf{B}_2|d_0) = -\eta|s(t)|.\end{aligned} \tag{13}$$

For some $\eta > 0$. This shows that in the time interval $[t_i, t_{i+1})$, for some $i \in Z \ge 0$, the trajectory is moving toward the sliding surface. For as long as sign $s(t_i)$ = sign $s(t)$, the interval is subsequently triggered. In the end, the tracking trajectory reaches the sliding surface in a limited time. However, there is no guarantee that the trajectory will still move on the sliding surface because no control signal is applied. Therefore, the trajectory passes through it after reaching the sliding surface. However, since relationship (9) holds, it will not be borderless, as shown below. We can get the maximum differential of the sliding trajectory at any time interval $[t_i, t_{i+1})$. It can be expressed by the following formula:

$$|s(t_i) - s(t)| = \left|\mathbf{c}^T x(t_i) - \mathbf{c}^T x(t)\right| \le ||\mathbf{c}||||\mathbf{e}(t)|| < \frac{\alpha}{L}. \tag{14}$$

If the trigger occurs when the trajectory just reaches the sliding mode surface, the maximum value of the actual sliding mode band can be obtained, so this boundary can be given as follows:

$$\Omega = \left\{\mathbf{x} \in \mathrm{D} : |\mathrm{s}| = |\mathbf{c}^T\mathbf{x}| < \frac{\alpha}{L}\right\}. \tag{15}$$

This indicates that the system trajectory ends up in the Ω region. Therefore, the certification is complete.

The above results have some similarities with linear systems. The first one is the relationship (9), which is essential for the existence of actual sliding modes in nonlinear systems. The Lipschitz constant that appears here corresponds to the induced norm of the system matrix of the LTI system. Another similarity is that the actual sliding mode band is obtained from a similar relationship (9) obtained with the LTI system.

3.2. System Stability Analysis. For the trigger conditions and control laws given above, we should analyze the closed-loop stability of the system. Redefine the sliding variable here, as shown below:

$$x_2(t) = -x_1(t) + s(t). \tag{16}$$

For the above algebraic dynamic equation, it can be proved that if $x_1(t)$ is bounded, then $x_2(t)$ must also be bounded. Below, we will prove the closed-loop stability of the system.

Here, $V_1 = (1/2){x_1}^T x_1$ is selected as the Lyapunov function. Next, we directly differentiate V_1 and bring equations (8) and (21) into the equation; we can get

$$\begin{aligned}\dot{V}_1 &= {x_1}^T(t)\dot{x_1}(t) = {x_1}^T(t)x_2(t) \le {x_1}^T(t)(-x_1(t) + s(t))\\ &\le -||x_1(t)||^2 + ||x_1(t)||||s(t)||\\ &\le -||x_1(t)||^2 + \frac{\alpha}{L}||x_1(t)||.\end{aligned} \tag{17}$$

If $||x_1(t)| | > \alpha/L$, then $\dot{V}_1 < 0$ holds, and then this $x_1(t)$ will approach the Ω region. Therefore, this state vector $x_1(t)$ is finally bounded and proved.

3.3. Event-Driven Control Strategy. The trigger condition design must ensure the stability of the system. As can be seen from the previous chapter, the relationship (9) is a sufficient condition for the existence of the actual sliding mode. Therefore, this relationship satisfies the stability of the system at any time. In other words, the choice of a driving scheme should make this relationship always hold. Therefore, the trigger scheme is expressed as follows:

$$t_{i+1} = \inf\{t > t_i : L||\mathbf{c}||||\mathbf{e}(t)|| > \sigma\alpha\}. \tag{18}$$

Here, $\sigma \in (0, 1)$. This trigger strategy satisfies the following relationship:

$$L||\mathbf{c}||||\mathbf{e}(t)|| > \sigma\alpha. \tag{19}$$

When $t > 0$, this relationship is always true.

Select $\{t_i\}_{i=0}^{\infty}$ as a trigger sequence. For the stability of the event-driven control system, there must be a positive lower bound between the two trigger intervals, so as to avoid the occurrence of the Zeno phenomenon. In fact, this is a very important process to perform this control task; otherwise, the system may be unstable. In practice, the control law is applied to discrete-time series, and this time series does not

consider the delay caused by control. If this delay is very small and does not affect the performance of the system, then this delay can be ignored. Through this delay-free control execution, we prove that the trigger sequence generated by (18) is the following theorem. Before proving this, we must first write the system dynamics equation (1) in the following format:

$$\dot{\mathbf{x}} = f(\mathbf{x}) + \mathbf{B}u + \mathbf{B}d. \tag{20}$$

$\mathbf{B}=[0, B_2]^T$, where 0 is a column vector with dimension n -1, and all parameters are zero.

Theorem 4. *Considering the above system and the given control law, it can be seen that this trigger sequence is eligible, that is, for the above trigger criteria given by* $\{t_i\}_{i=0}^{\infty}$, *the internal time trigger The interval* T_i *always has a positive lower bound. Here we can give*

$$T_i \geq \frac{1}{L} \ln\left(1 + \sigma \frac{\alpha}{||\boldsymbol{c}||(\rho_N(||\boldsymbol{x}(t_i)||) + \beta_N}\right). \tag{21}$$

In the above formula, β_N *is defined as*

$$\beta_N = \left|\left|\mathbf{B}\mathbf{B}_2^{-I}\right|\right|K + |\mathbf{B}_2|d_0. \tag{22}$$

$\rho_N(||\mathbf{x}(t_i)||)$ *is defined as*

$$\rho_N(||\mathbf{x}(t_i)||) = L\left(1 + \left|\left|\mathbf{B}\mathbf{B}_2^{-1}c^T\right|\right|\right)||\mathbf{x}(t_i)||. \tag{23}$$

Proof. The first thing to be clear is that $\|\mathbf{e}(t)\|$ grows from 0 to $\sigma\alpha/||\mathbf{c}|\,|\,L$; that is, it is bounded. Define the interval $\Gamma =: \{t \in [t_i, t_{i+1}): ||\mathbf{e}(t)|| = 0\}$. Then we can differentiate on $\|\mathbf{e}(t)\|$, and we get

$$\begin{aligned}\frac{d}{dt}\|\mathbf{e}(t)\| &\leq \left\|\frac{d}{dt}\mathbf{e}(t)\right\| = \left\|\frac{d}{dt}\mathbf{x}(t)\right\| \\ &= \|f(\mathbf{x}(t)) + \mathbf{B}u(t) + \mathbf{B}d(t)\| \\ &= \left\|f(\mathbf{x}(t)) - \mathbf{B}\mathbf{B}_2^{-1}c^T f(x(t_i))\right. \\ &\quad \left. - \mathbf{B}\mathbf{B}_2^{-1}K\text{signs}(t_i) + \mathbf{B}d(t)\right\|.\end{aligned} \tag{24}$$

The final equation is obtained by replacing the control expression (5). Using $x(t) = x(t_i) - \mathbf{e}(t)$. We can get further

$$\begin{aligned}\frac{d}{dt}||\mathbf{e}(t)|| \leq L\|\mathbf{x}(t)\| &+ \left\|\mathbf{B}\mathbf{B}_2\left(\mathbf{c}^T\mathbf{B}\right)^{-1}\mathbf{c}^T f(\mathbf{x}(t_i))\right\| \\ &+ \left|\left|\mathbf{B}\mathbf{B}_2^{-1}\right|\right|K + \|\mathbf{B}_2 d(t)\| \leq L(\|\mathbf{x}(t_i)\| \\ &+ \|\mathbf{e}(t)\|) + L\left\|\mathbf{B}\mathbf{B}_2\left(\mathbf{c}^T\mathbf{B}\right)^{-1}\mathbf{c}^T\right\|\|\mathbf{x}(t_i)\| \\ &+ \left|\left|\mathbf{B}\mathbf{B}_2^{-1}\right|\right|K + |\mathbf{B}_2|d_0 = L\|\mathbf{e}(t)\| \\ &+ \left(1 + \left|\left|\mathbf{B}\mathbf{B}_2^{-1}\mathbf{c}^T\right|\right|\right)L\|\mathbf{x}(t_i)\| + \beta_N = L\|\mathbf{e}(t)\| \\ &+ \rho_N(\|\mathbf{x}(t_i)\|) + \beta_N,\end{aligned} \tag{25}$$

where β_N and $\rho_N(\|\boldsymbol{x}(t_i)\|)$ are defined as (22) and (23), respectively. For $t \in [t_i, t_{i+1})$, the solution of the above differential inequality is to call Lemma 2 [38] with the initial condition $\|\boldsymbol{e}(t_i)\| = 0$, and we get

$$||\mathbf{e}(t)|| \leq \frac{\rho_N(||\boldsymbol{x}(t_i)||) + \beta_N}{L}\left(e^{L(t-t_i)} - 1\right). \tag{26}$$

Once (18) is satisfied, time t_{i+1} will be triggered. So we write (26) as

$$\frac{\sigma\alpha}{L||\mathbf{c}||} = ||\mathbf{e}(t_i)|| \leq \frac{\rho_N(||\boldsymbol{x}(t_i)||) + \beta_N}{L}\left(e^{LT_i} - 1\right). \tag{27}$$

Rearrange (27) to get expression (21) for execution time. It still shows that it is bounded by some finite positive number. Note that $\rho(||\mathbf{x}(t_i)||)$ and β_N are both finite positive numbers. Therefore, this means that T_i is proved to be bounded by a positive finite number all the time.

4. Variable Threshold Events Driven by the Sliding Mode Control

4.1. Problem Statement. As can be seen from the previous section, the choice of α determines the steady-state range of the system. Therefore, a large enough value must be selected so that the accumulation performed by the controller does not occur; that is, the driven time is greater than the given minimum time period. For example, for a given small α, the next trigger moment may be lower than the sampling interval corresponding to the processor bandwidth. If this situation happens, the control will not be performed until the trigger time exceeds the processor's bandwidth limit and eventually results in the Zeno phenomenon. In other words, T_i must have a positive lower bound to ensure that this phenomenon does not occur. For all $i \in T_i \geq 0$, we provide the following conditions under the condition of α to ensure that the interactive execution time T_i is greater than the processor bandwidth. A value large enough must be chosen to produce T_i that is greater than the processor's minimum internal execution time τ. However, higher α may increase the steady-state boundary of the sliding trajectory. Therefore, the appropriate optimal value of α is selected to make the system get the best performance under the expected steady-state boundary.

On the other hand, it can be known from Theorems 3 and 4 that the magnitude of the alpha value determines the difficulty of the event-driven and the size of the trigger interval. The larger the alpha value, the more difficult the event trigger occurs and the larger the corresponding event trigger interval. Therefore, under the condition that the above-mentioned system is stable, a larger value of α will reduce the number of events driven and reduce the actuator's frequency of execution. Based on the principle of sliding mode motion, there are two stages of sliding mode motion, as shown in Figure 2: the first stage is moving from the sliding mode surface to the sliding mode surface, and the second is moving on the sliding mode surface and finally reaches the system origin. It is generally known that chattering occurs on the sliding surface. If the current point of motion is far away from the sliding surface, an appropriate increase in K

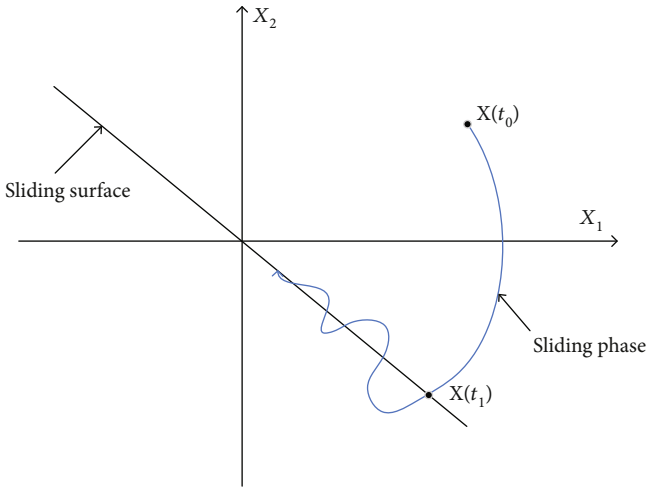

Figure 2: Sliding mode diagram.

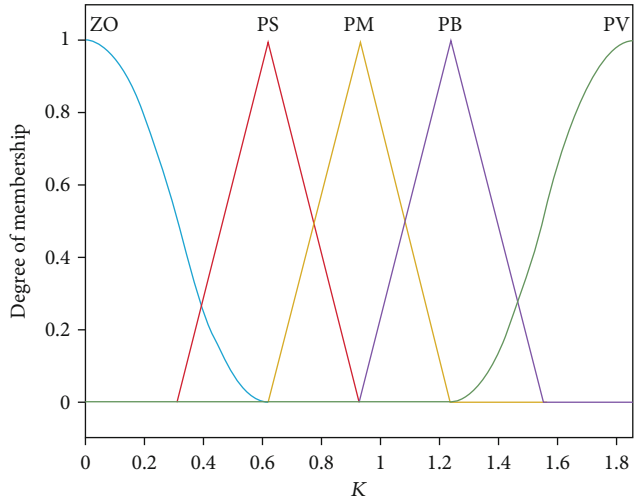

Figure 3: The membership function.

is required to speed up the control and improve the control performance. However, when the distance between the current moving point and the sliding surface is close, in order to reduce the tremor, the approach speed is expected to be reduced, which needs to be reduced by K. Based on the above knowledge and control experience, fuzzy control laws and fuzzy control systems can be designed. K_i may change with the distance between the current moving point and the sliding surface to reduce jitter and system steady-state error.

4.2. Design of Fuzzy Controller. Based on the above ideas, a two-dimensional fuzzy controller is used to directly design the event trigger parameter α and the parameter K of the approach law through the fuzzy control law. It adjusts α and K in real-time according to the absolute value of S and the modulus value of x.

The inputs of the fuzzy controller are set as $\|\mathbf{x}\|$ and $|S|$, which are fuzzification variables of $\mathbf{x}(t)$ and $s(t)$, respectively. The output of the fuzzy controller is the event trigger parameter α and the parameter K of the sliding mode controller blurring variable.

(1) Defining fuzzy sets

$$\begin{aligned} \text{PV} &= \text{positive oversized}, \\ \text{PB} &= \text{positive large}, \\ \text{PM} &= \text{positive middle}, \\ \text{PS} &= \text{positive small}, \\ \text{ZO} &= \text{zero} \end{aligned} \tag{28}$$

(2) According to the fuzzy control principle, $\|\mathbf{x}\|$and $|S|$ are defined as the inputs of the fuzzy controller, and the output of the fuzzy controller is alpha and K

$$\begin{aligned} \|\mathbf{x}\| &= \{\text{ZO, PS, PM, PB, PV}\}, \\ |S| &= \{\text{ZO, PS, PM, PB, PV}\}, \\ \text{Alpha} &= \{\text{ZO, PS, PM, PB, PV}\}, \\ K &= \{\text{ZO, PS, PM, PB, PV}\} \end{aligned} \tag{29}$$

Its field of discussion is as follows:

$$\begin{aligned} \|\mathbf{x}\| &= \{0,+1,+2,+3,+4\}, \\ |S| &= \{0,+1,+2,+3,+4\}, \\ \text{Alpha} &= \{0,+1,+2,+3,+4\}, \\ K &= \{0,+1,+2,+3,+4\} \end{aligned} \tag{30}$$

(3) The membership function setting is shown in Figure 3

(4) Determine the fuzzy control rules of the fuzzy sliding mode controller

According to control experience, when $|S|$ is PB, it means that the state of the system is far from the sliding surface. Therefore, a large approach law parameter is needed to accelerate the approach speed; that is, K should be PB; when $|S|$ is PS, it means that the system state is closer to the sliding mode surface, so a smaller K is required to slow the approach speed to reduce chattering; that is, K should be PS. When $\|\mathbf{x}\|$ is large, it means that the system is far away from the system equilibrium point and has a faster approach speed. The system needs a larger α to reduce the number of triggers. When $\|\mathbf{x}\|$ is small, the system enters near the sliding mold surface, α is not easy to be too large, and it will not trigger if it is too large. Based on the above experience, the control rule table

Table 1: Table of control rules.

Alpha		$\|\|\mathbf{x}\|\|$				
		ZO	PS	PM	PB	PV
$\|S\|$	ZO	ZO	PS	PM	PB	PS
	PS	ZO	PS	PS	PM	PM
	PM	ZO	PS	PM	PB	PB
	PB	ZO	PM	PB	PB	PV
	PV	ZO	PS	PM	PB	PV

Table 2: Table of control rules.

K		$\|\|\mathbf{x}\|\|$				
		ZO	PS	PM	PB	PV
$\|S\|$	ZO	ZO	PS	PM	PB	PS
	PS	ZO	PS	PS	PM	PM
	PM	ZO	PS	PM	PB	PB
	PB	ZO	PM	PB	PB	PV
	PV	ZO	PS	PM	PB	PV

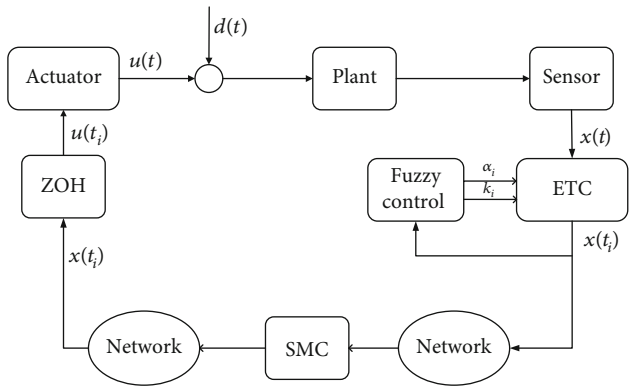

Figure 4: Block diagram of the control system.

shown in Tables 1 and 2 is used. The fuzzy rules used are as follows: if $\|\mathbf{x}\|$ is A and $|S|$ is B, then alpha is C and K is D.

(5) In anti-fuzzy, use the center of gravity method to refine the fuzzy output; the formula is as follows:

$$\varepsilon_0 = \frac{\sum_{i=1}^{n} \mu_{B'}(b_i) \bullet b_i}{\sum_{i=1}^{n} \mu_{B'}(b_i)} \tag{31}$$

The above-mentioned fuzzy controller is used to adjust s in real time, thereby forming a fuzzy reaching law of sliding mode control. The block diagram of the control system is shown in Figure 4.

The law of control is written as follows:

$$u(t) = -\mathbf{B}_2^{-1}\left(\mathbf{c}^T f(x(t_i)) + K_i \operatorname{sign} s(t_i)\right). \tag{32}$$

The trigger scheme is expressed as follows:

$$t_{i+1} = \inf\{t > t_i : L||\mathbf{c}||||\mathbf{e}(t)|| > \sigma\alpha_i\}. \tag{33}$$

Internal time trigger interval T_i is positive lower bound:

$$T_i \geq \frac{1}{L} \ln\left(1 + \sigma \frac{\alpha_i}{||\boldsymbol{c}||(\rho_N(||\boldsymbol{x}(t_i)||) + \beta_N}\right). \tag{34}$$

In the above formula, β_N is defined as

$$\beta_N = \left|\left|\mathbf{B}\mathbf{B}_2^{-1}\right|\right| K_i + |\mathbf{B}_2| d_0. \tag{35}$$

And $\rho_N(||\boldsymbol{x}(t_i)||)$ is defined as follows:

$$\rho_N(\|\mathbf{x}(t_i)\|) = L\left(1 + \left|\left|\mathbf{B}\mathbf{B}_2^{-1}\mathbf{c}^T\right|\right|\right)\|\mathbf{x}(t_i)\|. \tag{36}$$

5. Experimental Simulation

Numerical examples are used in this section to verify the above analysis. Consider the following second-order nonlinear continuous system:

$$\dot{x}_1 = x_2\, \dot{x}_2 = x_1 + x_2^2 + u + d. \tag{37}$$

The compact domain of the system is selected as $D = \{\mathbf{x} \in R^2 : \|\mathbf{x}\|^2 = 9\}$. The Lipschitz constant of the system in this domain D is chosen as $L = 10$. The perturbation is assumed to be bounded, and it is considered here as $d = 0.5 \cos t$, which results in $\triangle_d = 0.5$. The design of the sliding surface should ensure the stability of the system. We choose $\mathbf{c}^T = [0.5\ 1]$, so $\mathbf{s} = \mathbf{c}^T\mathbf{x}$ represents the sliding variable in the continuous-time setting. The SMC for (3) can be expressed as follows:

$$u = x_1 - 0.5x_2 - x_2^2 - \mathrm{Ksign}(s). \tag{38}$$

And $K > 0.5$. When the control law is implemented through an event-driven strategy, it remains constant in the time interval $[t, t_{i+1})$, that is, at $t \in [t_i, t_{i+1})$, $u(t) = u(t_i)$, and $i \in Z \geq 0$. The other parameters are chosen as $\tau^* = 0.0001$ and $\sigma = 0.8$. The initial value of $\alpha_{\min}$ is chosen to be 0.3. The initial value is $K = 0.8$, and the sampling period is set to $ts = 0.001$ s. The initial conditions is [-1 2].

Case 1. EDSM.

Figure 5 shows the simulation results of the response of EDSM to a nonlinear system.

It can be seen from Figure 5(a) that the actual sliding pattern occurs in the system in a limited time. For the selected value of a, the value of the sliding mode band is 0.03. The sliding trajectory entered the frequency band for a limited time and remained there. The same is true for different perturbation range values. The change of the state trajectory over time is shown in Figure 5(b), which shows that the trajectory is finally in a stable state, so the system is in a stable state. The interevent time versus time is shown in Figure 5(d). After entering the sliding mode, the driving time

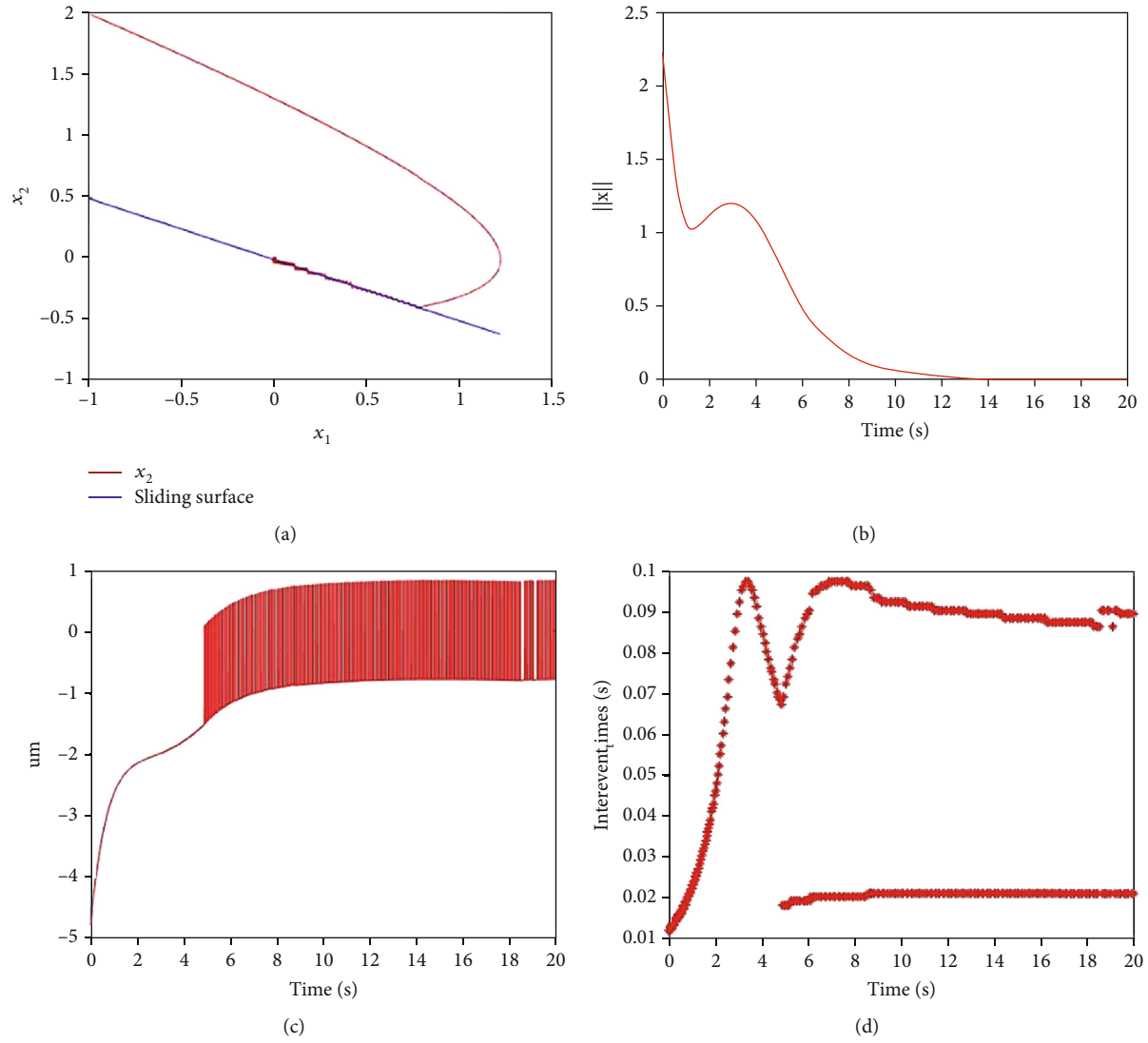

Figure 5: EDSMC system response diagram. (a) System trajectory diagram showing the actual sliding mode in a limited time. (b) System status. (c) Sliding mode control with event touch. (d) Mutual execution time of event-driven sliding mode control.

interval has a sequence of long and short. The controller output control signal is updated as shown in Figure 5(c). After entering the sliding mode, it is in a continuous oscillation state.

Case 2. AEDSM.

Figures 6–8 show the simulation results of AEDSM response to a nonlinear system.

It can be seen from Figure 6 that, as in the above case, the sliding track enters the frequency band in a limited time. For the selected α value, due to the variable adjustment of the K value, the sliding mode band is reduced to 0.02 compared to the above case. The same is true for different perturbation range values. The trajectory is finally in a stable state. The above illustrates the effectiveness of the proposed variable event-driven transmission strategy.

It can be seen from Figure 7 that α of AEDSMC is continuously adjusted and its corresponding threshold is continuously adjusted until the error reaches a steady state. In this case, α eventually converged to 0.2039. In this case, K eventually converged to a constant value.

Figure 8 shows the change in the S-function modulus. It can be seen that the S-function modulus is most stable in the sliding mode band, which is 0.02.

Compared with the EDSMC control scheme, the AEDSMC sliding mode band is 30% smaller than the above situation, effectively suppressing the sliding mode chattering phenomenon. The proposed driving scheme has a smaller number of driving events and a longer event driving interval, so it has better performance in terms of limited resource utilization. Table 3 summarizes the results and shows the number of trigger events.

6. Summary

In this paper, a variable threshold control method based on event driving was proposed and designed to solve the

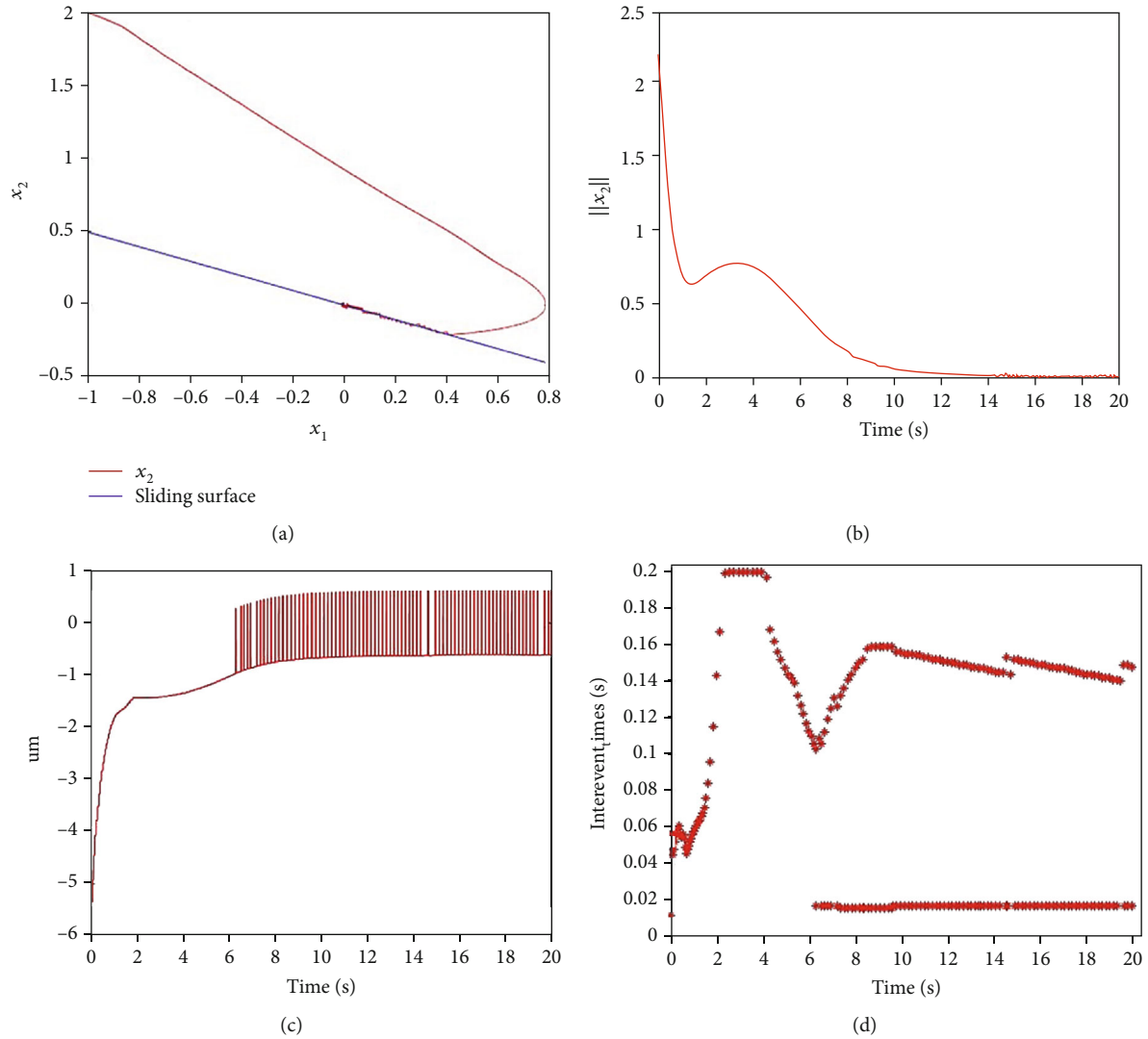

Figure 6: AEDSMC system response diagram. (a) System trajectory diagram showing the actual sliding mode in a limited time. (b) System status (c) Sliding mode control with event touch. (d) Mutual execution time of event-driven sliding mode control.

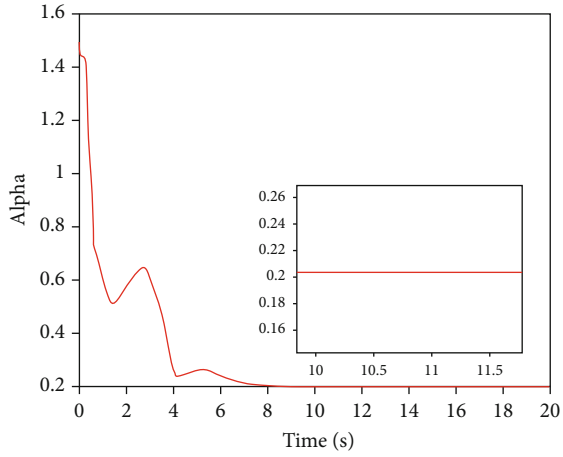

Figure 7: Variable parameter α adjustment.

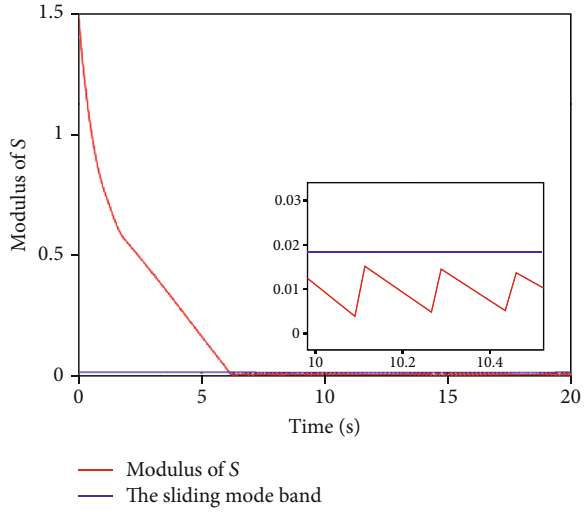

Figure 8: S-mode modulus change.

Table 3: Comparison of results.

	SMC	EDSMC	AEDSMC
Total number of triggers	20000	410	226
Stability error of 20 s	0	0.014	0.010
Sliding manifold	0.025	0.03	0.02
Min trigger event interval	0.001	0.012	0.016
Max trigger event interval	0.001	0.097	0.2

problem of insufficient robustness of a class of nonlinear network systems with external disturbances. Different from the current event-driven control system, the control scheme proposed in this paper can variably update the threshold parameter α according to the fuzzy rule after each event is driven and simultaneously update the parameter K of the sliding mode controller. In this scheme, the system with external disturbance has good robustness and adaptability. Simulation results show that the event-driven control scheme reduces the number of event triggers, saves system network resources, effectively suppresses the chattering phenomenon of sliding mode control, and meets system design performance requirements, which verifies the effectiveness and feasibility of the scheme. In the future work, we can consider other interferences, such as denial-of-service (DOS) attacks and study adaptive event-driven control in network control systems under DOS attacks.

Data Availability

The specific data description has been mentioned in detail in the paper.

Conflicts of Interest

The authors declare that they have no conflicts of interest.

Acknowledgments

This work was supported by the Key Fund of Shaanxi Province Natural Science Basic Research Program (2019JLZ-06) and Key Project of National Internet of Things Integrated Innovation and Integration (2018-470).

References

[1] D. Zhang, P. Shi, Q.-G. Wang, and L. Yu, "Analysis and synthesis of networked control systems: a survey of recent advances and challenges," *ISA Transactions*, vol. 66, pp. 376–392, 2017.

[2] X. Ge, Q.-L. Han, D. Ding, X.-M. Zhang, and B. Ning, "A survey on recent advances in distributed sampled-data cooperative control of multi-agent systems," *Neurocomputing*, vol. 275, pp. 1684–1701, 2018.

[3] X. Jia, D. Zhang, X. Hao, and N. Zheng, "Fuzzy H(infinity) tracking control for nonlinear networked control systems in T-S fuzzy model," *IEEE Transactions on Systems, Man and Cybernetics, Part B: Cybernetics*, vol. 39, no. 4, pp. 1073–1079, 2009.

[4] F. Yang and Q.-L. Han, "_H_ $_\infty$ control for networked systems with multiple packet dropouts," *Information Sciences*, vol. 252, pp. 106–117, 2013.

[5] C. Peng, Q.-L. Han, and D. Yue, "Communication-delay-distribution-dependent decentralized control for large-scale systems with ip-based communication networks," *IEEE Transactions on Control Systems Technology*, vol. 21, no. 3, pp. 820–830, 2013.

[6] W. Chen and L. Qiu, "Stabilization of networked control systems with multirate sampling," *Automatica*, vol. 49, no. 6, pp. 1528–1537, 2013.

[7] P. Ogren, E. Fiorelli, and N. E. Leonard, "Cooperative control of mobile sensor networks: adaptive gradient climbing in a distributed environment," *IEEE Transactions on Automatic Control*, vol. 49, no. 8, pp. 1292–1302, 2004.

[8] N. H. Gartner, C. Stamatiadis, and P. J. Tarnoff, "Development of advanced traffic signal control strategies for intelligent transportation systems: multilevel design," *Transportation Research Record*, vol. 1494, pp. 98–105, 1995.

[9] C. Meng, T. Wang, W. Chou, S. Luan, Y. Zhang, and Z. Tian, "Remote Surgery Case: Robot-Assisted Teleneurosurgery," in *Proceedings of the 2004 IEEE Conference on Robotics and Automation ICRA04)*, pp. 819–823, New Orleans, USA, 2004.

[10] T. C. Yang, "Networked control system: a brief survey," *IEE Proceedings-Control Theory and Applications*, vol. 153, no. 4, pp. 403–412, 2006.

[11] G. Buttazzo and A. Cervin, "Comparative assessment and evaluation of jitter control methods," in *Proceedings of the 15th conference on Real-Time and Network Systems*, pp. 163–172, Nancy, France, March 2007.

[12] R. Luck and A. Ray, "An observer-based compensator for distributed delays," *Automatica*, vol. 26, no. 5, pp. 903–908, 1990.

[13] C. Tan, L. Li, and H. Zhang, "Stabilization of networked control systems with both network-induced delay and packet dropout," *Automatica*, vol. 59, pp. 194–199, 2015.

[14] R. Luck and A. Ray, "An observer-based compensator for distributed delays," *Automatica*, vol. 26, no. 5, pp. 903–908, 2003.

[15] J. Nilsson and B. Bernhardsson, "Analysis of real-time control systems with time delays," in *Proceedings of the 35th IEEE Conference on Decision and Control*, vol. 3, pp. 3173–3178, Kobe, Japan, 1996.

[16] G. P. Liu, Y. Xia, J. Chen, D. Rees, and W. Hu, "Networked predictive control of systems with random network delays in both forward and feedback channels," *IEEE Transactions on Industrial Electronics*, vol. 54, no. 3, pp. 1282–1297, 2007.

[17] K. J. Aström, "Event based control," in *Analysis and Design of Nonlinear Control Systems*, pp. 127–147, Springer, Berlin, 2008.

[18] W. Heemels, J. Sandee, and P. Van Den Bosch, "Analysis of event-driven controllers for linear systems," *International Journal of Control*, vol. 81, no. 4, pp. 571–590, 2008.

[19] W. Heemels, K. H. Johansson, and P. Tabuada, "An introduction to event-triggered and selftriggered control," in *2012 IEEE 51st Annual Conference on Decision and Control (CDC)*, pp. 3270–3285, Hawaii, December 2012.

[20] Y. Ke-You and X. Li-Hua, "Survey of recent progress in networked control systems," *Acta Automatica Sinica*, vol. 39, no. 2, pp. 101–117, 2013.

[21] H. Yu and P. J. Antsaklis, "Event-triggered output feedback control for networked control systems using passivity:

achieving stability in the presence of communication delays and signal quantization," *Automatica*, vol. 49, no. 1, pp. 30–38, 2013.

[22] P. Tabuada, "Event-triggered real-time scheduling of stabilizing control tasks," *IEEE Transactions on Automatic Control*, vol. 52, no. 9, pp. 1680–1685, 2007.

[23] P. Tallapragada and N. Chopra, "Decentralized event-triggering for control of nonlinear systems," *IEEE Transactions on Automatic Control*, vol. 59, no. 12, pp. 3312–3324, 2014.

[24] W. Heemels and M. C. F. Donkers, "Model-based periodic event-triggered control for linear systems," *Automatica*, vol. 49, no. 3, pp. 698–711, 2013.

[25] E. Tian, D. Yue, and C. Peng, "Quantized output feedback control for networked control systems," *Information Sciences*, vol. 178, no. 12, pp. 2734–2749, 2008.

[26] W.-W. Che, J.-L. Wang, and G.-H. Yang, "Quantised H^{∞} filtering for networked systems with random sensor packet losses," *IET Control Theory & Applications*, vol. 4, no. 8, pp. 1339–1352, 2010.

[27] M. Mazo and P. Tabuada, "Decentralized event-triggered control over wireless sensor/actuator networks," *IEEE Transactions on Automatic Control*, vol. 56, no. 10, pp. 2456–2461, 2011.

[28] X. Wang and M. D. Lemmon, "Event-triggering in distributed networked systems with data dropouts and delays," in *Hybrid systems: computation and control, international conference, HSCC 2009*, pp. 366–380, San Francisco, Ca, USA, April 2009.

[29] F. Forni, S. Galeani, D. Nesic, and L. Zaccarian, "Event-triggered transmission for linear control over communication channels," *Automatica*, vol. 50, no. 2, pp. 490–498, 2014.

[30] A. Seuret, C. Prieur, and N. Marchand, "Stability of non-linear systems by means of event-triggered sampling algorithms," *IMA Journal of Mathematical Control and Information*, vol. 31, pp. 415–433, 2013.

[31] D. Yue, E. Tian, and Q.-L. Han, "A delay system method for designing event-triggered controllers of networked control systems," *IEEE Transactions on Automatic Control*, vol. 58, no. 2, pp. 475–481, 2013.

[32] S. Hu and D. Yue, "Event-triggered control design of linear networked systems with quantizations," *ISA Transactions*, vol. 51, no. 1, pp. 153–162, 2012.

[33] C. Peng, Q.-L. Han, and D. Yue, "To transmit or not to transmit: a discrete event-triggered communication scheme for networked Takagi-Sugeno fuzzy systems," *IEEE Transactions on Fuzzy Systems*, vol. 21, no. 1, pp. 164–170, 2013.

[34] S. Hu and D. Yue, "L2-Gain analysis of event-triggered networked control systems: a discontinuous Lyapunov functional approach," *International Journal of Robust and Nonlinear Control*, vol. 23, no. 11, pp. 1277–1300, 2013.

[35] V. I. Utkin, *Sliding Modes in Control and Optimization*, Springer-Verlag, 1992.

[36] S. K. S. Christopher Edwards, *Sliding Mode Control*, Taylor and Francis, 1998.

[37] X. H. Liu, X. H. Yu, G. Q. Ma, and H. S. Xia, "On sliding mode control for networked control systems with semi-Markovian switching and random sensor delays," *Information Sciences*, vol. 337, pp. 44–58, 2016.

[38] H. Khalil, *Nonlinear Systems*, NJ: Prentice-Hall, Upper Saddle River, 3rd edition, 2002.

Hindawi
Wireless Communications and Mobile Computing
Volume 2021, Article ID 8887445, 13 pages
https://doi.org/10.1155/2021/8887445

Research Article

Two-Stage Precoding Based on Overlapping User Grouping Approach in IoT-Oriented 5G MU-MIMO Systems

Djordje B. Lukic[1,2] **Goran B. Markovic**[1] **and Dejan D. Drajic**[1,3]

[1]*School of Electrical Engineering, University of Belgrade, Bulevar Kralja Aleksandra 73, 11120 Belgrade, Serbia*
[2]*Aspire Technology Unlimited, Vladimira Popovica 6, Unit B10, 11070 Belgrade, Serbia*
[3]*Innovation Centre of School of Electrical Engineering, Bulevar Kralja Aleksandra 73, 11120 Belgrade, Serbia*

Correspondence should be addressed to Djordje B. Lukic; djordje.lukic@aspiretechnology.com

Received 5 June 2020; Revised 10 November 2020; Accepted 17 December 2020; Published 8 January 2021

Academic Editor: Hongzhi Guo

Downlink transmission techniques for multiuser (MU) multiple-input multiple-output (MIMO) systems have been comprehensively studied during the last two decades. The well-known low complexity linear precoding schemes are currently deployed in long-term evolution (LTE) networks. However, these schemes exhibit serious shortcomings in scenarios when users' channels are strongly correlated. The nonlinear precoding schemes show better performance, but their complexity is prohibitively high for a real-time implementation. Two-stage precoding schemes, proposed in the standardization process for 5G new radio (5G NR), combine these two approaches and present a reasonable trade-off between computational complexity and performance degradation. Before applying the precoding procedure, users should be properly allocated into beamforming subgroups. Yet, the optimal solution for user selection problem requires an exhaustive search which is infeasible in practical scenarios. Suboptimal user grouping approaches have been mostly focused on capacity maximization through greedy user selection. Recently, overlapping user grouping concept was introduced. It ensures that each user is scheduled in at least one beamforming subgroup. To the best of our knowledge, the existing two-stage precoding schemes proposed in literature have not considered overlapping user grouping strategy that solves user selection, ordering, and coverage problem simultaneously. In this paper, we present a two-stage precoding technique for MU-MIMO based on the overlapping user grouping approach and assess its computational complexity and performance in IoT-oriented 5G environment. The proposed solution deploys two-stage precoding in which linear zero forcing (ZF) precoding suppresses interference between the beamforming subgroups and nonlinear Tomlinson-Harashima precoding (THP) mitigates interuser interference within subgroups. The overlapping user grouping approach enables additional capacity improvement, while ZF-THP precoding attains balance between the capacity gains and suffered computational complexity. The proposed algorithm achieves up to 45% higher MU-MIMO system capacity with lower complexity order in comparison with two-stage precoding schemes based on legacy user grouping strategies.

1. Introduction

Cellular Internet of things (IoT) has been recognized as a key enabler for digital transformation and automation of almost all industries. Before 5G New Radio (5G NR), cellular networks have been mainly designed and implemented for human-type communications. Hence, the connectivity needs of industry 4.0 can be addressed only with the implementation of massive machine type communication (mMTC) 5G NR use cases. Based on current predictions, around 5 billion cellular IoT connections are expected by 2025 [1]. Multiuser (MU) multiple-input multiple-output (MIMO) and its evolution, massive MIMO (mMIMO), have been identified as one of the most promising technologies to address the massive capacity demands in 5G networks and beyond. A combination of spatial multiplexing and transmit beamforming technique enables simultaneous transmission of independent data streams using the same radio resources and thus achieves higher throughput and spectral efficiency in MU-MIMO systems [2].

The performance of MU-MIMO system design is largely dependent on deployed user grouping method [3]. Actually,

the use of improper user grouping strategy can allocate users with highly correlated channels into the same beamforming subgroup and thus significantly reduce system capacity. In this paper, we consider practical cellular IoT scenario when the number of users K is larger than the number of transmit antennas N, i.e., $K > N$, which requires selection of G user subsets K_g. In general, in order to find the optimal subset of $K_g \leq N$ users, the complete search space of size $\sum_{k=1}^{N} \binom{K}{k}$ is required, which is prohibitively complex when the number of users becomes large [4]. Several suboptimal user grouping methods have been proposed with the aim to reduce complexity. K-means clustering is a widely used strategy for grouping of K users into the specified number of clusters, such that each user belongs to the cluster with the nearest mean [5]. However, the constraints on the cluster size cannot be imposed with K-means clustering. This presents an important disadvantage in MU-MIMO scenario since the number of users within the cluster should be less or equal to the number of base station antennas. Also, the number of clusters needs to be specified in advance and the final results are proven to be sensitive to initial parameters, while method often terminates at a local optimum [6]. In [7], Dimic and Sidiropoulos presented a suboptimal greedy user selection algorithm which iteratively selects user with the biggest contribution to the cumulative system capacity until further increase cannot be achieved. When this approach is applied, only those users characterized with the favorable channel conditions are selected, while users with less favorable channel conditions are dropped. Such behaviour can present a problem in the case of the fixed IoT endpoint devices with relatively low throughput requirements since these may be dropped in many consecutive iterations and thus not be served for a long period of time. In [8], Tian et al. introduced the concept of overlapping user grouping (OUG) based on the greedy approach (OUG-Greedy). They also demonstrated that the OUG-Greedy can achieve higher capacity than existing greedy user selection algorithms and ensure that each user will be selected in at least one beamforming subgroup. Such defined user grouping strategy takes the full advantage of the favorable propagation which represents a key property in massive MIMO systems [9]. An overlapping user grouping approach based on the spectral clustering (OUG-SC) has been also proposed in [8]. Spectral clustering method has many fundamental advantages comparing to the traditional K-means clustering. However, it also requires the number of clusters as an input. The OUG-SC algorithm has reduced computational complexity but it achieves lower throughput performance than OUG-Greedy algorithm [8]. This is due to the fact that OUG-Greedy algorithm directly optimizes sum capacity with the greedy user selection approach. On the other hand, OUG-SC algorithm uses indirect metric for channel similarity measure as a part of spectral clustering procedure [8, 10].

The joint decoding at the receiver side is not feasible in MU-MIMO system since users cannot cooperate due to their random geographic location. Hence, the successful data transmission is extremely dependent on the precoding technique deployed at the base station, i.e., the ability to simultaneously send independent signals and suppress interference between users as much as possible. When channel state information (CSI) is considered known at the transmitter side (i.e., reliably estimated), the nonlinear dirty paper coding (DPC) technique [11] can completely eliminate interuser interference and achieve the maximum MU-MIMO system capacity. The Tomlinson-Harashima precoding (THP) [12] represents the simplified version of DPC which combines symmetric modulo operation and achieves near maximum capacity performance. Another prominent nonlinear precoding technique is vector perturbation (VP) [13], which perturbs signal data vectors intended for different users in order to achieve better orthogonalization. Thus, a more reliable decoding can be achieved on the receiver side. Low complexity user grouping strategies based on VP technique were proposed to support adaptive modulation mechanism [14, 15]. In traditional VP algorithm, where the same modulation scheme is applied for all users, perturbation signal is found via closest-point lattice search which is the nondeterministic polynomial-time hard (NP-hard) problem. The lattice-reduction-aided (LR-aided) algorithm could be used to overcome this challenge. However, THP has lower complexity and it outperforms LR-aided VP in the case of the large-scale MIMO application scenario [16]. Anyhow, the computational complexity of nonlinear precoding schemes significantly increases with the number of users which complicates their practical implementation.

Conversely, the linear precoding schemes with the reduced complexity are also proposed for MU-MIMO systems, such as zero forcing (ZF) and block diagonalization (BD) [17]. These schemes are successfully deployed in long-term evolution (LTE) networks and can mitigate interuser interference by projecting signal of the intended user into the null space of all the other users. However, in the case of users with highly correlated channels, it is almost impossible to discriminate signals with the projection operation which results in high capacity loss. In order to enhance MU-MIMO system capacity and alleviate its complexity at the same time, a combination of linear and nonlinear precoding schemes, i.e., two-stage precoding scheme, is proposed in the Third Generation Partnership Project (3GPP) standardization phase for 5G NR [18, 19].

In [20], Zarei et al. proposed low-complexity two-stage H-L-THP precoding scheme which achieves performance close to the conventional THP. It was assumed that all users within the same group have identical CSI statistics. However, a concrete user grouping strategy was not considered in [20] even though it significantly contributes to the overall MU-MIMO system complexity. In [21], Trifan et al. proposed two-stage BD-THP precoding scheme based on the optimized K-means clustering with the imposed cluster size constraint and a distance metric based on the angles between users. Yet, this approach does not provide information on the channel separation between users associated with different clusters. Moreover, in this approach, user selection within the cluster is performed randomly. This can result in scheduling of users with the unsuitable mutual channel conditions and a degradation of MU-MIMO system performance.

In this paper, we propose an approach in which the existing hybrid two-stage precoding scheme is extended with the overlapping user grouping strategy. Also, the comprehensive

analysis on its computational complexity throughput and BER performance has been conducted for mMTC 5G NR use case. Instead of further modification of K-means clustering, like in [21], we here adopt the overlapping user grouping method from OUG-Greedy algorithm. This algorithm considers both user selection and user ordering in order to maximize MU-MIMO system capacity and to ensure that users with the favorable channel conditions are assigned to multiple beamforming subgroups simultaneously. Two-stage precoding technique is used afterwards to separate newly formed beamforming subgroups in the spatial domain. In the first stage, ZF scheme is used to block-diagonalize the channel matrix, i.e., to minimize the intergroup interference. In the second stage, for each subgroup, a THP scheme is used to eliminate the interuser interference. The main difference between our two-stage precoding technique and the ones proposed in [20, 21] is that calculation of precoding matrices for beamforming subgroups is done in the initial step by OUG-Greedy so that linear ZF precoder can directly use them for block diagonalization which simplifies overall beamforming procedure. It should be also noticed that application of OUG-Greedy algorithm yields to the significant capacity gain compared to the legacy user grouping when combined with two-stage precoding technique. Also, we adopted two-stage ZF-THP precoding in order to accomplish balance between the achieved capacity gains and the suffered computational complexity (i.e., in comparison to the case in which only THP is used). While the existing works on two-stage precoders based on legacy user grouping strategies compare their performance only with the performance of linear precoders or two-stage schemes with two-stage linear precoding, we here benchmark proposed algorithm against nonlinear precoders and two-stage schemes with nonlinear precoding as well. Hence, this paper also provides the comparative analysis of all precoding types combined with legacy and overlapping user grouping methods.

The rest of the paper is organized as follows. System model is introduced and user grouping problem is formulated in Section 2. In Section 3, the proposed two-stage precoding scheme based on overlapping user grouping strategy is proposed. Complexity evaluation of the proposed algorithm is carried out in Section 4. Numerical simulation results and comparative analysis with the algorithms that employ existing user grouping methods and precoding schemes are presented in Section 5. Section 6 concludes this paper and presents research directions for the future work.

2. System Model and Problem Formulation

2.1. System Model. The downlink of a single-cell MU-MIMO system is considered, in which a base station with a uniform rectangular antenna array of N antennas simultaneously transmits data to K single-antenna IoT devices (IoT users). We did not consider IoT devices equipped with multiple antennas since these are generally considered as a small and simple devices. It would not be practical to equip them with MIMO antennas because it would not provide sufficient spatial diversity between the antennas to enable effective operation. The choice of multiple antennas would demand independent RF chains per each antenna and advanced digital processing to separate the data streams. This would increase cost and complexity of IoT devices, and also increase energy consumption that is not appropriate for the battery powered devices. Channel matrix is assumed fixed during the channel coherence time and can be expressed as $\mathbf{H} = [\mathbf{h}_1, \cdots, \mathbf{h}_K]^{\mathrm{T}} \in \mathbb{C}^{K\times N}$, where $(\bullet)^{\mathrm{T}}$ denotes matrix or vector transpose, and $\mathbf{h}_k \in \mathbb{C}^{N\times 1}$ is the channel vector between the base station and user k. As in the previous work in this area, we assume that CSI is known at the base station. Let denote y_k as the received signal at user k. The signals received by users can be written as follows:

$$\mathbf{y} = \mathbf{HBd} + \mathbf{n}, \tag{1}$$

where $\mathbf{y} \in \mathbb{C}^{K\times 1}$ denotes the received data for all K users in a single time slot, $\mathbf{B} \in \mathbb{C}^{N\times K}$ is the precoding matrix, $\mathbf{d} \in \mathbb{C}^{K\times 1}$ is the data vector intended for transmission to K users where $d_k \in A = \{a_{\mathrm{I}} + ja_{\mathrm{Q}} \mid a_{\mathrm{I}}, a_{\mathrm{Q}} \in \{\pm 1, \pm 3, \cdots, \pm(\sqrt{M} - 1)\}\}$ is M-QAM modulated data symbol of the kth user with modulation order M, and $\mathbf{n} \sim CN(0, \mathbf{I}_K)$ is the additive white Gaussian noise (AWGN) vector with zero mean and unit variance. The choice of this particular modulation scheme is made since the traditional THP precoder only applies for M-QAM signaling. Modified THP, which is characterized with similar complexity as traditional THP, was recently designed to support M-PSK modulations included in 5G standardization for millimeter wave communications [22]. Described system model operates on sub-6 GHz band; hence, the traditional THP precoder is sufficient for this scenario and it also simplifies receiver design. The total power of transmitted signal $\mathbf{x} = \mathbf{Bd} \in \mathbb{C}^{N\times 1}$ is constrained to $\mathbb{E}[\mathbf{xx}^{\mathrm{H}}] \leq P_T$, where $\mathbb{E}(\bullet)$ stands for the expectation operator and $(\bullet)^{\mathrm{H}}$ denotes matrix or vector Hermitian transpose. Throughout this manuscript, bold uppercase and lowercase symbols are used to denote matrices and vectors, respectively, and the normal symbols are used to represent scalars.

In many urban mMTC 5G NR use cases, IoT devices are located indoor, whereas macrobase station is located outdoor. Hence, we here consider that base station communicates with users over the spatially correlated Rayleigh channels characterized with the non-line-of-sight (NLOS) propagation [8].

In the considered scenario, base station is elevated and free of local scattering, which results in high correlation among the transmit antennas. We model spatial correlation matrix at the transmitter $\mathbf{R}_{TX} \in \mathbb{C}^{N\times N}$ using the one-ring MIMO channel scattering model shown in Figure 1, which was firstly employed by Jakes [23] and adopted in [24]. Let θ be the azimuth angle of the user located at distance S from base station and surrounded by a ring of scatterers with radius r. From Figure 1, it follows that angular spread of transmitted signal Δ can be approximated as $\Delta \approx \mathrm{arctg}(r/S)$. Spatial correlation coefficient between transmit antennas $1 \leq p, q \leq N$ is modelled as follows [24]:

$$[\mathbf{R}_{TX}]_{p,q} = \frac{1}{2\Delta} \int_{-\Delta}^{\Delta} e^{j\mathbf{g}^{\mathrm{T}}(\alpha+\theta)\left(\mathrm{u}_p - \mathrm{u}_q\right)} d\alpha, \tag{2}$$

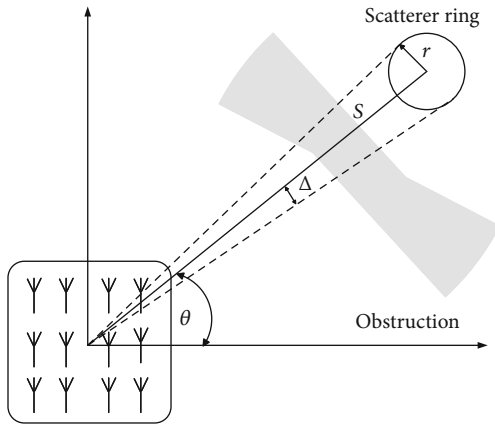

Figure 1: One-ring MIMO channel scattering model.

where $\mathbf{g}(\alpha+\theta) = -(2\pi/\lambda_c)[\cos(\alpha+\theta)\ \sin(\alpha+\theta)]^{\mathrm{T}}$ is the vector for a planar wave impinging the transmit antenna array with the angle of arrival (AoA) α, λ_c is the wavelength that corresponds to carrier frequency f_c, and $\mathbf{u}_p$, $\mathbf{u}_q \in \mathbb{R}^2$ are vectors indicating the position of base station antennas p, q in two-dimensional (2D) coordinate system.

From Equation (2), it can be verified that $\mathbf{R}_{TX}$ is a normal matrix which can be eigendecomposed as follows:

$$\mathbf{R}_{TX} = \mathbf{U}_{TX}\,\mathbf{\Sigma}_{TX}\mathbf{U}_{TX}^{\mathrm{H}}, \tag{3}$$

where $\mathbf{U}_{TX} \in \mathbb{C}^{N\times N}$ represents a unitary matrix composed of the eigenvectors of $\mathbf{R}_{TX}$ and $\mathbf{\Sigma}_{TX} \in \mathbb{R}^{N\times N}$ is a diagonal matrix whose elements are eigenvalues of $\mathbf{R}_{TX}$.

IoT devices located indoor usually experience fluctuation of the received signal power due to the obstacles on the transmission path, i.e., shadow fading. The channels of geographically proximate devices are significantly correlated when affected by the same shadowing. Spatial correlation of the channels between users $1 \le i, j \le K$ is modelled using Gudmundson's model defined in [25] and adapted for IoT networks in [26] as follows:

$$[\mathbf{R}_{RX}]_{i,j} = \frac{\sigma_s^2}{d_{\mathrm{cor}}} e^{-|d_{i,j}|/d_{\mathrm{cor}}}, \tag{4}$$

where $|d_{i,j}|$ denotes the distance between users i and j, σ_s is the standard deviation of shadow fading, and d_{cor} is the correlation distance, i.e., distance at which correlation drops to 0.5. $\mathbf{R}_{RX} \in \mathbb{C}^{K\times K}$ is also a normal matrix with eigendecomposition similar to Equation (3)

$$\mathbf{R}_{RX} = \mathbf{U}_{RX}\,\mathbf{\Sigma}_{RX}\mathbf{U}_{RX}^{\mathrm{H}}, \tag{5}$$

where unitary matrix $\mathbf{U}_{RX} \in \mathbb{C}^{K\times K}$ and diagonal matrix $\mathbf{\Sigma}_{RX} \in \mathbb{R}^{K\times K}$ include the corresponding eigenvectors and eigenvalues of $\mathbf{R}_{RX}$, respectively. We here adopted Kronecker correlation model [27], which assumes complete correlation separability between transmitter and receiver. Hence, channel matrix can be expressed as follows:

$$\mathbf{H} = \mathbf{R}_{RX}^{1/2}\mathbf{H}_{\mathrm{iid}}\mathbf{R}_{TX}^{1/2}, \tag{6}$$

where $\mathbf{H}_{\mathrm{iid}} \in \mathbb{C}^{K\times N}$ is an uncorrelated Rayleigh channel matrix whose elements are independent and identically distributed (i.i.d.) complex Gaussian random variables with zero mean and unit variance. Substitution of decomposed spatial correlation matrices at transmitter (Equation (3)) and receiver (Equation (5)) in Equation (6) gives the following channel matrix expression:

$$\mathbf{H} = \mathbf{U}_{RX}\mathbf{\Sigma}_{RX}^{1/2}\mathbf{H}_{\mathrm{iid}}\mathbf{\Sigma}_{TX}^{1/2}\mathbf{U}_{TX}. \tag{7}$$

2.2. User Grouping Problem Formulation. The performance of MU-MIMO system largely depends on the channel correlation among the users included in the same beamforming subgroup. Hence, the proper user grouping is necessary in order to suppress interuser interference and maximize system capacity.

Let $\mathbb{S} = \{k \mid k = 1, 2, \cdots, K\}$ denote the whole set of users clustered into G subgroups. Deterministic MIMO channel capacity for each beamforming subgroup $\mathbb{S}_g$, $g = 1, 2, \cdots, G$ is defined as [28]:

$$R_g(\mathbf{H}, \mathbf{B}) = \sum_{k\in\mathbb{S}_g} \log_2\left(1 + \beta_k \left\|\mathbf{h}_k^{\mathrm{H}}\mathbf{b}_k\right\|\right), \tag{8}$$

where $\|\bullet\|$ denotes the vector 2-norm operator. Parameters β_k symbolize the power allocation factors derived from the water-filling algorithm [29]:

$$\beta_k = \left(\frac{1}{\mu} - \frac{1}{\lambda_k}\right)^+, \tag{9}$$

where $(\bullet)^+$ is the operation defined as $(x)^+ = \max\{0, x\}$ and μ is the water level satisfying

$$\sum_{k\in\mathbb{S}_g}\left(\frac{1}{\mu} - \frac{1}{\lambda_k}\right) = P_T, \tag{10}$$

and λ_k is the effective channel gain after beamforming procedure:

$$\lambda_k = \left\|\mathbf{h}_k^{\mathrm{H}}\mathbf{b}_k\right\|, \tag{11}$$

which represents the kth eigenvalue of the effective channel matrix $\mathbf{H}_{\mathrm{eff}} = \mathbf{HB}$ [3].

Different user selections for beamforming subgroups g give different values of Equation (8). Furthermore, different user ordering within the same beamforming subgroup also yields different MU-MIMO sum capacity. In general, user grouping strategy depends on the channel matrix $\mathbf{H}$ and the transmitted signal power P_T. Thus, we define the optimal user grouping method $\mathbf{S}^*(\mathbf{H}, P_T) \triangleq \{\mathbb{S}_1, \cdots, \mathbb{S}_G\}$ as the one that maximizes MU-MIMO system capacity. The corresponding

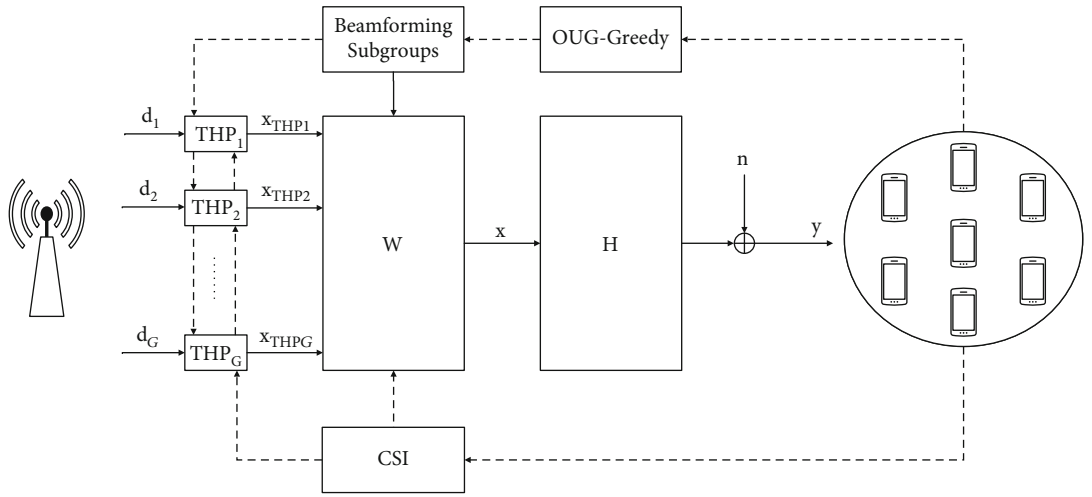

Figure 2: System model for two-stage precoding with overlapping user grouping approach.

optimal power allocation defined by $\boldsymbol{\beta}^*(\mathbf{H}, P_T) \triangleq \{\beta_1, \cdots, \beta_K\}$ gives the maximum sum capacity under the user grouping strategy $\mathbf{S}^*(\mathbf{H}, P_T)$. Putting all together, the optimal user grouping problem can be formulated as in [8]:

$$\{\mathbf{S}^*(\mathbf{H}, P_T), \boldsymbol{\beta}^*(\mathbf{H}, P_T)\} = \arg\max \sum_{g=1}^{G} R_g, \tag{12}$$

subject to $\bigcup_{g=1}^{G} \mathbb{S}_g = \mathbb{S}$ and $\sum_{k=1}^{K} \beta_k \leq P_T$. As can be seen from the previous expression, the sum capacity can be optimized with respect to the overlapping among beamforming subgroups and power allocation when solving the optimization problem (Equation (12)).

3. Two-Stage Precoding Based on Overlapping User Grouping Approach

The system model for the proposed two-stage precoding scheme based on overlapping user grouping strategy is depicted in Figure 2.

User grouping is achieved by employing the overlapping method from OUG-Greedy algorithm introduced in [8]. Let $\mathbb{S}_i$ be the set of users that have been assigned in iteration i and $\mathbb{C}_i$ be the set of remaining users that have not been selected yet. In each iteration, algorithm selects users from $\mathbb{C}_i$ in order to form the subgroup $\mathbb{S}_i$ which gives the maximum capacity defined in Equation (8) with the corresponding water-filling power allocation. This procedure is known as zero forcing with user selection (ZFS) [7] and is repeated until all users are assigned to their respective beamforming subgroups. In the next step, the searching space of subgroup $\mathbb{S}_i$ is widened to the users that have been already assigned to one of the previous subgroups. More specifically, the searching space for subgroup $\mathbb{S}_i$ obtained from ZFS algorithm is reset as follows:

$$\mathbb{C}_{i,o} = \bigcup_{j=1}^{i-1} \mathbb{S}_j, \tag{13}$$

to perform the overlapping user grouping [8]. Using the extended searching space, users with the favorable channel conditions are reselected and assigned to several beamforming subgroups at the same time. Accordingly, we obtain the set of overlapping user groups $\mathbb{S}_{1,o}, \cdots, \mathbb{S}_{G,o}$ and corresponding set of matrices $\mathbf{H}_1, \cdots, \mathbf{H}_G$ where $\mathbf{H}_g \in \mathbb{C}^{K_g \times N}$ denotes the row-reduced channel matrix which includes channel vectors of K_g users selected in beamforming subgroup $\mathbb{S}_{g,o}$.

Once users are grouped according to the OUG-Greedy algorithm, linear ZF precoding scheme is applied to suppress interference between already formed beamforming subgroups. For this purpose, precoder $\mathbf{W} = [\mathbf{W}_1, \cdots, \mathbf{W}_G]$ with $\mathbf{W}_g \in \mathbb{C}^{N \times K_g}$ is designed to null off-diagonal elements of the effective ZF channel matrix:

$$\mathbf{HW} = \begin{bmatrix} \mathbf{H}_1\mathbf{W}_1 & \mathbf{H}_1\mathbf{W}_2 & \cdots \mathbf{H}_1\mathbf{W}_G \\ \mathbf{H}_2\mathbf{W}_1 & \mathbf{H}_2\mathbf{W}_2 & \cdots \mathbf{H}_2\mathbf{W}_G \\ \vdots & \vdots & \vdots \\ \mathbf{H}_G\mathbf{W}_1 & \mathbf{H}_G\mathbf{W}_2 & \cdots \mathbf{H}_G\mathbf{W}_G \end{bmatrix}. \tag{14}$$

In order to cancel intergroup interference, the effective ZF channel matrix from Equation (14) must be diagonalized, i.e., $\mathbf{H}_i\mathbf{W}_j = 0$ for every $i \neq j$. This is possible when precoding matrix for each beamforming subgroup is a Moore-Penrose pseudoinverse of the row-reduced channel matrix [30].

$$\mathbf{W}_g = \mathbf{H}_g^{\mathrm{H}} \left(\mathbf{H}_g \mathbf{H}_g^{\mathrm{H}} \right)^{-1}. \tag{15}$$

Hence, the user data in each beamforming subgroup is ideally transmitted in the null space of the channel matrix made of channel vectors related to users from all other subgroups. However, it should be noticed that it is not necessary to determine previous Equation (15) since the corresponding precoding matrices are already obtained in OUG-Greedy algorithm when calculating Equation (8). This leads to simplified ZF precoding which only includes multiplication of

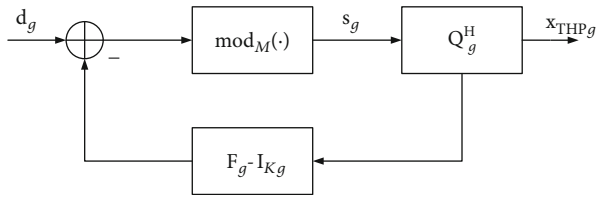

Figure 3: System model for THP scheme.

precoding matrices obtained from OUG-Greedy algorithm with the corresponding row-reduced channel matrices.

After the ZF precoding technique is performed, remaining interuser interference in each beamforming subgroup is mitigated by using the nonlinear THP precoding scheme. THP precoded signal for beamforming subgroup g is given by $\mathbf{x}_{\mathrm{THP}g} = \mathbf{Q}_g^{\mathrm{H}}\mathbf{s}_g \in \mathbb{C}^{K_g \times 1}$ as shown in Figure 3. Thus, $\mathbf{Q}_g \in \mathbb{C}^{K_g \times K_g}$ is an unitary feedforward matrix obtained from LQ decomposition of gth diagonal element of the effective channel matrix $\check{\mathbf{H}}_g = \mathbf{H}_g\mathbf{W}_g \in \mathbb{C}^{K_g \times K_g}$, and $\mathbf{s}_g \in \mathbb{C}^{K_g \times 1}$ is a data vector whose elements are calculated according to the following:

$$\left[\mathbf{s}_g\right]_{k,1} = \mathrm{mod}_M\left(\left[\mathbf{d}_g\right]_{k,1} - \sum_{l=1}^{k-1}\left[\mathbf{F}_g - \mathbf{I}_{K_g}\right]_{k,l}\left[\mathbf{s}_g\right]_{l,1}\right), \quad (16)$$

where $\mathbf{F}_g \in \mathbb{C}^{K_g \times K_g}$ represents the feedback matrix, $\mathbf{I}_{K_g} \in \mathbb{C}^{K_g \times K_g}$ denotes the identity matrix, and $\mathrm{mod}_M(\bullet)$ is a symmetric modulo function which limits transmitted power of modulated data symbols and ensures that they lie inside the Voronoi region of the original constellation and is given by the following:

$$\begin{aligned}\mathrm{mod}_M(x) = x &- 2\sqrt{M}\left\lfloor\frac{1}{2} + \Re\left\{\frac{x}{2\sqrt{M}}\right\}\right\rfloor \\ &- 2j\sqrt{M}\left\lfloor\frac{1}{2} + \Im\left\{\frac{x}{2\sqrt{M}}\right\}\right\rfloor,\end{aligned} \quad (17)$$

with $\Re\{\cdot\}$ and $\Im\{\cdot\}$ representing the real and imaginary part of complex number x. The main purpose of the feedback matrix $\mathbf{F}_g$ is to cancel the interference caused by already detected data symbols and is defined as follows:

$$\mathbf{F}_g = \mathbf{G}_g\mathbf{L}_g, \quad (18)$$

where $\mathbf{G}_g = \mathrm{diag}\left(l_{11}^{-1}, \cdots, l_{K_gK_g}^{-1}\right) \in \mathbb{C}^{K_g \times K_g}$ is the diagonal scaling matrix and $\mathbf{L}_g \in \mathbb{C}^{K_g \times K_g}$ is the lower triangular matrix derived from LQ decomposition of $\check{\mathbf{H}}_g$. Hence, THP precoding matrix $\mathbf{P}_g \in \mathbb{C}^{K_g \times K_g}$ for beamforming subgroup g can be expressed as follows:

$$\mathbf{P}_g = \mathbf{Q}_g^{\mathrm{H}}\mathbf{L}_g^{-1}\mathbf{G}_g^{-1}. \quad (19)$$

As can be seen, the proposed hybrid mechanism is based on two-stage precoding. The first stage consists of the linear precoder used to eliminate intergroup interference. To suppress interference inside every group, the nonlinear precoding is employed in the second stage. In other words, beamforming matrix $\mathbf{B}$ consists of two parts:

$$\mathbf{B} = \mathbf{WP}, \quad (20)$$

where $\mathbf{W} \in \mathbb{C}^{N \times K}$ denotes the linear ZF beamforming matrix and $\mathbf{P} \in \mathbb{C}^{K \times K}$ is the cumulative nonlinear THP beamforming matrix.

The achievable sum rate of the proposed algorithm is calculated as $\sum_{g=1}^{G} R_g$ where R_g represents channel capacity for overlapped beamforming subgroup $\mathbb{S}_{g,o}$ defined as in [28]:

$$R_g(\mathbf{H}, \mathbf{B}) = \sum_{k \in \mathbb{S}_g} \log_2\left(1 + \beta_k\left\|\mathbf{h}_k^{\mathrm{H}}\mathbf{b}_k\right\|\right), \quad (21)$$

which is equivalent to Equation (8) and derived for the case of perfect MIMO channel estimation. Previous formula was used for the performance evaluation of all existing algorithms and the proposed one in Section 5.

4. Computational Complexity Analysis

Computational complexity is an important design parameter, especially in implementation of IoT-oriented 5G systems where a massive number of IoT devices have limited battery lifetime. This section covers complexity analysis of the proposed scheme with two-stage ZF-THP precoding based on overlapping user grouping approach (marked as OUG ZF-THP algorithm). In order to achieve this, the computational complexity for deployed overlapping user grouping method and two-stage ZF-THP precoding is derived. The total computational capacity is defined as the sum of these two parts (excluding the calculations from the prior steps that can be reused in the former steps). Also, in order to compare computational complexity for the proposed and the referent algorithms, the complexity for these algorithms is given. As the referent algorithms, we here observed previously introduced OUG-Greedy grouping with the linear ZF precoding (marked as OUG-Greedy ZF algorithm) proposed in [8], two-stage BD-THP precoding based on the optimized K-means clustering (marked as K-means BD-THP algorithm) proposed in [21], and linear ZFS algorithm proposed in [7]. We here also consider scheme with THP precoding based on overlapping user grouping strategy (marked as OUG THP), a combination that was not previously observed in the literature. More on this referent scheme is given in the next section where the capacity performance analysis is presented. Since all these algorithms also comprise user grouping and the precoding part, the computational complexity is presented for the both of these parts separately, and the total complexity is given as the sum of these two (in the same way as for the proposed algorithm).

The complexity for all the observed algorithms is quantified by the number of floating-point operations (FLOPs) [30] required for multiplication (division) and addition (subtraction) of complex-valued numbers. For the sake of accuracy, we use a common assumption and count each complex-

valued multiplication as 6 FLOPs and each complex-valued addition as 2 FLOPs. Also, computational complexity required for T_c precoded data vectors is considered, where T_c represents the channel coherence time interval.

First, we consider complexity of the overlapping user grouping method. For the sake of brevity, it was assumed that each beamforming subgroup has $K_g = K/G$ users. Derivation of the effective channel gains represents the most computationally expensive operation in the overall OUG-Greedy algorithm [7]. As an alternative to Equation (11), the simplified sequential water-filling (SWF) approach for channel matrix pseudoinverse Equation (15) and channel gain Equation (11) calculation is introduced in [4] as follows:

$$\lambda_k = \left|\mathbf{h}_k \mathbf{P}_k^{\perp}\right|^2, \tag{22}$$

where $\mathbf{P}_k^{\perp} \in \mathbb{C}^{N\times N}$ is a projection matrix onto the orthogonal complement of the subspace spanned by the channels $\mathbf{h}_1, \cdots, \mathbf{h}_{k-1}$ of the currently selected users in that beamforming subgroup. Vector-matrix multiplication in Equation (21) requires $2N(4N-1)$ FLOPs [31]. In the worst-case scenario, this procedure is performed for all K users in K_g iterations. Repetition over G beamforming subgroups gives the total number of FLOPs:

$$C_{\text{OUG-Greedy}} = 2G^2K_g^2N(4N-1), \tag{23}$$

which can be formulated after substitution $K_g = K/G$ as follows:

$$C_{\text{OUG-Greedy}} = 2K^2N(4N-1). \tag{24}$$

Hence, the computational complexity of the overlapping user grouping strategy is no more than $O(K^2N^2)$ which is of the same order as ZFS with SWF mechanism [4] and two-order simpler comparing to the conventional capacity-based ZFS algorithm [32] as outlined in Table 1. In practice, the number of beamforming subgroups G will be more than 2; thus, OUG-Greedy algorithm also outperforms optimized K-means clustering method used by K -means BD-THP algorithm [21].

Next, we derive the computational complexity of two-stage ZF-THP precoding scheme. Matrix-matrix multiplication is executed in order to obtain diagonal elements of the effective channel matrix $\check{\mathbf{H}}_g$ which requires $2K_g^2(4N-1)$ FLOPs. Note that complexity of calculating Moore-Penrose pseudoinverses $\mathbf{W}_g$ has been already evaluated as part of the user grouping procedure. LQ decomposition of matrix $\check{\mathbf{H}}_g$ requires approximately $16K_g^3/3$ FLOPs [33]. Calculation of diagonal scaling matrix $\mathbf{G}_g$ requires K_g FLOPs which is used for generating feedback matrix $\mathbf{F}_g$ with complexity of $2K_g^2(4K_g-1)$ FLOPs. Subtracting identity matrix $\mathbf{I}_{K_g}$ from feedback matrix $\mathbf{F}_g$ requires K_g FLOPs. Calculating T_c data vectors $\mathbf{s}_g$ requires $4T_c(K_g^2 + K_g - 2)$ FLOPs [34]. Multiplication of $\mathbf{W}_g$ with the unitary feedforward matrix Hermitian $\mathbf{Q}_g^{\mathrm{H}}$ requires $2NK_g(4K_g-1)$ FLOPs. Previous steps are repeated G times for each beamforming subgroup.

Table 1: Computational complexity of user grouping algorithms.

User grouping algorithm	Number of FLOPs
Capacity-based ZFS	$O(KN^5)$
ZFS with SWF	$O(KN^3)$
OUG-Greedy	$O(K^2N^2)$
Optimized K-means clustering	$O(K^{G+1}G)$

Finally, $2T_cN(4K-1)$ FLOPs are needed to multiply the cumulative product $\mathbf{W}_g\mathbf{Q}_g^{\mathrm{H}}$ with data vectors $\mathbf{s}_g$ for all K users and generate T_c two-stage precoded data vectors $\mathbf{x}$. Thus, the total number of FLOPs required for two-stage ZF-THP precoding is as follows:

$$C_{\text{ZF-THP}} = \frac{40GK_g^3}{3} - 4GK_g^2 + 2GK_g - 2GK_gN + 16GK_g^2N + T_c\left(4GK_g^2 + 4GK_g + 8KN - 8G - 2N\right). \tag{25}$$

Application of the corresponding substitution $K_g = K/G$ gives more concise expression:

$$C_{\text{ZF-THP}} = \frac{2K\left(3G^2 - 3G^2N + 20K^2 - 6GK + 24GKN\right)}{3G^2} + \frac{2T_c\left(2K^2 - 4G^2 + 2GK - GN + 4GKN\right)}{G}. \tag{26}$$

As summarized in Table 2, two-stage ZF-THP precoding scheme has the same computational complexity as two-stage BD-THP scheme. The expressions for complexity of the precoding techniques summarized in Table 2 are adopted from [20] in the case of ZF precoding and THP schemes, and from [21] for BD-THP scheme.

Moreover, two-stage ZF-THP technique has the lowest complexity among conventional linear and nonlinear precoding schemes. The computational complexity required to generate one two-stage precoded data vector in the case of 32 antennas and IoT devices grouped in 4 beamforming subgroups is illustrated in Figure 4. For this choice of parameter values, presented precoding schemes have similar complexity when the number of IoT devices is less than 20. As the number of users in the cell increases, a computational complexity of ZF and THP precoders substantially escalates in comparison with ZF-THP and BD-THP. As expected, nonlinear THP scheme has the highest complexity.

Based on the previously defined computational complexity for different user grouping and precoding schemes, the total complexity for all observed algorithms is presented in Table 3. The total complexity is calculated as a sum of corresponding user grouping and precoding schemes for each

Table 2: Computational complexity of precoding schemes.

Precoding scheme	Number of FLOPs
ZF	$4K^3 + 2KN(4K-1) + K(4N-1)(K+1) + 2NT_c(4K-1) + 8K^2 + 6K$
THP	$\frac{16K^3}{3} + 2K(4KN - K + 2) + 2T_c(2K + 2K^2 + N(4K-1) - 4)$
BD-THP	$\frac{2K(3G^2 - 3G^2N + 20K^2 - 6GK + 24GKN)}{3G^2} + \frac{2T_c(2K^2 - 4G^2 + 2GK - GN + 4GKN)}{G}$
ZF-THP	$\frac{2K(3G^2 - 3G^2N + 20K^2 - 6GK + 24GKN)}{3G^2} + \frac{2T_c(2K^2 - 4G^2 + 2GK - GN + 4GKN)}{G}$

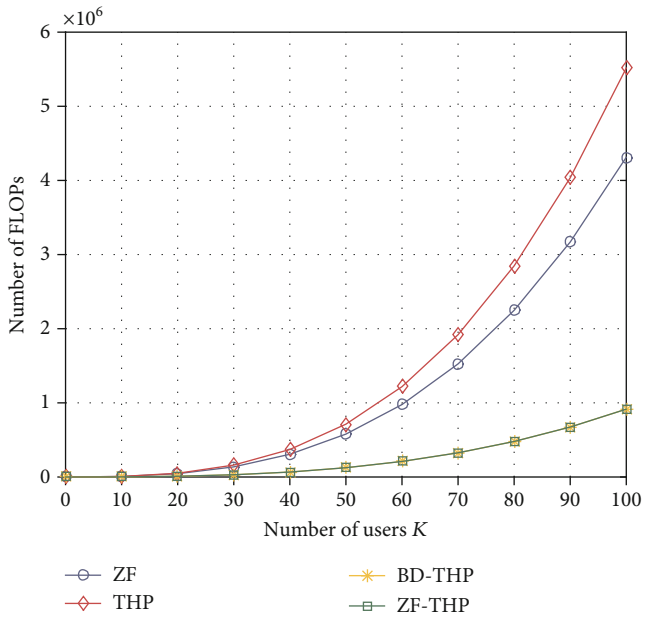

Figure 4: Computational complexity of precoding schemes.

algorithm (excluding the complexity related to calculation of beamforming matrices when ZF precoding is employed, since these were calculated as a part of user grouping procedure in ZFS, OUG ZF-THP, and OUG-Greedy ZF algorithms).

As evident in Table 3, ZFS and OUG-Greedy ZF algorithms have somewhat lower computational complexity than OUG ZF-THP algorithm. Such behaviour could be expected since these two schemes employ only linear ZF precoding with lower complexity due to the reuse of beamforming matrices already calculated as a part of user grouping procedure (similarly as for OUG ZF-THP algorithm). However, as will be presented in the next section, these schemes achieve lower overall MU-MIMO system capacity than OUG ZF-THP due to the less efficient ZF precoding in comparison to ZF-THP precoding. This is particularly evident in the case of the correlated MIMO channels (i.e., mutually dependent user channels) when linear ZF precoding cannot sucesfully mitigate all interuser interference, and more complex two-stage ZF-THP precoding achieves significantly better performance and thus enables larger capacity gains.

On the other hand, OUG ZF-THP algorithm has lower computational complexity than OUG THP and K-means BD-THP algorithms. The higher complexity of OUG THP algorithm is a consequence of using THP precoding, which possess significantly higher complexity than ZF-THP precoding. However, this more complex precoding scheme enables somewhat higher capacity gains, as will be shown in the next section. If we observe OUG ZF-THP and K-means BD-THP complexity, it is obvious in Table 2 and Figure 4 that ZF-THP and BD-THP precoding schemes require the same amount of FLOPs. However, complexity order of the optimized K-means clustering adopted in K-means BD-THP algorithm increases linearly with the number of beamforming subgroups G [21] which is not the case with overlapping user grouping method deployed in OUG ZF-THP algorithm. Hence, overall OUG ZF-THP algorithm is more computationally efficient than K-means BD-THP algorithm.

Also, it is worth mentioning that in K-means BD-THP algorithm, the computational complexity of singular value decomposition (SVD) procedure for the linear precoding part (i.e., BD procedure) is neglected since it has to be determined very infrequently from the long-term CSI. In here proposed OUG ZF-THP algorithm, calculation of beamforming matrices is done as a part of user grouping procedure which simplifies subsequent linear ZF precoding. This gives more realistic evaluation of OUG ZF-THP complexity.

5. Results and Discussion

To evaluate the performance of the proposed two-stage ZF-THP precoding based on overlapping user grouping approach (OUG ZF-THP algorithm), we compared the MU-MIMO system capacity for this algorithm with the linear OUG-Greedy ZF algorithm [8] and two-stage BD-THP precoding based on optimized K-means clustering (K-means BD-THP) [21]. First algorithm introduces the overlapping user grouping method which showed good performance in IoT-oriented MU-MIMO system. Latter one considers concrete user grouping strategy in junction with two-stage precoding scheme for the first time. Thus, these algorithms represent suitable candidates for the performance benchmarking. For the sake of completeness, we also show simulation results for ZFS [7] and THP precoding [12], combined with the overlapping user grouping strategy (OUG THP) that defines practical lower and upper bound of the MU-MIMO capacity region for this particular case,

Table 3: Computational complexity of all observed algorithms comprising the user grouping and precoding.

Algorithm	Number of FLOPs
ZFS	$O(KN^3) + 2KN(4K-1) + 2NT_c(4K-1)$
OUG-Greedy ZF	$O(K^2N^2) + 2KN(4K-1) + 2NT_c(4K-1)$
K-means BD-THP	$O(K^{G+1}G) + \frac{2K(3G^2 - 3G^2N + 20K^2 - 6GK + 24GKN)}{3G^2} + \frac{2T_c(2K^2 - 4G^2 + 2GK - GN + 4GKN)}{G}$
OUG ZF-THP	$O(K^2N^2) + \frac{2K(3G^2 - 3G^2N + 20K^2 - 6GK + 24GKN)}{3G^2} + \frac{2T_c(2K^2 - 4G^2 + 2GK - GN + 4GKN)}{G}$
OUG THP	$O(K^2N^2) + \frac{16K^3}{3} + 2K(4KN - K + 2) + 2T_c(2K + 2K^2 + N(4K-1) - 4)$

respectively. 2D MU-MIMO system environment has been created using the MATLAB software package. The MU-MIMO system capacity for all the observed algorithms was estimated according to Equation (21) defined in the Section 3. The Monte-Carlo simulation of these algorithms is performed by averaging 500 random channel realizations.

We assumed a single-cell MU-MIMO system with a base station located at the center of the cell and equipped with 128 omnidirectional antennas which represent the typical configuration of the commercial massive MIMO antenna. It simultaneously transmits data in 3.5 GHz band to 300 single-antenna IoT devices. This frequency band has been identified as a global International Mobile Telecommunications-2020 (IMT-2020) band for 5G NR deployment by International Telecommunication Union Radiocommunication Sector (ITU-R) [35]. Configuration of the planar antenna array is 8×16 (i.e., 8 antenna elements vertically and 16 antenna elements horizontally) with the aim to exploit 2D beamforming in horizontal domain. The base station antenna spacing is normalized with respect to the wavelength and set to 0.5. Data symbols are modulated with 16-QAM technique which was shown sufficient for mMTC 5G NR use cases [36]. To simulate the transmit and receive antenna correlation, we adopted Jakes' one-ring MIMO channel model [23] and Gudmundson's shadowing model [25] commonly used in cellular IoT scenarios, respectively.

Parameter values for both correlation models were taken from [8] since the same type of propagation environment was considered. The scattering objects are located around devices in radius of 30 meters [24], while correlation distance between devices is 20 meters and shadow fading varies with standard deviation of 0.4 [26]. IoT devices are uniformly distributed around base station with dedicated azimuth values at distance between 100 and 300 meters. The angular spread of the signal transmitted from the base station is derived as in [24]. This is aligned with the expected beam arrival distance in rich scattering radio environment for chosen antenna configuration and operating frequency band. An overview of the main system parameter configuration used in Monte-Carlo simulations is provided in Table 4.

In [8], it was mathematically shown that overlapping user beamforming subgroup $\mathbb{S}_{g,o}$ can select more users with a higher probability than the corresponding beamforming subgroup $\mathbb{S}_g$ and that searching space extension always results in larger capacity. We demonstrate numerically the superiority of here proposed approach that combines overlapping user grouping method with two-stage ZF-THP precoding scheme in terms of the achievable MU-MIMO system capacity.

Table 4: System parameter configuration.

Parameter	Value	Parameter	Value
θ	[-180°, 180°]	N	128
Δ	[5°, 15°]	K	300
d_{cor}	20 m	D	0.5
r	30 m	σ_s	0.4
f_c	3.5 GHz	M	16

First, we have evaluated the proposed algorithm performance in the case of the environment with uncorrelated Rayleigh fading where users' channels are mutually independent. Equivalent channel-based received signal-to-noise ratio (SNR) to throughput mapping method adopted by 3GPP [19] is used for performance evaluation. MU-MIMO system capacity comparison of the analyzed algorithms is outlined in Figure 5.

It can be seen that proposed OUG ZF-THP algorithm achieves approximately the same capacity as OUG THP and OUG-Greedy ZF algorithms. The same finding holds for the conventional ZFS and K-means BD-THP algorithms. This is due to the fact that linear precoding has almost the same performance as nonlinear precoding when users have uncorrelated channel vectors. Hence, linear precoder can efficiently suppress both intergroup and interuser interference and there is no need to use two-stage hybrid precoding mechanism. K-means BD-THP algorithm has lower throughput performance due to a lack of overlapping approach which could further populate formed subgroups using the favorable propagation property. In the case of uncorrelated MIMO channels, the capacity improvement is mainly achieved by overlapping user grouping strategy among beamforming subgroups.

Next, we consider more realistic scenario with correlated shadow fading which imposes dependency between user channels. Results in Figure 6 show that proposed OUG ZF-THP algorithm achieves significant improvement on sum capacity over the existing suboptimal approaches. We can

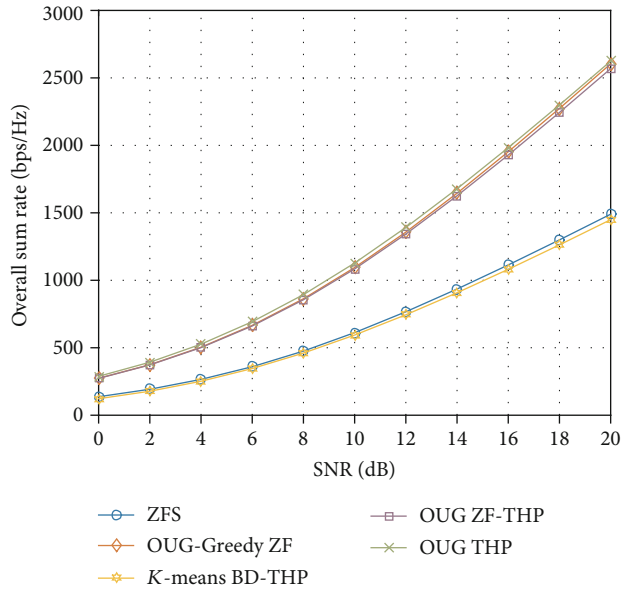

Figure 5: Sum rate comparison under uncorrelated MIMO channels.

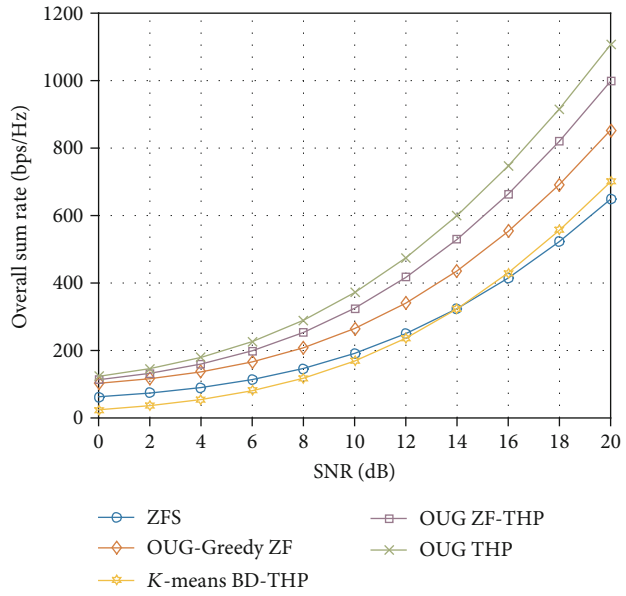

Figure 6: Sum rate comparison under correlated MIMO channels.

observe capacity increase from 10% and 30% in low SNR regime (4 dB) to 25% and 45% in high SNR regime (20 dB) comparing to OUG-Greedy ZF and K-means BD-THP algorithms, respectively. SNR reference values are chosen according to real 5G urban NLOS radio conditions at 3.5 GHz [37].

Obtained large performance gain of OUG ZF-THP algorithm is the result of the proposed combination of more advanced two-stage signal processing and overlapping among beamforming subgroups. Linear OUG-Greedy ZF algorithm achieves lower sum rate due to the correlation of user channel vectors, whereas the poor performance of K-means BD-THP algorithm comes from the random user selection within clusters. Additionally, high SNR regime improves transmission reliability and beam steering which contribute to the higher achievable system throughput. Algorithms that use overlapping user grouping based on greedy user selection methods are exploiting the favorable propagation property without generating much interuser interference which greatly enhances MU-MIMO system capacity. From Figure 6, it can also be seen that nonlinear THP precoding based on overlapping user grouping strategy (i.e., OUG THP) provides the best sum rate. However, here proposed algorithm requires significantly less FLOPs as shown in Section 4. Thus, OUG ZF-THP approach represents a good trade-off between computational complexity and MU-MIMO system performance in terms of capacity.

In order to give further performance comparison for the observed algorithms which comprise user grouping and precoding procedures, we considered the average uncoded bit error rate (BER) as the performance metric (i.e., achieved BER prior to forward error correction decoding at the receiver), where averaging is performed over a sufficient number of channel realizations and over all users. The uncoded BER is calculated as in [16], in which the upper bound for symbol error rate (SER) in the case of different precoding techniques is given, with the additional averaging realized over all users for all beamforming subgroups. The use of Gray coding for the adopted 16-QAM modulation technique is presumed for all schemes. It should be noticed that these BER values are derived in [16], under the assumption that transmitter for each user in each subgroup essentially fixes the minimum required SNR ($\gamma_{\min}$) for which it encodes data at the rate $R = \log_2(1 + \gamma_{\min})$ corresponding to the possible capacity. However, if the actual SNR value is smaller than $\gamma_{\min}$, decoding errors occur with the probability $p_{\text{outage}} = P_r(\gamma < \gamma_{\min})$ [16]. Thus, given BER represents the upper bound for the observed scenario in which the ideal CSI data is used.

The comparison of the estimated average uncoded BER for all the observed algorithms is presented in Figures 7 and 8, in the case of the environment with correlated and uncorrelated Rayleigh fading, respectively. As obviously shown in Figures 7 and 8, the algorithms which deploy more complex nonlinear precoding (i.e., K-means BD-THP, OUG ZH-THP, and OUG THP) significantly outperform those with linear ZF precoding (i.e., ZFS and OUG-Greedy). Such behaviour is expected due to more successful mitigation of interuser interference with nonlinear precoding techniques, as was already shown in the literature [20]. Also, much better BER performance is achieved for all the observed algorithms in the case of uncorrelated MIMO channels, due to the significantly lower interuser interference. The best average uncoded BER is achieved in the case of OUG THP algorithm, while proposed OUG ZF-THP algorithms have somewhat higher BER in the case of uncorrelated MIMO channels, and essentially same BER as OUG THP algorithm in the case of correlated MIMO channels.

Previous findings are summarized in Table 5 where numerical performance of all the observed algorithms in good radio conditions (i.e., 20 dB in the case of achievable sum rate and 40 dB in the case of BER analysis) is presented.

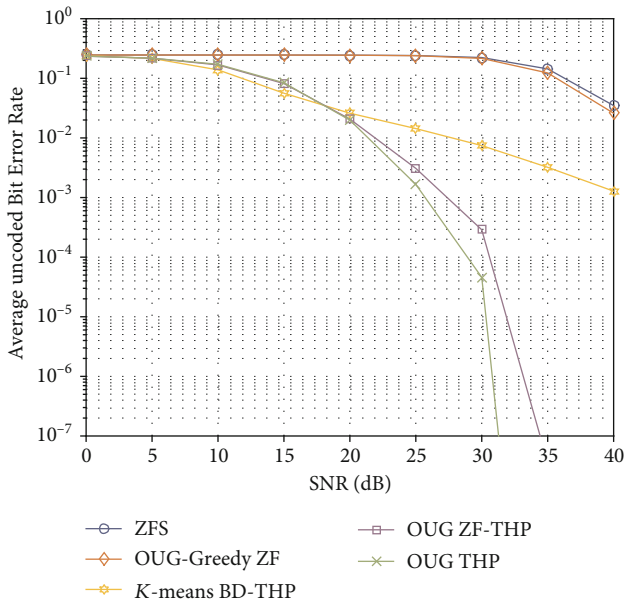

Figure 7: Average uncoded BER comparison under uncorrelated MIMO channels.

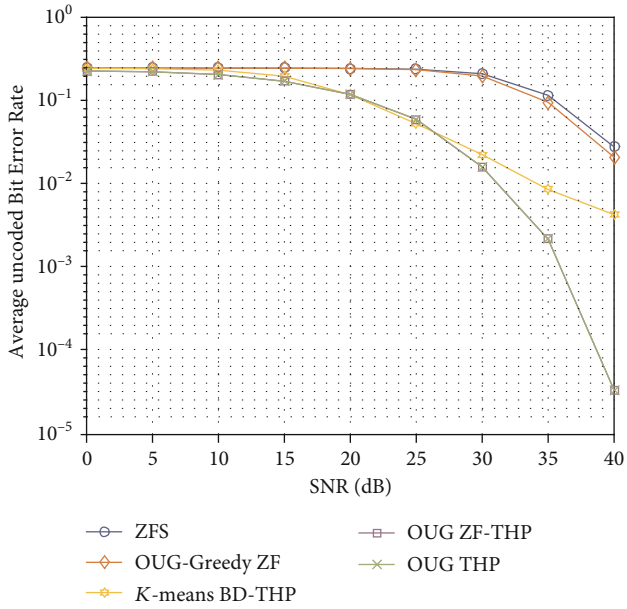

Figure 8: Average uncoded BER comparison under correlated MIMO channels.

When the number of users K increases for the same number of base station antennas N, it was shown that ZF-based user grouping strategies achieve the sum rate which approaches the capacity upper bound [4]. This comes from the fact that more combinations within the search space $\sum_{k=1}^{N}\binom{K}{k}$ are covered. Asymptotically, when user number goes to infinity, the optimal sum rate is achieved since searching among all possible combinations is done. Previous findings apply to our case as well with additional benefit from the introduction of overlapping user grouping approach. In this approach, even more users can be added in unpopulated beamforming subgroups since probability that users' channels are spatially uncorrelated increases. However, this leads to the increased number of beamforming subgroups that should be precoded, and hence, computational complexity becomes prohibitively high because of its polynomial relation with the number of users and their subgroups. To overcome this challenge, we can increase the number of base station antennas. In that way, the same number of users will be served and selected in the lower number of beamforming subgroups keeping the complexity of signal processing on reasonable level. In that case, we could exploit both beamforming and multiplexing gains. However, the increase in the number of base station antennas results with the increased hardware complexity on base station side, especially in the observed 5G NR midband where digital beamforming is envisioned. The trade-off between these two approaches is to choose reasonably a large number of base station antennas and numerous users in the cell but to keep the ratio between them relatively small. The last statement holds in the case of IoT-oriented MU-MIMO system with numerous IoT devices served in 5G cell unlike in massive MIMO case where the number of base station antennas is typically much larger than the number of users [28].

Table 5: Performance of all observed algorithms in good radio conditions.

Algorithm	Achievable sum rate (bps/Hz)	Average BER
ZFS	650	$2.9 * 10^{-2}$
OUG-Greedy ZF	825	$2.1 * 10^{-2}$
K-means BD-THP	710	$4.5 * 10^{-3}$
OUG ZF-THP	1030	$3.5 * 10^{-5}$
OUG THP	1100	$3.5 * 10^{-5}$

6. Conclusions

In this paper, we have studied user grouping and scheduling problem in IoT-oriented 5G MU-MIMO systems. We have proposed two-stage hybrid precoding scheme based on overlapping user grouping strategy for mMTC 5G NR use case. In this framework, user grouping is performed using the greedy approach that allows users with favorable channel conditions to be scheduled into the multiple beamforming subgroups simultaneously. Two-stage hybrid precoding scheme is then applied on created beamforming subgroups in order to minimize the interference in MU-MIMO system. Linear ZF precoding cancels interference among beamforming subgroups while the nonlinear THP precoding reduces remaining interference between scheduled users within each beamforming subgroup. Comparative analysis with other precoding schemes based on different user grouping methods has been presented. Numerical results demonstrate that proposed algorithm achieves much higher MU-MIMO system capacity in comparison to the existing two-stage precoding schemes based on legacy user grouping strategies, especially in large SNR regime (from 30% at 4 dB to 45% at 20 dB). Also, thorough complexity analysis has shown that despite its good

throughput performance, the proposed approach has lower computational complexity as the existing algorithms that employ user grouping methods and two-stage precoding schemes. Also, the proposed OUG ZF-THP algorithm achieves very good BER performance in the observed application scenario.

Obtained numerical results encourage further research in the area of user grouping and scheduling in 5G MU-MIMO systems. Future work will include evaluation of the proposed two-stage precoding based on overlapping user grouping approach in heterogeneous 5G network consisting of both IoT devices and legacy users with different quality of service (QoS) requirements and assessment of its performance in more realistic radio environment which imposes channel imperfections. In order to support given QoS requirements for the observed users, a deployment of adaptive modulation mechanism might be necessary. In that case, the low complexity VP precoding techniques could be observed as a promising solution, instead of here considered THP schemes.

Data Availability

The data generated from Monte-Carlo simulations to support the findings of this study are available from the corresponding author upon request.

Conflicts of Interest

The authors declare that there is no conflict of interest regarding the publication of this paper.

Acknowledgments

This work has been supported by the Ministry of Education, Science and Technological Development of the Republic of Serbia.

References

[1] A. Zaidi, A. Branneby, A. Nazari, M. Hogan, and C. Kuhlins, *Cellular IoT in the 5G Era*, Ericsson White paper, 2020.

[2] T. van Chien and E. Björnson, *Massive MIMO Communications, 5G Mobile Communications*, Springer, Basel, Switzerland, 2017.

[3] E. Castaneda, A. Silva, A. Gameiro, and M. Kountouris, "An overview on resource allocation techniques for multi-user MIMO systems," *IEEE Communications Surveys and Tutorials*, vol. 19, no. 1, pp. 239–284, 2017.

[4] J. Wang, D. J. Love, and M. D. Zoltowski, "User selection with zero-forcing beamforming achieves the asymptotically optimal sum rate," *IEEE Transactions on Signal Processing*, vol. 56, no. 8, pp. 3713–3726, 2008.

[5] S. Lloyd, "Least squares quantization in PCM," *IEEE Transactions on Information Theory*, vol. 28, no. 2, pp. 129–137, 1982.

[6] N. Ganganath, C.-T. Cheng, and C. K. Tse, "Data clustering with cluster size constraints using a modified k-means algorithm," in *2014 International Conference on Cyber-Enabled Distributed Computing and Knowledge Discovery*, pp. 158–161, Shanghai, China, 2014.

[7] G. Dimic and N. D. Sidiropoulos, "On downlink beamforming with greedy user selection: performance analysis and a simple new algorithm," *IEEE Transactions on Signal Processing*, vol. 53, no. 10, pp. 3857–3868, 2005.

[8] R. Tian, Y. Liang, X. Tan, and T. Li, "Overlapping user grouping in IoT oriented massive MIMO systems," *IEEE Access*, vol. 5, pp. 14177–14186, 2017.

[9] H. Q. Ngo, E. G. Larsson, and T. L. Marzetta, "Aspects of favorable propagation in massive MIMO," in *Proc. 22nd Eur. Signal Process. Conf. (EUSIPCO)*, pp. 76–80, 2014.

[10] U. von Luxburg, "A tutorial on spectral clustering," *Statistics and Computing*, vol. 17, no. 4, pp. 395–416, 2007.

[11] M. H. M. Costa, "Writing on dirty paper (corresp.)," *IEEE Transactions on Information Theory*, vol. 29, no. 3, pp. 439–441, 1983.

[12] R. F. H. Fischer, C. Windpassinger, A. Lampe, and J. B. Huber, "Space-time transmission using Tomlinson-Harashima precoding," in *Proc. ITG SCC*, pp. 139–147, 2002.

[13] B. M. Hochwald, C. B. Peel, and A. L. Swindlehurst, "A vector-perturbation technique for near-capacity multiantenna multiuser communication—Part II: perturbation," *IEEE Transactions on Communications*, vol. 53, no. 3, pp. 537–544, 2005.

[14] R. Chen, C. Li, J. Li, and Y. Zhang, "Low complexity user grouping vector perturbation," *IEEE Wireless Communications Letters*, vol. 1, no. 3, pp. 189–192, 2012.

[15] A. Li and C. Masouros, "A constellation scaling approach to vector perturbation for adaptive modulation in MU-MIMO," *IEEE Wireless Communications Letters*, vol. 4, no. 3, pp. 289–292, 2015.

[16] S. Zarei, W. Gerstacker, and R. Schober, "Comparison of lattice-reduction-aided vector perturbation and Tomlinson-Harashima Precoding," in *Proc. 2019 IEEE WCNC*, Marrakech, Morocco, 2019.

[17] Q. H. Spencer, A. L. Swindlehurst, and M. Haardt, "Zero-forcing methods for downlink spatial multiplexing in multiuser MIMO channels," *IEEE Transactions on Signal Processing*, vol. 52, no. 2, pp. 461–471, 2004.

[18] R1-1701678, "Non-linear precoding for downlink multiuser MIMO," Huawei, Hisilicon, 3GPP TSG RAN WG1 Meeting 88, Athens, Greece, 2017.

[19] R1-1703187, "On MU MIMO non-linear precoding in NR," Nokia, Alcatel-Lucent Shanghai Bell, 3GPP TSG RAN WG1 Meeting 88, Athens, Greece, 2017.

[20] S. Zarei, W. Gerstacker, and R. Schober, "Low complexity hybrid linear/Tomlinson–Harashima precoding for downlink large-scale MU-MIMO systems," in *Proc. 2016 IEEE Globecom Workshops*, Washington DC, USA, 2016.

[21] R. F. Trifan, A. A. Enescu, and C. Paleologu, "Hybrid MU-MIMO precoding based on K-means user clustering," *Algorithms*, vol. 12, no. 7, pp. 146–163, 2019.

[22] S. Sheikhzadeh, A. R. Forouzan, and F. Parvaresh, "Tomlinson–Harashima precoding for transmitter-side inter-symbol interference cancellation in PSK modulation," *IET Communications*, vol. 13, no. 5, pp. 610–619, 2019.

[23] W. C. Jakes, *Microwave Mobile Communications*, Wiley, New York, USA, 1974.

[24] A. Adhikary, Junyoung Nam, Jae-Young Ahn, and G. Caire, "Joint spatial division and multiplexing—the large-scale array regime," *IEEE Transactions on Information Theory*, vol. 59, no. 10, pp. 6441–6463, 2013.

[25] M. Gudmundson, "Correlation model for shadow fading in mobile radio systems," *Electronics Letters*, vol. 27, no. 23, pp. 2145-2146, 1991.

[26] P. Agrawal and N. Patwari, "Correlated link shadow fading in multi-hop wireless networks," *IEEE Transactions on Wireless Communications*, vol. 8, no. 8, pp. 4024–4036, 2009.

[27] K. Yu and B. Ottersten, "Models for MIMO propagation channels: a review," *Wireless Communications and Mobile Computing*, vol. 2, no. 7, pp. 653–666, 2002.

[28] T. L. Marzetta, E. G. Larsson, H. Yang, and H. Q. Ngo, *Fundamentals of Massive MIMO*, Cambridge University Press, Cambridge, UK, 2016.

[29] P. He, L. Zhao, S. Zhou, and Z. Niu, "Water-filling: a geometric approach and its application to solve generalized radio resource allocation problems," *IEEE Transactions on Wireless Communications*, vol. 12, no. 7, pp. 3637–3647, 2013.

[30] A. Wiesel, Y. C. Eldar, and S. Shamai, "Zero-forcing precoding and generalized inverses," *IEEE Transactions on Signal Processing*, vol. 56, no. 9, pp. 4409–4418, 2008.

[31] R. Hunger, *Floating Point Operations in Matrix-Vector Calculus*, Technische Universität München, Associate Institute for Signal Processing, Tech. Rep. TUM-LNS-TR-05-05 Ver. 1.3, 2007.

[32] Z. Shen, R. Chen, J. G. Andrews, R. W. Heath, and B. L. Evans, "Low complexity user selection algorithms for multiuser MIMO systems with block diagonalization," *IEEE Transactions on Signal Processing*, vol. 54, no. 9, pp. 3658–3663, 2006.

[33] M. Arakawa, *Computational Workloads for Commonly Used Signal Processing Kernels*, MIT, Lincoln Laboratory, Tech. Rep. ESC-TR-2006-071, 2006.

[34] A. Garcia-Rodriguez and C. Masouros, "Power-efficient Tomlinson-Harashima precoding for the downlink of multi-user MISO systems," *IEEE Transactions on Communications*, vol. 62, no. 6, pp. 1884–1896, 2014.

[35] J. Lee, E. Tejedor, K. Ranta-aho et al., "Spectrum for 5G: global status, challenges, and enabling technologies," *IEEE Communications Magazine*, vol. 56, no. 3, pp. 12–18, 2018.

[36] C. Bockelmann, N. Pratas, H. Nikopour et al., "Massive machine-type communications in 5G: physical and MAC-layer solutions," *IEEE Communications Magazine*, vol. 54, no. 9, pp. 59–65, 2016.

[37] J. Zhang, Z. Zheng, Y. Zhang, J. Xi, X. Zhao, and G. Gui, "3D MIMO for 5G NR: several observations from 32 to massive 256 antennas based on channel measurement," *IEEE Communications Magazine*, vol. 56, no. 3, pp. 62–70, 2018.

Hindawi
Wireless Communications and Mobile Computing
Volume 2020, Article ID 3093581, 12 pages
https://doi.org/10.1155/2020/3093581

Research Article

Mobile Data Traffic Offloading through Opportunistic Vehicular Communications

Liqiang Qiao

Institute of Information Science and Technology at Beijing Foreign Studies University, Beijing 100089, China

Correspondence should be addressed to Liqiang Qiao; liqiang.qiao@bfsu.edu.cn

Received 28 December 2019; Revised 11 November 2020; Accepted 13 December 2020; Published 23 December 2020

Academic Editor: Hongzhi Guo

To cope with an exponentially increasing demand on mobile data traffic in cellular network, proximity-based opportunistic vehicular communications can be exploited as a complementary mean to offload and reduce the load of cellular network. In this paper, we propose a two-phase approach for mobile data traffic offloading, which exploits opportunistic contact and future utility with user mobility. The proposed approach includes one phase of initial source selection and subsequent phase of data forwarding. In phase 1, we build a weighted reachability graph, which is a very useful high-level abstraction for studying vehicular communication over time. Then, we propose an initial source selection algorithm, named VRank, and apply it in the weight reachability graph to identify some influential vehicles to serve as initial sources according to the rank of VRank. In phase 2, we formulate the forwarding schedule problem as a global utility maximization problem, which takes heterogeneous user interest and future utility contribution into consideration. Then, we propose an efficient scheme MGUP to solve the problem by providing a solution that decides which object should be broadcast. The effectiveness of our algorithm is verified through extensive simulation using real vehicular trace.

1. Introduction

With the development of wireless communication technologies and the increase in the number of mobile devices such as smartphones, tablets, and cars, cellular communication is facing a critical challenge of explosively increasing traffic demands [1, 2]. According to a recent report from Cisco, mobile data traffic will grow at a compound annual growth rate of 47 percent from 2016 to 2021, reaching 49.0 exabytes per month by 2021 [3]. Although the fourth-generation mobile cellular network is able to provide content downloading with broad coverage and high bandwidth, the immense mobile traffic demand has imposed a heavy burden on current cellular networks. Especially during peak time and in urban central areas, cellular-based communication will face extreme performance hits in terms of low network bandwidth, missed calls, and unreliable coverage [4, 5]. Therefore, it is essential to come up with an efficient and effective method to ease the burden of cellular networks.

Recently, an efficient alternative, generally known as mobile data offloading, which delivers mobile data traffic originally planned for transmission over cellular networks to other networks, has attracted much attention in the literature [6–10]. Traffic offloading can be implemented by Wi-Fi [11], femtocells [12], or opportunistic networks [6]. Wi-Fi and femtocells have evolved as mature technologies, but they rely on infrastructures. On the other hand, opportunistic networks allow users without permanent connection to communicate using the low-cost proximity-based connection when they encounter opportunistically. Therefore, opportunistic networks offer a very powerful alternative to relieve part of the mobile traffic from the cellular infrastructure. Vehicular networks [13] are an important class of opportunistic networks because the contacts, or the transmission opportunities, between vehicles happen in a dynamical and unexpected manner. In addition, vehicles are highly mobile and can communicate with each other using the dedicated short-range communication (DSRC) radio, 802.11p, and LTE-V [14]. These features make vehicular networks a suitable candidate for cellular traffic offloading.

The offloading process for disseminating content objects to certain interested subscribers (vehicles) can be described

as follows: the cellular base station can firstly deliver the content objects to only a small group of users (we use the terms vehicle, user, and subscriber interchangeably), called *seeds* or *initial sources*. After that, the initial sources can propagate the objects to all the subscribers through opportunistic forwarding, and any user that receives the data further forwards the data to others resulting in an information epidemic. As seen, the efficiency of such opportunistic traffic offloading is highly determined by two key factors: (1) initial source selection and (2) opportunistic forwarding strategy. A suitable set of initial sources can quickly distribute content objects over vehicular networks. In addition, different forwarding sequences of a user with multiple objects to transmit can result in different results. Hence, it is essential to address these two key issues in an opportunistic traffic offloading system.

In the literature, there have been some existing studies on traffic offloading through opportunistic communication. For the issue of initial source selection, most works choose the initial sources using various centrality metrics [15–17] or according to the features and properties of users' contact in the historical trace [7, 18]. Although these works are helpful to understand how to select preferable seeds, the main limitation is that they are suitable for static social network where the topology of the network is relatively stable. In addition, it is hard to accurately infer the uses' future centrality due to the highly dynamic network topology of the vehicular network. For the issue of data forwarding, most existing works mainly focus on forwarding performance in terms of delivery ratio, delay, and network overhead [19–21]. The users' interests and forwarding scheduling of multiple content objects are seldomly taken into consideration. However, how to schedule the objects to maximally satisfy users' interest in the limited contact duration should also be addressed.

Based on these insights, in this paper, we propose a two-phase approach for mobile data traffic offloading. Especially, phase 1 selects the initial sources based on a weighted reachability graph, which characterizes vehicles' transmission opportunities via instantaneous communication and opportunistic communication. We apply the proposed algorithm VRank to identify influential users as the initial sources, which lead to quick and wide spreading of content objects. After that, it follows with phase 2 for data forwarding to accommodate heterogeneous users' preferences to distribute the appropriate objects in short periods of time. As such, objects can be more effectively scheduled to satisfy users' interests and gained the maximal utility.

The major contributions of this paper are as follows:

(1) For the issue of initial source selection, we propose an algorithm, named VRank, which is expected to exploit opportunistic communication with user mobility, and apply it on weighted reachability graph to select some influential users to serve as the initial sources

(2) For the data forwarding, we formulate the problem as global utility maximization, which takes heterogenous users' interests and future utility into consideration. An optimal solution MGUP is proposed to solve the problem

(3) We conduct extensive simulations with real vehicular trace to evaluate the performance of our proposed approach. The simulation results show that the two-phase approach can effectively improve offloading rate and global utility to satisfy users' interests

The rest of the paper is organized as follows: Section 2 reviews related work regarding the mobile data traffic offloading. The system scenario and network model are introduced in Section 3. The initial source selection algorithm is given in Section 4. In Section 5, we formulate the forwarding scheduling as the global utility maximization problem and solve it. The effectiveness of our approach is verified using real vehicular trace in Section 6. The last section is for a brief summary.

2. Related Work

With the growing popularity of mobile accesses to the cellular, a number of innovative solutions have emerged to offload data traffic and reduce the load of cellular networks. According to [11], the methods roughly fall into three categories: traffic offloading through small cells, traffic offloading through Wi-Fi networks, and traffic offloading through opportunistic networks.

2.1. Traffic Offloading through Small Cells. Traffic offloading through small cells is an effective way to reduce traffic load and network energy consumption. Small cells are small cellular base stations typically designed for indoor use, which deliver wireless services to a small coverage area and are most likely to be user-installed. Existing works have shown most of the mobile traffic is generated indoors. The cellular network operators thus have the opportunities to offload heavy data to small cells and provide users with seamless quality of experience. In [22], Wang et al. proposed to use an auction-based algorithm, femto-matching, to achieve both load balancing among base station and fairness among users. The potentials of social and spatial proactive aching in small networks in terms of mobile data traffic were investigated in [23]. The results show that precaching strategic contents at the network edge engenders significant backhaul offloading gains and resource savings.

2.2. Traffic Offloading through Wi-Fi Networks. Recent research [11] has shown that Wi-Fi networks have already carried and offloaded a large amount of mobile data traffic. It has been shown that approximately 65% of cellular traffic can be offloaded by merely switching from cellular networks to Wi-Fi when Wi-Fi connectivity is available [12, 24]. Bulut and Szymanski [25] compared different methods of deploying Wi-Fi APs for efficient offloading of mobile data traffic. In order to reduce cellular network congestion and improve the user-perceived network performance, an offloading mobile data offloading scheme by leasing wireless bandwidth and caching space of residential 802.11 (Wi-Fi APs) was proposed in [26]. In addition, Sou and Peng [27] presented an analytical model for multipath Wi-Fi offloading in deriving the aggregate offloading time via an alternative path for the use of multipath offloading.

2.3. Traffic Offloading through Opportunistic Networks. Opportunistic communications have been lately considered as an important way for offloading mobile data traffic [6]. Using opportunistic communications to offload cellular traffic for mobile content dissemination applications is a novel and interesting idea and it has drawn great attention of the researchers. The architecture is actual a hybrid SDVN (Software Defined Vehicular Network). In [28], Zhao et al. investigate the routing-related issues in SDVNs and present a comprehensive overview of the state-of-the-art architectures, protocols, challenges, and potential solutions.

A number of studies have been developed to explore the opportunistic mobile network for mobile data traffic offloading. In [6, 29], Han et al. were the first to exploit opportunistic communications to facilitate information dissemination and reduce the amount of mobile data traffic. They studied how to select the target set with k users, such that the mobile data traffic over cellular networks is minimized. Greedy, heuristic, and random algorithms are proposed to solve this problem. The simulation results show the heuristic algorithm can offload mobile data traffic by up to 73.66% for a real-world mobility trace. In order to avoid the information is disseminated in the same community, a community-based algorithm is proposed in [7] to diffuse the information to the entire network as soon as possible. They are taken into both the contact probability and social relationship into account to select the initial seeds belonging to different communities. In [30], Liu et al. proposed a multiple source selection method to find the optimal number of initial sources. In addition, a multilayer-based seed selection approach is designed in [31] to maximally satisfy users' interest. The results show that multilayer-based seed scheme allows to maximize content utility.

With the short contact duration and the large content size taken into consideration, Li et al. [32] developed a contact-duration-aware offloading scheme, named Coff, which adopts the network coding to better utilize the short contacts. In [33], they qualitatively analyzed how the D2D communication can benefit from social features, and quantitatively evaluated the huge potential gains attainable in a practical social aware D2D communication system. Sciancalepore [34] et al. developed a theoretical model to analyze the performance of opportunistic dissemination when data can be selectively injected through a cellular network.

3. System Model

3.1. System Scenario. We consider a mobile traffic offloading scenario as illustrated in Figure 1. The network system is composed of base stations and mobile vehicles equipped with two different network interfaces: a cellular interface and a short range communication interface. The former is used to communicate with the base stations and the latter is devoted to the opportunistic communication between vehicles. The base stations of the cellular network are connected to the content servers in the Internet through wired links. Content server has some objects to distribute to a set of users before deadline. The information to be delivered may include weather forecasts, multimedia newspapers, and movie trailer generated by content service providers. Due to the delay-tolerant nature of non-real-time applications, service provider may deliver the objects to a small fraction of selected users, which are referred to *initial sources*. The initial sources will further disseminate the objects to the corresponding vehicles that request them through opportunistic communication, which occurs when two vehicles move into the communication range of each other. In addition, a vehicle may receive multiple objects, but it can only broadcast a single object at a time. As a result, different forwarding schedules, i.e., the forwarding sequence of the forwarder's objects, could result in different utilities. Each forwarder should carefully consider when to deliver which content objects. Therefore, the problem considered in this paper has two components: (1) *initial source selection*, how to identify some important vehicles to be the initial sources to assign the objects and (2) *opportunistic forwarding strategy*, how to schedule the sequence of objects to achieve the maximum utility.

3.2. Network Model. Due to the highly dynamic network topology of the vehicular network, the real vehicular networks are actual temporal graph where the existence of links may only last for a short period [35]. Therefore, we represent the vehicular network as a temporal graph $\mathcal{G} = (\mathcal{V}, \mathcal{E})$, where $\mathcal{V}$ represents all the vehicles and $\mathcal{E}$ represents the links between two vehicles, of which the Euclidean distance is smaller than the wireless communication range R. An undirected edge $e \in \mathcal{E}$ is a quadruple (u, v, t, λ), where $u, v \in \mathcal{V}$, t is the contact time between u and v, λ is the link duration time to go from u to v (also from v to u) starting at time t, and $t + \lambda$ is the link ending time. We denote the starting time of e by $t(e)$ and the duration time of e by $\lambda(e)$. As a pair of nodes may communicate at multiple time instances, the number of temporal edges between u and v can be large.

3.2.1. Time-Ordered Path or Journey. A time-ordered path $\mathcal{P}$ in a temporal graph $\mathcal{G}$ is a sequence of vertices $\mathcal{P} = <v_1, v_2, \cdots, v_k, v_{k+1}>$ where $(v_i, v_{i+1}, t_i, \lambda_i) \in \mathcal{E}$ is the i-th temporal edge on $\mathcal{P}$ for $1 \le i \le k$, and $(t_i + \lambda_i \le t_{i+1})$ for $1 \le i \le k$. In the literature [36], the terms "journey" and "time-respecting path" have also been used for time-ordered path. We denote by start($\mathcal{P}$) and end($\mathcal{P}$), the starting time t_1 and the ending time $t_k + \lambda_k$ of a time-ordered path $\mathcal{P}$. Time-ordered paths can be thought of as opportunistic communication routes over time from a source to a destination. We also define the temporal distance of $\mathcal{P}$ as dist($\mathcal{P}$) = end ($\mathcal{P}$) – start($\mathcal{P}$) corresponding to the delay of route. Objects or resources can be transmitted through opportunistic communication from node u to node v in vehicular networks only if they are joined by a time-ordered path.

4. Phase 1: VRank-Based Initial Source Assignment

In this section, we present how to identify a set of vehicles to be the initial sources to distribute the objects. We propose an algorithm named VRank which can rank the nodes in a directed graph. Reachability graph [37, 38] is a very useful high-level abstraction for studying vehicular communication

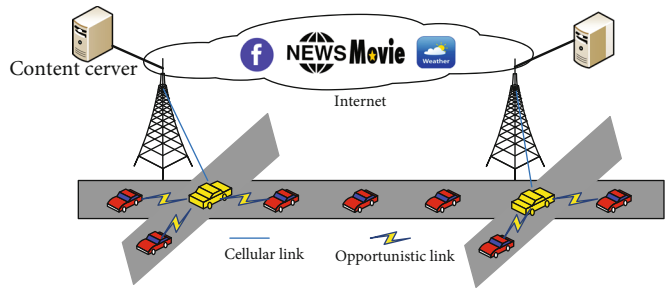

Figure 1: System scenario.

over time in vehicular networks. Therefore, we firstly introduce the concept of reachability graph and how to construct it. Next, we apply the VRank algorithm in reachability graph to select some influential vehicles to serve as initial sources.

4.1. Weighted Reachability Graph. For a given temporal graph $\mathcal{G}$ and any time interval $[t_1, t_k]$, we define $\mathcal{C}_k = (\mathcal{V}_k, \mathcal{J}_k)$ to be the reachability graph of $\mathcal{G}$ at time k. The set of nodes $\mathcal{V}_k$ is subset of $\mathcal{V}$ and represents the set of vehicles that were sampled in the given time interval. The set of arcs $\mathcal{J}_k$ represents every available direct link or time-ordered path $\mathcal{P}$ in $\mathcal{G}$ within t_k. In other words, if $(u, v) \in \mathcal{J}_k$, it means that u is able to communicate with v through instantaneous communication or along the temporal path from u to v. Notice that is not symmetric: the existence of time-ordered path from u to v does not imply there is a path from v to u. The reachability graph of a temporal graph can be obtained by computing the time-ordered paths between any two pairs of nodes, and then adding a link between two nodes u and v of the reachability graph if the temporal distance from u to v is finite or a direct link exists between u and v. Figure 2 illustrates an example of reachability graph which consists of six nodes and twelve directed links. The weight w_{uv} of each edge is the number of direct links and time-ordered paths within a duration between the two nodes.

4.2. VRank Algorithm. Identifying a set of influential nodes is a challenging problem in complex networks. A number of centrality metrics have been proposed to address this problem, such as degree centrality, closeness centrality, and between centrality [39, 40]. PageRank [41] is the most famous web page ranking employed by Google to rank web pages. It measures the relative importance of a page within a web graph. LeaderRank [42] has been shown as an effective and efficient method to identify influential spreaders in directed networks, which is a simple variant of PageRank. Motivated by the success of this algorithm, we propose an algorithm named VRank. Instead of considering degree of node only, we also take encounter times between any two vehicles into account to depict the weight. The main idea is that nodes with a higher VRank value will generally be more important vehicles to disseminate the objects, given that popular nodes are more likely to meet other nodes in the networks.

Given a weighted directed network consisting of N nodes and E edges, a *ground node* is then added by establishing bidirectional edges between it and all the other nodes. Then, the network becomes strongly connected and consists of $N + 1$ nodes and $E + 2N$ edges. Initially, each node in the network, except for the ground node, is assigned to one unit of resource, while the ground node is assigned with no resource. And then each node distributes its resource to neighbors along the outgoing edges. Next is to update resource distribution as summing up the resource each node derives from its incoming edges. This process of distribution and updating of resources continues until steady state is attained. The whole process can be described mathematically as follows.

Assuming $v_i(t)$ is the score of node i at time step t, the initial state can be represented as follows:

$$\begin{aligned} &v_g(0) = 0, \text{ where } g \text{ is ground node,} \\ &v_i(0) = 1, \text{ others.} \end{aligned} \tag{1}$$

And each node can update its score according to the following equation:

$$v_i(t+1) = \sum_{j=1}^{N+1} \frac{w_{ji}}{\text{sum}w(j)} v_j(t), \tag{2}$$

where w_{ji} is the weight of the edge (j, i) and $\text{sum}w(j)$ is the sum of weight of node j. Consider vehicular network where a user i is called a fan of user j if there is a directed link from i to j, namely, i could receive information from j and thus j will receive scores from i (if node's fans are of high influence, this node will be highly influential as well). Obviously, the number of fans is an important local indicator for a user's influence in spreading.

When the score $v_i(t)$ of all nodes converges to a unique steady state at time t_c, the score of the ground node is then evenly distributed to all other nodes, and the final score distribution on node i is as follows:

$$v_i = v_i(t_c) + \frac{v_g(t_c)}{N}, \text{ where } i \in \{1, 2, \cdots, N\}. \tag{3}$$

To illustrate the ranking process, we provide a simple ranking example in Figure 2. After convergence, the final scores of the six nodes are $v_1 = 1.5050$, $v_2 = 1.1835$, $v_3 = 1.1002$, $v_4 = 1.0764$, $v_5 = 1.2014$, and $v_6 = 0.9335$, respectively. Therefore, node 1 is ranked top by the VRank algorithm.

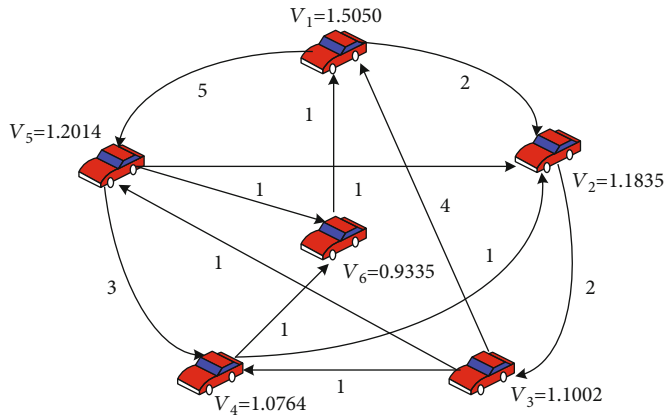

Figure 2: An illustration of the reachability graph and the VRank algorithm.

5. Phase 2: Opportunistic Forwarding Strategy

After phase 1, initial sources receive the assign objects via cellular communication; they can disseminate those objects to other vehicles through opportunistic communication. How to schedule those objects to maximally satisfy users' interests is addressed in this section. We first introduce the user interest and utility model. Next, we formulate the forwarding scheduling as a global utility maximization problem and design an effective scheme to solve it.

5.1. Interest Model. In a system with multiple content objects, a user will have different interests in different objects. Some objects are popular that are interested by many subscribers, whereas some other objects are not popular data, which may only be interest to a small number of subscribers. Keyword set is a set of keywords selected to depict the object and user interest. Let $\mathcal{K} = \{K_1, K_2, \cdots, K_M\}$ be a keyword set, where each K_i denotes one topic that can be rated. For any object, $o \in \mathcal{O}$ is described by a subset of keywords, which is denoted by $\mathcal{K}_c$, and weight v_{k_c}, which indicates the importance of keyword $k_c \in \mathcal{K}_c$. An object is described by a $M \times 1$ vector $\mathbf{D} = [d_1, d_2, \cdots, d_M]$, where $d_{k_c} = v_{k_c}$, and all the other elements are 0. We assumed each v_{k_c} is normalized, i.e., $\sum_{i=1}^{K_c} v_{k_c} = 1$.

In order to model the interest of different subscribers to different objects, a $M \times 1$ vector $\mathbf{P}_s = [P_s^1, P_s^2, \cdots, P_s^M]$ is to represent the interest profile of subscriber s, where each P_s^i denotes the degree of how subscriber s is interested in keyword K_i. In practice, P_s^i is used to compare the subscriber's interest in different keywords. Hence, without loss of generality, we define $\sum_{j=1}^{M} P_s^j = 1$. Finally, the interest probability of subscriber s for object o is computed:

$$p_{s,o} = \mathbf{P}_s \mathbf{D}^{\mathrm{T}} = \sum_{K_c \in \mathcal{K}_c} v_{k_c} P_s^{K_c}, \tag{4}$$

where $(\cdot)^{\mathrm{T}}$ indicates matrix transpose.

5.2. Utility Model. When a subscriber s receives an object o regarding a subset of keywords $\mathcal{K}_c$, the partial interest of s can be met. We define $u_{s,o}$ to represent the local utility of subscriber s and the value of $u_{s,o} = p_{s,o}$.

Once a vehicle obtains an object from base station or any other forwarder, it will become a forwarder. Let $\mathcal{O}_f^\tau$ denote the set of objects owned by the forwarder f at instant τ. When the forwarder f meets a group of neighboring vehicles $\mathcal{V}_f^\tau$ in time slot τ, each vehicle is required to explicitly provide its interest in different predefined topics $\mathcal{K}$. The forwarder f can know the local utility of each neighbor vehicle and broadcast any object $o_j \in \mathcal{O}_f^\tau$ to all its neighbors. Each vehicle $i \in \mathcal{V}_f^\tau$ who does not own object o_j can then obtain the utility u_{i,o_j}. The local utility that the forwarder f can produce to its neighbors for the object o_j at time τ is computed as follows:

$$\omega^l_{(f,o_j,\tau)} = \sum_{i \in \mathcal{V}_f^\tau} u_{i,o_j}. \tag{5}$$

However, solely considering the local utility is not enough due to the lack of consideration of the utility contribution by vehicle $i \in \mathcal{V}_f^\tau$ to their future contacts. Let $U_{i,o_j,\tau}$ denote the future utility of vehicle i if it gets the object o_j in time slot τ. Thus, the global utility that the forwarder f can produce to its neighbors for the object o_j at time τ is computed as follows:

$$\omega^g_{(f,o_j,\tau)} = \sum_{i \in \mathcal{V}_f^\tau} U_{i,o_j,\tau}. \tag{6}$$

5.3. Problem Formulation. We know that the contacts between forwarder f and its neighbors occur only during a short period, allowing them to exchange a limited volume of data. Therefore, the neighbors of f can only receive part of interested objects. Which objects to forward and how to schedule these objects to maximally satisfy user interests is required to be addressed when the forwarder f has multiple objects to broadcast.

Intuitively, the forwarder f can schedule those objects to maximize the global utility for the current slot. However,

such a greedy approach can not guarantee the long-term highest level of user satisfaction. Consider such a scenario shown in Figure 3, where the forwarder f owns three objects (o_1, o_2, o_3) and has contact with u_1 and u_2 at time slot τ. The contact durations with u_1 and u_2 are four and two time slots, respectively. Each vehicle $u_i (i \in \{1, 2\})$ has the future utility $U_{u_i,o_j,\tau}$ for object $o_j (j \in \{1, 2, 3\})$ as shown in Figure 3. We use $U_{u_i,o_j,\tau}$ to approximate $U_{u_i,o_j,\tau+1}$ in this example. According to the greedy strategy, the forwarder f distributes those objects in the following order: $[o_3, o_1, o_2]$, since the utility that can be obtained is 0.13,0.12,0.11, respectively. The link between f and u_2 is maintained for two time slots, such that u_2 can only receive two objects. The cumulative utility obtained after the broadcast of all the objects of the forwarder f is $0.27(0.13 + 0.12 + 0, 02)$. However, if we consider consecutive time slots, the object o_2 is more important to u_2 than object o_1. The forwarder f can send the objects in the following order $[o_3, o_2, o_1]$ and the utility obtained is $0.31(0.13 + 0.11 + 0.07)$. Therefore, the greedy algorithm that results in immediate optimum cannot guarantee the long-term optimum.

From the above example, we observe that the forwarder f should consider more consecutive time slots if it can exactly know the contact duration d_{fi} for all neighbors $i \in \mathscr{V}_f^\tau$. We define a set of available time slots $\mathscr{T} = \{\tau, \tau + 1, \cdots, \tau_{\max}\}$, where $\tau_{\max} = \max_{i \in \mathscr{V}_f^\tau} \tau + d_{fi}$. The transmission scheduling decision for each time slot can be represented by a vector:

$$\mathscr{A}(t) = \left\{a_1(t), a_2(t), \cdots, a_{|\mathscr{O}_f^\tau|}(t)\right\}, \quad t \in \mathscr{T}, \tag{7}$$

where

$$a_i(t) = \begin{cases} 1 & \text{object } o_i \text{ is broadcast in time slot } t, \\ 0 & \text{others.} \end{cases} \tag{8}$$

There is a constraint $\sum_{i=1}^{|\mathscr{O}_f^\tau|} a_i(t) \le 1$ for the vector $\mathscr{A}(t)$, which means that, at most, one object will be scheduled to broadcast for slot t.

With multiple slots to be considered, the problem is formulated as finding the best time slot allocation $\mathscr{A} = \{\mathscr{A}(\tau), \mathscr{A}(\tau + 1), \cdots, \mathscr{A}(\tau_{\max})\}$ for a total time period $\tau_{\max}$ to schedule the transmission, such that the global utility is maximized. Therefore, we formulate the global utility maximization problem (GUMP) as follows:

$$U = \max_{\mathscr{A}} \sum_{t=\tau}^{\tau_{\max}} \sum_{i=1}^{|\mathscr{O}_f^\tau|} U_{i,o_j,t}. \tag{9}$$

Subject to

$$\sum_{l=1}^{|\mathscr{O}_f^\tau|} a_l(t) \le 1, \quad t \in \mathscr{T}, \tag{10}$$

$$a_j(t) = \{0, 1\}, \quad j \in \mathscr{O}_f^\tau, \quad t \in \mathscr{T}, \quad i \in \mathscr{V}_f^\tau. \tag{11}$$

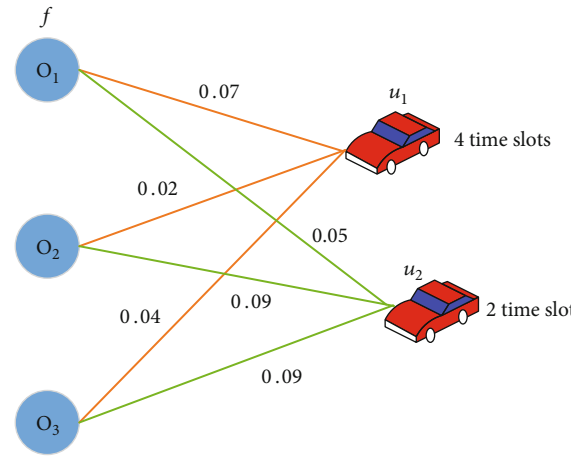

Figure 3: Example of utility contribution.

The objective is hence to find the optimal forwarding schedule for all $o_j \in O_f^t$ and $t \in \mathscr{T}$, such that forwarder f can contribute the maximal total global utility.

5.4. Prediction of the Future Utility. We assume that the random variable $N_{ij}(t)$ denotes the cumulative number of contacts between nodes i and j at time t and any two contacts between them are independent from each other. Thus, $N_{ij}(t)$ can be modeled as a homogeneous Poisson process with rate λ_{ij}. Assuming the length of a time slot is Δt, the number of contacts $N_{ij}(t + \Delta t) - N_{ij}(t)$ between nodes i and j within time Δt follows the Poisson distribution, which can be expressed as follows:

$$P\left(N_{ij}(t + \Delta t) - N_{ij}(t) = k\right) = \frac{\left(\lambda_{ij}\Delta t\right)^k \exp\left(-\left(\lambda_{ij}\Delta t\right)\right)}{k!}. \tag{12}$$

Then, the contact probability between nodes i and j within time Δt can be expressed as follows:

$$q_{ij} = 1 - \exp\left(-\left(\lambda_{ij}\Delta t\right)\right). \tag{13}$$

The value of $U_{(i,o,t)}$ can be determined by two factors: (1) the probability that forwarder i can meet other contacts who have not owned object o after time slot t and (2) the utility of i's contact on object o. Now, we first derive the probability that a contact $j \in \mathscr{V}$ has not received object o in time slot t' from any contacts $k \in \mathscr{V}$, denoted by $\Phi_{j,o}(t')$. In [18], they considered that user j will not able to download object o from user k before time slot t if and only if the two following events occur: (1) j and k never met before time slot t, i.e., $N_{jk}(t - 1) = 0$ or (2) the last contact between j and k was in time slot $z < t$, but k did not have object o in time slot z. Therefore, the probability $\phi_{j,k,o}(t)$ that j cannot download object o from k before time slot t can be computed by the following:

$$\phi_{j,k,o}(t) = \left(1 - q_{jk}\right)^{t-1} + \sum_{z=1}^{t-1} q_{jk}\left(1 - q_{jk}\right)^{t-1-z} \Phi_{k,o}(z). \quad (14)$$

Then, the probability $\Phi_{j,o}(z)$ that user j has not downloaded object o until time slot t equals the probability that j cannot download object o from any user k before t.

$$\Phi_{j,o}(t) = \prod_{j \neq k} \phi_{j,k,o}(t). \quad (15)$$

Since only the data sources have object o in the initial time slot 1, we have $\Phi_{j,o}(1) = 0$ if j is a data source of object o and $\Phi_{j,o}(1) = 1$ otherwise. Given the initial value of $\Phi_{j,o}(1)$, we can compute the value of $\Phi_{j,o}(z)$ for each time slot $z = 2, 3, \cdots, t-1$ iteratively for all users.

Thus, the expected utility that i can contribute to contact j between t and $T_o^{\max}$ for object o is as follows:

$$\kappa_{i,j,o}(t) = p_{j,o} \sum_{z=t}^{T_o^{\max}-1} q_{ij}\left(1 - q_{ij}\right)^{T_o^{\max}-1-z} \Phi_{j,o}(z), \quad (16)$$

where $T_o^{\max}$ is the expiration time of object o. Last, the future utility of user i can be approximated by the following:

$$U_{(i,o,t)} \approx \sum_{j \in \mathscr{V}\{i\}} \kappa_{i,j,o}(t). \quad (17)$$

5.5. Optimal Solution. The global utility maximization problem can be solved by searching all the states. Obviously, the computational complexity is very high. Here, we design a simple yet effective algorithm to achieve the maximum global utility.

The total number of time slots that each vehicle $i \in \mathscr{V}_f^\tau$ will stay with the forwarder f can be calculated as follows:

$$ns_i = \frac{d_{fi}}{\Delta t}. \quad (18)$$

As described earlier, more consecutive time slots should be considered in the optimal problem. The maximum possible global utility achieved for each object $o_j \in \mathscr{O}_f^\tau$ can be estimated if the object can always be transmitted. The average global utility potential of object o_j in the next successive n slots U_n is defined as the total amount of global utility obtained during the next successive n slots over n, which is computed as follows:

$$U_n = \frac{\sum_{i=1}^{n} \omega^g_{(f,o_j,\tau+i)}}{n}. \quad (19)$$

The computation of average global utility potential can be considered to find the object that can bring the highest utility in the following couple of slots. Therefore, the maximum average global utility potential $\max(U_1, U_2, \cdots, U_n)$ should be computed for the scheduling, which is shown in Algorithm 1. With the average global utility potential computed, all the objects will be sorted according the global utility potential. The object with the highest global utility potential will be selected to transmit during the current time slot.

6. Performance Evaluation

We now evaluate the performance of VRank-based initial source scheme and the forward schedule strategy using the realistic vehicular traces from the city of Beijing, which gathered from 12:00 am to 11:59 pm on Jan. 05, 2009, in the local time [43]. The number of subject taxis is 2927 and we assume all vehicles are subscribers.

The experiments could be divided into two parts: (1) performance comparison with other seed selection methods and (2) global utility gain of the proposed forward strategy.

6.1. Performance Comparison with Other Seed Selection Methods. In this section, the proposed VRank initial source selection algorithm and some other alternative methods were implemented in the experiments. The alternative methods include LeaderRank [42], PageRank [41], and POST [16]. In LeaderRank strategy, the initial sources are selected based on the ranking of the algorithm, where the probability that a random walker at a vehicle goes to other in the next step is mainly determined by the vehicle's out-degree. PageRank is also used to choose the initial sources with damping factor $\alpha = 0.9$. The POST method is based on inferring the future centrality of vehicle and ranking all vehicles according to their predicted centrality values.

(1) Offloading Ratio versus the Number of the Initial Sources. To evaluate the performance of our solution and those alternative methods, we use offloading ratio as the metric, which refers to the ratio of the number of successfully received vehicles to the total number of vehicles in the network. We select an observation interval from 7 : 30 am to 9 : 30 am to analyze the performance of different algorithms. The first half of the trace is used as the warm-up period for the vehicles to accumulate the necessary network information and construct the reachability graph.

Table 1 shows the top 8 vehicles' IDs ranked by the four approaches. From Table 1, we can see that the initial source sets are different from each other.

Figure 4 plots the average offloading ratio as a function of the number of the initial sources. It can be seen that the VRank scheme outperforms other algorithms in all conditions. Especially, the offloading rate of VRank can achieve 45%, while that of LeaderRank, PageRank, and POST is around 33% when the number of the initial sources is 20. Similarly, the VRank also has a higher offloading rate than other strategies when the number of the initial sources arises from 40 to 200. We also notice that offloading rate increases as the number of the initial sources increases. In VRank, the offloading rate increases from 43% to 54% as the number of the initial sources increases from 20 to 120. It is obvious that the more initial sources the BS selects to distribute the objects, the more mobile vehicles can obtain the objects opportunistically. However, we observe that offloading rate

Input: the contact time τ and the contact duration d_{fi} of each vehicle $i \in \mathscr{V}_f^\tau$
Output: the maximum global utility potential of object o_j
1: Compute the total number of time slots that the vehicle $i \in \mathscr{V}_f^\tau$ will stay with forwarder f: $ns_i \leftarrow d_{fi}/\Delta t$
2: Vehicle $i \in \mathscr{V}_f^\tau$ reports its future utility $U_{i,o_j,t}$ in each time slot
3: The maximum available time slot $\tau_{\max} = \tau + \max(ns_i)$
4: **for** $t = \tau$ to $\tau_{\max}$ **do**
5: $\omega^g_{(f,o_j,t)} = \sum_{i \in \mathscr{V}_f^\tau} U_{i,o_j,t}$
6: **end for**
7: Initialize the $\max_{utility} \leftarrow -1$
8: **for** $i = 1$ to $\max(ns_i)$ **do**
9: $utility \leftarrow (\sum_{i=1}^{\max(ns_i)} \omega^g_{(f,o_j,\tau+i)})/i$
10: **if** $utility > \max_{utility}$ **then**
11: $\max_{utility} \leftarrow utility$
12: **end if**
13: **end for**
14: **return** $\max_{utility}$

Algorithm 1: Max global utility potential (MGUP) algorithm.

Table 1: The top 8 vehicles' ID ranked by different algorithms.

Algorithm	No. 1	No. 2	No. 3	No. 4	No. 5	No. 6	No. 7	No. 8
VRank	5079	11788	28496	18292	8407	18102	11722	11009
PageRank	5447	11009	20415	6187	5079	25351	29143	5678
LeaderRank	28522	8154	11301	18687	20406	5644	28841	19695
POST	17682	31260	6348	28489	6725	19613	28162	17921

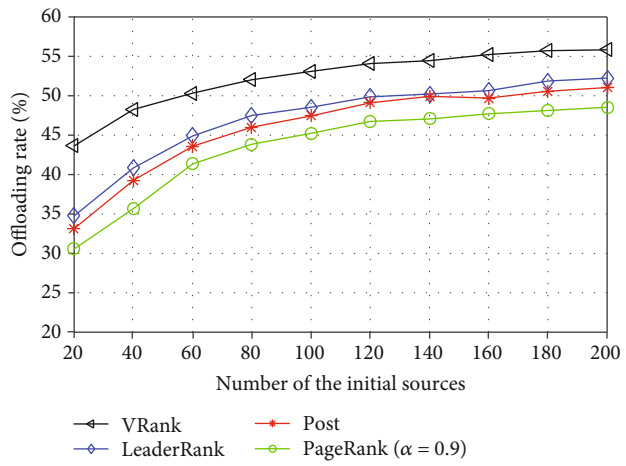

Figure 4: Offloading ratio versus the number of the initial sources with Beijing taxi data set.

reveals a trend of a slow increase when the number of the initial sources exceeds a certain value. The first 120 seeds can achieve offloading rate about 53%, but adding another 80 seeds can only bring an extra 1% offloading rate in VRank. The similar phenomenon is also observed in other schemes. This is due to the fact that as the number of seed vehicles increases, the probability of two selected vehicles having similar network positions also increases, which means they are redundant and therefore choosing both of them may not be able to gain as large coverage as possible.

(2) Offloading Ratio versus Time Scale. We future examine the impact of time scale on the performance of VRank. We set the number of the initial sources to 100 and run all methods using the mobility trace and get the average.

The performance of average offloading ratio as a function of time scale for the four schemes is shown in Figure 5. We can see the similar results that VRank outperforms the rest of other schemes. As the time scale increases, VRank always achieves the best performance. Particularly, the offloading ratio of VRank is up to 34.28% comparing with LeaderRank and POST are up to 22.20% and 20.95%, respectively. Meanwhile, we notice the performances of LeaderRank and the POST are very close both in Figures 4 and 5. That is because those two schemes both take the degree of vehicle into consideration to select the initial sources.

6.2. Global Utility Gain of the Proposed Forward Strategy

(1) User Interest Profile in Different Keywords. The user interest profiles are generated based on a key set $\mathscr{K}$ with $M = 20$ and we assume that keyword $K_j \in \mathscr{K}$ is the j-th popular keyword in the network.

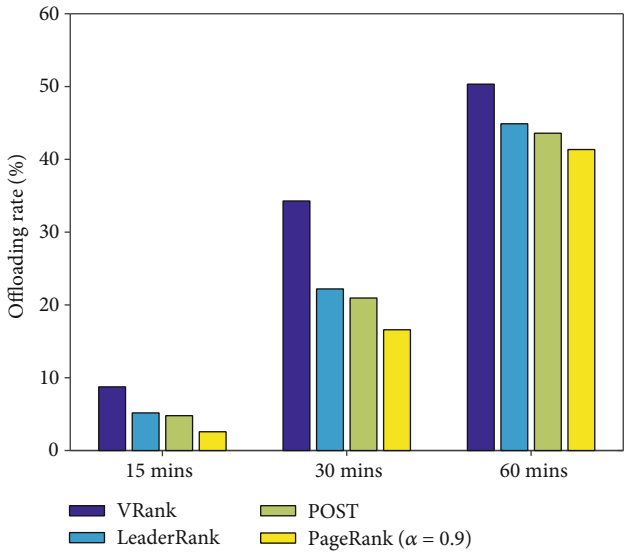

FIGURE 5: Offloading ratio versus the time scale with Beijing taxi data set.

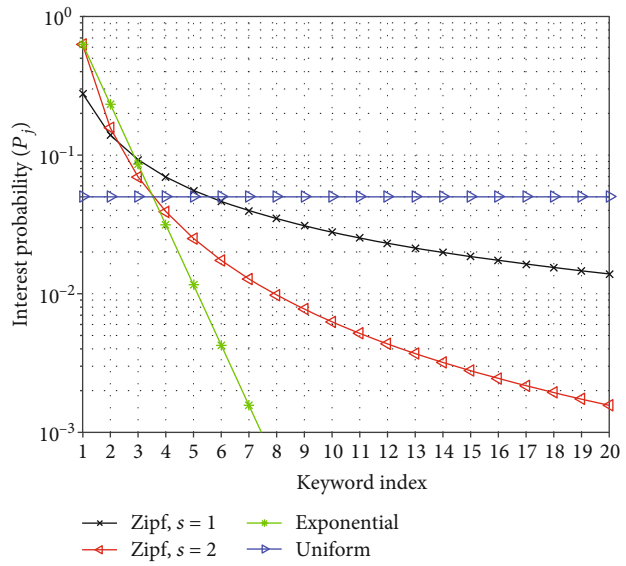

FIGURE 6: User interest profile in different keywords.

According to the interest model, the user interest profile in each keyword K_j is randomly drawn from a normal distribution with P_j as the mean value. We exploit various distributions for generating P_j of different keywords.

(i) Zipf distribution with exponent s : $P_j = (1/j^s)/\sum_{i=1}^{M} (1/i^s)$

(ii) Exponential distribution: $P_j = \exp(-j)/\sum_{i=1}^{M} \exp(-i)$

(iii) Uniform distribution: $P_j = 1/M$

P_j with different distributions are shown in Figure 6.

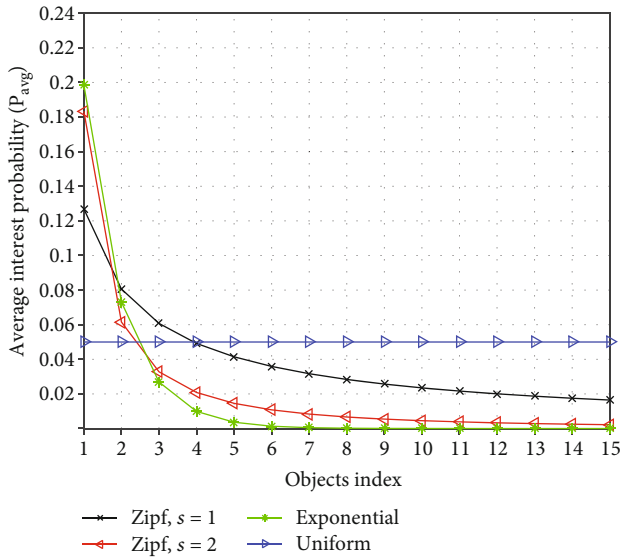

FIGURE 7: Average interest probability in different objects.

(2) Average User Interest Probability in Different Objects. We assume there are 15 objects to be disseminated in our system. Each object o_j is described by 5 keywords with equal weights. To ensure that different objects have different popularity, the keyword indices of object o_j are $\{j, \cdots, j+4\}$. Thus, we can computerize the interest probability of each user for object o_j according to Equation (4). Figure 7 shows the average user interest probability in different objects. It is easy to be seen that when P_j is generated exponentially or Zipf with exponent $s = 2$, most of the user interests concentrate on popular objects. For Zipf with exponent $s = 1$, such concentration on popular objects decreases. Therefore, Figure 7 actually represents different object interest patterns of mobile users in our system.

(3) Global Utility Gain versus the Time Scale. We evaluate the global utility gain of proposed algorithm MGUP with greedy, local utility maximum, and random schemes. We let all the schemes select a fixed number (20 in our experiment) of initial sources with VRank. The user interest probabilities are generated by following the Zipf distribution with exponent $s = 2$. In Figure 8, the global utility gain as a function of time scale is shown. We can see that global utility of all the schemes increases with the time scale increases. Meanwhile, we notice that MGUP can produce 13.65 and 23.48 percent higher global utility than greedy and local utility maximum, respectively, until 45 minutes later. The improvements are mainly because each forwarder in MGUP considers the future utility contribution of its members and more consecutive time slots in the scheduling process. Especially, the future utility of neighbor i in MGUP not only considers different user interests in different objects but also predicts how many users can gain utility by obtaining object o_j from neighbor i. Therefore, the forwarder f can select the object that benefits all users in the system. The figure also shows both MGUP and greedy have higher global utility than local utility maximum and random. This further indicates the future utility has a great impact on the performance.

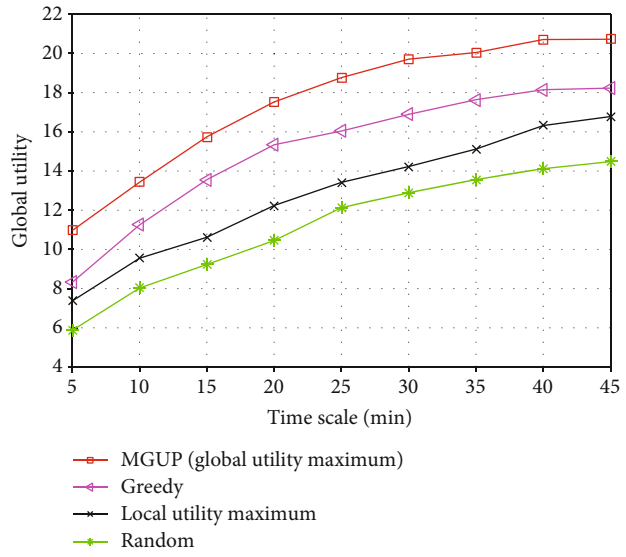

Figure 8: Global utility gain versus the time scale with Beijing taxi data set under 15 objects.

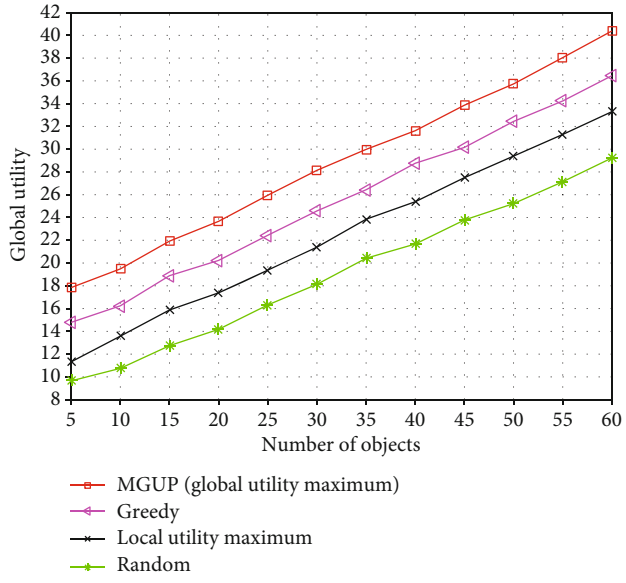

Figure 9: Global utility gain versus the number of objects.

(4) Global Utility Gain versus the Different Numbers of Objects. We future evaluate the impact of the number of objects on the performance of comparison schemes. We vary the number from 5 to 60. Figure 9 plots the global utility gain under the different numbers of objects. It is obvious that global utility increases as the number of objects increases in all schemes. This is because more objects can meet users' different interests in different objects and produce a higher global utility.

7. Conclusion

As the increasing popularity of mobile devices and user demands, the amount of mobile data traffic in cellular networks grows explosively. Users will face extreme performance hits in terms of low or even no network bandwidth, missed calls, and unreliable coverage. It is an urgent agenda for cellular provider to offer quick and promising solutions. Therefore, proximity-based opportunistic communication as a mean to offload and reduce the load of cellular network attracts the attention of service providers. In this paper, we study how to exploit opportunistic vehicular communications to offload mobile data traffic. We propose a two-phase approach, which includes one phase of initial source selection and subsequent phase of data forwarding. For the issue of initial source selection, we propose an algorithm named VRank to identify some influential vehicles to server as initial sources, which lead to quick and wide spreading of content objects. For the issue of data forwarding, we formulate the problem as the global utility maximization, which takes into heterogenous users' interests and future utility consideration. An optimal solution MGUP is proposed to solve the problem. The effectiveness of our approach is verified through extensive simulation using real vehicular trace.

Data Availability

The data used to support the findings of this study are included in the article.

Conflicts of Interest

The author declares that there are no conflicts of interest.

References

[1] W. Cao, G. Feng, S. Qin, and M. Yan, "Cellular offloading in heterogeneous mobile networks with D2D communication assistance," *IEEE Transactions on Vehicular Technology*, vol. 66, no. 5, pp. 4245–4255, 2017.

[2] G. Mao, Z. Zhang, and B. D. O. Anderson, "Cooperative content dissemination and offloading in heterogeneous mobile networks," *IEEE Transactions on Vehicular Technology*, vol. 65, no. 8, pp. 6573–6587, 2016.

[3] "Cisco visual networking index: global mobile data traffic forecast update, 2016–2021 white paper," https://www.cisco.com/c/en/us/solutions/collateral/service-provider/visual-networking-index-vni/mobile-white-paper-c11-520862.html.

[4] Y. Li, D. Jin, H. Pan, and S. Chen, "Contact-aware data replication in roadside unit aided vehicular delay tolerant networks," *IEEE Transactions on Mobile Computing*, vol. 15, no. 2, pp. 306–321, 2016.

[5] J. Gozálvez, M. Sepulcre, and R. Bauza, "IEEE 802.11 p vehicle to infrastructure communications in urban environments," *IEEE Communications Magazine*, vol. 50, no. 5, 2012.

[6] B. Han and H. Pan, "Mobile data offloading through opportunistic communications and social participation," *IEEE Transactions on Mobile Computing*, vol. 11, no. 5, pp. 821–834, 2012.

[7] Y.-J. Chuang and K. C.-J. Lin, "Cellular traffic offloading through community-based opportunistic dissemination," in *2012 IEEE Wireless Communications and Networking Conference (WCNC)*, pp. 3188–3193, Paris, France, 2012.

[8] S. Kashihara, M. Sanadidi, and M. Gerla, "Mobile, personal data offloading to public transport vehicles," in *Proceedings*

of the 2012 IEEE International Conference on Mobile Computing and Ubiquitous Networking (ICMU), pp. 142–147, Okinawa, Japan, 2012.

[9] Y. Go, Y. G. Moon, G. Nam, and K. S. Park, "A disruption-tolerant transmission protocol for practical mobile data offloading," in *Proceedings of the Third ACM International Workshop on Mobile Opportunistic Networks-MobiOpp '12*, pp. 61–68, Zürich, Switzerland, 2012.

[10] X. Li, Z. Cheng, G. Bo, K. Yamori, and Y. Tanaka, "Optimal pricing and service selection in the mobile cloud architectures," *IEEE Access*, vol. 7, pp. 43564–43572, 2019.

[11] K. Lee, J. Lee, Y. Yi, I. Rhee, and S. Chong, "Mobile data offloading: how much can WiFi deliver?," *IEEE/ACM Transactions on Networking*, vol. 21, no. 2, pp. 536–550, 2013.

[12] A. Aijaz, H. Aghvami, and M. Amani, "A survey on mobile data offloading: technical and business perspectives," *IEEE Wireless Communications*, vol. 20, no. 2, pp. 104–112, 2013.

[13] A. Hawbani, E. Torbosh, W. Xingfu, P. Sincak, L. Zhao, and A. Y. Al-Dubai, "Fuzzy based distributed protocol for vehicle to vehicle communication," *IEEE Transactions on Fuzzy Systems*, p. 1, 2019.

[14] S. Chen, J. Hu, Y. Shi, and L. Zhao, "LTE-V: a TD-LTE-based V2X solution for future vehicular network," *IEEE Internet of Things Journal*, vol. 3, no. 6, pp. 997–1005, 2016.

[15] Y. Zhao, W. Song, and H. Zhu, "Social-aware data dissemination via device-to-device communications: fusing social and mobile networks with incentive constraints," *IEEE Transactions on Services Computing*, vol. 12, no. 3, pp. 489–502, 2016.

[16] J. Qin, H. Zhu, Y. Zhu, L. Lu, G. Xue, and M. Li, "POST: exploiting dynamic sociality for mobile advertising in vehicular networks," *IEEE Transactions on Parallel and Distributed Systems*, vol. 27, no. 6, pp. 1770–1782, 2016.

[17] Y. Zhao and W. Song, "Social-aware data dissemination via opportunistic device-to-device communications," in *2016 IEEE 84th Vehicular Technology Conference (VTC-Fall)*, pp. 1–6, Montreal, QC, Canada, 2016.

[18] H.-H. Cheng and K. C.-J. Lin, "Source selection and content dissemination for preference-aware traffic offloading," *IEEE Transactions on Parallel and Distributed Systems*, vol. 26, no. 11, pp. 3160–3174, 2015.

[19] H. Zhu, M. Dong, S. Chang, Y. Zhu, M. Li, and X. S. Shen, "Zoom: scaling the mobility for fast opportunistic forwarding in vehicular networks," in *2013 Proceedings IEEE INFOCOM*, pp. 2832–2840, Turin, Italy, 2013.

[20] T. Wang, L. Song, H. Zhu, and B. Jiao, "Dynamic popular content distribution in vehicular networks using coalition formation games," *IEEE Journal on Selected Areas in Communications*, vol. 31, no. 9, pp. 538–547, 2013.

[21] X. Chen, J. Wu, Y. Cai, H. Zhang, and T. Chen, "Energy-efficiency oriented traffic offloading in wireless networks: a brief survey and a learning approach for heterogeneous cellular networks," *IEEE Journal on Selected Areas in Communications*, vol. 33, no. 4, pp. 627–640, 2015.

[22] W. Wang, X. Wu, L. Xie, and S. Lu, "Femto-matching: efficient traffic offloading in heterogeneous cellular networks," in *2015 IEEE Conference on Computer Communications (INFOCOM)*, pp. 325–333, Kowloon, Hong Kong, 2015.

[23] E. Bastug, M. Bennis, and M. Debbah, "Social and spatial proactive caching for mobile data offloading," in *2014 IEEE International Conference on Communications Workshops (ICC)*, pp. 581–586, Sydney, NSW, Australia, 2014.

[24] N. Cheng, N. Lu, N. Zhang, X. S. Shen, and J. W. Mark, "Opportunistic WiFi offloading in vehicular environment: a queueing analysis," in *2014 IEEE Global Communications Conference*, pp. 211–216, Austin, TX, USA, 2014.

[25] E. Bulut and B. K. Szymanski, "WiFi access point deployment for efficient mobile data offloading," *ACM SIGMOBILE Mobile Computing and Communications Review*, vol. 17, no. 1, pp. 71–78, 2013.

[26] K. Poularakis, G. Iosifidis, I. Pefkianakis, L. Tassiulas, and M. May, "Mobile data offloading through caching in residential 802.11 wireless networks," *IEEE Transactions on Network and Service Management*, vol. 13, no. 1, pp. 71–84, 2016.

[27] S.-I. Sou and Y.-T. Peng, "Performance modeling for multipath mobile data offloading in cellular/Wi-Fi networks," *IEEE Transactions on Communications*, vol. 65, no. 9, pp. 3863–3875, 2017.

[28] Z. Liang, A. Al-Dubai, A. Y. Zomaya, G. Min, A. Hawbani, and J. Li, "Routing schemes in software-defined vehicular networks: design, open issues and challenges," *IEEE Intelligent Transportation Systems Magazine*, 2020.

[29] B. Han, H. Pan, V. S. Kumar, M. V. Marathe, G. Pei, and A. Srinivasan, "Cellular traffic offloading through opportunistic communications: a case study," in *Proceedings of the 5th ACM Workshop on Challenged Networks-CHANTS '10*, pp. 31–38, Chicago, Illinois, USA, 2010.

[30] B. Liu, W. Zhou, J. Jiang, and K. Wang, "K-source: multiple source selection for traffic offloading in mobile social networks," in *2016 8th International Conference on Wireless Communications & Signal Processing (WCSP)*, pp. 1–5, Yangzhou, China, 2016.

[31] F. Mezghani, M. Mezghani, A. Kaouk, A.-L. Beylot, and F. Sedes, "Evaluating seed selection for information diffusion in mobile social networks," in *2017 IEEE Wireless Communications and Networking Conference (WCNC)*, pp. 1–6, San Francisco, CA, USA, 2017.

[32] Z. Li, Y. Liu, H. Zhu, and L. Sun, "Coff: contact-duration-aware cellular traffic offloading over delay tolerant networks," *IEEE Transactions on Vehicular Technology*, vol. 64, no. 11, pp. 5257–5268, 2015.

[33] Y. Li, T. Wu, H. Pan, D. Jin, and S. Chen, "Social-aware D2D communications: qualitative insights and quantitative analysis," *IEEE Communications Magazine*, vol. 52, no. 6, pp. 150–158, 2014.

[34] V. Sciancalepore, D. Giustiniano, A. Banchs, and A. Hossmann-Picu, "Offloading cellular traffic through opportunistic communications: analysis and optimization," *IEEE Journal on Selected Areas in Communications*, vol. 34, no. 1, pp. 122–137, 2016.

[35] Z. Liang, Z. Li, J. Li, A. Al-Dubai, G. Min, and A. Y. Zomaya, "A temporal-information-based adaptive routing algorithm for software defined vehicular networks," in *ICC 2019-2019 IEEE International Conference on Communications (ICC)*, pp. 1–6, Shanghai, China, 2019.

[36] H. Wu, J. Cheng, S. Huang, Y. Ke, Y. Lu, and Y. Xu, "Path problems in temporal graphs," *Proceedings of the VLDB Endowment*, vol. 7, no. 9, pp. 721–732, 2014.

[37] J. Whitbeck, M. D. de Amorim, V. Conan, and J.-L. Guillaume, "Temporal reachability graphs," in *Proceedings of the 18th Annual International Conference on Mobile Computing and Networking*, pp. 377–388, Istanbul, Turkey, 2012.

[38] M. Barjon, A. Casteigts, S. Chaumette, C. Johnen, and Y. M. Neggaz, "Testing temporal connectivity in sparse dynamic graphs," 2014, https://arxiv.org/abs/1404.7634.

[39] G. Sabidussi, "The centrality index of a graph," *Psychometrika*, vol. 31, no. 4, pp. 581–603, 1966.

[40] D. Chen, L. Lü, M.-S. Shang, Y.-C. Zhang, and T. Zhou, "Identifying influential nodes in complex networks," *Physica A: Statistical Mechanics and Its Applications*, vol. 391, no. 4, pp. 1777–1787, 2012.

[41] S. Brin and L. Page, "The anatomy of a large-scale hypertextual web search engine," *Computer Networks and ISDN Systems*, vol. 30, no. 1-7, pp. 107–117, 1998.

[42] L. Lü, Y.-C. Zhang, C. H. Yeung, and T. Zhou, "Leaders in social networks, the delicious case," *PLoS One*, vol. 6, no. 6, article e21202, 2011.

[43] M. Sathiamoorthy, A. G. Dimakis, B. Krishnamachari, and F. Bai, "Distributed storage codes reduce latency in vehicular networks," *IEEE Transactions on Mobile Computing*, vol. 13, no. 9, pp. 2016–2027, 2014.

Hindawi
Wireless Communications and Mobile Computing
Volume 2020, Article ID 8849541, 20 pages
https://doi.org/10.1155/2020/8849541

Research Article

Data-Driven Predictive Control of Building Energy Consumption under the IoT Architecture

Ji Ke,[1] Yude Qin,[1] Biao Wang,[1] Shundong Yang,[2] Hao Wu,[1] Hang Yang,[1] and Xing Zhao[1]

[1]*College of Electronic & Control engineering Chang'an University, Xi'an 710061, China*
[2]*KunYi Co., Ltd., Wuxi 214000, China*

Correspondence should be addressed to Biao Wang; wangbiao@chd.edu.cn

Received 5 June 2020; Revised 10 November 2020; Accepted 27 November 2020; Published 15 December 2020

Academic Editor: Hongzhi Guo

Model predictive control is theoretically suitable for optimal control of the building, which provides a framework for optimizing a given cost function (e.g., energy consumption) subject to constraints (e.g., thermal comfort violations and HVAC system limitations) over the prediction horizon. However, due to the buildings' heterogeneous nature, control-oriented physical models' development may be cost and time prohibitive. Data-driven predictive control, integration of the "Internet of Things", provides an attempt to bypass the need for physical modeling. This work presents an innovative study on a data-driven predictive control (DPC) for building energy management under the four-tier building energy Internet of Things architecture. Here, we develop a cloud-based SCADA building energy management system framework for the standardization of communication protocols and data formats, which is favorable for advanced control strategies implementation. Two DPC strategies based on building predictive models using the regression tree (RT) and the least-squares boosting (LSBoost) algorithms are presented, which are highly interpretable and easy for different stakeholders (end-user, building energy manager, and/or operator) to operate. The predictive model's complexity is reduced by efficient feature selection to decrease the variables' dimensionality and further alleviate the DPC optimization problem's complexity. The selection is dependent on the principal component analysis (PCA) and the importance of disturbance variables (IoD). The proposed strategies are demonstrated both in residential and office buildings. The results show that the DPC-LSBoost has outperformed the DPC-RT and other existing control strategies (MPC, TDNN) in performance, scalability, and robustness.

1. Introduction

One major challenge in today's society concerns energy savings and CO_2 footprint in existing and new buildings. To date, the building sector has witnessed immense development in the way by which building systems are managed [1, 2],which aimed at alleviating the significant environmental impact of this sector (40% of the world energy consumption and a third of the associated CO_2 emissions [3]). Decreasing this impact could be achieved by elegant controlling the resources [4]; building energy management systems (BEMS) provides sustainable and efficient solutions.

An expected BEMS aims to increase energy efficiency while maintaining the required comfort levels and enhance environmental effects. However, based on a large number of practical implementations, it is found that the current problems in existing BEMS are mainly concentrated in the following aspects: (1) the traditional BEMS mostly has relatively sole functions. For example, the systems lack effective monitoring and linkage management of the dynamic environment and energy-related equipment, (2) the family of BEMS is still far from the standardization of communication protocols and data formats, and (3) many systems only collect and store data employing local databases for monitoring and lack supervisory applications (advanced control, human-machine interactions, data analysis). The dilemma attributes to the usage of supervisory control and data acquisition (SCADA) architecture in existing BEMS [5].

The popularity of the Internet of Things (IoT) and its successful industrial applications provide a new perspective

for us to deal with the dilemma above [6–8]. Utilizing the IoT technology, a massive amount of data is aggregated into a unified energy management platform. GÃ¼nter Alce proposes a new concept of IoT interaction [9]. However, some challenges have arisen. How to manage big data (transferring, storing, preprocessing, optimization, and control under a suitable IoT framework) [10]. On the other hand, delivering useful information to different stakeholders based on their use is another challenge [1, 11–13]. These challenges pose new questions: what is the complex SCADA-based BEMS framework under IoT, and how to build it? On top of these, what are suitable control strategies for achieving optimal BEMS performance?

Numerous studies have proven that an advanced control strategy could significantly reduce energy use and alleviate greenhouse gas emissions, see, e.g., [14–16]. However, many buildings currently adopt rule-based control (RBC) with limited energy-saving capabilities [17–19]. Many studies have proved that the building sector can significantly benefit from replacing the current RBC for more advanced control strategies like model predictive control (MPC) [18]. MPC's perfect performance is achieved by accounting to minimize consumed energy and maintain high comfort indexes while considering physical constraints, weather forecasts, and building dynamics. In recent years, many energy-efficient MPC approaches have been validated to control the building systems [20–24]. Despite these tries, RBC-based control remains business as usual in the building sector. A key factor prohibiting this technology transfer to the commercial sector is the cost, time, and effort associated with capturing first-principle-based dynamical models of the building. Also, a gap always exists between the modeled and the real building, and the domain expert must then manually tune the model to match the measured data from the building [25, 26].

An alternative approach for implementing MPC is using control-oriented data-driven predictive models. In the literature, this approach is called data predictive control (DPC) [25]. In [27, 28], the authors proposed MPC closed-loop optimization strategies based on neural networks (NN) for energy-saving control in buildings both in commercial and residential buildings, respectively. However, these approaches are not easily scrabbled to different types of buildings [29]. NN is employed in the closed-loop control scheme to determine control performance indexes instead of neural network-based system state dynamics. Unfortunately, since NN, a nonlinear nature, the complementary MPC-based optimization problem becomes computationally more demanding when the neural network's complexity is high.

To overcome this complexity above, the regression tree-based approaches were employed in the literature to develop data-driven predictive models. Authors in [30, 31] developed RT and random forest for building control in different settings. However, the simulation results demonstrated that these models were trapped in limitations due to overfitting and high variance [5]. In [18], a well-performing approximate MPC via machine learning has been developed based on two multivariate regression algorithms, namely, deep time-delay neural networks (TDNN) and regression trees (RT) on Hollandsch Huys, which is an office building in Belgium. This approach mentioned above is an advantage which is the simplified control laws that retain comparable performances with MPC. However, the RT-based controller scored worse in performance than a well-tuned PID controller, which dates back to modeling inaccuracy. To overcome the drawbacks of previous works above, we present an ensemble learning algorithm, called least-squares boosting (LSBoost), which integrate multiple decision trees to produce robust models. The residential building model data in [18] will also be used in our simulation and validation. What is different from prior studies is our work focus on data-driven optimization control of BEMS both in residential and office buildings under the IoT framework.

In this paper, we develop a data-driven energy optimization control strategy based on an improved LSBoost under a layered building energy IoT framework, which improves the occupants' comfort and reduces energy consumption. We validate the proposed control scheme by numerical simulation with two types of buildings: residential building and office building. The work has the following contributions:

(1) We develop a novel four-tier building energy internet architecture. This architecture is used for managing data from both IoT devices and BEMS, by using a cloud-based user-friendly human-machine interaction interface. The motivating factor behind the developed architecture will be elaborated details in Section 2. The platform above can provide useful data representations to different stakeholders (end-user, building energy manager, and/or operator), enabling flexibility and scalability.

(2) An optimization strategy is the first strategy proposed for building energy management based on the improved LSBoost. The LSBoost algorithm is used to enhance the building model's interpretability and reduce complexity without losing accuracy. The optimization problem takes the optimal index of human comfort into account the constraints to ensure a good living and office environment.

The remainder of this paper is organized as follows. A novel building energy internet architecture is presented in Section 2. In Section 3, two types of buildings, namely, residential and office buildings, are built. Section 4 defines the finite receding horizon control problem with the DPC framework. We compare the performance of the DPC-LSBoost with the MPC, the TDNN, and the DPC-RT in Section 5. Conclusions and further work are provided in Section 6.

2. Building Energy IoT System Architecture

This section describes a complex cloud SCADA-based BEMS framework under the IoT, which is necessary for successfully implementing DPC in public buildings.

2.1. Cloud SCADA System. When the existing SCADA-based BEMS framework meets the IoT, the local servers will feel

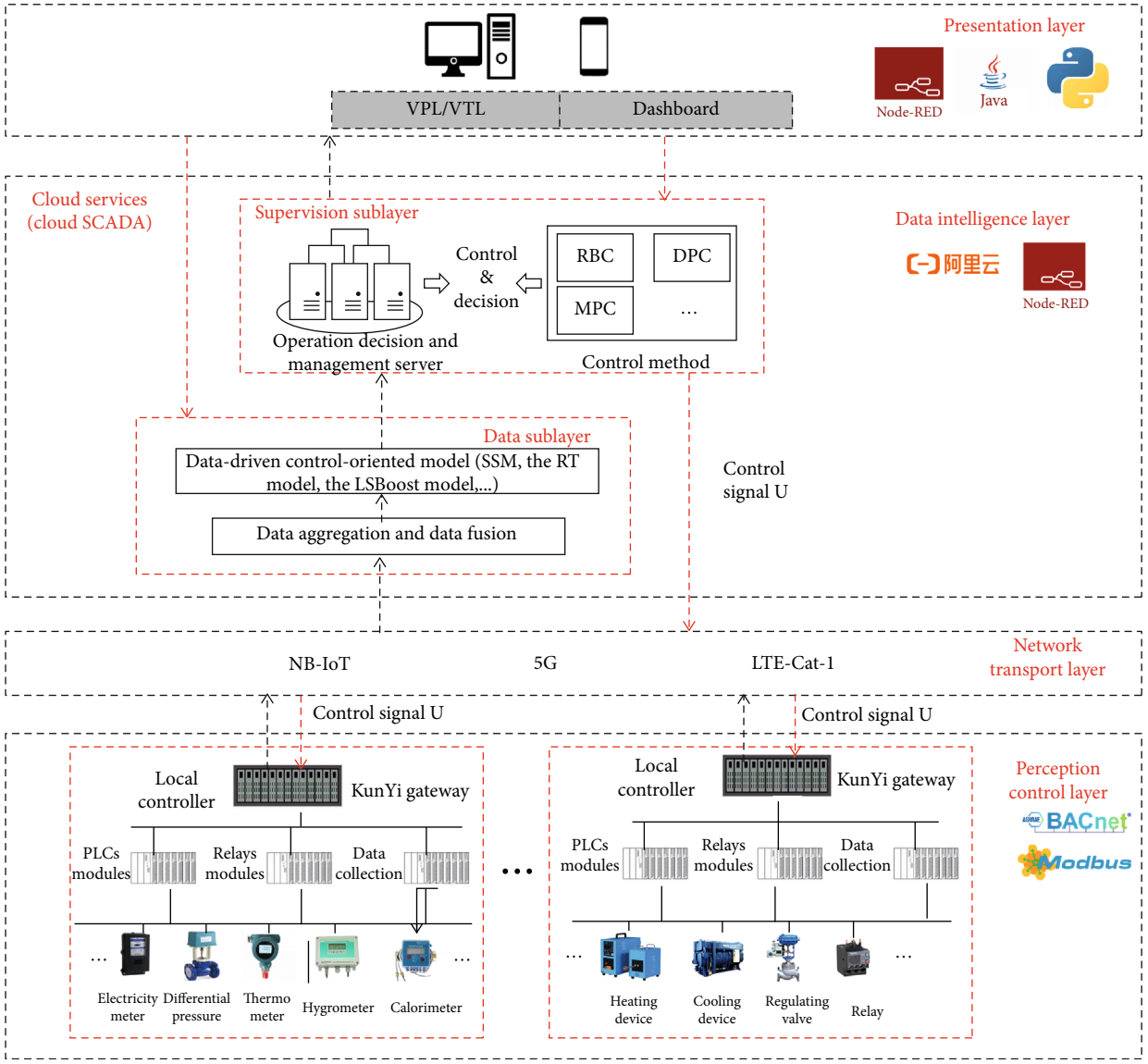

Figure 1: The overall architecture of the IoT in the building energy system.

helpless against a massive amount of data. Also, the existing SCADA-based BEMS is still far from the standardization of communication protocols and data formats, which is unfavorable for advanced control strategies implementation. We decided to develop a cloud-based SCADA system and its ecosystem to deal with the problem above. The cloud-based solution's motivation is its compatibility with user-friendly and easy access to the real data, instead of additional hardware investments [32].

2.2. Four-Tire Building Energy IoT System Architecture. The existing SCADA-based control layers in a BEMS constitute three separated layers [33], and those are (1) field layer (sensors, actuators, controllers), (2) automation layer (signal processing, controlling, alarms activating), and (3) management layer (system data presentation, trending, logging, and archival). The IoT also consists of three separate layers: (1) perception layer, (2) network layer, and (3) application layer. However, we introduce a four-tire client-server software architecture web platform consisting of four layers: perception control layer, network transmission layer, data intelligence layer, and representation layer.

The motivation factor behind the four-tire architecture is the complementary advantages for the SCADA architecture and the IoT architecture. One of the main advantages of using a SCADA configuration is that the control and communication flows can be presented sequentially [5]. However, the strength of the IoT configuration is the ability of data processing in-depth. Based on the reasons mentioned above, we define the first 3 layers. In addition, to make IoT data form building useful to different stakeholders, we decide to develop the presentation layer as the fourth layer. The idea is inspired by a building lifecycle data management strategy in [1]. The architecture of the IoT in the building energy system is shown in Figure 1.

(1) *Perception control layer*: in BEMS, this layer is endowed with two primary functions:

(a) Collecting sensor data of environment parameters (such as indoor and outdoor temperature, humidity, and wind speed), power consumption, pressure difference, water flow, and heat

(b) Receiving control signals from the field controllers or executing agencies to ensure that the control objectives, i.e., heating unit refrigeration unit, works properly.

(2) *Network transmission layer*: the Internet of Things communication technology such as NB-IoT, 5G, is utilized to ensure the sensor data upload and control signal U transmission.

(3) *Data intelligence layer*: this layer consists of two sublayers: the data sublayer and the supervision layer. The data collected by sensors will be filtered and fused first, and the abnormal signals are checked to ensure the data's integrity and accuracy, which is stored in the database. Then, the existing data is used to establish the control-oriented building models. The supervision sublayer is based on the data-driven predictive model, according to the set optimization objectives, using the optimization control technology developed in this paper (such as the MPC, the DPC-RT, the DPC-LSBoost, and the TDNN), to form the control strategy, such as ensuring the building's indoor environment control requirements while making the building energy consumption lowest.

(4) *Presentation layer*: the presentation layer endows two main functions: visual programming Language (VPL) interface and textual programming language (TPL) interface—dashboard. The dashboard is an information management tool for different stakeholders, including the environmental parameters setting, real-time monitoring data display, the PMV value, and energy consumption prediction.

3. Building Modeling and Analysis

This section describes the linear time invariant (LTI) state space model (SSM) for residential buildings used in this study.

Firstly, the internal structure of complex building is modeled. Its purpose is to accurately build the HVAC system and internal housing structure. Moreover, the house is easily affected by the natural environment. The disturbance of the external environment to the building should be considered. Common disturbances include ambient temperature, light intensity, wind speed, humidity, and other disturbance information so that the mathematical model can be close to the real building.

3.1. Residential Building Modeling

3.1.1. Model Description. The building model is located in a six-bedroom townhouse in Bruges, Belgium. The residential building consists of 6 guest rooms, 5 windows, and 11 single buildings with external walls. For the temperature control system of residential buildings, the central steam furnace is used for heating. For the building's parameters, including building area, room orientation, and other information, please refer to the literature [18].

Table 1: Dimensions of key variables in the building model.

Notation	Description	Values
n_x	Number of states	286
n_u	Number of inputs	6
n_y	Number of outputs	6
n_r	Number of output references	6
n_d	Number of measured disturbances	44

At the beginning of building the model, the Modelica building envelope model is implemented by using idea library, but its complexity cannot be directly used as a state-space model. A large number of collected data are nonlinear and need to be linearized before they can be used. For example, the heat generated by solar radiation: the equation of sunlight transmission and absorption through windows is highly nonlinear, so if you want to deal with it, you have to use a nonlinear filtering algorithm. For these unprocessed data, to remove the burr, the processing algorithm is extended Kalman filter [34]. After linearization, the state space expression can be constructed. For a complete description of building state-space expressions, please read the paper [35]. The sampling interval for humidity, temperature, wind speed, light, and other sensors is 15 minutes in the sensor and control layer. Therefore, the discrete space expression is constructed as follows:

$$x_{k+1} = Ax_k + Bu_k + Ed_k, \tag{1a}$$

$$y_k = Cx_k + Du_k. \tag{1b}$$

In the above equation, x_k, u_k, and d_k, respectively, represent the state, input, and disturbance variables at time k; y is the output variable; the model's sampling frequency is Ts = 900 sec. The disturbance signal d_k presents the heat absorbed and the direct and diffuse solar radiation transmitted by each window such as radiation temperature of ambient and sky temperature, ambient temperature, and ground temperature. Table 1 summarizes the dimensions of the building model variables used.

3.1.2. Model Analysis. House analysis is the analysis of the established model (SSM). From the house's perspective, entering a changing curve to reflect the change of the indoor temperature of the model without the control of the controller. Entering U

$$\begin{aligned} U_{50*1348} &= [R_{6*1348} D_{44*1348}], \\ R_{6*1348} &= 20 + 3 * \sin\,(t + k * ts)(k = 1, 2 \cdots 1348), \end{aligned} \tag{2}$$

with R_{6*1348} as the input temperature input, the external environmental disturbance as $D_{44*1348}$, k as the sampling

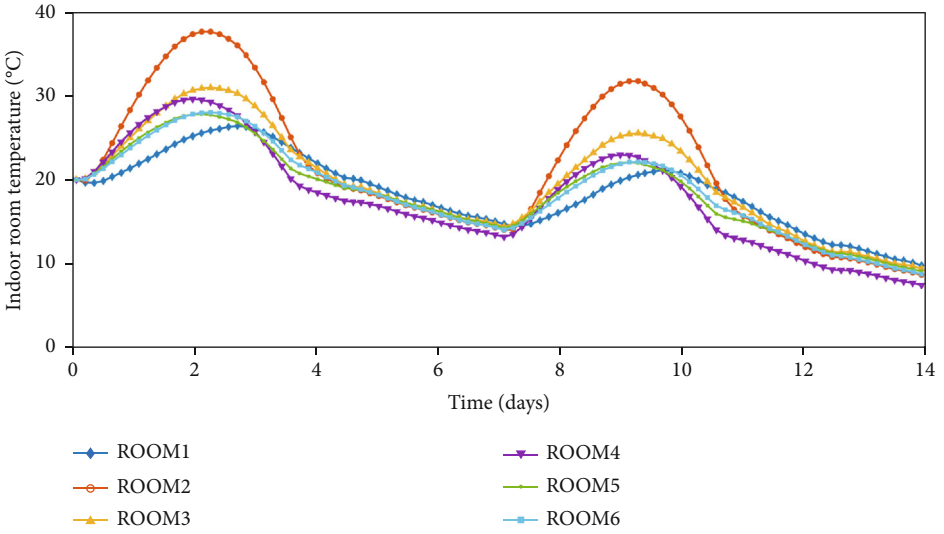

Figure 2: 14-day temperature variations of 6 rooms.

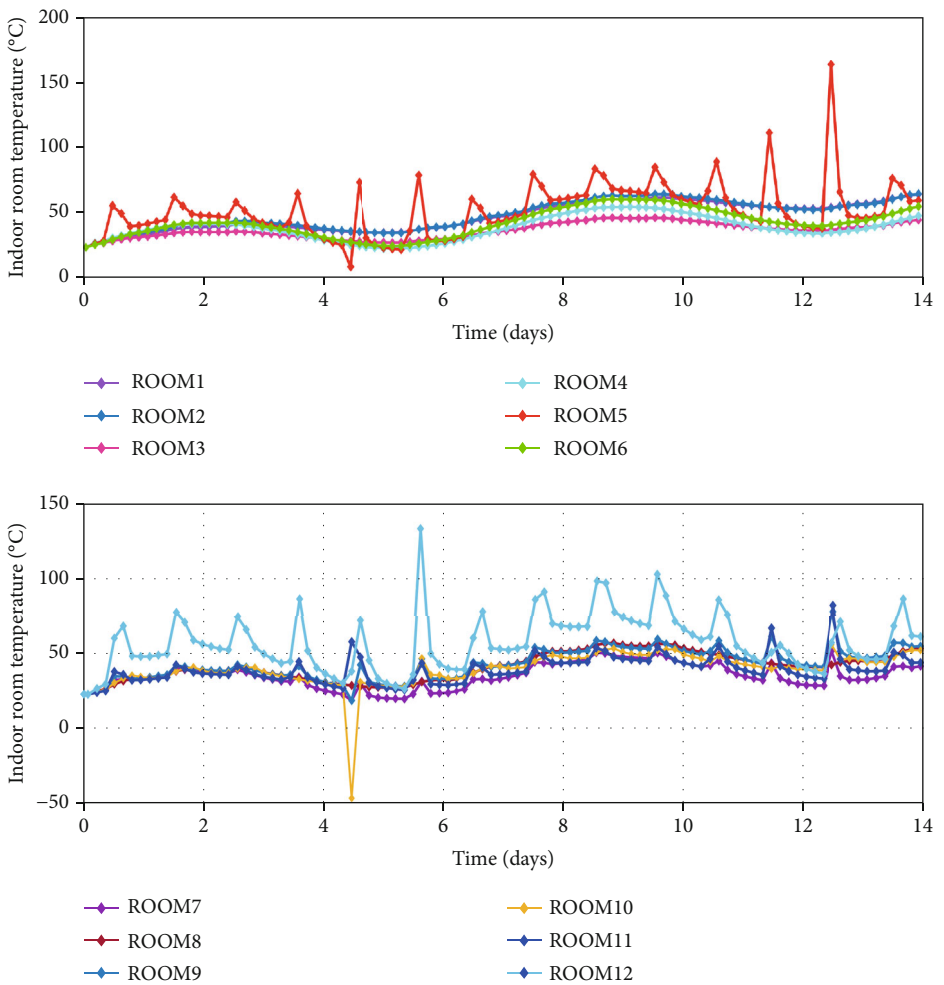

Figure 3: 14-day temperature variations with office building.

Table 2: Notation and meaning of the variables used in optimization control.

Notation	Units	Description	Control setup
x	[K]	Building temperatures	States
y	[K]	Controlled temperature	Outputs
r	[K]	Reference temperature	References
u	[W]	Radiators heat flows	Inputs
d	[K,W]	Temperatures, heat flows, and radiation gains	Disturbances
s	[K]	Comfort band violations	Slack variables
ub	[K]	Upper comfort boundary	Constraints
$1b$	[K]	Lower comfort boundary	Constraints

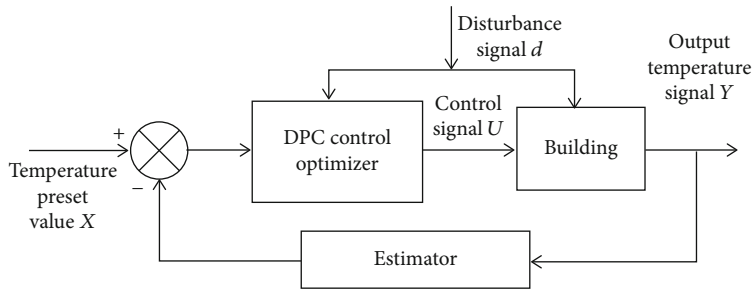

Figure 4: Schematic representation of the building optimal control closed-loop system using the DPC controller.

time, and the sampling interval as 4 hours $ts = 4$ (hour). The total number of simulation days is 14 days. Two weeks can reflect the changing trend of the model temperature, so as to better design the controller. Figure 2 shows the temperature change of 6 rooms in 14 days.

The overall trend of changes in the 6 rooms is consistent with the gradual decrease in temperature. However, it is quite different from the preset temperature. The maximum temperature of the ROOM2 can reach 37°C, which is 10°C higher than the other two models. The same goes for other room temperature trends. Therefore, for the model, the stability of the model is the most important. A major feature of the choice of the building body model is stability and robustness. Such a building conforms to the human habitation. And when the controller is not added, the temperature of the room will gradually decrease, and, finally, drop to 7°C.

Table 3: Corresponding level of CIHB index.

CIHB	Level	Corresponding to human feeling
>85	4	Very hot and uncomfortable Need to protect against heatstroke
~ 85	3	Too hot; need to heatstroke prevention
~ 79	2	Hot, uncomfortable, needs to be cooled
~ 75	1	Warm, comfortable
59 ~ 70	0	Most comfortable and acceptable feeling
~ 58	-1	Cold and uncomfortable
~ 50	-2	Cold and uncomfortable. Keep warm
~ 38	-3	Very cold, keep warm, and cold protection
≤25	-4	Extreme cold, prevent frostbite

3.2. Office Building Modeling

3.2.1. Model Description. The office building is modeled by Hollandsch Huys, and the building is located in Hasselt, Belgium. Hollandsch Huys represents a class of geotab buildings [36]. Hollandsch Huys is a 5-storey building, including 3-storey office areas located in the ground floor, first floor, and second floor; underground garage; and top loft. When building the office building model, considering the complexity of the model and the personnel distribution, it is mainly to build a model for the three floors of the office area. Please refer [37] for the main parameters of relevant building structures.

Similarly, the office building's SSM is established by using the method described in 3.1. The office building's SSM construction is consistent with that of the residential building construction, please refer to Equations (1a) and (1b). Compared with residential buildings, the SSM of office buildings is more complex, and the variable dimension is higher. The dimensions of the Hollandsch Huys building model variables n_x, n_u, n_y, n_r, and n_d are 700, 20, 12, 20, and 301, respectively.

3.2.2. Model Analysis. For an excellent mathematical model, we hope that the model we build can be applied, so we need to simulate the established SSM and simulate the output-

Require: A, B, C, D, E matrix, temperature boundary lb, wb, DPC horizon N, data set, model (select control method such as RT, $LSboost$)
Ensure: U
Step 1: Build a prediction model.
(A) Data dimensionality reduction, feature selection (Algorithm 2 and Algorithm 3).
(B) Training data to build a model.
if Model==RT **then.**
  Build RT model M_{RT}. (Algorithm 4).
else if Model==$LSBoost$ **then.**
  Build LSBoost model $M_{LSBoost}$. (Algorithm 5).
ends
Step 2: Model optimization cossntrol.
while $k < N$ **do.**
(A) Calculate the $u_k{}'$ from M_{RT} or $M_{LSBoost.}$
(B) Through Equation 1, calculate $y_k{}'$.
(C) Update $u_k{}'$, $y_k{}'$.
(D) Solve Equation 5 and obtain $(u^*_{k|k}, u^*_{k+1|k}, \cdots, u^*_{k+N-1|k})$.
(E) $u_k \longleftarrow u^*_{k|k}$ and $k \leftarrow k+1$.
end
return $U = \{u_0, u_1, \cdots, u_{N-1}\}$

Algorithm 1. Building data-driven predictive control.

Require: feature vector x important features p.
Step 1: Compute the covariance matrix of the feature vector x: $\Sigma = (1/\mathrm{m})x^T x$
Step 2: SVD decomposition of the covariance matrix Σ, $\Sigma = USV^T * U$, S are the principal component coefficients and variances.
Step 3: Matrix S accounts for the proportion of total features, and call it as v_i,
$$v_i = S_{i,i}/tr(S)$$
$*tr(S)$ is the trace of the matrix S.
Step 4: Select the principal component variance corresponding to the q most significant singular values,
$$\max q \text{ s.t.} \sum_{i=1}^{q} v_i \le \eta$$
Step 5: Compute the normalized contribution v^j of the j-th feature x_j on selected principal components.
$$v^j = \sum |U_{j,1,\cdots,q}| / \max_{1 \le k \le n_x} \left(\sum_{i=1}^{q} |U_{k,1}|\right)$$
Step 6: The p most important features that satisfy ψ are selected,
return $p = \{i \mid v^j \ge \psi, \forall \in N_0^{n_x}\}$

Algorithm 2. PCA feature selection.

Require: Perturbation matrix E in equation 1
Ensure: most important features q
Step 1: Compute the l_1 norm of each column vector in matrix E, given as IOD_i.
$$IOD_i = \sum_{j=1}^{n_x} \|E_{i,j}\|_{l_1} \; i \in 1, \cdots, n_d$$
Step 2: IOD_i Feature normalization,
$$AIOD_i = (IoD_i / \sum_{i=1}^{n_d} IoD_i) i \in 1, \cdots, n_d$$
Step 3: Select the disturbance feature q that satisfies the threshold ζ.
return $q = \{i \mid AIoD_i \ge \zeta\} \; i \in 1, \cdots, n_d$

Algorithm 3. The importance of disturbing variables (IoD).

output relationship to evaluate the established model's quality. The input we take this time is U

$$\begin{aligned} U_{321*1348} &= [\, R_{20*1348} \quad D_{301*1348} \,], \\ R_{20*1348} &= 23 + 3 * \sin\left(t + k * ts\right)(k = 1, 2 \ldots 1348), \end{aligned} \tag{3}$$

with $R_{20*1348}$ as the input temperature, external environment disturbance as $D_{301*1348}$, k as the sampling time, the sampling interval as 4 hours, ts = 4hours, and the total number of simulation days as 14 days. The simulation results are shown in Figure 3.

It can be seen from Figure 3 that the SSM is constructed. The temperature change is greatly affected by external

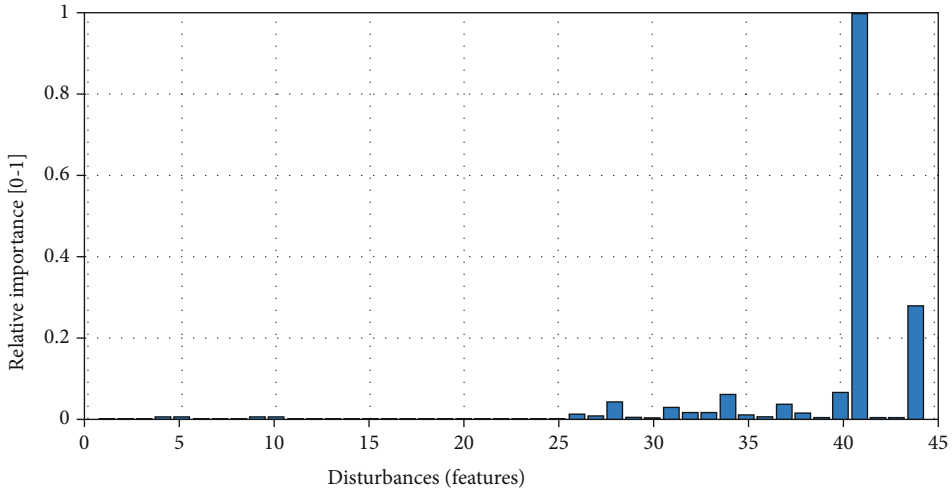

(a) The importance of building disturbances in residential buildings

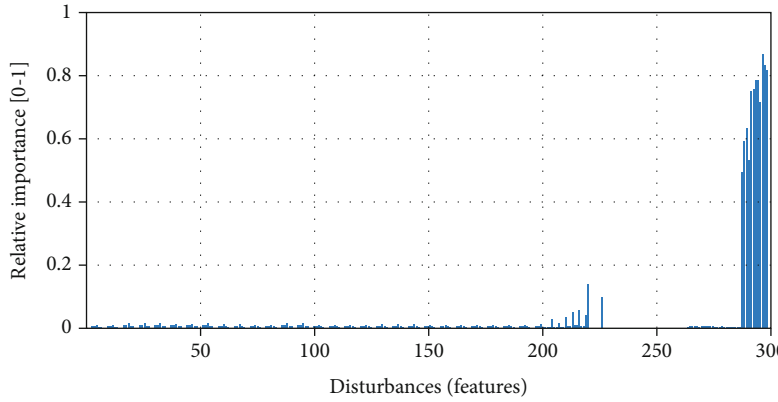

(b) The importance of building disturbances in the office building

Figure 5: The IoD profile on two types of buildings.

disturbance. As long as the input has a temperature change, the output temperature will be severely affected. The building model itself is a time-delay system, so the temperature of the output will change greatly. It is difficult to output the input of tracking. From Figure 3, The temperature of each room may change abruptly, and either it becomes very high or very low. This established model has a certain distance from the actual model. However, it is still in a stable state for the entire system. Therefore, it is necessary to design a controller for the built house building model. The most significant purpose of the controller is to achieve stability and stability within the human comfort zone.

4. Data-Driven Predictive Control

The supervision sublayer design's primary purpose is to design the controller, which plays the role of the control decision. Because the control effect of the designed controller will directly affect the indoor temperature and human comfort, the controller design should be deeply analyzed from the complexity, real-time, and robustness. The more commonly used controllers in the market should be comprehensively analyzed, and finally, the DPC-LSBoost controller should be selected. Because the DPC-LSBoost controller has a perfect explanation, the regression tree constructed is straightforward and easy to understand, convenient for management, and decision-making.

Table 4: Comparison of the disturbance features of the two buildings.

	No. of the original	No. of the (PCA)	No. of the (E)	No. of the selected	Reduction rate (%)
Residential	44	12	8	8	81.81
Office	301	14	16	12	96.01

4.1. Control Optimization Design for Comfort Objective. In the building energy management system, most of the designed design controllers need to meet certain comfort and economic practicality. Therefore, when designing the controller, the reference input is a range instead of a specific

value, which is called the comfort zone. This paper adopts the ISO-7730 standard [38], which specifies the upper limit of temperature between $ub \in [23, 26]$ and the lower limit of $lb \in [20, 23]$. Equation (4) defines the mathematical expression of the temperature comfort zone.

$$lb_k - s_k \le y_{i,k} \le ub_k - s_k, \tag{4}$$

with s as a slack variable, k as a time series, and $y_{i,k}$ represents the ith room temperature at time k. It is necessary to ensure that the output temperature is within the comfort zone, so as to minimize the s_k and the room energy consumption. However, the ideal comfort and energy consumption are contradictory. In order to solve this problem, the control problem is transformed into an optimization problem. Table 2 lists the symbols and meanings of variables frequently used in this section.

Figure 4 is a control structure diagram designed to solve this optimization problem. The purpose of control is to achieve minimum energy consumption and maximum human comfort, which involves two variables: the control signal U and the output temperature Y. In summary, Equation 5 established an optimization function.

$$\min_{u_0,\cdots,u_{N-1}} \sum_{k=0}^{N-1} \left(Q_s \|s_k\|_2^2 + Q_u \|u_k\|_2^2\right), \tag{5a}$$

$$s.t. x_{k+1} = Ax_k + Bu_k + Ed_k, k \in N_0^{N-1}, \tag{5b}$$

$$y_k = Cx_k + Du_k, k \in N_0^{N-1}, \tag{5c}$$

$$lb_k - s_k \le y_k \le ub_k - s_k, k \in N_0^{N-1}, \tag{5d}$$

$$x_0 = x(t), \tag{5e}$$

$$d_0 = d(t), \tag{5f}$$

$$\frac{59 + 3 \cdot 2\sqrt{v} - 32 - 0.143 + 0.143RH}{0.81 + 0.143 + 0.143RH} \le y_k \le \frac{70 + 3.2\sqrt{v} - 32 - 0.143 + 0.143RH}{0.81 + 0.99RH}, \tag{5g}$$

with $N_a^b = \{a, a+1, \cdots, b\}$ as a set of integers, and x_k,u_k,y_k and d_k represent state, input, output, and disturbance variables, respectively. The prediction range is N, and k is the k-th moment in the prediction range. (5b) and (5c) are the time-invariant state space expressions of the building (5d). The lower boundary lb_k and the upper boundary ub_k are taken into consideration. (5g) introduces the popular Comfort Index of Human Body (CIHB) in recent years [39] and divides it into 9 levels to evaluate comfort Table 3. The index also considers the effects of average temperature, relative humidity and wind speed on human comfort. Equation (6) is shown below.

$$\text{CIHB} = 1.8y - 0.55(1.8y - 0.26)(1 - RH) - 3.2\sqrt{V} + 32 \tag{6}$$

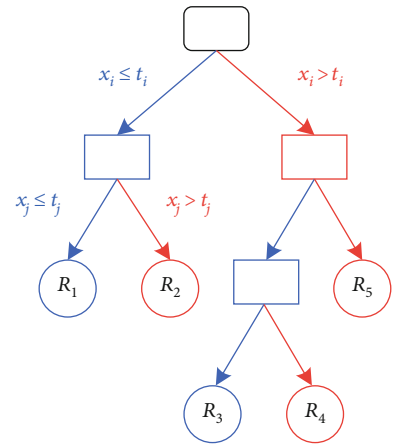

Figure 6: After dividing the regression tree twice, we get 5 sets $R_1, \cdots, R_5$.

with y as the average temperature °C, RH as the average humidity (%), and V as the wind speed (m/s). According to Table 3, comfort level 0 is the most liveable environment for the human body. The CIHB index should be the most reasonable at 59 ~ 70, which is converted into an inequality (5 h) about temperature, to construct a constraint (5e). Limit the maximum and minimum boundaries of the control signal u_k. (5f) and (5g) set the initial parameters. (5a) indicates that the objective function finally constructed by the optimization problem outputs a sequence $u_0, u_1, \cdots, u_{N-1}$ under the influence of 7 constraints, so that the output control amount is minimized, the objective function $\|\cdot\|_2^2$ represents the square of the second norm, s_k is a slack variable, u_k is a control variable, Q_s represents the weight of human comfort, and Q_u represents the weight of energy consumption. The weighting matrices Q_s and Q_u are given as positive definite diagonal matrices. Set it to $Q_s/Q_u = 10^7$. The first term in the objective function is the square with the lowest degree of comfort violation, and the second term is the square with the lowest energy consumption.

The architecture of DPC is shown in Algorithm 1. The DPC-LSBoost is a DPC algorithm with the LSBoost model. The DPC-RT is a DPC algorithm with the RT model.

4.2. Feature Selection. This section proposes a simple and systematic approach for the efficient feature selection (FS) of predictive models in the context of building energy control applications. Because the method introduced in this section is versatile, it can be used to identify and select the most relevant variables in a dynamic building model, reducing model complexity, or reducing the cost of sensing equipment in practice. For current building data, feature selection based on principal component analysis (PCA) is first proposed. The simplicity and the PCA algorithm efficiency are well known, so we choose the method described in [40] to perform feature selection on the dataset we build. Algorithm 2 shows the PCA feature selection progress.

Require: Data in Equation (7) and a Loss Function Equation (11)
Ensure: $T_{\min}$
Step 1: Using Equation (11) to recursive binary splitting makes a large tree T_0 on the training data.
Step 2: Use K-fold cross-validation to choose best tree.
For k = 1,...,K:
Apply cost complexity pruning(prune) to the large tree in order to obtain a sequence of best subtrees, as a function of α.
end
Step 3: After k-th fold, An optimal tree T_{iin} is selected. $T_{\min} = \underset{T_k}{\operatorname{argmin}} \alpha_k, k = 1, \cdots, K$
return $T_{\min}$

Algorithm 4. Regression tree algorithm.

Now, we consider that there are N sets of observations in a data set, and each set of observations contains s features and n outputs, written as a mathematical expression as follows:

$$\begin{aligned} x^i &:= \left[x_1^i, x_2^i, \cdots, x_s^i\right] \in R^s \\ y^i &:= \left[y_1^i, y_2^i, \cdots, x_n^i\right] \in R^n \cdot \\ & \quad i \in \{1, 2, \cdots, N\} \end{aligned} \tag{7}$$

The x^i shown in Equation (7) encapsulates all parameters that change over time, for example, the current state quantity $x(t)$, the current and future disturbance variable $d(t), \cdots, d(t + kTs)$ in Equation 1, and comfort boundary signals $lb(t), \cdots, lb(t + kTs)$ and $ub(t), \cdots, ub(t + NTs)$. Among them, the feature selection for disturbance is mainly considered in the degree of influence of the disturbance variable d_t on the system. Among them, the feature selection of the disturbance is mainly considered to the degree of influence of the disturbance variable d_t on the system.

In algorithm 2,the data variables have a large dimension, so the PCA feature selection is utilized to reach a more appropriate dimension, and the accuracy thresholds $\eta = 0.99$ and $\psi = 0.99$ are chosen.

Then, with the house disturbance model, the matrix E of the LTI model constructed in Equation 1 considers the disturbance's influence on the system.

Figure 5 shows the impact of construction disturbance both in residential and office buildings. The higher the index of $AIOD_i$ means the higher impact of the disturbance on the system performance.

Therefore, from the above two types of algorithms, the most relevant features can be filtered, and the intersection of the two sets is taken as the FS that is finally selected.

$$FS = p \cap q, \tag{8}$$

where p is the important feature set, and q is the important disturbance set.

So, the distribution features of the models can be obtained, as shown in Table 4. The features of residential buildings and office buildings are 81.81% and 96.01%, respectively. It is shown that the more features mean better results using this feature selection method. It also means that many of these features are redundant.

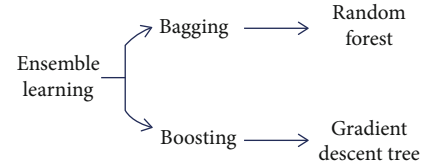

Figure 7: Ensemble learning classification.

4.3. Design of the DPC-RT Controller. This section focuses on the prediction modeling of multiple output regression tree. Because of a lot of advantages of the regression tree, the controller adopts a very representative The controller adopts a very representative regression tree method in machine learning because of the RT advantages. Tree method in machine learning. The regression tree, as the name implies, is to use tree model to do regression problems, and each leaf will output a prediction value. The predicted value is generally the mean value of the output of the training set elements contained in the leaf,

$$y_m = \operatorname{ave}\left(y^i \mid x^i \in \operatorname{leaf}_m\right), \tag{9}$$

with y_m as the predicted output value of the m-th leaf. When $x_i \in \operatorname{leaf}_m$, the training set outputs y_i. ave means averaging.

The nodes of the tree split are shown in Figure 6. With each split, the regression tree divides the current data set into two subsets. For example, in i-th divided nodes, the left branch tree R_L contains data divided by $x_i \le t_i$, and the right branch tree R_R contains data divided by $x_i > z_i$. Then, the optimal segmentation point of each node is determined by minimizing the sum of the mean square errors of the two branches. The equation is

$$(x_k, t_k) = \operatorname{argmin} \sum_{\{i \mid x^i \in R_L\}} \left(y_1^i - \bar{y}_L\right)^2 + \sum_{\{i \mid x^i \in R_R\}} \left(y_1^i - \bar{y}_R\right)^2, \tag{10}$$

with $\bar{y}_L, \bar{y}_R \in R$, respectively, that represents the average output of all points of the left branch tree R_L and the right branch tree R_R and finds the smallest x_k corresponding t_k by traversing in sequence. In this way, we can introduce the

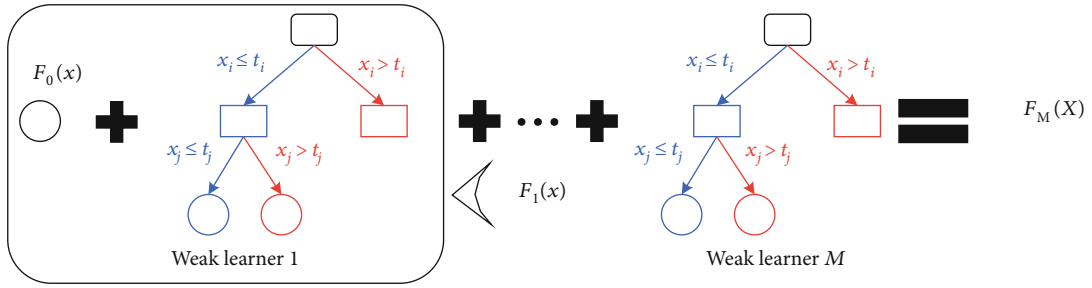

Figure 8: Schematic representation of the LSBoost model.

Require: Data $\{(x, y)\}_{i=1}^{n}$ and a Loss Function $L(y_i, F(x))$
Ensure: $F_M(x)$
Step 1: Initialize model with a constant value:
Step 2:for m =1 to M:
(A) Compute
$r_{im} = -[\partial L(y_i, F(x_i))/\partial F(x_i)]_{F(x)=F_{m-1}(x)}$ for $i = 1, \cdots, n$
(B) Fit a regression tree to the R_{im} values and create terminal regions R_{im} for $j = 1 \cdots J_m$.
(C) For $j = 1 \cdots J_m$ compute
$\gamma_{im} = \underset{\gamma}{\operatorname{argmin}} \sum_{x_i \in R_{ij}} L(y_i, F_{m-1}(x_i) + \gamma)$
(D) Update
$F_m(x) = F_{m-1}(x) + \nu \sum_{j=1}^{J_m} \gamma_{im} I(x \in R_{jm})$
Step 3:
return $F_M(x)$

Algorithm 5. LSBoost algorithm.

Table 5: Complexity comparison of multiple methods.

	PCA	RT	LSBoost	IOD	DCP-RT	DCP-LSBoost
Time complexity	$O(knd)$	$O(n \log(n)d)$	$O(n \log(n)dk)$	$O(n2)$	$O(n \log(n)dk)$	$O(n \log(n)d)$
Spatial complexity	$O(kn)$	$O(D)$	$O(Dk)$	$O(nd)$	$O(kn + dk + nd)$	$O(kn + nd + D)$

Figure 9: A snapshot of the developed building energy management system (the building image data source: [18]).

Table 6: Machine learning parameters and dimension overview.

Notation	Variable description	ML setup	Residential dimensions		Office dimensions	
			RT and LSBoost	TDNN	RT and LSBoost	TDNN
$\tilde{x}$	Training input	All features	27	36	41	62
y	Output	Selected features	6	6	12	12
lb	Comfort zone lower border	Selected features	1	1	1	1
$\tilde{d}$	Disturbance	Selected features	8	8	12	12
t	Time	Transformed features	3	3	3	3
u	Training output/training output	Targets	6	6	20	20

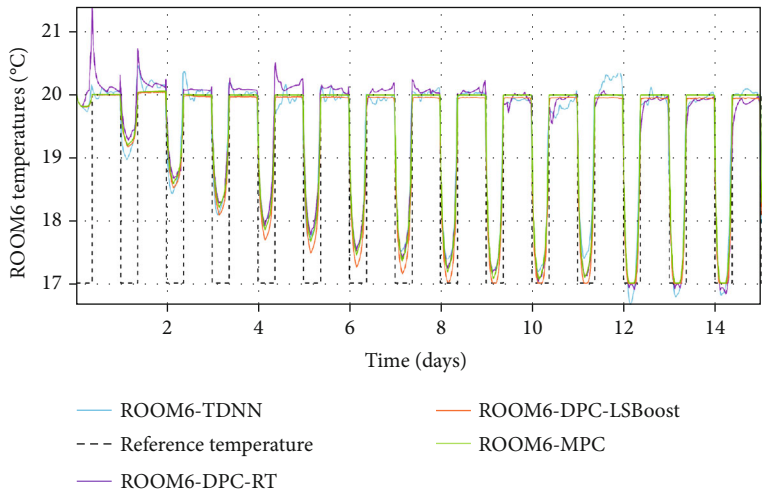

Figure 10: Comparison of the investigated temperature control performance in ROOM6.

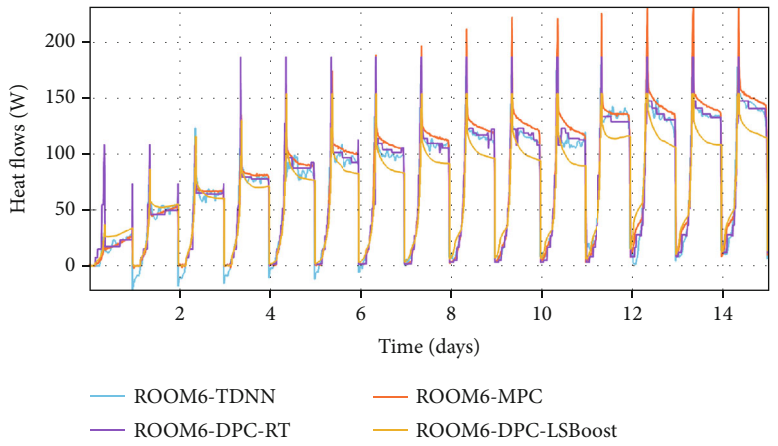

Figure 11: Comparison of the investigated controllers with respect to energy consumption in ROOM6.

weight matrix $Q \in R^{n*n}$ and introduce it into the quadratic optimization function as an adjustable parameter.

$$(x_k, t_k) = \operatorname{argmin} \sum_{\{i|x^i \in R_L\}} \left(y^i - \bar{y}_L\right)^{\mathrm{T}} Q\left(y^i - \bar{y}_L\right) + \sum_{\{i|x^i \in R_R\}} \left(y^i - \bar{y}_R\right)^{\mathrm{T}} Q\left(y^i - \bar{y}_R\right). \tag{11}$$

Both Equation (10) and Equation (11) provide two solutions to get the optimal $(x_k > t_k)$. The more times the tree is split, the more accurate the result. In terms of (9) and (10), the end conditions for building a tree are the same.

The process described above may produce good predictions on the training set but is likely to overfit the data, leading to poor test set performance. A smaller tree with fewer splits (that is, fewer regions $R_1, \cdots, R_m$) might lead to lower

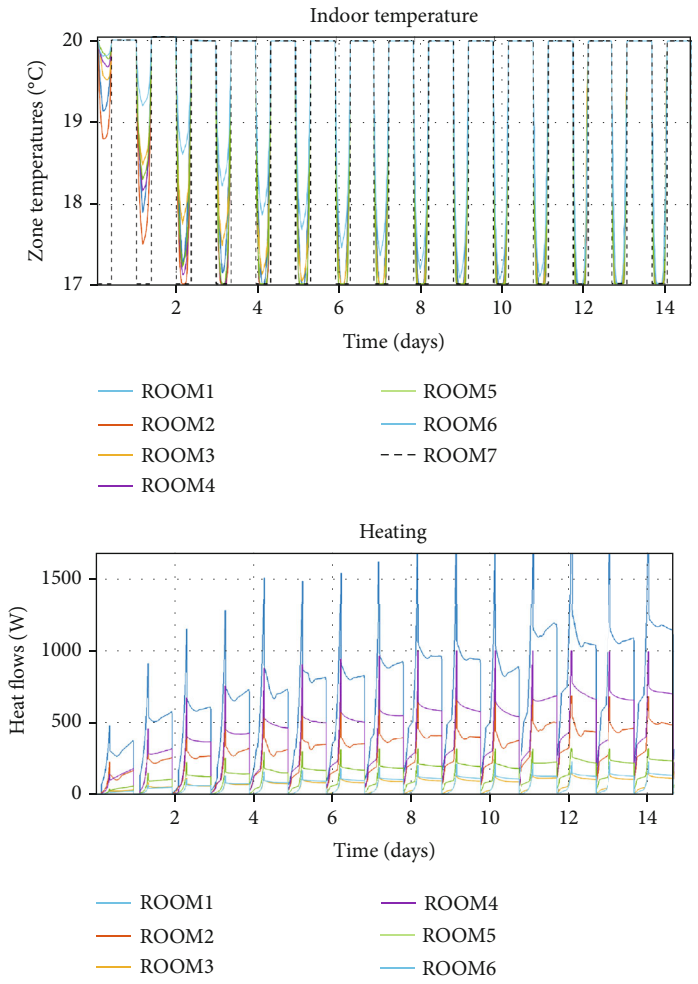

Figure 12: Control profiles of the DPC-LSBoost controller.

variance and better interpretation at the cost of a little bias. Therefore, a better strategy is to grow a very large tree T_0 and then prune it back in order to obtain a subtree. Intuitively, our goal is to select a subtree that subtree leads to the lowest test error rate.

$$T_{\min} = \min \sum_{m=1}^{|T|} \sum_{i:x_i \in R_m} \left(y^i - \bar{y}_m\right)^2 + \alpha |T|. \tag{12}$$

For each value of α, there corresponds a subtree $T \in T_0$ such that is as small as possible. Here, $|T|$ indicates the number of terminal nodes of the tree T, Rm is the rectangle (i.e., the subset of predictor space) corresponding to the mth terminal node, and y^m is the predicted response associated with R_m-, that is, the mean of the training observations in R_m. It turns out that as we increase α from zero in prune, branches get pruned from the tree in a nested and predictable fashion, so obtaining the whole sequence of subtrees as a function of α is easy. This process is summarized in Algorithm 4.

In short, when the data set is a continuous variable, the objective function of the optimal segmentation of each input feature is determined firstly. And then the input element with the lowest cost is used as the segmentation variable. In this way, we obtain the tree model $T_{\min}$ from Algorithm 4.

4.4. Design of the DPC-LSBoost Controller. Although the regression tree has the advantages of faster training and prediction speed, it is also good at obtaining the nonlinear relationship in the dataset; however, it still suffers from regression tree's poor scalability that needs to be solved. We change the regression tree structure from a single tree to multiple trees, enhancing the system's stability and robustness. Figure 7 illustrates that the enhanced tree belongs to the branch of ensemble learning and includes two types of boosting and bagging. The main focus is on reducing bias. The latter is mainly about reducing variance. Representative learning algorithms are random forest and gradient descent tree. The full name of LSBoost is least-squares boosting which is a boosting algorithm in ensemble learning. It inherits the advantages of regression trees and is developed on the classification and regression tree (CART) algorithm. Actually, a regression tree is a weak learner.

The LSBoost is an improvement on the gradient boosting decision tree (GBDT) algorithm. It has been improved from a previous classification algorithm to a regression algorithm.

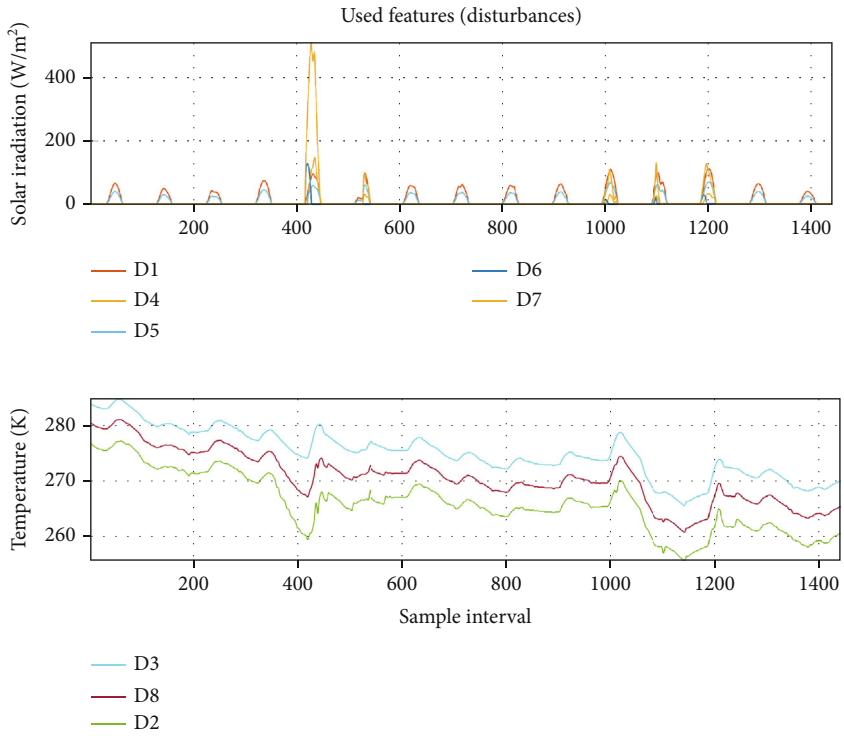

Figure 13: Selected most relevant external disturbance signals (8 signals).

Table 7: Detailed description of the disturbance signal.

Variable	Unit	Disturbance description
D1	[W]	Direct sunlight in horizontal plane Weight sun radiation
D2	[K]	Temperature between ground and sky temperature 1 Weight sun radiation
D3	[K]	Temperature between ground and sky temperature 2
D4	[W/m^2]	Direct sun radiation on vertical surface with orientation 3
D5	[W/m^2]	Diffuse sun radiation on vertical surface with orientation 3
D6	[W/m^2]	Direct sun radiation on vertical surface with orientation 4
D7	[W/m^2]	Direct sun radiation on vertical surface with orientation 5
D8	[K]	Ambient temperature

Like other boosting trees, LSBoost is training hundreds or thousands of weak learners like CART and iteratively updates the error and eventually becomes a strong learner, which is also the advantage of ensemble learning. Namely, each tree is part of the training of the current optimal. All the optimal are combined to build the strongest integrated tree. The schematic description of the LSBoost model is shown in Figure 8.

The difference between LSBoost and GBDT is that GBDT chooses to use the Gini index when the tree splits nodes, while LSBoost uses the minimum error square as the loss function at the tree split nodes as shown in Equation (13).

$$L(y_i, F(x)) = \frac{1}{2}(y_i - F(x_i))^2, \tag{13}$$

with x_i that represents the i -th set of feature data in the training set, x_i as the observation value corresponding to x_i in the training set, and $F(x)$ as the current prediction data. The loss function setting here is not fixed. The degree of fit can be checked through the trained data, evaluate through some indicators, such as R-square and RMSE, and choose a suitable loss function for the current data.

LSBoost uses Equation 13 as a loss function to facilitate the data differentiation, simplify operations, reduce computational complexity, and reduce training time. For the entire system, it speeds up the system response and enhances robustness. Therefore, the constructed LSBoost algorithm is as follows.

Algorithm 5 shows the method of constructing the LSBoost controller by training on the data set. The input training data is the same as Equation (7), the number of trainings is M times, the loss function uses Equation (13), and the second step (B) is the RT weak learner established. v is the learning rate, ranging from 0 to 1, with a default value of 0.1. Finally, the prediction value $F_M(x)$ after M trainings is output.

4.5. Algorithm Complexity Analysis. The algorithm complexity can reflect the actual operation of the algorithm, which is divided into time complexity analysis and space complexity

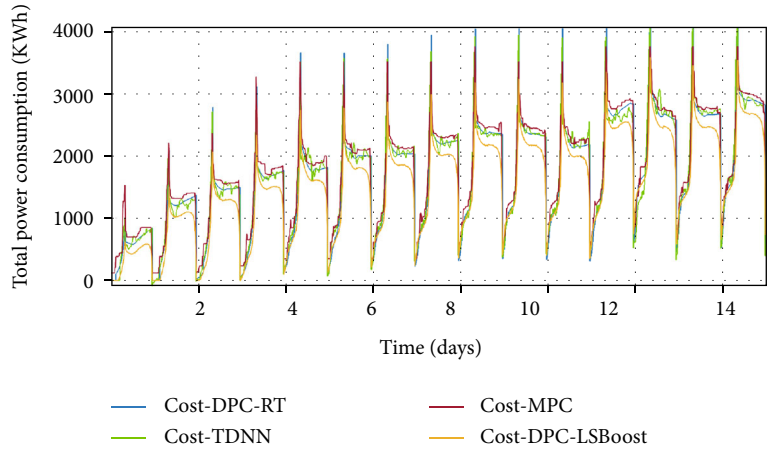

Figure 14: Comparison of total power consumption with the investigated controllers.

analysis. For this reason, the DPC based on Algorithm 1 is used to analyze the influence of RT and LSBoost algorithms on the system. Table 5 shows the comparative analysis of time complexity and spatial complexity in multiple methods.

D means the maximum depth of tree. n means the number of samples in the training set. d means the dimension of the data. k means the number of principal components.

5. Simulation and Verification

The Internet of Things platform used in this simulation experiment is a network service platform built by Nod-RED, MQTT broker, and other tools. Figure 9 demonstrates the current operation state, such as real-time sensor data display, energy consumption prediction curve, and log.

In this section, the case study's simulation results for indoor temperature control and energy consumption of residential buildings and office buildings for 15 days are demonstrated. We mainly focus on validating the proposed control strategies' performance for all investigated controllers (the TDNN, the MPC, the DPC-RT, and the DPC-LSBoost). The simulation objects selected this time are residential buildings (Section 3.1) and office buildings (Section 3.2). Based on the feature selection introduced in Section 4.4, we construct the reduced feature space $\tilde{x}$ dimension of the LSBoost model and the RT model to participate in training, following Equation (14).

$$n_y + 2(n_{\tilde{r}} + n_{\tilde{d}}) + n_t, \tag{14}$$

with n_y as the number of output variables, and n_t as time converted into three sinusoidal signals with different frequencies, which correspond to days, weeks, and months, respectively. $n_{\tilde{r}}$ is the reference input, and $n_{\tilde{d}}$ is the number of disturbance signals after feature selection. An overview of control variables and machine learning parameters is given in Table 6.

For the residential building, the dimension of $\tilde{x}$ is calculated by Equation (14): $*n_y = 6, n_{\tilde{r}} = 1,\ n_{\tilde{d}} = 8$,and $n_t = 3$. For the office building, the dimension of $\tilde{x}$ is calculated by Equation (14): $*n_y = 12, n_{\tilde{r}} = 1, n_{\tilde{d}} = 12$,and $n_t = 3$. Moreover, the reference input lb and the disturbance d at the current time and the next time are required during training. For more details, please see Table 6.

Table 8: Performance comparison of multiple controllers in the residential building.

Methods	Heating cost (kWh)	Cooling cost (kWh)	Total cost (kWh)	PMV viol (-)	Prediction time (s)
MPC	658.15	0	658.15	0	81.6
TDNN	660.67	1.29	661.96	1.2	11.6
DPC-RT	613.68	0	613.68	0.02	9.9
DPC-LSBoost	583.02	0.02	583.05	0	9.6

Table 9: Performance comparison of RMSE, R-square, and mean error for the RT and the LSBoost in the residential building.

	RMSE	R-square	Mean error
DPC-RT	0.0088	98.51%	52.1883
DPC-LSBoost	0.1244	99.99%	38.97

TDNN consists of one input layer, two hidden layers, and one output layer. Set the delay parameter $N = 22$, iterate 1000 times, and learn rate $\alpha = 0.01$. The main parameter of MPC is to set prediction horizon $N = 22$. For ideal training results, the dataset is divided into training set, validation set, and test set, which are 80%, 10%, and 10%, respectively.

5.1. Residential Building Simulation Analysis. This section presents the simulation results for a 6-room residential building's performance validation with the investigated controllers. The closed-loop profiles of 15 days are chosen from the simulation test. To clearly show the control effects of the building, ROOM6 is selected as the control object to analyze the temperature control and energy consumption, and

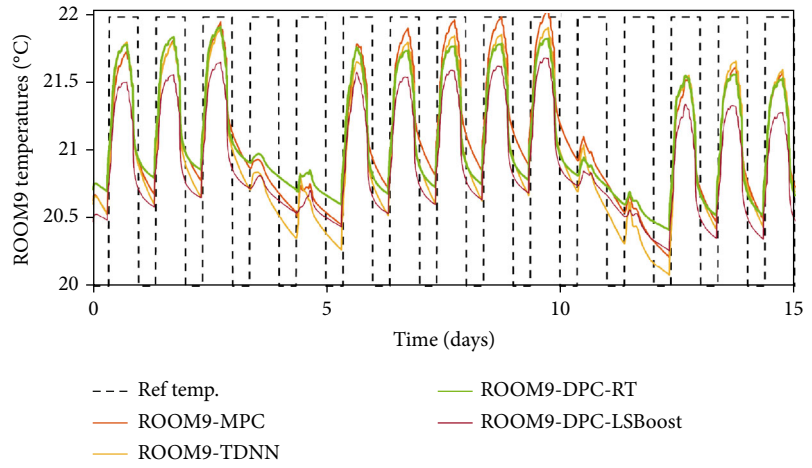

Figure 15: Comparison of the investigated temperature control performance in ROOM9.

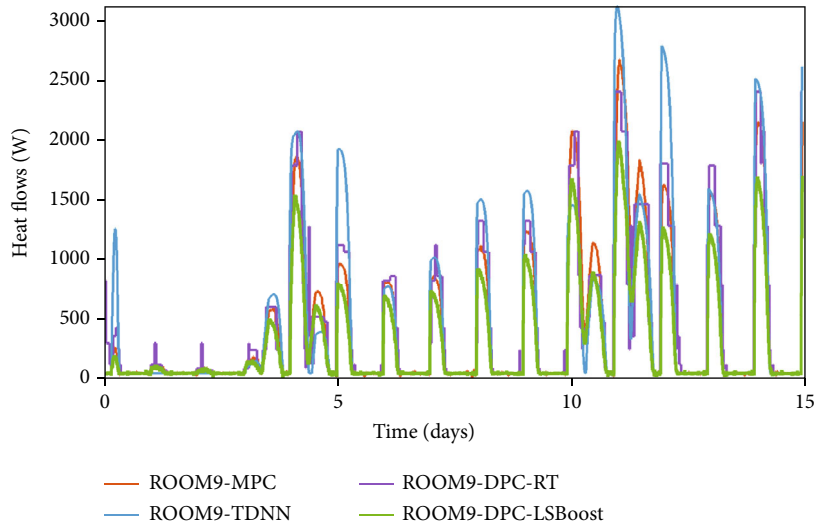

Figure 16: Comparison of the investigated controllers with respect to energy consumption in ROOM9.

the results are shown in Figures 10 and 11. The other rooms have similar behavior.

Figure 10 shows the comparison of temperature control effects with different control actions in ROOM6. It can be seen that both the MPC and the DPC-LSBoost have better control performance than the others. Under the MPC controller's action, the reference room temperature is well tracked. The temperature obtained by the TDNN fluctuates greatly, especially from the tenth to the thirteenth day. The control effect obtained by the DPC-RT is relatively general. Temperature changes abruptly on the first day, and there are more burrs in the waveform, but they will still closely follow the input. With the DPC-LSBoost, room temperature can be tracked well, make up for the DPC-RT's shortage, and achieve a good control effect. Under the MPC controller's action, the temperature change in the room is very smooth, and the temperature difference is small. The reference room temperature is well tracked to achieve a good control effect.

Figure 11 shows the effects of the investigated controllers with energy consumption. It can be seen that the DPC-LSBoost has the lowest energy cost.

Figure 12 shows the temperature and energy consumption of 6 rooms under the DPC-LSBoost control method. It can be found that the system will adjust the controller to varying degrees according to the state of the room. Compared with the second and sixth rooms, the first room will spend much energy stabilizing the temperature. Through this kind of fine management and control, each room's temperature can be controlled independently.

The indoor temperature changes are greatly affected by external disturbances. For the investigated residential buildings, there are a total of 44 external disturbances. Through the feature selection, the eight most relevant features are selected. Figure 13 shows the eight disturbances profiles. Three of them are the external ambient temperature (K), and five are the effects of solar radiation on various rooms in the house. The abscissa is a time interval of 15 days, a total

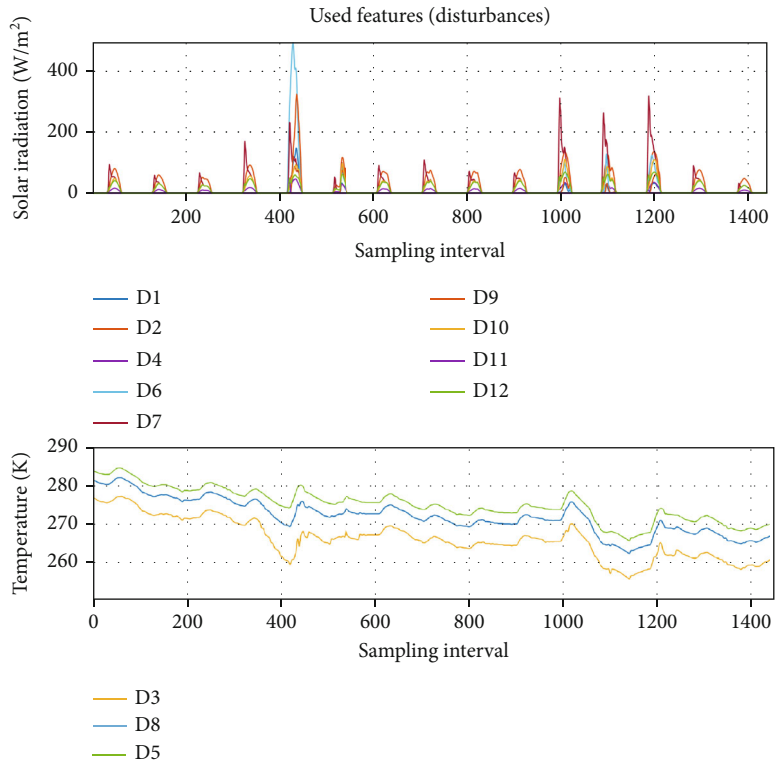

Figure 17: Selected most relevant external disturbance signals (12 signals).

Table 10: Detailed description of selected disturbance features.

Variable	Unit	Disturbance description
D1	[W/m^2]	Direct sun radiation on vertical surface with orientation 1
D2	[W/m^2]	Diffuse sun radiation on vertical surface with orientation 1
D3	[K]	Weight sun radiation temperature between ground and sky temperature 1
D4	[W/m^2]	Diffuse sun radiation on vertical surface with orientation 2
D5	[K]	Weight sun radiation temperature between ground and sky temperature 2
D6	[W/m^2]	Direct sun radiation on vertical surface orientation 3
D7	[W/m^2]	Diffuse sun radiation on vertical surface with orientation 3
D8	[K]	Weight sun radiation temperature between ground and sky temperature 3
D9	[W/m^2]	Direct sun radiation on vertical surface with orientation 4
D10	[W/m^2]	Diffuse sun radiation on vertical surface with orientation 4
D11	[W/m^2]	Direct sun radiation on vertical surface with orientation 5
D12	[W/m^2]	Diffuse sun radiation on vertical surface with orientation 6

of 1440 time samples. Table 7 describes the specific information of the eight disturbances D1-D8.

For power consumption, a holistic analysis is required. Figure 14 shows the comparison results of the total power consumption of the four controllers for 15 days. Figure 14 shows that the TDNN consumes the most energy, followed by the MPC and the RT, and the lowest energy consumption is the DPC-LSBoost. The detailed comparison results are shown in Table 8. Power consumption is analyzed from five dimensions: heating cost (kWh), cooling cost (kWh), total cost (kWh), PMV, and prediction time (s). It can be seen from the table that the overall power consumption of the DPC-LSBoost is the least, which is reduced by 78.909 kWh compared to the TDNN, and the overall energy consumption is reduced by 11.92% compared to the TDNN. With the prediction time, the DPC-LSBoost has the shortest time cost. The quantitative comparison of RMSE, *R*-square, and mean error for model accuracy is summarized in Table 9. It is observed that the DPC-LSBoost has the better model fitting capability.

5.2. Office Building Simulation Analysis. The analysis methods for office buildings and residential buildings are consistent. However, the temperature setting is between 20°C and 22°C in the office building.

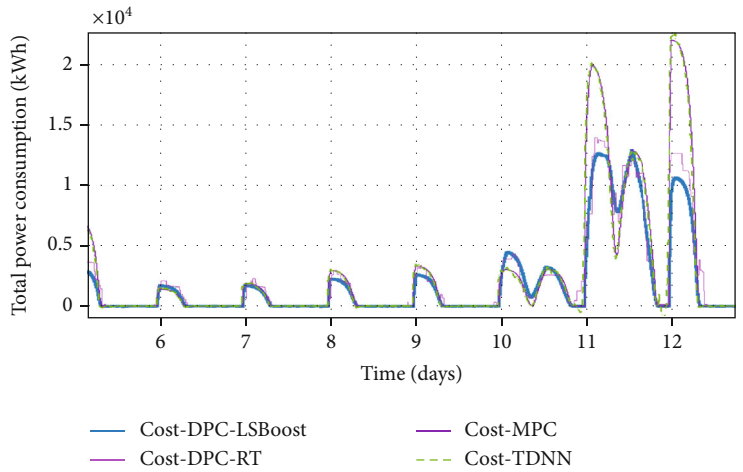

Figure 18: Comparison of the investigated controllers with respect to the total energy consumption.

Table 11: Performance comparison of multiple controllers in the office building.

Methods	Heating cost (kWh)	Cooling cost (kWh)	Total cost (kWh)	PMV viol (-)	Prediction time (s)
MPC	713.37	0.02	713.39	0	302.2
TDN	728.31	12.58	740.8	0	9.2
DPC-RT	582.86	0.0	582.87	0	8.7
DPC-LSBoost	514.2	1.41	515.61	0	7.5

Similar to residential buildings, the TDNN, the MPC, the DPC-RT, and the DPC-LSBoost methods are used for comparative simulation verification. We chose ROOM9 as the control object. The 15-day comparison results are shown in Figures 15and 16.

Figure 15 shows the room temperature controlled by all control strategies. The tracking effect is not desirable from the results, although they are all within the comfort zone. Figure 16 shows the energy consumption comparison of the four control methods. It is also found that the daily energy consumption of the MPC and the TDNN is relatively high, but the temperature change is not large, and even there is a certain energy loss due to the DPC-RT algorithm's single tree structure, which contributes to the control satisfaction violation. The DPC-LSBoost controller consumes the lowest daily energy and makes the room temperature more stable with little fluctuation.

The indoor temperature change shown in Figure 3, which is greatly affected by external disturbances. The 12 most relevant features are selected from 301 external disturbances by *FS* for the investigated office buildings. Figure 17 below shows the 12 perturbed features. Three of them are outside ambient temperature (K), and there are 9 solar radiation effects on each room. Table 10 gives detailed information on the 12 interferences D1-D12.

Table 12: Performance comparison of RMSE, *R*-square, and mean error for the RT and the LSBoost in the office building.

	RMSE	*R*-square	Mean error
DPC-RT	0.9877	93.68%	17.8487
DPC-LSBoost	0.0328	99.99%	0.8229

Figure 18 shows the total power consumption with the investigated controllers. The TDNN and the MPC almost have similar control profiles with a higher peak value of the curve, especially from the tenth day, the power consumption began to soar, and the power consumption reached its peak in 12 days. Table 11 shows the comparative analysis of the control energy consumption and predicted time of the four controllers. It is found that the TDNN has the highest energy consumption, which is as high as 740.89 kWh. Compared with the TDNN, both the DPC-RT and the DPC-LSBoost are reduced significantly, which are 582.87 kWh and 515.61 kWh, respectively. It can be seen from the table that the overall power consumption of the DPC-LSBoost is the least, which is 225.28 kWh reduced compared to the TDNN, and the overall energy consumption is reduced by 30.4% compared to the TDNN. From the 15-day simulation test, the DPC-LSBoost takes the shortest prediction time comparing with other algorithms.

The quantitative comparison with three indicates (RMSE, *R*-square, and mean error) is demonstrated in Table 12. The same conclusion is achieved that the LSBoost has the better model fitting capability.

6. Conclusion and Prospect

This paper reports an innovative study combining the data-driven predictive control strategy with a complex cloud SCADA-based building energy management platform, which attempts to standardize communication protocols and data formats and further implement advanced control strategies. The platform also provides useful data representations to

different stakeholders (end-user, building energy manager, and/or operator), enabling the platform flexibility and scalability.

We present two algorithms, based on RT and LSBoost, to create control-oriented models for the DPC. Moreover, an efficient feature selection method, which depends on the principal component analysis and the importance of disturbance variables, is leveraged to decrease the model's dimension and further alleviate the DPC optimization problem's complexity. We then apply the DPC to two different case studies for energy consumption in residential and office buildings. The numerical simulation shows that the DPC-LSBoost provides lower energy consumption while maintaining the required thermal comfort compared to the MPC, the TDNN, and the DPC-RT. With the same environmental comfort demand, compared with the TDNN, the peak power consumption with the DPC- LSBoost can be reduced by 11.92% and 30.4%, even compared to the DPC-RT 4.99% and 11.54% that are achieved. These advantages make the DPC-LSBoost an attractive tool for large-scale cyber-physical energy systems to reduce energy consumption. Also, in the context of prediction time, comparing with the MPC, the prediction time of the DPC-LSBoost is reduced by 72 s and 294.7 s, respectively.

Future work will focus on the combination of IoT with DPC (IoT-DPC), which will apply to more complex buildings. IoT-DPC applications are not limited to building energy management and include critical infrastructures such as water supply networks, district heating, and cooling.

Data Availability

(1) The building data of Hollandsch Huys is shown in chapter 2 of the report from the links as https://lirias.kuleuven.be/retrieve/453505 and https://github.com/drgona/BeSim/tree/master/buildings/HollandschHuys, and (2) the building data of the residential building is in the third chapter of this paper, linked as https://www.sciencedirect.com/science/article/pii/S0306261918302903 and https://github.com/drgona/BeSim/tree/master/buildings/Reno.

Conflicts of Interest

The authors declare that they have no conflicts of interest.

Acknowledgments

This work was supported by the Key Fund of Shaanxi Province Natural Science Basic Research Program (2019LZ-06) and the Key Project of National Internet of Things Integrated Innovation and Integration (2018-470).

References

[1] M. M. Abdelrahman, S. Zhan, and A. Chong, *A three-tier architecture visual-programming platform for building-lifecycle data management*, SimAUD, Preprint, 2020.

[2] J. K. W. Wong, H. Li, and S. W. Wang, "Intelligent building research: a review," *Automation in Construction*, vol. 14, no. 1, pp. 143–159, 2005.

[3] International Energy Agency taff, *Transition to Sustainable Buildings: Strategies and Opportunities to 2050*, OECD, 2013.

[4] H. Allcott and S. Mullainathan, "Behavior and energy policy," *Science*, vol. 327, no. 5970, pp. 1204-1205, 2010.

[5] J. Drgoňa, J. Arroyo, I. C. Figueroa et al., "All you need to know about model predictive control for buildings," *Annual Reviews in Control*, 2020.

[6] F. Al-Turjman, A. Kamal, M. H. Rehmani, A. Radwan, and A.-S. K. Pathan, "The green internet of things (g-iot)," *Wireless Communications and Mobile Computing*, vol. 2019, Article ID 6059343, 2 pages, 2019.

[7] M. Amjad and F. Iradat, "An active network-based open framework for iot," *Wireless Communications and Mobile Computing*, vol. 2019, Article ID 5741708, 8 pages, 2019.

[8] J. Paek, O. Gnawali, M. A. M. Vieira, and S. Hao, "Embedded iot systems: network, platform, and software," *Mobile Information Systems*, vol. 2017, Article ID 5921523, 2 pages, 2017.

[9] G. Alce, A. Espinoza, T. Hartzell, S. Olsson, D. Samuelsson, and M. Wallergård, "Ubicompass: an iot interaction concept," *Advances in Human-Computer Interaction*, vol. 2018, 12 pages, 2018.

[10] S. Choudhury, Q. Ye, M. Dong, and Q. Zhang, "Iot big data analytics," *Wireless Communications and Mobile Computing*, vol. 2019, 2019.

[11] S. Bhardwaj, L. Jain, and S. Jain, "Cloud computing: a study of infrastructure as a service (IAAS)," *International Journal of Engineering and Information Technology*, vol. 2, no. 1, pp. 60–63, 2010.

[12] T. Dillon, C. Wu, and E. Chang, "Cloud computing: issues and challenges," in *2010 24th IEEE International Conference on Advanced Information Networking and Applications*, pp. 27–33, Perth, WA, Australia, April 2010.

[13] P. Mell and T. Grance, *The Nist Definition of Cloud Computing*, Communications of the ACM, 2011.

[14] M. del Mar Castilla, J. D. Álvarez, F. Rodrguez, and M. Berenguel, *Comfort control in buildings, chapter 4*, Springer, Berlin, Germany, 2014.

[15] D. Gyalistras, M. Gwerder, F. Oldewurtle, C. Jones, and M. Morari, "Analysis of energy savings potentials for integrated room automation," in *Clima-RHEVA World Congress*, number CONF, 2010.

[16] K. W. Roth, D. Westphalen, J. Dieckmann, S. D. Hamilton, and W. Goetzler, *Energy Consumption Characteristics of Commercial Building Hvac Systems Volume III: Energy Savings Potential*, US Department of Energy, 2002.

[17] C. Aghemo, J. Virgone, G. V. Fracastoro et al., "Management and monitoring of public buildings through ict based systems: control rules for energy saving with lighting and hvac services," *Frontiers of Architectural Research*, vol. 2, no. 2, pp. 147–161, 2013.

[18] J. Drgoňa, D. Picard, M. Kvasnica, and L. Helsen, "Approximate model predictive building control via machine learning," *Applied Energy*, vol. 218, pp. 199–216, 2018.

[19] H. E. Mechri, A. Capozzoli, and V. Corrado, "Use of the anova approach for sensitive building energy design," *Applied Energy*, vol. 87, no. 10, pp. 3073–3083, 2010.

[20] Y. Ma, F. Borrelli, B. Hencey, B. Coffey, S. Bengea, and P. Haves, "Model predictive control for the operation of building cooling systems," *IEEE Transactions on Control Systems Technology*, vol. 20, no. 3, pp. 796–803, 2011.

[21] F. Oldewurtel, A. Parisio, C. N. Jones et al., "Use of model predictive control and weather forecasts for energy efficient building climate control," *Energy and Buildings*, vol. 45, pp. 15–27, 2012.

[22] F. Oldewurtel, A. Parisio, C. N. Jones et al., "Energy efficient building climate control using stochastic model predictive control and weather predictions," in *Proceedings of the 2010 American Control Conference*, pp. 5100–5105, Baltimore, MD, USA, June-July 2010.

[23] J. Široký, F. Oldewurtel, J. Cigler, and S. Prívara, "Experimental analysis of model predictive control for an energy efficient building heating system," *Applied Energy*, vol. 88, no. 9, pp. 3079–3087, 2011.

[24] Z. Váňa, J. Cigler, J. Široký, E. Žáčeková, and L. Ferkl, "Model-based energy efficient control applied to an office building," *Journal of Process Control*, vol. 24, no. 6, pp. 790–797, 2014.

[25] A. Jain, M. Behl, and R. Mangharam, "Data predictive control for building energy management," in *2017 American Control Conference (ACC)*, pp. 44–49, Seattle, WA, USA, May 2017.

[26] J. R. New, J. Sanyal, M. Bhandari, and S. Shrestha, "Autotune e + building energy models," *Proceedings of SimBuild*, vol. 5, no. 1, pp. 270–278, 2012.

[27] A. Afram, F. Janabi-Sharifi, A. S. Fung, and K. Raahemifar, "Artificial neural network (ann) based model predictive control (mpc) and optimization of hvac systems: a state of the art review and case study of a residential hvac system," *Energy and Buildings*, vol. 141, pp. 96–113, 2017.

[28] M. Macarulla, M. Casals, N. Forcada, and M. Gangolells, "Implementation of predictive control in a commercial building energy management system using neural networks," *Energy and Buildings*, vol. 151, pp. 511–519, 2017.

[29] P. M. Ferreira, A. E. Ruano, S. Silva, and E. Z. E. Conceicao, "Neural networks based predictive control for thermal comfort and energy savings in public buildings," *Energy and Buildings*, vol. 55, pp. 238–251, 2012.

[30] A. Jain, R. Mangharam, and M. Behl, "Data predictive control for peak power reduction," in *BuildSys '16: Proceedings of the 3rd ACM International Conference on Systems for Energy-Efficient Built Environments*, pp. 109–118, New York, NY, USA, November 2016.

[31] F. Smarra, A. Jain, T. de Rubeis, D. Ambrosini, A. D'Innocenzo, and R. Mangharam, "Data-driven model predictive control using random forests for building energy optimization and climate control," *Applied Energy*, vol. 226, pp. 1252–1272, 2018.

[32] J. Drgoňa, D. Picard, and L. Helsen, "Cloud-based implementation of white-box model predictive control for a geotabs office building: a field test demonstration," *Journal of Process Control*, vol. 88, pp. 63–77, 2020.

[33] T. Yang, D. Clements-Croome, and M. Marson, "Building energy management systems," *Encyclopedia of Sustainable Technologies*, vol. 36, pp. 291–309, 2017.

[34] P. Radecki and B. Hencey, "Online building thermal parameter estimation via unscented kalman filtering," in *2012 American Control Conference (ACC)*, pp. 3056–3062, Montreal, QC, Canada, June 2012.

[35] D. Picard, F. Jorissen, and L. Helsen, "Methodology for obtaining linear state space building energy simulation models," in *Proceedings of the 11th International Modelica Conference*, Versailles, France, September 2015.

[36] E. Van Kenhove, J. Laverge, W. Boydens, and A. Janssens, "Design optimization of a geotabs office building," *Energy Procedia*, vol. 78, pp. 2989–2994, 2015.

[37] D. Picard and L. Helsen, *Report on the Building Energy Simulation Models of an Office Building, a Retirement Home, a School, and a Block of Flats*, KU Leuven, 2017.

[38] B. W. Olesen and K. C. Parsons, "Introduction to thermal comfort standards and to the proposed new version of en iso 7730," *Energy and Buildings*, vol. 34, no. 6, pp. 537–548, 2002.

[39] G. L. Lei, Y. C. Yu, Z. P. Liu, and X. M. Liu, "Human comfort index forecast of Nanchang," *Jiangxi Meteorological Science & Technology*, vol. 22, no. 2, pp. 40-41, 1999.

[40] F. Song, Z. Guo, and D. Mei, "Feature selection using principal component analysis," in *2010 International Conference on System Science, Engineering Design and Manufacturing Informatization*, pp. 27–30, Yichang, China, November 2010.

Hindawi
Wireless Communications and Mobile Computing
Volume 2020, Article ID 8856459, 13 pages
https://doi.org/10.1155/2020/8856459

Research Article

SIR Meta Distribution in the Heterogeneous and Hybrid Networks

Yuhong Sun, Qinghai Liu, and Hua Wang

School of Computer Science, Qufu Normal University, Rizhao, Shandong 276826, China

Correspondence should be addressed to Yuhong Sun; sun_yuh@163.com

Received 7 June 2020; Revised 16 October 2020; Accepted 11 November 2020; Published 2 December 2020

Academic Editor: Chaoyun Song

With the development of the technology, the wireless systems are becoming more heterogeneous with the introduction of various power nodes including femtocells, relays, or distributed antennas. Among the research of wireless network performance, the meta distribution of the signal-to-interference ratio (SIR) has attracted significant attention. Compared to the standard success (coverage) probability, the meta distribution provides much more fine-grained information about the network performance. In this paper, we analyze the meta distribution of the SIR in the multi-tier heterogeneous and hybrid networks, where each tier is based on a homogeneous independent Poisson point process model. For the open tiers (the users can associate with any tier) and the closed tiers (the users can only associate with a certain tier), we study the bth moment of the conditional success probability for the typical user and give the beta approximation of the meta distribution from analysis and simulations. Furthermore, we analyze the per-link rate control for open tiers and closed tiers, which answers the question: "how to set the SIR threshold to meet a target reliability?". We give the approximate value of the SIR threshold to meet a target reliability and show how the value is related to the path loss exponent and densities.

1. Introduction

1.1. Motivation. The developing technology makes the wireless communication influence more and more on the daily life of human beings. In 5G, the objective of the wireless technology is to support three generic services with vastly heterogeneous requirements: enhanced mobile broadband (eMBB), mass machine-type communications (mMTC), and ultra-reliable and low latency communications (URLLC). Under such a background, the structure of the network is becoming more and more heterogeneous. Meanwhile, direct communication between mobile devices can save transmit power and help utilize the network resources more efficiently, such as the device-to-device (D2D), machine-to-machine (M2M), and vehicle-to-vehicle (V2V), which makes the network more hybrid. A modern wireless network usually consists of some open tiers of nodes that can be accessed by users through its association rule, such as the heterogeneous cellular networks (HCNs), and some closed tiers that users are served only by partial tiers, such as some direct communications. More heterogeneous and hybrid is becoming one of the characteristics of the future wireless networks. In this paper, a heterogeneous network with the direct communications is called a het-hybrid network.

The conventional SIR analysis or the mean success probability provides limited information about the network performance [1]. It is defined as the complementary cumulative distribution function (CCDF) of the SIR evaluated at the typical link. Such a performance metric is merely a macroscopic quantity by averaging the conditional success probability (CSP) $P_s(\theta) \triangleq \mathbb{P}(\mathrm{SIR} > \theta \mid \Phi)$ over the underlying point process Φ. Hence, it provides no information about the difference between links. It cannot answer such questions as "How are the link reliability distributed among users in different tiers ?" or "What is the reliability level that the '5% user' can achieve in each tier?". To obtain a fine-grained information on the SIR performance, the notion of meta distribution, as the distribution of CSP was introduced in [2]. The concept characterizes the distribution of the CSP of the individual links given the point process and is widely researched in many network scenarios, such as the cellular networks [3–5], the HCNs [6–9], the millimeter wave networks [10, 11],

the large-scale non-orthogonal multiple access (NOMA) networks [12], the dual-hop Internet-of-Things (IoT) networks [13], and the ultra-dense networks [14].

In this paper, we mainly investigate the SIR meta distribution in the het-hybrid networks that consist of open tiers and closed tiers, to get a fine-grained analysis on the success transmission probability and analyze the rate control based on the SIR meta distribution.

1.2. Related Work. The meta distribution of the SIR has been applied to different scenarios since it was formally formulated in [2]. For instance, [3] focused on the SIR meta distribution in cellular networks with fractional power control. Some bounds, the analytical expression, the mean local delay, and the beta approximation of the meta distribution were provided. Recently, the joint meta distribution of the SIR at different locations and its applications to physical layer security and cooperative reception were studied in [4]. And for moving networks, the SIR meta distribution was researched in [5], which demonstrated that the moving BSs can reduce the variance of users while keeping the mean success probability constant.

The SIR meta distribution of k-tier downlink HCNs with cell range expansion was researched in [6], where the bth moments of the CSP for each tier and for the entire network were derived, and the metrics including the mean success probability, the variance of the CSP, the mean local delay, and the asymptotic SIR gains of each tier were also obtained. The SIR meta distribution in HCNs with base station cooperation was researched in [7], where the meta distribution in HCNs with downlink coordinated multipoint transmission/-reception (CoMP) was derived. For the HetNet, [8] derived the meta distribution of the downlink SIR in a Poisson cluster process-based model. And for the general cellular networks, [9] provided the AMAPPP (approximate meta distribution analysis using PPP) in the SIR meta distribution analysis to obtain the meta distribution of an arbitrary stationary and ergodic point process from the meta distribution of the Poisson point process (PPP).

The meta distribution of the SINR and the data rate for millimeter wave (mm-wave) D2D networks were derived in [10], where the approximation by using higher moments of the conditional SINR distribution was also proved to be effective. Using stochastic geometry tools, [11] analyzed the meta distributions of the downlink SIR/SNR and data rate of the typical device in a cellular network with coexisting sub-6GHz and mm-wave spectrums. The meta distribution and moments of the conditional success probability (CSP) in large-scale NOMA networks were studied in [12], where a tractable framework was developed to analyze both the uplink NOMA and downlink NOMA. The meta distribution of the downlink SIR attained at a typical device in a dual-hop IoT network was characterized in [13], where the IoT device associates with either a serving macro base station for direct transmissions or associates with a decode and forward relay for dual-hop transmissions. For ultra-dense networks, [14] studied the meta distributions of SIR in a near-optimally short, perfect, Euclidean distance edge-weighted, bipartite matching between two binomial point processes, to obtain a bipartite Euclidean matching and investigate the reliability of communication. For the SIR meta distribution of D2D communication underlaying cellular wireless networks, [15] derived the moments of the conditional SIR distribution to calculate analytical expressions and the mean local delay of the typical receiver.

Another important application of the SIR meta distribution or the rate control was considered in [16]. From [16], the per-link reliability and rate control were proved to be the two facets of the SIR meta distribution.

The work mentioned above considered the SIR meta distribution either in a single tier or a hybrid network, or in a heterogeneous network with only open tiers. The SIR meta distribution of the multi-tier heterogeneous network with hybrid structure has not been covered yet.

1.3. Contributions. In this paper, we focus on the heterogeneous and hybrid network that consists of open tiers and closed tiers and analyze the SIR meta distribution under Rayleigh fading to provide a fine-grained analysis on the network performance. Specifically,

(i) We derive the bth moments of the CSP for both the open tiers and the closed tiers. We find the open tiers and closed tiers make different effects on the bth moment of open tiers, while they impact the bth moment of the closed tiers in the same way.

(ii) We give the beta approximation for the SIR meta distribution by matching the first and second moments of CSP for the open tiers and closed tiers. The simulations show that the beta distribution is an effective approximation in the het-hybrid networks.

(iii) We analyze the mean local delay for the users of open tiers in a het-hybrid network based on the b th moments of the CSP.

(iv) We study the rate control by setting the SIR threshold to meet a target reliability and derive the approximate values of SIR threshold for open tiers and closed tiers. We find that the path loss exponent affects the SIR threshold settings differently in open tiers and closed tiers.

2. System Model and Method

2.1. Network Model. The het-hybrid network is modeled as a K-tier $(K \geq 1)$ wireless network where each tier consists of the transmitting nodes of a particular class. The nodes across tiers may differ in terms of the transmit power, the supported data rate, and their spatial density. We assume that the transmitting nodes of the ith tier are spatially distributed as an independent PPP Φ_i with density λ_i, and transmit power P_i. All transmitting nodes are active, and we do not consider any cooperation between the transmitters.

All tiers are classified into open tiers and closed tiers. The open tiers mean a group of (≥1) tiers of transmitting nodes that can be accessed openly by users through the association

rule, also named as open group. In this paper, we consider the downlink performance and the average strongest signal association rule in open tiers. Hence, a transmitter from any open tier can be the signal provider only if it can provide the average strongest signal. There is no need to distinguish the users of each open tier, since they can connect to the arbitrary tier of the open group. The corresponding users of the open tiers are called open users and are assumed to be distributed as an independent PPP.

Each closed tier means a single tier of transmitting nodes. The corresponding users can only associate with the single tier of transmitters, which seems like this tier is closed to other tiers. Moreover, each transmitter is assumed to have a dedicated receiver located at a fixed distance in a random direction in our assumption, such as some direct communications [15, 17]. In such cases, the transmitters and receivers of the closed tier form a Poisson bipolar network. Although in many bipolar networks, the transmitters are active with a probability, here, we only consider the active transmitters at a time slot, or a snapshot of the active nodes. The network can have several closed tiers at the same time, where each tier is closed to other tiers.

In the rest of the paper, we use $\Phi_B = \bigcup \Phi_{i|i\in B}$ to denote the group of open tiers, where $B \subseteq \{1, 2, \cdots K\}$, and $\Phi_{i|i\notin B}$ denote one of the closed tiers. The notation x is used to denote both the location of a transmitter and the transmitter itself, and $|x|$ is used to denote the distance between the transmitter and the origin.

2.2. SIR. Without loss of generality, we conduct analysis on the typical user located at the origin. To analyze the open tiers, we condition on that typical user to be an open user and vice versa when analyzing the closed tier. The fading between a transmitter located at point x and the typical user is denoted by h_x, which is assumed to be i.i.d. exponential (Rayleigh fading). The standard power-law path loss model is $l(r) = r^{-\alpha}$ with exponent $\alpha > 2$. For open tiers, assume the typical user is associated with x_0 in the kth $(k \in B)$ tier, and the fading is h^o_{x0}; the received SIR can be given by

$$\mathrm{SIR}_{o|k} = \frac{P_k h^o_{x0} |x_0|^{-\alpha}}{\sum_{x\in\Phi_k, x\neq x_0} P_k h_x |x|^{-\alpha} + \sum_{i\neq k} \sum_{x\in\Phi_i} P_i h_x |x|^{-\alpha}}, \quad (1)$$

where the numerator is the desired signal and the denominator is the aggregate interference suffered by the user.

Similarly, the SIR received by the typical closed user of tier $j(j \notin B)$ is

$$\mathrm{SIR}_{c|j} = \frac{P_k h^c_{x0} d_j^{-\alpha}}{\sum_{x\in\Phi_j, x\neq x_0} P_j h_x |x|^{-\alpha} + \sum_{i\neq j} \sum_{x\in\Phi_i} P_i h_x |x|^{-\alpha}}, \quad (2)$$

where d_j is the fixed distance between the jth tier transmitters and their receivers, and h^c_{x0} is the fading.

The difference between the open tiers and the closed tiers lies in the association rule, besides the open tiers usually being a group of tiers while each closed tier being a single tier. Since the average strongest association rule in open tiers, node x_0 of the kth tier in fact is the signal provider with a certain probability (equation (6)). Other node in Φ_B can also be the potential signal provider. That means the serving power and the serving distance are not certain until the link is established. Even when the open group has only one tier, the serving distance is uncertain due to the Poisson distribution of nodes. While in a closed tier, the user is definitely served by the transmitter with a certain power and the determined serving distance.

2.3. The Meta Distribution. The SIR meta distribution of the typical user for a threshold θ and a reliability ν is given as follows:

$$\bar{F}(\theta, \nu) = \bar{F}_{P_s}(\theta, \nu) \triangleq \mathbb{P}(P_s(\theta) > \nu), \theta \in R^+, \nu \in [0, 1], \quad (3)$$

where $P_s(\theta)$ is a random variable that represents the link success probability conditioned on the point process $\bigcup_{(i\in\{1\ldots K\})} \Phi_i$. It can be given by

$$P_s(\theta) \triangleq \mathbb{P}\left(\mathrm{SIR} > \theta \mid \bigcup_{i\in\{1\cdots K\}} \Phi_{\mathrm{i}}\right), \quad (4)$$

where the probability is taken with respect to the fading. The meta distribution is the CCDF of the conditional link success probability $P_s(\theta)$.

The standard success (coverage) probability $p_s(\theta)$ (the SIR distribution) can be obtained from the SIR meta distribution as the mean of the conditional success probability $P_s(\theta)$, i.e., $p_s(\theta) \triangleq \mathbb{P}(SIR > \theta) = \mathbb{E}(P_s(\theta)) = \int_0^1 \bar{F}(\theta, x)dx$. Clearly, the distribution of $P_s(\theta)$ provides much more fine-grained information than merely the average of $P_s(\theta)$.

The exact meta distribution can be expressed by the Gil-Pelaez theorem [18] as

$$\bar{F}(\theta, \nu) = \frac{1}{2} + \frac{1}{\pi} \int_0^\infty \frac{\mathfrak{J}\left(e^{-jt \log \nu} M_{jt}\right)}{t} dt, \quad (5)$$

where $\mathfrak{J}(z)$ denotes the imaginary parts of $z \in \mathbb{C}$, $j = \sqrt{-1}$, and M_b denotes the bth moment of $P_s(\theta)$, i.e., $M_b = E(P_s(\theta)^b)$, $b \in \mathbb{C}$.

2.4. Method. Based on the above model, we analyze the SIR meta distribution of the typical user for open tiers and closed tiers, respectively. Different from the HCNs [6], the users of the open tiers suffer more interference for the existence of closed tiers. For the similar reason, the receivers of the closed tiers also receive the interference from open tiers. We try to probe the impacts of the tiers on the SIR meta distributions of the open tiers and the closed tiers. The bth moments of the CSP are derived firstly, and then, the mean local delay or the -1st moment of the open tiers is analyzed. The numerical analysis of the SIR meta distribution is mainly approximated by the beta distribution with the first and the second moments. For the per-link rate control of the open tiers and closed tiers, the stochastic interference equivalence [19, 20] is considered to facilitate the analysis. In such a framework, the signal received by the user can be simplified as

the serving signal from a tier with density λ_S plus the interference signal from a tier with density λ_I.

For brief expression, we use δ to denote $2/\alpha$, $F_{b,\delta,\theta}$ to denote ${}_2F_1(b,-\delta;1-\delta;-\theta)$, and $\Gamma_{b,\delta}$ to denote $(\Gamma(b+\delta))/(\Gamma(b)\Gamma(1+\delta))$ in the rest of the paper.

3. The SIR Meta Distribution in the Het-Hybrid Network

3.1. The bth Moment of the CSP. In this section, we firstly give the bth moment of the CSP for the typical user of the open tiers, and then the bth moment for a closed tier.

For the open tiers, the desired signal received by the typical user is possibly from any transmitter in Φ_B. Assume that the provider of the desired signal x_0 is from the kth ($k\in$ B) tier, and the distance is R_0; the access probability that the typical user is associated with the kth tier is

$$P_{a^-R_0}^{(k)} = \prod_{\Phi_{j\mid j\in B, j\neq k}} \exp\left(-\pi\lambda_j\left(\frac{P_j}{P_k}\right)^{\delta} {R_0}^2\right). \tag{6}$$

It can be found in Lemma 5 of [6]. By considering the conditional access probability in (6), the bth moment of the CSP for the open tiers can be easily obtained.

Theorem 1. *For the typical open user served by the kth tier in a het-hybrid network, the bth moment of the conditional success probability is given by*

$$M_{b,(k)}^{open} = \frac{1}{\sum_{\Phi_{i\mid i\in B}}(\lambda_i/\lambda_k)(P_i/P_k)^{\delta}F_{b,\delta,\theta} + \sum_{\Phi_{j\mid j\notin B}}(\lambda_j/\lambda_k)(P_j/P_k)^{\delta}\theta^{\delta}(\pi\delta/(\sin(\pi\delta)))\Gamma_{b,\delta}}. \tag{7}$$

Proof. See Appendix A.

Since the open group consists of several tiers, the bth moment of the typical user CSP for the overall open tiers is given by

$$\mathrm{M}_b^{\mathrm{open}} = \sum_{k\in B}\frac{1}{\sum_{\Phi_{i\mid i\in B}}(\lambda_i/\lambda_k)(P_i/P_k)^{\delta}F_{b,\delta,\theta} + \sum_{\Phi_{j\mid j\notin B}}(\lambda_j/\lambda_k)(P_j/P_k)^{\delta}\theta^{\delta}(\pi\delta/\sin(\pi\delta))\Gamma_{b,\delta}}. \tag{8}$$

Remark 2. From (7), the closed tiers affect the bth moment of the open tiers by $\sum_{\Phi_{j\mid j\notin B}}(\lambda_j/\lambda_k)(P_j/P_k)^{\delta}\theta^{\delta}(\pi\delta/\sin(\pi\delta))\Gamma_{b,\delta}$ as a term of the denominator. It is different from that of the open tiers $\sum_{\Phi_{i\mid i\in B}}(\lambda_i/\lambda_k)(P_i/P_k)^{\delta}F_{b,\delta,\theta}$, due to their different association rules. When there is no closed tier or $\Phi_B = \bigcup_{i\in\{1..K\}}\Phi_i$, the bth moment of CSP for the kth tier user can be simplified as

$$M_{b,k} = \frac{1}{\sum_{i=1}^{K}(\lambda_j/\lambda_k)(P_j/P_k)^{\delta}F_{b,\delta,\theta}}, \tag{9}$$

and the bth moment of the CSP for the overall network is

$$M_b = \frac{1}{F_{b,\delta,\theta}}. \tag{10}$$

It just describes the bth moment of the CSP for the typical user of HCNs without any range expansion [6].

For the bth moment of the CSP of the typical closed user, we have the following theorem.

Theorem 3. *The typical closed user of jth tier with the distance d_j in a het-hybrid network has the bth moment of the CSP as*

$$M_{b,(j)}^{closed} = \exp\left(-\pi\theta^{\delta}d_j^2(\pi\delta/\sin(\pi\delta)).\Gamma_{b,\delta}\sum_{i=1}^{K}\lambda_i(P_i/P_k)^{\delta}\right). \tag{11}$$

Proof. See Appendix B.

Remark 4. From Theorem 3, we can see there is no difference among the tiers that affect the bth moment of the closed tier. Adding more tiers or increasing any tier density, whether for an open tier or a closed tier, will only reduce the bth moment. The quantity is also an exponential function of the square of distance d_j.

3.2. Mean Local Delay. Based on the bth moment of the SIR, we further consider the mean local delay which is defined as the mean number of transmission attempts waiting for a packet successfully decoded over a wireless link [2, 15]. Generally, the mean local delay is the -1st moment of the CSP, i.e. M_{-1}. But we find that M_{-1} cannot be derived directly from (7) because the $\Gamma_{b,\delta}$ is not defined when $b=-1$. Fortunately, the distribution of the conditional local delay is geometric with mean M_{-1} and the local delay can be seen as the expectation of the CSP with respect to the static elements of a network [21]. Based on this idea, we derive the mean local delay for the typical user of the open tiers as

$$M_{-1,(k)}^{\mathrm{open}} = \sum_{\Phi_{i\mid i\in B}}\left(\frac{\lambda_i}{\lambda_k}\right)\left(\frac{P_i}{P_k}\right)^{\delta}F_{1,\delta,\theta} + \sum_{\Phi_{j\mid j\notin B}}\left(\frac{\lambda_j}{\lambda_k}\right)\left(\frac{P_j}{P_k}\right)^{\delta}\theta^{\delta}\frac{\pi\delta}{\sin(\pi\delta)}, \tag{12}$$

for $\Gamma_{1,\delta}=1$.

Specially, if there is no closed tier, the mean local delay for the typical user can be derived from (7):

$$M_{-1,k} = \frac{1-\delta}{\sum_{j=1}^{K}(\lambda_j/\lambda_k)(P_j/P_k)^{\delta}(1-\delta(1+\theta))}, \tag{13}$$

for ${}_2\mathrm{F}_1(-1,b;c;z)\equiv 1-bz/c$.

The mean local delay is only related to the path loss exponent α and the SIR threshold θ in a single tier Poisson network [2]. But in a multi-tier network, the mean local delay is also related to the ratio of density and power of each tier, as (13). It can be seen that the mean local delay is finite when $\theta < (1/\delta)-1$ from (13). Conversely, if $\theta \geq (1/\delta)-1$, the mean local delay is infinite due to the correlated interference

in the system. The value of $\theta = (1/\delta) - 1$ is called the critical value for phase transition.

For the same reason, the -1st moment of the closed tier cannot be obtained from (11) directly. In our assumed model, there is no transmission waiting in the closed tier, because all transmitters are active and each transmitter has a dedicated receiver. Otherwise, the local delay may be infinite if there are more receivers, unless the transmit probability is less than 1 [2], which has been discussed in [15].

3.3. Beta Approximation. Even though the expression of the meta distribution in (5) is exact, it is hard to gain direct insights due to its complexity, and it is not very convenient to evaluate numerically. Fortunately, the beta distribution can be taken as an approximation to analyze the meta distribution.

Beta distribution, as a conjugate prior distribution of the Bernoulli distribution and the binomial distribution, is a natural choice to approximate the distribution of the $P_s(\theta)$. It has been verified that the standard beta distribution can provide an efficient approximation by matching the first and the second moments of the CSP [2, 3, 6, 7, 9, 10, 15, 22]. Specifically,

$$\bar{F}(\theta, \nu) \approx 1 - I_\nu\left(\frac{\beta M_1}{1 - M_1}, \beta\right), \nu \in [0, 1], \tag{14}$$

where $\beta = ((M_1 - M_2)(1 - M_1))/(M_2 - M_1^2)$, and I_ν is the regularized incomplete beta function.

It is worth noting that recently, as shown in [23], the meta distribution can also be directly obtained from the moments by a simple linear transform, which is a more convenient way for efficient calculations. And [24] showed that the entire meta distribution can be reconstructed from its moments using the Fourier-Jacobi expansion.

3.4. Per-Link Rate Control. Another important application of the SIR meta distribution is the rate control. It has been proved in [16] that the SIR meta distribution as a function of the SIR threshold is equivalent to the SIR threshold distribution such that each link is guaranteed a target reliability. For the Poisson bipolar networks, [16] studied the rate control and revealed the trade-off between the SIR threshold (equivalently, the distribution of the transmission rate) and the reliability. In our network model, we also consider the per-link rate control based on the SIR meta distribution. The problem to be solved in this section is "how to set the SIR threshold θ, i.e., the rate control, such that the link can achieve exactly the target reliability ν?".

Firstly, the mean CSP over the fading and the point processes is just the first moment M_1. For the typical link of the k th tier in the open group, the value of the SIR threshold is the solution of θ:

$$\frac{1}{\sum_{\Phi_{i|i\in B}}(\lambda_i/\lambda_k)(P_i/P_k)^\delta F_{1,\delta,\theta} + \sum_{\Phi_{j|j\notin B}}(\lambda_j/\lambda_k)(P_j/P_k)^\delta \theta^\delta (\pi\delta/\sin(\pi\delta))} = \nu, \tag{15}$$

where ν is the target reliability. It is difficult to express θ in an exact closed form. Here, we give an approximate value of θ based on two lemmas.

Lemma 5. *For a Poisson point process Ψ, let r_i denote the distance from node $x_i \in \Psi$, $i = 0, 1, \cdots n$ to the origin, and $r_0 = \min\{r_i\}$; then, the mean of the sum of the r_0/r_i satisfies $\mathbb{E}[\sum_i (r_0/r_i)^\alpha] = 2/(\alpha - 2)$.*

Proof. The $\{r_0/r_i\}_{i=1\cdots n}$ constitutes a relative distance process (RDP), see Definition 2 in [25].

Lemma 6. *For a Poisson point process Ψ, if the distance from the node $x_i \in \Psi$, $i = 0, 1, \cdots n$ to the origin is r_i, and $r_0, r_1, \cdots r_n$ are in ascending order, then $\mathbb{E}(\sum_{i=0}^n r_i^{-\alpha}) = (\lambda\pi)^{\alpha/2}\Gamma(n - (\alpha/2))/\Gamma(n))$.*

Proof. It is derived from the probability density function of r_i in a PPP as [26]:

$$f_{r_i}(X) = \exp\left(-\lambda\pi X^2\right).\frac{2\left(\lambda\pi \mathrm{X}^2\right)^{\mathrm{i}}}{X\Gamma(\mathrm{i})}. \tag{16}$$

Theorem 7. *Given the reliability ν, the SIR threshold of the typical open user connecting to the kth ($k \in B$) tier can be approximated as*

$$\theta \approx \frac{\log(1/\nu)}{(2/(\alpha - 2)\alpha - 2) + \Gamma(1 + (\alpha/2))((\lambda_I/\lambda_s))^{\alpha/2}}, \tag{17}$$

where $\lambda_S = \sum_{\Phi_{i|i\in B}}\lambda_i(P_i/P_k)^\delta$ and $\lambda_I = \sum_{\Phi_{j|j\notin B}}\lambda_j(P_j/P_k)^\delta$ are called service density and interference density, respectively.

Proof. See Appendix C.

Remark 8. From (17), it can be seen that the approximate SIR threshold is related to both the service density and the interference density. Since the serving node can be anyone of the open tiers, the service density is the combined density of all the open tiers as $\lambda_S = \sum_{\Phi_{i|i\in B}}\lambda_i(P_i/P_k)^\delta$. The interference density means that the density of nodes acting only as interference. For the open user, the densities of the closed tiers are combined as the interference density, which is expressed as $\lambda_I = \sum_{\Phi_{j|j\notin B}}\lambda_j(P_j/P_k)^\delta$. From (17), the effect of the closed tiers on the approximate SIR threshold of open tiers is expressed as $\Gamma(1 + (\alpha/2))(\lambda_I/\lambda_s)^{\alpha/2}$ in the denominator. That is to say, the approximate SIR threshold can be maintained if the ratio of the λ_S and λ_I is constant.

A special case is that the network consists of only the open tiers, or just $B = \{1, 2, \cdots, K\}$, the value of the SIR threshold can be approximated as $\theta \approx ((\alpha - 2)\log(1/\nu))/2$, which is the SIR approximate value in a K-tier HCN.

Similarly, we can get the approximate SIR threshold for the closed link. For the closed tier (assume the jth tier), the SIR threshold can be approximated as the following theorem.

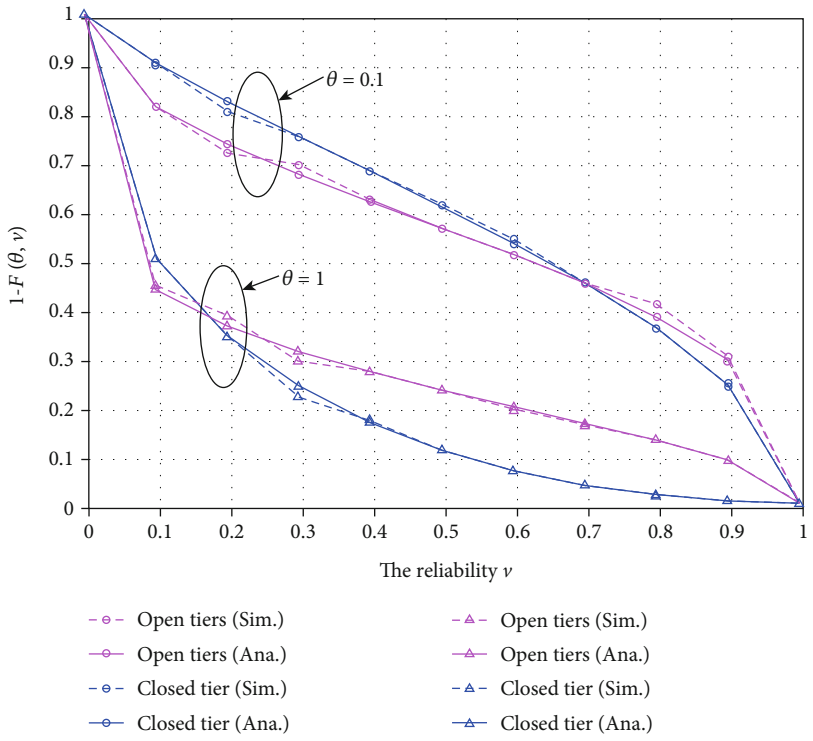

Figure 1: The CCDF of the CSP as a function of the reliability.

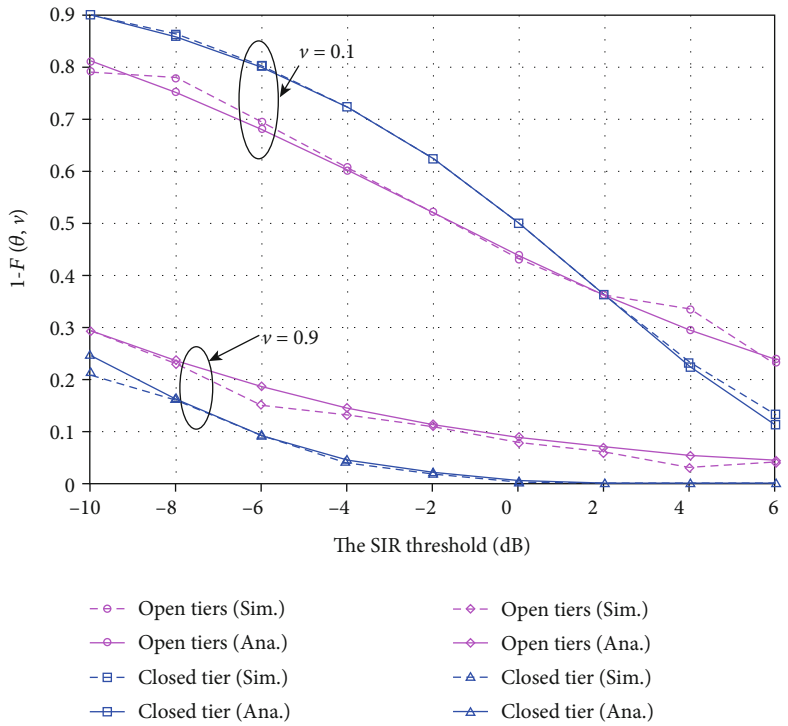

Figure 2: The CCDF of the CSP as a function of the SIR threshold.

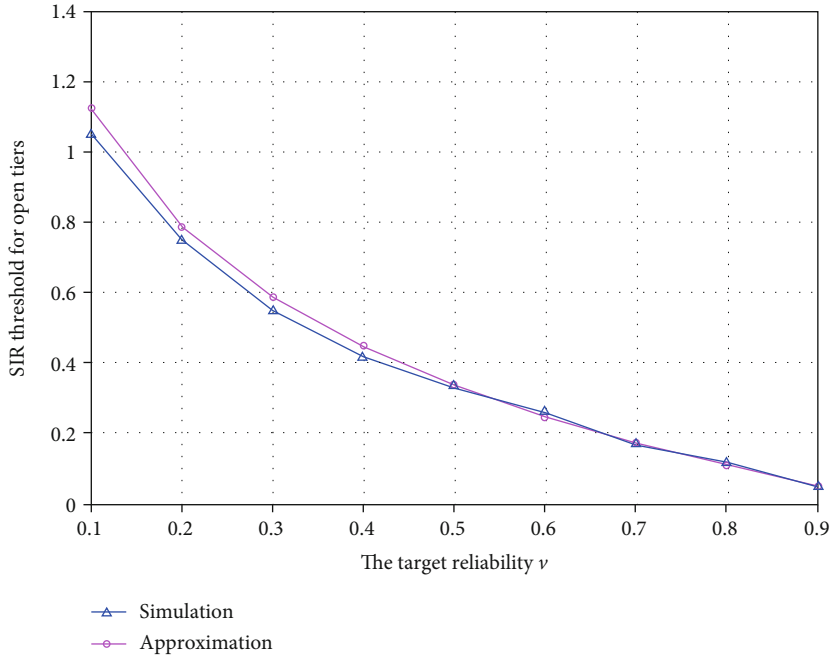

Figure 3: The SIR threshold settings for the open tiers.

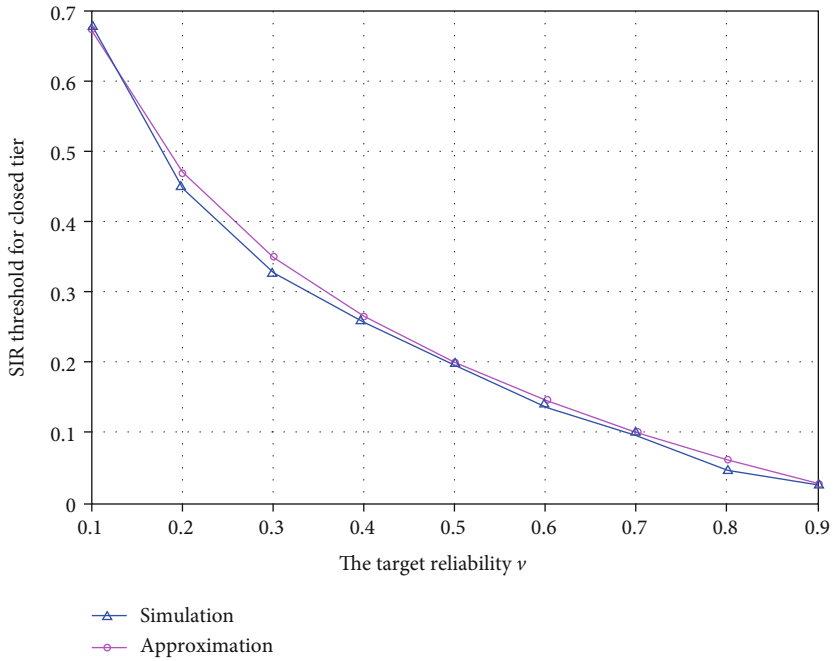

Figure 4: The SIR threshold settings for the closed tier.

Theorem 9. *Given the reliability v, the SIR threshold of the typical closed user can be approximated as*

$$\theta \approx \frac{\log(1/v)}{d_j^{\alpha}\left((\lambda_S\pi)^{\alpha/2} + (\lambda_I\pi)^{\alpha/2}\right)}, \tag{18}$$

where $\lambda_S = \lambda_j$ is the density of this closed tier, and $\lambda_I = \sum_{i\neq j} \lambda_i (P_i/P_k)^{\delta}$ is the density of interference from all other tiers.

Proof. See Appendix D.

Remark 10. For the closed user of jth tier, the signal provider is the only transmitter in a fixed distance d_j with a random orientation. It is obvious that the increase of d_j may lead to a lower SIR threshold setting. Besides the distance, we can see from (18) that the approximate value is inversely proportional to densities by $(\lambda_S\pi)^{\alpha/2} + (\lambda_I\pi)^{\alpha/2}$. That means densities of the open tiers and the closed tiers affect the SIR

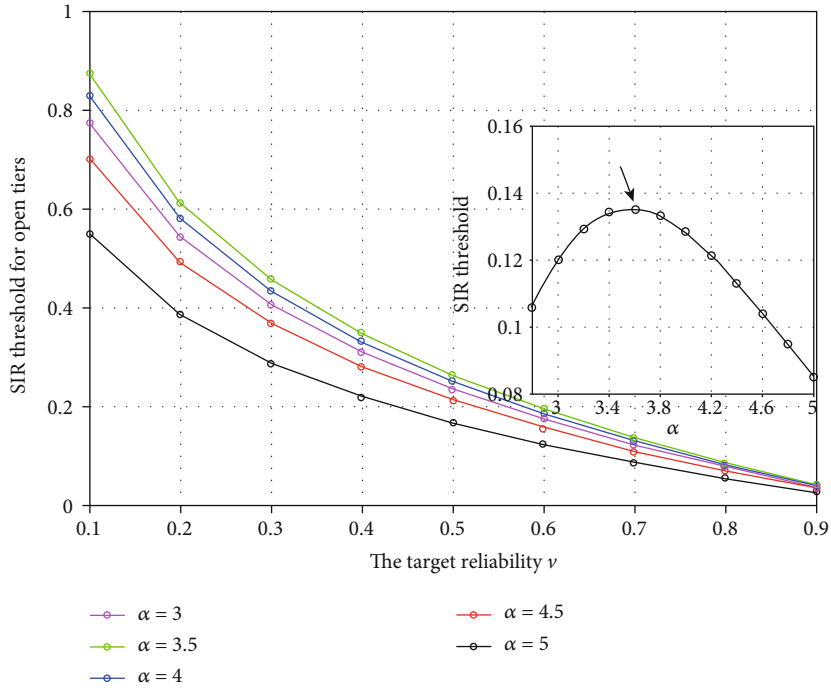

Figure 5: The SIR threshold settings for open tiers follow with the path loss exponent.

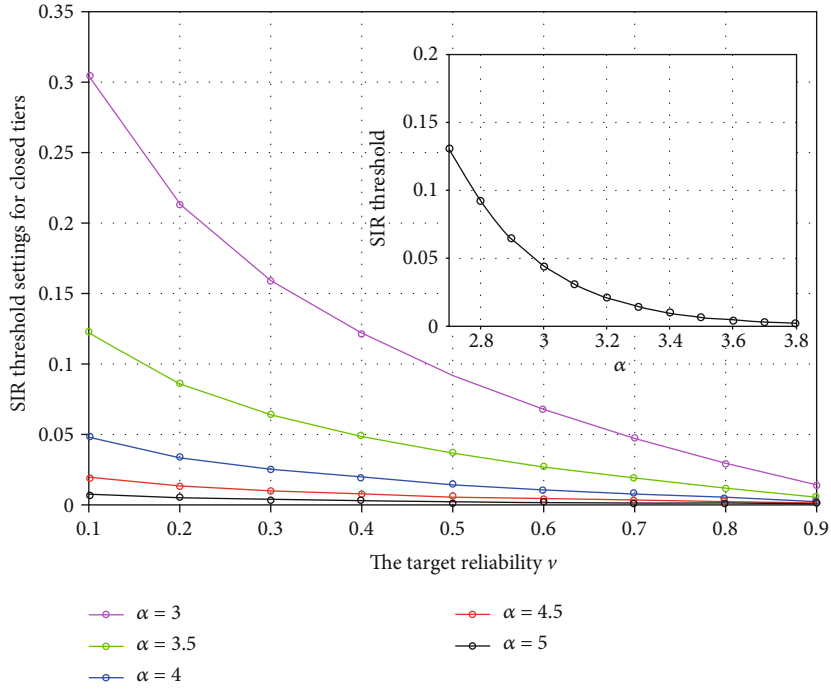

Figure 6: The SIR threshold settings for a closed-2 tier follow with the path loss exponent.

threshold in the same way. The reason lies in that all the other nodes of the same tier and all the other tiers are interference definitely. It is different from that in the open tiers; any transmitter can be the serving node with a probability. Consequently, the increase of any node in the interference tier or the serving tier will only cause a lower SIR threshold.

4. Results and Discussion

In this section, we will present the simulation results of the SIR meta distribution, or the distribution of the CSP ($P_s(\theta)$), and the per-link rate control for open tiers and closed tiers in the model mentioned above. The platform we used is MATLAB, and the distributed range of transmitters is $[0,100] \times [0,100]$.

The het-hybrid network consists of 3 tiers, named tier-1, tier-2, and tier-3, where tier-1 and tier-2 form the group of open tiers, and tier-3 is a closed tier. The corresponding transmitters densities are set as $\lambda_1 = 0.01$, $\lambda_2 = 0.02$, and $\lambda_3 = 0.05$, and the transmitting power is set as $P_1 = 10$, $P_2 = 5$, and $P_3 = 3$, respectively. The fading is distributed as exponential random variables with mean 1, and the path loss exponent α is 4 in our assumption. The density of open users is set as 0.05, and the distance from the transmitter to the dedicated user is set as 10 in the closed tier. We repeat 300 transmissions to calculate the success transmission probability and the reliability.

Firstly, the results of the SIR meta distribution for the open tiers and the closed tier are shown in Figures 1 and 2. The numerical results approximated by beta distribution based on the bth moments are also shown in the two figures. For open users, we show the performance for the overall open tiers. Figure 1 is the SIR meta distribution as a function of reliability ν with the given SIR thresholds $\theta = 1$ and $\theta = 0.1$. Figure 2 is the SIR meta distribution as a function of the SIR threshold with the given reliabilities $\nu = 0.1$ and $\nu = 0.9$.

As Figures 1 and 2 illustrate, the beta distribution provides a good match for the distribution of the link success probabilities, which verifies that the approximation of beta distribution is effective in the het-hybrid network. Moreover, we can find some indications from the figures based on our settings. In Figure 1, the users of open tiers have a higher quantity of success transmission than the closed tier when the SIR threshold is set 1, but more percentage of the closed users can successfully transmit when the SIR threshold is deduced to 0.1. That means the meta distribution of the closed tier is more sensitive to the SIR threshold than that of the open tiers. A similar trend can be found in Figure 2. For the same SIR threshold, more percentage of the open users can be covered when the reliability is set a high value ($\nu = 0.9$), while with decreasing the value of ν, the closed users are easier to get a higher success probability. In other words, the meta distribution of the closed tier is also more sensitive to the reliability than that of the open tiers in our settings. The hidden reason is the difference of association rules, that the users of open tiers have more opportunities to associate with a favorable transmitter while the users of closed tier have the fixed transmitter.

For the per-link rate control, it is intuitively that the SIR threshold declines with the increasing reliability, shown in Figures 3 and 4. Figure 3 shows the SIR threshold settings for open tiers to meet the reliability. Figure 4 shows the SIR threshold settings for the closed tier. The path loss exponent α is set 4 in both figures. According to Figures 3 and 4, we can see the approximate values calculated as (17) and (18) are close to the simulations, so the SIR threshold can be set conveniently by the formulas to control the rate to meet the target reliability.

Besides the service density and interference density, we can see from (17) and (18) that the approximate value of SIR threshold is related to the path loss exponent for a target reliability. Figure 5 shows the trend of the SIR threshold following the path loss exponent for open tiers. It is noticed that the trend is not monotonous, and the SIR threshold can get a peak value when the path loss exponent $\alpha = 3.6$ or so. A lower or greater value of α leads to a lower threshold to meet the same target reliability. However, the effect of the path loss exponent in the approximate SIR threshold is different in the closed tier, as Figure 6, where the trend is monotonous and a lower α only leads to a greater SIR threshold setting.

5. Conclusions

The meta distribution is a fine-grained key performance metric of wireless systems. In this paper, we study the SIR meta distribution in the multi-tier heterogeneous and hybrid network characterized by different powers, different densities, and different association rules of each tier. At first, we derive the bth moments of conditional success probability for the users of the open tiers and the closed tiers, respectively. Based on the bth moments, we give the expressions of SIR meta distribution or the CCDF of the conditional success probability and approximate the expressions by beta distribution. The accuracy of the approximation is confirmed by simulations. Then, the mean local delay for users of the open tiers is also analyzed. Furthermore, using another facet of SIR meta distribution, we study the per-link rate control for the open tiers and closed tiers and derive the corresponding approximate value of SIR threshold to control the link rate. The simulations show that the approximate value we derived can be used effectively for setting the SIR threshold to meet the specified reliability.

Appendix

A. Proof of Theorem 1

Conditioned on the typical user associated with the transmitter x_0 of the kth tier in the open group and assume the distance from x_0 to the user is R_0, the CSP is expressed as

$$P_{s,(k)}^{\text{open}} = \mathbb{P}\left(\frac{P_k h_0 R_0^{-\alpha}}{\sum_{x\in\Phi_k, x\neq x_0} P_k h_x |x|^{-\alpha} + \sum_{i\neq k}\sum_{x\in\Phi_i} P_i h_x |x|^{-\alpha}} > \theta \middle| \bigcup \Phi_i\right). \tag{A.1}$$

By averaging over the fading, we get the conditional bth moment of the CSP, given by

$$\begin{aligned} M_{b,R_0} &= \prod_{x\in\Phi_k, x\neq x_0} \frac{1}{\left(1+\theta\left(R_0/|x|\right)^{\alpha}\right)^b} \prod_{i\neq k}\prod_{x\in\Phi_i} \frac{1}{\left(1+\theta\left(P_j/P_k\right)\left(R_0/|x|\right)^{\alpha}\right)^b} \\ &= \prod_{x\in\Phi_k, x\neq x_0} \frac{1}{\left(1+\theta\left(R_0/|x|\right)^{\alpha}\right)^b} \prod_{i\in B, i\neq k}\prod_{x\in\Phi_i} \frac{1}{\left(1+\theta\left(P_j/P_k\right)\left(R_0/|x|\right)^{\alpha}\right)^b} \\ &\quad \prod_{i\notin B}\prod_{x\in\Phi_i} \frac{1}{\left(1+\theta\left(P_j/P_k\right)\left(R_0/|x|\right)^{\alpha}\right)^b} \end{aligned} \tag{A.2}$$

The notation M_{b,R_0} is used to denote that the bth moment conditioned on R_0 and the event that the typical user

connects to the k-th tier, which occurs with the probability given in (6). Then, the bth moment of the open tiers can be expressed as

$$M_{b,(k)}^{\text{open}} = \mathbb{E}_{R_0,\Phi_{i|i\in\{1\cdots K\}}}\left[\prod_{\Phi_{i|i\in B,i\neq k}} \exp\left(-\pi\lambda_i\left(\frac{P_i}{P_k}\right)^{\delta} {R_0}^2\right) \prod_{x\in\Phi_k, x\neq x_0} \frac{1}{(1+\theta(R_0/|x|)^{\alpha})^b} \prod_{i\in B,i\neq k}\prod_{x\in\Phi_i} \frac{1}{(1+\theta(P_i/P_k)(R_0/|x|)^{\alpha})^b} \prod_{i\notin B}\prod_{x\in\Phi_i} \frac{1}{(1+\theta(P_i/P_k)(R_0/|x\,|\,)^{\alpha})^b}\right]$$

$$\overset{(a)}{=} \mathbb{E}_{R_0}\left[\prod_{\Phi_{i|i\in B,i\neq k}} \exp\left(-\pi\lambda_i\left(\frac{P_i}{P_k}\right)^{\delta} {R_0}^2\right).\exp \cdot\left(-2\pi\lambda_k\int_{R_0}^{\infty}\left(1-\frac{1}{(1+\theta(R_0/|x\,|\,)^{\alpha})^b}\right)xdx\right).$$

$$\prod_{i\in B,i\neq k}\exp\left(-2\pi\lambda_i\int_{r_i}^{\infty}\left(1-\frac{1}{(1+\theta(P_i/P_k)(R_0/|x|)^{\alpha})^b}\right)xdx\right).$$

$$\prod_{j\notin B}\exp\left(-\lambda_j\int_{R^2}\left(1-\frac{1}{\left(1+\theta\left(P_j/P_k\right)(R_0/|x|)^{\alpha}\right)^b}\right)dx\right)$$

$$\overset{(b)}{=} \int_0^{\infty} 2\pi\lambda_k r_k e^{-\pi\lambda_k {r_k}^2} \exp\left(\sum_{i\in \mathrm{B},i\neq k} -\pi\lambda_i\left(\frac{P_i}{P_k}\right)^{\delta} {r_k}^2\right).\exp \cdot\left(-2\pi\lambda_k\int_{r_k}^{\infty}\left(1-\frac{1}{(1+\theta(R_0/|x|)^{\alpha})^b}\right)xdx\right).\prod_{i\in B,i\neq k}\exp \cdot\left(-2\pi\lambda_i\int_{r_i}^{\infty}\left(1-\frac{1}{(1+\theta(P_i/P_k)(r_k/|x|)^{\alpha})^b}\right)xdx\right).\prod_{j\notin B}\exp \cdot\left(-\lambda_j\int_{R^2}\left(1-\frac{1}{\left(1+\theta\left(P_j/P_k\right)(R_0/|x|)^{\alpha}\right)^b}\right)dx\right)$$

$$\overset{(c)}{=} \int_0^{\infty} e^{-z\left(1+\sum_{i\in B,i\neq k}(\lambda_i/\lambda_k)(P_i/P_k)^{\delta}\right)}.\exp \cdot\left(-2z\int_0^1\left(1-\frac{1}{(1+\theta u^{\alpha})^b}\right)u^{-3}du\right).\prod_{i\in B}\exp \cdot\left(-2z\frac{\lambda_i}{\lambda_k}\int_0^{r_k/r_i}\left(1-\frac{1}{(1+\theta(P_i/P_k)u^{\alpha})^b}\right)u^{-3}du\right).\prod_{j\notin B}\exp \cdot\left(-z\frac{\lambda_j}{\lambda_k}\left(\frac{P_i}{P_k}\right)^{\delta}\theta^{\delta}\frac{\pi\delta}{\sin(\pi\delta)}\Gamma_{b,\delta}\right)dz$$

$$\overset{(d)}{=} \int_0^{\infty} e^{-z}.\exp\left(-z\int_1^{\infty}\left(1-\frac{1}{(1+\theta v^{-\alpha/2})^b}\right)dv\right).\exp \cdot\left(-z\left(\sum_{i\in B,i\neq k}\frac{\lambda_i}{\lambda_k}\left(\frac{P_i}{P_k}\right)^{\delta}\int_1^{\infty}\left(1-\frac{1}{(1+\theta t^{-\alpha/2})^b}\right)dt\right)\right).\exp \cdot\left(\sum_{j\notin B}-z\theta^{\delta}\left(\frac{\lambda_j}{\lambda_k}\right)\left(\frac{P_j}{P_k}\right)^{\delta}\frac{\pi\delta}{\sin(\pi\delta)}\Gamma_{b,\delta}\right)\right)dz$$

$$\overset{(e)}{=} \int_0^{\infty}\exp\left(-zF_{b,\delta,\theta}\right).\exp\left(-z\sum_{i\in B,i\neq k}\frac{\lambda_i}{\lambda_k}\left(\frac{P_i}{P_k}\right)^{\delta}F_{b,\delta,\theta}\right).\exp \cdot\left(-z\theta^{\delta}\sum_{j\notin B}\left(\frac{\lambda_j}{\lambda_k}\right)\left(\frac{P_j}{P_k}\right)^{\delta}\frac{\pi\delta}{\sin(\pi\delta)}\Gamma_{b,\delta}\right)dz = \frac{1}{\sum_{\Phi_{i|i\in B}}(\lambda_i/\lambda_k)(P_i/P_k)^{\delta}F_{b,\delta,\theta}+\sum_{\Phi_{j|j\notin B}}\left(\lambda_j/\lambda_k\right)\left(P_j/P_k\right)^{\delta}\theta^{\delta}(\pi\delta/\sin(\pi\delta))\Gamma_{b,\delta}}. \tag{A.3}$$

In the above derivation, (a) is by the probability generating functional (PGFL) of the PPP and the polar coordinate, and (b) is by using the probability density function of R_0. In step (c), we use the variable substitution $\pi\lambda_k {r_k}^2 = z$, and $r_k/|x\,| = u$ in the $\exp\left(-2\pi\lambda_k\int_{r_k}^{\infty}(1-1/(1+\theta(R_0/|x|)^{\alpha})^b)xdx\right)$ term and the $\prod_{i\in B,i\neq k}\exp\left(-2\pi\lambda_i\int_{r_i}^{\infty}(1-1/(1+\theta(P_i/P_k)(r_k/|x|)^{\alpha})^b)xdx\right)$ term and use

$$\int_{R^2}\left(1-\left(\frac{1}{1+\theta_1|x|^{-\alpha}}\right)^b\right)dx = \pi{\theta_1}^{\delta}\frac{\pi\delta}{\sin(\pi\delta)}\frac{\Gamma(b+\delta)}{\Gamma(b)\Gamma(1+\delta)}, \tag{A.4}$$

in the $\prod_{j\notin B}\exp\left(-\lambda_j\int_{R^2}(1-1/(1+\theta(P_j/P_k)(R_0/|x|)^{\alpha})^b)dx\right)$ term, where $\theta_1 = (P_j/P_k)r_k^{\alpha}\theta$. (A.4) can be obtained from [2, 15]. The step (d) is by using the variable substitution $u^{\alpha} = v^{-\alpha/2}$, and $(P_j/P_k)u^{\alpha} = t^{-\alpha/2}$; and step (e) holds for ${}_2F_1\left(b,-\delta;1-\delta;-\theta\right) \equiv 1+\int_1^{\infty}(1-1/(1+\theta t^{-\alpha/2})^b)dt$. Thus, $M_{b,(k)}^{\text{open}}$ is derived.

B. Proof of Theorem 3

Assume the jth ($j \notin$ B) tier is the closed tier, the CSP of the typical user is expressed as

$$P_{s,(k)}^{\text{closed}} = \mathbb{P}\left(\frac{P_j h_0 d_j^{-\alpha}}{\sum_{x\in\Phi_j, x\neq x_0} P_k h_x |x|^{-\alpha} + \sum_{i\neq j}\sum_{x\in\Phi_i} P_i h_x |x|^{-\alpha}} > \theta \middle| \bigcup\Phi_i\right). \tag{B.1}$$

By averaging over the fading, we get the conditional bth moment as

$$M_{b,(j)}^{\text{closed}} = E\left(\prod_{x\in\Phi_j, x\neq x_0}\frac{1}{\left(1+\theta\left(d_j/|x|\right)^{\alpha}\right)^b}\prod_{j\neq i}\prod_{\Phi_i}\frac{1}{\left(1+\theta\left(P_i/P_j\right)\left(d_j/|x|\right)^{\alpha}\right)^b}\right)$$

$$\begin{aligned}
&\overset{(a)}{=} \exp\left(-\lambda_j \int_{R^2}\left(1-\frac{1}{\left(1+\theta\left(d_j/|x|\right)^{\alpha}\right)^{b}}\right)dx\right)\cdot\prod_{i\neq j}\exp\\
&\quad\cdot\left(-\lambda_i\int_{R^2}\left(1-\frac{1}{\left(1+\theta\left(P_i/P_j\right)\left(d_j/|x|\right)^{\alpha}\right)^{b}}\right)dx\right)\\
&\overset{(b)}{=} \exp\left(-\pi\lambda_j\theta^{\delta}d_j^2\frac{\pi\delta}{\sin(\pi\delta)}\frac{\Gamma(b+\delta)}{\Gamma(b).\Gamma(1+\delta)}\right)\cdot\prod_{i\neq j}\exp\\
&\quad\cdot\left(-\pi\lambda_i\left(\frac{P_j}{P_k}\right)^{\delta}\theta^{\delta}d_j^2\frac{\pi\delta}{\sin(\pi\delta)}\frac{\Gamma(b+\delta)}{\Gamma(b).\Gamma(1+\delta)}\right)\\
&= \exp\left(-\pi\sum_{i=1}^{K}\lambda_i\left(\frac{P_i}{P_j}\right)^{\delta}\theta^{\delta}d_j^2\frac{\pi\delta}{\sin(\pi\delta)}\Gamma_{b,\delta}\right),
\end{aligned} \tag{B.2}$$

where (a) is by the PGFL of the PPP, and (b) holds for equation (A.4).

C. Proof of Theorem 7

Due to the displacement theorem, the stochastic equivalence model has been used in [19, 20]. Here, we make use of the stochastic equivalence to simplify the het-hybrid network as an equivalent two-tier network. One tier is the service-tier Φ_S (all open tiers), and the other is the interference-tier Φ_I (all closed tiers). For a link of the open tier k, the service density can be equivalent to $\lambda_S = \sum_{j\in B}\lambda_j(P_j/P_k)^{\delta}$, and the density of interference is equivalent to $\lambda_I = \sum_{j\notin B}\lambda_j(P_j/P_k)^{\delta}$. Assume the number of nodes in the service tier is n_1, the number of nodes in the interference tier is n_2, and the serving node is x_0 with distance R_0, the interference node is x_i, the CSP can be given by

$$\begin{aligned}
P_{s,(k)}^{\text{open}} &= \mathbb{P}\left(\frac{P_k h_0 R_0^{-\alpha}}{\sum_{x_i\in\Phi_k, i\neq 0}P_k h_x|x_i|^{-\alpha}+\sum_{j\neq k}\sum_{x_i\in\Phi_j}P_j h_x|x_i|^{-\alpha}} > \theta\middle|\bigcup\Phi_i\right)\\
&= \prod_{j\in B}\prod_{x_i\in\Phi_j, x_i\neq x_0}\frac{1}{1+\theta\left(P_j/P_k\right)\left(R_0/|x_i|\right)^{\alpha}}\prod_{j\notin B}\prod_{x_i\in\Phi_j}\frac{1}{1+\theta\left(P_j/P_k\right)\left(R_0/|x_i|\right)^{\alpha}}
\end{aligned}$$

$$\begin{aligned}
&\overset{(a)}{=} \prod_{\Phi_{S,x_i\neq x0}}\frac{1}{1+\theta(R_0/|x_i|)^{\alpha}}\prod_{\Phi_I}\frac{1}{1+\theta(R_0/|x_i|)^{\alpha}}\\
&\geq \frac{1}{\left((1/n_1)\sum_{i=1}^{n_1}(1+\theta(R_0/|x_i|)^{\alpha})\right)^{n_1}\left((1/n_2)\sum_1^{n_2}(1+\theta(R_0/|x_i|)^{\alpha})\right)^{n_2}}\\
&= \frac{1}{\left(1+\theta(1/n_1)\sum_{i=1}^{n1}(R_0/|x_i|)^{\alpha}\right)^{n1}\left(1+\theta(1/n_2)\sum_{i=1}^{n_2}((R_0/|x_i|))^{\alpha}\right)^{n_2}},
\end{aligned} \tag{C.1}$$

where (a) holds for the equivalent network; the "≥" holds for the relation between the geometric mean and the arithmetic mean, as [20], Lemma 5.

For a target reliability ν,

$$\frac{1}{\nu}\leq\left(1+\frac{1}{n_1}\theta\sum_{i=1}^{n_1}\left(\frac{R_0}{|x_i|}\right)^{\alpha}\right)^{n_1}\left(1+\frac{1}{n_2}\theta\sum_{i=1}^{n_2}\left(\frac{R_0}{|x_i|}\right)^{\alpha}\right)^{n_2}$$

$$\begin{aligned}
&\overset{(b)}{\approx}\left(1+\frac{1}{n_1}\theta\frac{2}{\alpha-2}\right)^{n_1}\\
&\quad\cdot\left(1+\frac{1}{n_2}\theta\frac{\Gamma(1+(\alpha/2))}{(\lambda_S\pi)^{\alpha/2}}\frac{(\lambda_I\pi)^{\alpha/2}\Gamma(n_2-(\alpha/2))}{\Gamma(n_2)}\right)^{n_2}\\
&\leq\left(1+\frac{1}{n_1}\theta\frac{2}{\alpha-2}\right)^{n_1}\left(1+\frac{1}{n_2}\theta\frac{(\lambda_I)^{\alpha/2}}{(\lambda_S)^{\alpha/2}}\Gamma\left(1+\frac{\alpha}{2}\right)\right)^{n_2}\\
&\approx\lim_{\substack{n_1\to\infty\\ n_2\to\infty}}\left(1+\frac{1}{n_1}\theta\frac{2}{\alpha-2}\right)^{n_1}\left(1+\frac{1}{n_2}\theta\left(\frac{\lambda_I}{\lambda_S}\right)^{\alpha/2}\Gamma\left(1+\frac{\alpha}{2}\right)\right)^{n_2}
\end{aligned}$$

$$\overset{(c)}{=}\exp\left(\theta\left(\frac{2}{\alpha-2}+\left(\frac{\lambda_I}{\lambda_S}\right)^{\alpha/2}\Gamma\left(1+\frac{\alpha}{2}\right)\right)\right), \tag{C.2}$$

where (b) holds for the $R_0/|x_i|$ in Lemma 5 and Lemma 6, and r_0 is taken a mean value by the probability density function $f_{r_0}(r) = 2\pi\lambda re^{-\pi\lambda r^2}$ in open tiers. The last "=" (c) is derived from the $\lim_{n\to\infty}(1+(x/n))^n = e^x$. The equation (17) is thus derived.

D. Proof of Theorem 9

We also start from the CSP for the closed user. Similar as the open tiers, the service density is the kth tier density itself $\lambda_S = \lambda_j$, and density of interference from other tiers is $\lambda_I = \sum_{i\neq j}\lambda_i(P_i/P_k)^{\delta}$. Assume the link distance is fixed as d_j, the CSP is

$$\begin{aligned}
P_{s,(j)}^{\text{closed}} &= \mathbb{P}\Big(P_j h_0 d_j^{-\alpha}/\textstyle\sum_{x_i\in\Phi_j, i\neq 0}P_j h_x|x_i|^{-\alpha}\\
&\qquad+\textstyle\sum_{j\neq k}\sum_{x_i\in\Phi_k}P_k h_x|x_i|^{-\alpha} > \theta\Big|\bigcup\Phi_i\Big)\\
&= \textstyle\prod_{x_i\in\Phi_j, x_{i\neq x_0}}\left(1/1+\theta\left(d_j/|x_i|\right)^{\alpha}\right)\prod_{j\neq k}\prod_{x_i\in\Phi_j}\\
&\quad\cdot\left(1/1+\theta\left(P_k/P_j\right)\left(d_j/|x_i|\right)^{\alpha}\right)((a)/=)\textstyle\prod_{\Phi_{j,x_i\neq x0}}\\
&\quad\cdot\left(1/1+\theta\left(d_j/|x_i|\right)^{\alpha}\right)\textstyle\prod_{\Phi_I}\left(1/1+\theta\left(d_j/|x_i|\right)^{\alpha}\right)\\
&\geq 1/\left((1/n_1)\textstyle\sum_{i=1}^{n_1}\left(1+\theta\left(d_j/|x_i|\right)^{\alpha}\right)\right)^{n_1}\\
&\quad\cdot\left((1/n_2)\textstyle\sum_1^{n_2}\left(1+\theta\left(d_j/|x_i|\right)^{\alpha}\right)\right)^{n_2},
\end{aligned} \tag{D.1}$$

where (a) holds for the interference nodes as an equivalent tier with density λ_I, and the "≥" holds for the relation between the geometric mean and the arithmetic mean, as [20], Lemma 5. Therefore,

$$\frac{1}{\nu} \leq \left(1+\frac{1}{n_1}\theta\sum_{i=1}^{n_1}\left(\frac{d_j}{|x_i|}\right)^{\alpha}\right)^{n_1}\left(1+\frac{1}{n_2}\theta\sum_{i=1}^{n_2}\left(\frac{d_j}{|x_i|}\right)^{\alpha}\right)^{n_2}$$

$$\begin{aligned}
&\overset{(b)}{\approx} \left(1+\frac{d_j^{\alpha}}{n_1}\theta\frac{(\lambda_S\pi)^{\alpha/2}\Gamma(n_1-(\alpha/2))}{\Gamma(n_1)}\right)^{n_1}\\
&\quad\cdot\left(1+\frac{d_j^{\alpha}}{n_2}\theta\frac{(\lambda_I\pi)^{\alpha/2}\Gamma(n_2-(\alpha/2))}{\Gamma(n_2)}\right)^{n_2}\\
&\leq \left(1+\frac{d_j^{\alpha}}{n_1}\theta(\lambda_S\pi)^{\alpha/2}\right)^{n_1}\left(1+\frac{d_j^{\alpha}}{n_2}\theta(\lambda_I\pi)^{\alpha/2}\right)^{n_2}\\
&\approx \lim_{\substack{n_1\to\infty\\ n_2\to\infty}}\left(1+\frac{d_j^{\alpha}}{n_1}\theta(\lambda_S\pi)^{\alpha/2}\right)^{n_1}\left(1+\frac{d_j^{\alpha}}{n_2}\theta(\lambda_I\pi)^{\alpha/2}\right)^{n_2}\\
&\overset{(c)}{=} \exp\left(\theta d_j^{\alpha}\left((\lambda_S\pi)^{\alpha/2}+(\lambda_I\pi)^{\alpha/2}\right)\right), \qquad (D.2)
\end{aligned}$$

where (b) stems from Lemma 6, and (c) holds for $\lim_{n\to\infty}(1+(x/n))^n = e^x$. Equation (18) is thus derived.

Data Availability

All data in this paper are fully available without restriction.

Conflicts of Interest

The authors declare that they have no conflicts of interests.

Acknowledgments

This work is supported by the National Science Foundation of China under grant 61672321.

References

[1] H. S. Dhillon, R. K. Ganti, F. Baccelli, and J. G. Andrews, "Modeling and analysis of k-tier downlink heterogeneous cellular networks," *IEEE Journal on Selected Areas in Communications*, vol. 30, no. 3, pp. 550–560, 2012.

[2] M. Haenggi, "The meta distribution of the SIR in Poisson bipolar and cellular networks," *IEEE Transactions on Wireless Communications*, vol. 15, no. 4, pp. 2577–2589, 2016.

[3] Y. Wang, M. Haenggi, and Z. Tan, "The meta distribution of the SIR for cellular networks with power control," *IEEE Transactions on Communications*, vol. 66, no. 4, pp. 1745–1757, 2018.

[4] X. Yu, Q. Cui, Y. Wang, and M. Heanggi, "The joint and product meta distributions of the SIR and their applications to secrecy and cooperation," *IEEE Transactions on Wireless Communications*, vol. 19, no. 7, pp. 4408–4423, 2020.

[5] X. Tang, X. Xu, and M. Heanggi, "Meta distribution of the SIR in moving networks," *IEEE Transactions on Communications*, vol. 68, no. 6, pp. 3614–3626, 2020.

[6] Y. Wang, M. Haenggi, and Z. Tan, "SIR meta distribution of *K-tier* downlink heterogeneous cellular networks with cell range expansion," *IEEE Transactions on Communications*, vol. 67, no. 4, pp. 3069–3081, 2019.

[7] Q. Cui, X. Yu, Y. Wang, and M. Haenggi, "The SIR meta distribution in Poisson cellular networks with base station cooperation," *IEEE Transactions on Communications*, vol. 66, no. 3, pp. 1234–1249, 2018.

[8] S. Chiranjib, A. Mehrnaz, and H. S. Dhillon, "Meta distribution of downlink SIR in a Poisson cluster process-based Het Net model," *IEEE Wireless Communication Letters*, vol. 99, p. 1, 2020.

[9] S. S. Kalamkar and M. Haenggi, "Simple approximations of the SIR meta distribution in general cellular networks," *IEEE Transactions on Communications*, vol. 67, no. 6, pp. 4393–4406, 2019.

[10] N. Deng and M. Haenggi, "A fine-grained analysis of millimeter-wave device-to-device networks," *IEEE Transactions on Communications*, vol. 65, no. 11, pp. 4940–4954, 2017.

[11] H. Ibrahim, H. Tabassum, and U. T. Nguyen, "The meta distributions of the SIR/SNR and data rate in coexisting sub-6GHz and millimeter-wave cellular networks," *IEEE Open Journal of the Communications Society*, vol. 1, pp. 1213–1229, 2020.

[12] M. Salehi, H. Tabassum, and E. Hossain, "Meta distribution of SIR in large-scale uplink and downlink NOMA networks," *IEEE Transactions on Communications*, vol. 67, no. 4, pp. 3009–3025, 2019.

[13] H. Ibrahim, H. Tabassum, and U. T. Nguyen, "Meta distribution of SIR in dual-hop internet-of-things (iot) networks," in *ICC 2019-2019 IEEE International Conference on Communications (ICC).IEEE*, Shanghai, China, 2019.

[14] A. P. Kartun-Giles, K. Koufos, and S. Kim, "Meta distribution of SIR in ultra-dense networks with bipartite Euclidean matchings," in *ICC 2020-2020 IEEE International Conference on Communications (ICC)*, Dublin, Ireland, 2020.

[15] M. Salehi, A. Mohammadi, and M. Haenggi, "Analysis of D2D underlaid cellular networks: SIR meta distribution and mean local delay," *IEEE Transactions on Communications*, vol. 65, no. 7, pp. 2904–2916, 2017.

[16] S. S. Kalamkar and M. Haenggi, "Per-link reliability and rate control: two facets of the SIR meta distribution," *IEEE Wireless Communications Letters*, vol. 8, no. 4, pp. 1244–1247, 2019.

[17] Z. Zhang, R. Q. Hu, and Y. Qian, "D2D communication underlay in uplink cellular networks with distance based power control," in *2016 IEEE International Conference on Communications (ICC)*, pp. 1–6, Kuala Lumpur, Malaysia, 2016.

[18] J. Gil-Pelaez, "Note on the inversion theorem," *Biometrika*, vol. 38, no. 3-4, pp. 481-482, 1951.

[19] M. Wilderneersch, T. Q. S. Quek, M. Kountouris, A. Rabbachin, and C. H. Slump, "Successive interference cancellation in heterogeneous networks," *IEEE Transactions on Communications*, vol. 62, no. 12, pp. 4440–4453, 2014.

[20] C. Ma, W. Wu, Y. Cui, and X. Wang, "On the performance of successive interference cancellation in D2D-enabled cellular networks," in *Proceedings of the 7th ACM international symposium on Mobile ad hoc networking and computing*, pp. 37–45, Kowloon, Hong Kong, 2015.

[21] Z. Gong and M. Haenggi, "The local delay in mobile Poisson networks," *IEEE Transactions on Wireless Communications*, vol. 12, no. 9, pp. 4766–4777, 2013.

[22] Y. Wang, Q. Cui, M. Haenggi, and Z. Tan, "On the SIR Meta distribution for Poisson networks with interference

cancellation," *IEEE Wireless Communications Letters*, vol. 7, no. 1, pp. 26–29, 2018.

[23] M. Haenggi, "Efficient calculation of meta distributions and the performance of user percentiles," *IEEE Wireless Communications Letters*, vol. 7, no. 6, pp. 982–985, 2018.

[24] S. Guruacharya and E. Hossain, "Approximation of meta distribution and its moments for Poisson cellular networks," *IEEE Wireless Communications Letters*, vol. 7, no. 6, pp. 1074–1077, 2018.

[25] R. K. Ganti and M. Haenggi, "Asymptotics and approximation of the SIR distribution in general cellular networks," *IEEE Transactions on Wireless Communications*, vol. 15, no. 3, pp. 2130–2143, 2019.

[26] F. Baccelli and B. Blaszczyszyn, *Stochastic Geometry and Wireless Networks, Volume I: Theory*, Now, Paris, 2009.

Hindawi
Wireless Communications and Mobile Computing
Volume 2020, Article ID 8876669, 10 pages
https://doi.org/10.1155/2020/8876669

WILEY | Hindawi

Research Article

RO-RAW: Run-Time Restricted Access Window Optimization in IEEE 802.11ah Network with Extended Kalman Filter

Zhao Liu and Peng Lv

The School of Computer and Communication Engineering, University of Science and Technology Beijing, Beijing, China

Correspondence should be addressed to Peng Lv; b1901775@ustb.edu.cn

Received 1 August 2020; Revised 16 September 2020; Accepted 29 September 2020; Published 21 October 2020

Academic Editor: Chaoyun Song

In 2016, the IEEE task group ah (TGah) published a new standard IEEE 802.11ah, aimed at providing network connectivity among a large number of Internet of Things (IoT) devices. Restricted access window (RAW) is one of the fundamental MAC mechanisms of IEEE 802.11ah. It reduces the contention overhead in the dense wireless environment by dividing stations into different RAW groups. However, how to optimize the RAW parameters is still an open issue, especially in the run-time environment. In this paper, we propose a run-time RAW optimization scheme, namely RO-RAW, to improve the performance of RAW in the IEEE 802.11ah networks. RO-RAW adopts the Extended Kalman Filter method to estimate the channel status and adjusts the RAW parameters according to the number of competing stations in real-time. The evaluation via NS-3 simulations shows that, by tuning the RAW parameters appropriately, RO-RAW substantially improves throughput, latency, and packet loss performance compared with another RAW optimization scheme in different simulation scenarios. The results further show that, when the channel is relatively congested, RO-RAW improves the RAW performance more significantly.

1. Introduction

Smart manufacturing [1, 2] and Industry 4.0 production environments modernize the traditional plants and factories. To remain competitive, several intelligent applications need to be deployed to upgrade the current plants, such as remote operation and maintenance [3], flexible production [4], and AI manufacturing automation [5]. To provide a better support for these applications, the industrial wireless network should also be deployed as the communication infrastructure. Compared with the traditional wired industrial communication systems, choosing wireless networks is a better option because it is easy to maintain and cost-effective.

Wireless local area networks (WLANs) have become the most popular and widely deployed networks. Thus, it is a good candidate for different industrial wireless applications with various requirements [6, 7]. In 2016, a new Wi-Fi standard named IEEE 802.11ah was released [8], which targets low-power and large-scale Internet of Things (IoT) network scenarios, including industrial IoT. IEEE 802.11ah has a transmission range up to 1 km with the advent of sub-GHz technologies and supports up to 8192 nodes in a WLAN. On the Media Access Control (MAC) layer, the most important issue is to increase the efficiency when a large number of energy-constrained stations deployed densely. Thus, several novel MAC mechanisms are introduced, such as short MAC header, Restricted Access Window (RAW), Target Wake Time (TWT), and Traffic Indication Map (TIM) segmentation.

The RAW mechanism is aimed at addressing the collision problem in a dense wireless network, where a large number of nodes are associated with a single access point (AP). The basic idea of the RAW mechanism is to divide stations into groups, and the stations in one group are only permitted to access the channel during a specific time slot. Thus, the collision probability is highly reduced by limiting the number of stations which simultaneously access the channel. However, the hierarchical RAW mechanism has several parameters to be adjusted, including the number of RAW slots, the duration of each RAW slot, and the RAW period, which are not defined in the standard. In order to obtain a better network performance, these parameters must be considered

jointly according to the channel status. In fact, there are already some related works [9–11] which provide the relationship between the parameter settings and the performance metrics (throughput, average latency, transmission success probability, etc.). But, the dynamicity of the channel contention status is rarely considered in these models, which could be a key factor affecting the network performance.

In this paper, the authors propose a run-time RAW optimization scheme, namely, RO-RAW, which adaptively optimizes the network performance by adjusting the RAW parameters according to the channel status. It first estimates the current channel status and returns the estimated station numbers by the Extended Kalman Filter (EKF) method. Based on the estimated number of competing stations, RO-RAW adjusts the RAW parameters to the optimal parameter settings which are calculated in advance corresponding to the number of stations. The main contributions of this paper are summarized as follows:

(i) We propose a run-time RAW parameter optimization scheme RO-RAW, which adaptively adjusts the RAW parameters to the theoretical optimal values based on the channel status

(ii) In order to estimate the channel status, we adopt the Extended Kalman Filter method to obtain the current competing stations. We clearly provide the system state equations of the 802.11ah networks and the way to measure the number of stations. Then, the estimated channel status can be easily obtained by iteration using EKF

The remainder of the paper is organized as follows. Section 2 reviews related work and the background on this research. Section 3 presents the proposed run-time RAW optimization scheme in detail. Section 4 shows the simulation results of the proposed scheme in detail. Finally, the conclusions are given in Section 5.

2. Background

2.1. IEEE 802.11 DCF and EDCA. IEEE 802.11ah inherits the most basic features of IEEE 802.11 MAC, such as distributed coordination function (DCF) and Enhanced Distributed Channel Access (EDCA). DCF is the fundamental MAC mechanism of the IEEE 802.11 family. It is a simple and flexible scheme to share the wireless medium among multiple stations. In DCF (Figure 1), stations adopt the Carrier Sense Multiple Access mechanism with Collision Avoidance (CSMA/CA) to contend for the channel access opportunity. Before a new transmission, each station must monitor the state of the wireless medium. If the medium is found idle for a DCF Interframe Space (DIFS) duration, the station is permitted to transmit its data. Otherwise, the transmission procedure must be frozen until the channel is sensed idle again. When the transmission of a station fails due to the collision or bit error, DCF adopts the Binary Exponential Backoff (BEB) algorithm to look for the next transmission opportunity [12]. The backoff duration is composed of several time slots, and the number of backoff slot value is selected randomly from $[0, CW - 1]$, where CW is the contention window size. In the initialization phase, CW is set to the minimal value (CW_{min}). Once the CW increases to the maximum value (CW_{max}), it is maintained at CW_{max} even if the next transmissions are still failed. After a successful data transmission, the CW is set back to CW_{min}.

In the IEEE 802.11e standard, a new channel access mechanism called EDCA is proposed to provide priority-based differentiated QoS. As shown in Figure 2, there are four access categories (AC) defined in EDCA, namely, voice (AC_VO), video (AC_VI), best-effort (AC_BE), and background (AC_BK). By differentiating the backoff parameters, high-priority traffic is able to transmit with a higher transmission chance than the low-priority traffic. Specifically, high-priority traffic uses shorter arbitration inter-frame space (AIFS), which is the interval that a frame needs to wait before it is transmitted. The size of the contention window is also set according to the priority of each kind of AC.

2.2. IEEE 802.11ah RAW Mechanism. The IEEE 802.11ah standard allows up to 8192 stations to associate with an AP, which is a highly attractive feature for a lot of IoT use cases. However, how to mitigate collisions and improve performance in such dense IoT networks is an urgent problem to be solved. Among the new mechanisms in 802.11ah, RAW is the core mechanism aimed at enabling fair channel access for a large number of stations and avoiding too many stations contending for channel access simultaneously. In this mechanism, the channel time is divided into several intervals, namely, the RAW periods and the shared channel access periods. Only the RAW stations from a specific group are allowed to access the channel and transmit in their corresponding RAW period. On the contrary, all stations are permitted to contend the channel in the shared channel access periods. The example of the different periods in RAW mechanism is shown in Figure 3.

For each AP, it broadcasts a beacon frame carrying a RAW Parameter Set (RPS), which specifies the RAW parameter configurations. Stations retrieve the RAW information from the beacon frame and access the channel in their corresponding RAW slot. The RPS information specifies the RAW related information, such as the RAW group, group start time, the number of RAW slots, and slot duration. The RAW slot duration is determined as follows:

$$D = 500\mu s + C \times 120\mu s. \quad (1)$$

In equation (1), D stands for the RAW slot duration, and C is the slot duration count subfield. Another parameter called the slot format subfield determines the number of RAW slots and C. If the slot format subfield is filled with 1, a single RAW period is composed of at most eight RAW slots and the maximum value of C is 2047; the duration of each slot is up to 246.14 ms. Otherwise, a RAW period is composed of at most 64 RAW slots and the maximum value of C is 255, and the duration of each

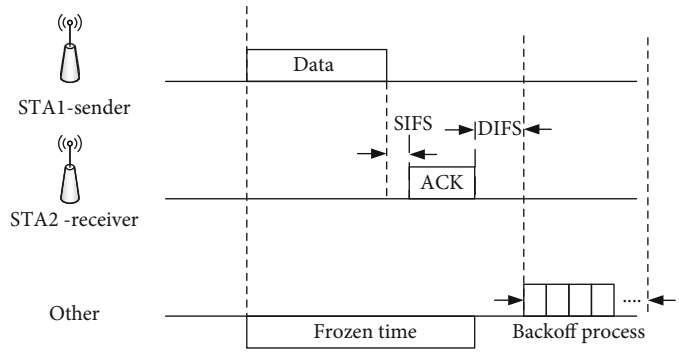

Figure 1: IEEE 802.11 DCF.

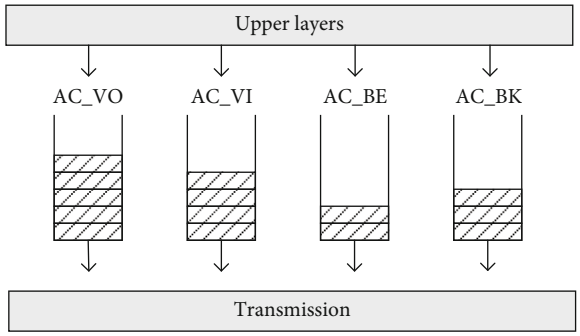

Figure 2: IEEE 802.11 EDCA.

slot is limited to 31.1 ms. The RAW stations are mapped to these slots according to the following rule:

$$i_{\text{slot}} = (x + N_{\text{offset}}) \bmod N_{\text{RAW}}. \quad (2)$$

In equation (2), i_{slot} represents the index of the RAW slot which the station is mapped. N_{RAW} is the number of slots predefined in one RAW period. N_{offset} is the offset value in the mapping function, and x is the index of the station.

The RPS also has a subfield called cross-slot boundary (CSB), which determines whether the stations are allowed to continue their transmissions when the current RAW slot ends. If CSB is set to 1, the stations can continue transmitting even though their RAW slot ends. Otherwise, stations should not trigger a transmission if the transmissions cannot be finished in the current RAW slot.

The backoff mechanism in RAW is also different to some extent compared with the previous IEEE 802.11 standards. Each station uses two kinds of backoff states of EDCA to manage data transmission inside and outside its allocated RAW slots. The first backoff state is used outside the RAW period, in which all stations contend for the channel freely. The stations in the first backoff state freeze their backoff timer at the beginning of each RAW period and resume the backoff timer at the end of the RAW period. On the contrary, the second backoff state is used inside the RAW period, where only the designated group of stations are allowed to contend for the channel. The stations in the second backoff state start to backoff inside their own RAW slot and discard the backoff state when their RAW slot ends.

2.3. Related Work on RAW Mechanism Optimization. Although the IEEE 802.11ah standard was published in 2016, research on IEEE 802.11ah has been conducted for more than five years. A few articles [11, 13–16] introduce a high-level overview of the core PHY/MAC mechanisms in IEEE 802.11ah and describe the advantages and challenges when designing these schemes. As one of the key technologies in IEEE 802.11ah, the RAW mechanism has been widely studied in many aspects. The work focusing on RAW analysis and optimization is more relevant to the research presented in this paper.

Several studies have been conducted to model and optimize the RAW parameter configuration in different network and traffic conditions. Raeesi et al. [9] propose an analytical model to derive the IEEE 802.11ah network performance, including throughput and energy consumption. It also shows the advantage of the RAW mechanism in throughput and delay compared with the basic scheme. In [10], the authors propose an analytical approach to investigate the RAW mechanism. Based on the analytical model, the paper provides the time distribution of the successful transmission by a Markov model. In [17], the authors provide a RAW enhancement scheme in the machine-to-machine scenario. The proposed scheme determines the optimal size of RAW by estimating the number of devices for the uplink access. However, the works mentioned above either only conduct a basic analytical model under a certain circumstance or provide a basic RAW optimization scheme with a simple channel sensing method, which may not be enough to reflect the real channel status. This will cause the network performance deviating from the calculated optimal value. In [18], the author proposes an adaptive RAW optimization scheme called CA-CWA. It estimates the channel state and adjusts the channel contention parameters to improve the real-time performance of the IEEE 802.11ah network. However, CA-CWA only considers and adapts the contention window to improve the RAW performance. Other RAW parameters, such as RAW slot duration and RAW slot number, are not considered and optimized. In this paper, the authors provide RO-RAW to adaptively adjust the IEEE 802.11ah RAW parameters in the run-time environment. Based on the

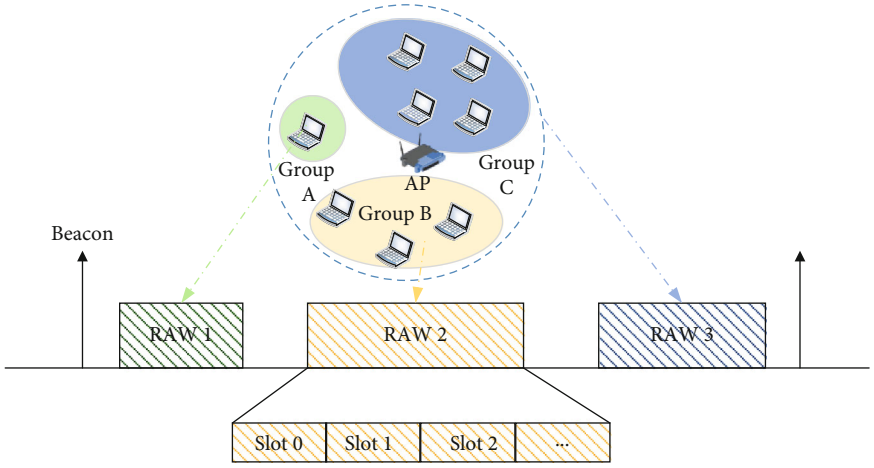

Figure 3: IEEE 802.11ah RAW mechanism.

estimated number of competing stations, RO-RAW is able to adjust RAW parameters in time to ensure the performance of RAW.

3. RAW Mechanism Optimization with Extended Kalman Filter

In this section, we introduce the system model and the RAW optimization problem first and subsequently provide a detailed description of the proposed RO-RAW. RO-RAW is a run-time adaptive scheme to improve the performance of the RAW mechanism. It adjusts the RAW parameters to the optimal parameter settings based on the estimated number of competing stations. Table 1 provides an overview of the variables used in the description of the system model and RO-RAW.

3.1. System Model. In this paper, we only consider a single wireless cell with a star topology. Assuming the wireless network has a total number of N nodes, each node supports the RAW mechanism defined in the IEEE 802.11ah standard. According to the RAW mechanism definition introduced in Section 2.2, if there are M RAW station groups, and the number of stations in ith group is G_i, we can have the following equations:

$$N = \sum_{i=1}^{M} G_i. \tag{3}$$

Because each group of stations monopolizes its allocated RAW period, in a certain group i in RAW period i, if there are r_i RAW slots in the RAW period, the number of stations in a RAW slot N^i_{RAW} is:

$$N^i_{\mathrm{RAW}} = G_i / r_i. \tag{4}$$

In each RAW slot, the stations still adopt basic DCF to compete for transmission. According to the Bianchi [19] model, let p be the probability that a transmitted packet collides with others in the RAW slot, and τ be the probability that a station transmits in a random slot time; we can obtain the following equations:

$$p = 1 - (1 - \tau)^{n-1}, \tag{5}$$

$$\tau = \frac{2(1-2p)}{(1-2p)(W+1) + pW(1-(2p)^m)}, \tag{6}$$

where W is the minimal contention window size and m is the retry limit. Both values are the predefined constant backoff parameters. From equation (5) and equation (6), we obtain the number of current competing stations in the RAW slot:

$$n = y(p) = 1 + \frac{\log(1-p)}{\log\left(1 - \left((2(1-2p))/(1-2p)(W+1) + pW(1-(2p)^m)\right)\right)} < N^i_{\mathrm{RAW}}. \tag{7}$$

Besides, the network throughput S is calculated as:

$$S = \frac{P_s P_{tr} L}{(1-P_{tr})\sigma + P_{tr} P_s T_s + P_{tr}(1-P_s) T_c}, \tag{8}$$

where

$$P_s = \frac{n\tau(1-\tau)^{n-1}}{1-(1-\tau)^n}, \qquad P_{tr} = 1 - (1-\tau)^n. \tag{9}$$

L is the average packet length. From the above derivations, it is obvious that the throughput is a function of the competing station number n. Since other variables in equation (8) are constant values, it exists the optimal value of n, which achieves the maximum throughput [20, 21]. The optimal value is easy to be obtained from equation (8) by calculating the derivative (equation (10)). Here we use n_{opt} to represent the optimal station number.

$$\frac{dS}{dn} = 0. \tag{10}$$

Table 1: Summary of the main notations and abbreviations.

Notation	Description
N	The total number of stations
M	The number of RAW station groups
G_i	The number of stations in ith group
N^i_{RAW}	The number of stations in ith RAW slot
r_i	The RAW slot number in a RAW
p	Transmission collision probability
τ	The transmission probability in a random slot time
L	The average packet length
T_c	The number of busy slots
T_p	The number of collision slots
$\hat{n}_k$	The estimated value of n at time k
K_k	Kalman gain
Q_k	Variance of random variable u_k
R_k	Variance of random variable v_k

1: **Step 1:** Initialize all the network and algorithm parameters.
2: **Step 2:** Compute the optimal station numbers n_{opt}.
3: **Step 3:** After the network has been initialized and running normally, each station calculates the current channel status $\hat{n}^i_k$ by the method introduced in Section 3.2 for ith RAW slot at time k.
4: **Step 4:** If $\hat{n}^i_k$ is beyond the value of n_{opt} for a period T_p, $n_{\mathrm{opt}} - \hat{n}^i_k$ stations should be redistributed to other RAW groups/slots evenly.
5: **Step 5:** Repeat step 3.

Algorithm 1: RAW adaption algorithm in RO-RAW.

If the number of competing stations is beyond the optimal value, some of the stations should be reallocated to other RAW groups. However, how to estimate the current competing stations is another problem to be solved.

3.2. Channel-State Estimation with Extended Kalman Filter. In order to estimate the current competing station number, we get inspiration from equation (7). If we measure the collision probability p, we can calculate the number of stations n by equation (7). Luckily, p can be simply measured by monitoring the channel state for each station. Specifically, one station can monitor the channel for all backoff slot times. If T is the total number of the observed slots, T_b is the number of busy slots sensed by the station (other stations are transmitting) and T_c is the number of collision slots (failed transmission for the station); it is obvious that p can be calculated as:

$$p = \frac{T_c + T_b}{T}. \tag{11}$$

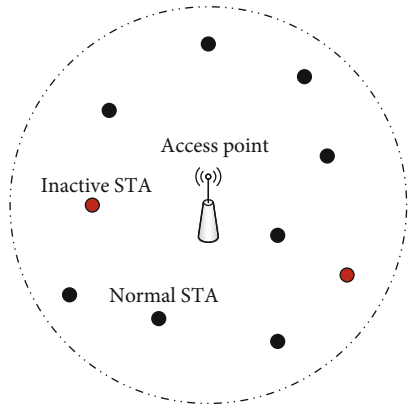

Figure 4: Example of the test topology.

Table 2: The parameters used in simulation.

PHY layer parameters	
Reception energy threshold	-116.0 dbm
Noise figure	3 db
Channel bandwidth	2 MHz
Data rate	2.4 Mbps
Maximal distance between AP and stations	250 m
MAC layer parameters	
$\mathrm{CW}_{\mathrm{min}}$	15
$\mathrm{CW}_{\mathrm{max}}$	1023
Traffic interval	0.1 s
Packet payload size	250/400 bytes
Number of groups	1
Algorithm parameters	
P_0	100
n_0	1
Q	0.6
R	1

Since the value of p is obtained, it is easy to calculate the instantaneous number of competing stations n. However, only the run-time estimation for a certain period can be really used by the optimization algorithms. We decide to adopt the Kalman filter to provide a run-time adaptive estimation of n. In fact, there are several simple estimation methods such as autoregressive and autoregressive moving average, but they are proven to be too simple to track the variations of the channel status accurately [22]. Thus, we decide to adopt the Kalman filter to provide a run-time adaptive estimation of n.

According to the definition of the network system, the system state can be represented by the following equations at discrete time k:

$$n_k = n_{k-1} + u_k, \tag{12}$$

$$p_k = y^{-1}(n_k) + v_k = h(n_k) + v_k. \tag{13}$$

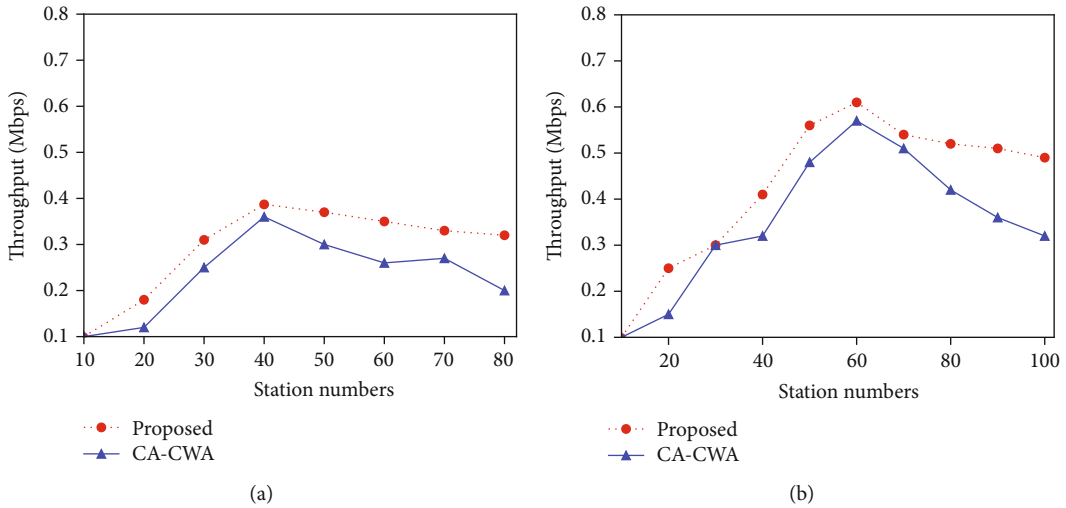

Figure 5: Performance of throughput of each scheme in the first scenario. (a) Throughput comparison when the payload size = 250 B, (b) Throughput comparison when the payload size = 400 B.

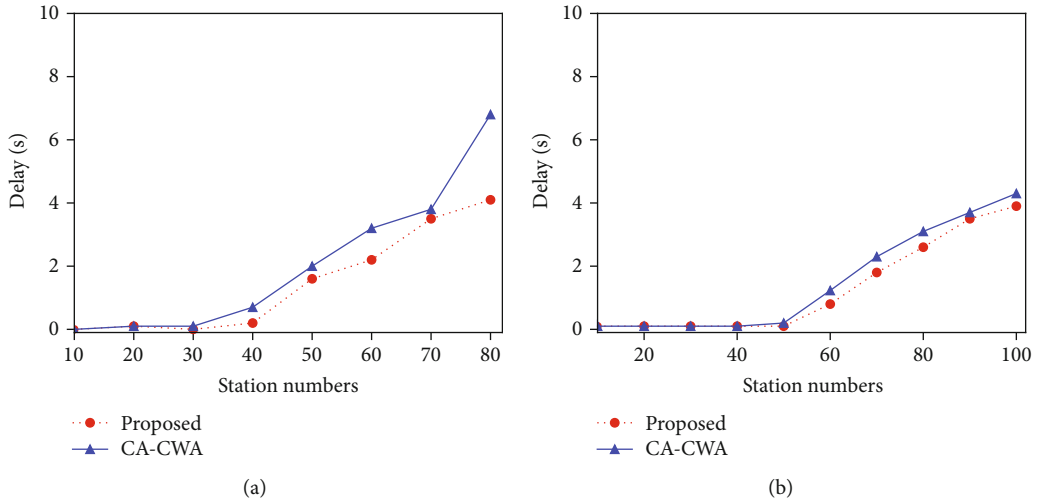

Figure 6: Performance of average delay of each scheme in the first scenario. (a) Average delay comparison when the payload size = 250 B, (b) Average delay comparison when the payload size = 400 B.

In equation (12), n_k stands for the number of stations at time k and v_k is the state random noise. This equation implies the approximate value of current n can be represented by the value of last state n plus a random variable. In equation (13), p_k is the collision probability at time k, and $y^{-1}(n_k)$ is the inverse function of equation (7). This equation means we can also obtain another approximate value of current n by measuring the collision probability.

Since the system state model is formulated, according to the general extended Kalman filter definition, it is easy to build the following iteration equations of the algorithm:

$$\hat{n}_k = \hat{n}_{k-1} + K_k z_k, \tag{14}$$

where K_k is the Kalman gain, and z_k is the measurement at time k. These two variables can be described by the following equations according to the definition:

$$z_k = p_k - \hat{h}(k-1), \tag{15}$$

$$K_k = \frac{(P_{k-1} + Q_k)h_k}{(P_{k-1} + Q_k)h_k^2 + R_k}. \tag{16}$$

In equation (16), Q_k and R_k are the variances of the random variable u_k and v_k, which are the noise in the updating process and measurement process, respectively. h_k is the

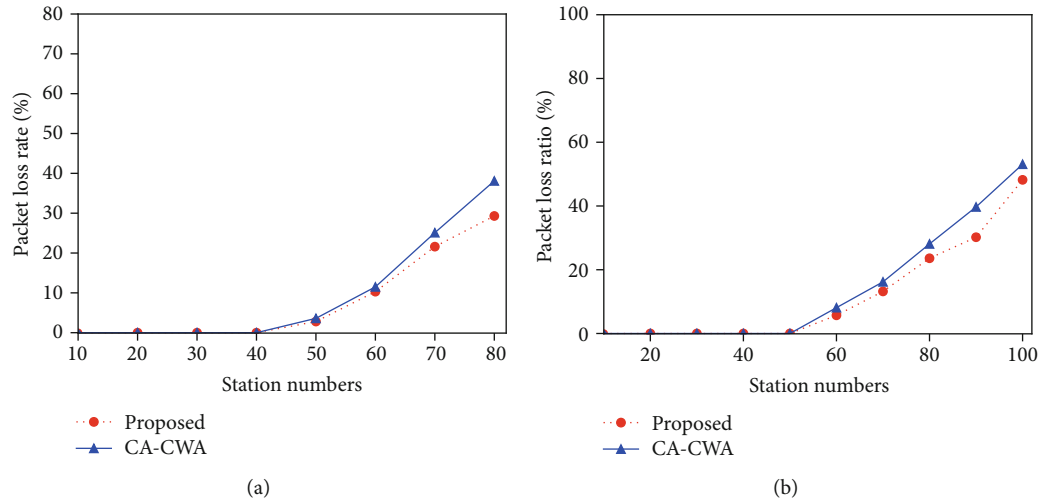

FIGURE 7: Performance of packet loss rate of each scheme in the first scenario. (a) Packet loss rate comparison when the payload size = 250 B, (b) Packet loss rate comparison when the payload size = 400 B.

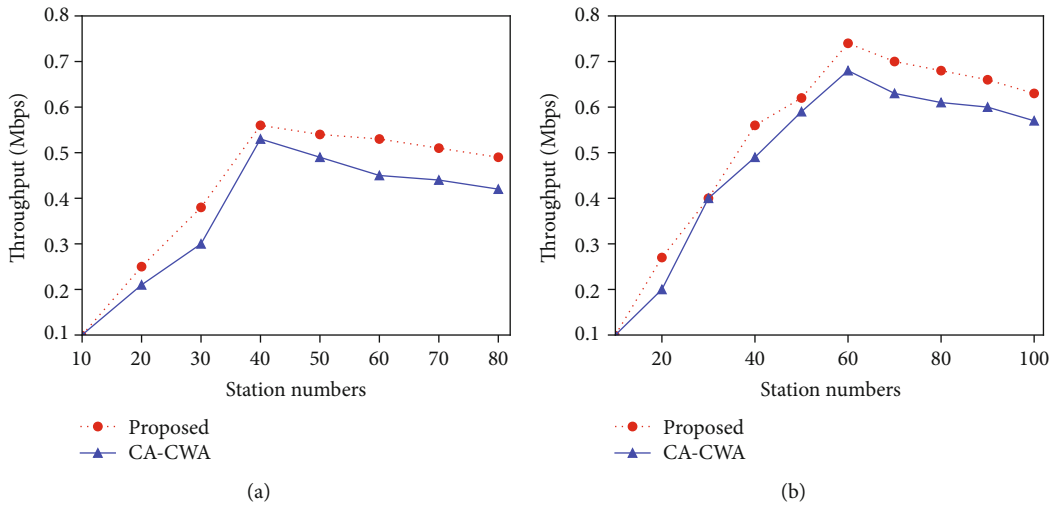

FIGURE 8: Performance of throughput of each scheme in the second scenario. (a) Throughput comparison when the payload size = 250 B, (b) Throughput comparison when the payload size = 400 B.

measurement sensitivity, which is linearized around the last estimated value n_{k-1}. It is calculated by taking the derivative:

$$h_k = \frac{\mathrm{d}h(n)}{\mathrm{d}n}. \tag{17}$$

The error variance of the new estimation can be calculated recursively:

$$P_k = (1 - K_k h_k)(P_{k-1} + Q_k). \tag{18}$$

In the last step to complete the design of the EKF-based estimation method, it remains to specify several parameters including the state noise Q and R, which affects the convergence rate of the estimator to some extent. According to the general applications of the Kalman filter, Q and R are usually given the constant values. Thus, these parameters are given by simple tests in this paper. We set $Q = 0.6$, $R = 1$, and $P_0 = 100$ for relatively quick convergence performance. A more accurate parameter analysis and optimization are beyond the scope of this paper. Based on the EKF-based run-time channel state estimation method, it is simple to adjust the RAW parameters according to the estimated number of current competing stations $\hat{n}_k$.

3.3. RAW Adaption Algorithm. As discussed in Section 3.1, there exists a competing station number n_{opt} to optimize the network performance in each RAW slot. Since the number of current competing stations is obtained from the method introduced in Section 3.2, it is easy to adjust the RAW parameters to reallocate the distribution of the stations. Specifically, all stations should observe the channel for the total backoff period and estimate the number of active stations by the method introduced in Section 3.2. If the

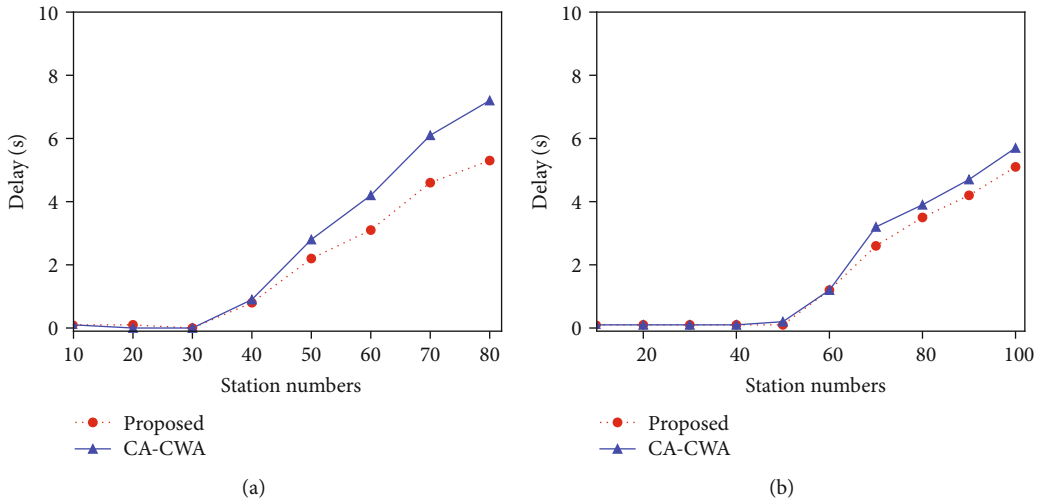

Figure 9: Performance of the average delay of each scheme in the second scenario. (a) Average delay comparison when the payload size = 250 B, (b) Average delay comparison when the payload size = 400 B.

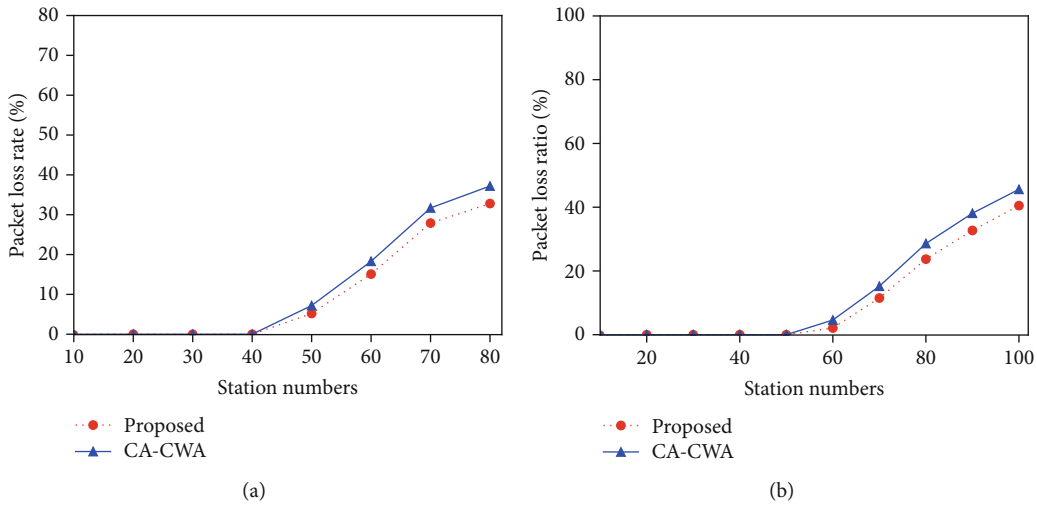

Figure 10: Performance of the packet loss rate of each scheme in the second scenario. (a) Packet loss rate comparison when the payload size = 250 B, (b) Packet loss rate comparison when the payload size = 400 B.

estimated value $\hat{n}_k$ is beyond the value of n_{opt} for a period T_p, then the active stations should be reallocated to other RAW groups evenly. Otherwise, the RAW group allocation should not be changed. The process of the RAW adaption algorithm is summarized in Algorithm 1.

4. Performance Evaluation

In this section, we present the simulation results and corresponding analysis to demonstrate the performance of the proposed RO-RAW scheme in the IEEE 802.11ah networks.

4.1. Simulation Setup. All the evaluations are performed in the NS-3 simulator with the 802.11ah module, which is proposed in [23, 24]. The simulation is based on a typical WLAN scenario, where one AP is located in the center, and other stations are distributed around the AP randomly. 10% of the stations are set inactive (associate with AP but transmit almost no data). The test topology example is given in Figure 4. In the simulation, the DCF parameters, including CW_{min} and CW_{max}, are set to the default values. Other PHY and MAC network parameters used in the simulation are shown in Table 2. Besides, in the algorithm design, initial iteration values have a significant impact on the convergence speed of the algorithm. In the simulation, we set $P_0 = 100$ and $n_0 = 1$ for quick convergence. The other algorithm parameters used in the simulation are also listed in Table 2.

The performance of the RAW mechanism can be evaluated in terms of three metrics: throughput, delay, and packet loss rate. Throughput is computed by the average received payload bytes by the AP per second. Delay is obtained by measuring the average time a packet experienced between the sender and the receiver. The packet loss is calculated by counting the number of packets not received, and the total

number of packets sent. Each simulation runs 300 s, which is enough to show the performance of the proposed RAW optimization scheme. Besides, to improve the reliability of the simulation results, each simulation was conducted five times, and the final results are the average of the five. The proposed RAW adaption scheme is compared with another RAW optimization scheme CA-CWA, which is also based on the channel status estimation. However, CA-CWA just tunes the contention window to improve the network performance, while RO-RAW adjusts the number of stations in a different RAW period.

4.2. Simulation Results. In the simulation, to validate the effectiveness of the proposed algorithms more precisely, the simulation is conducted in two simulation scenarios for two different RAW configurations. In the first scenario, the slot format subfield is filled with 1, and the RAW slots and C is set to 4 and 200. This configuration provides less slots in a RAW period, but a longer time for each slot.

Figures 5(a) and 5(b) show the throughput performance of the two RAW optimization schemes when varying the number of RAW stations. We observed that the network throughput associated with each algorithm increased as the number of RAW stations n increased until a maximum point ($n = 40$ in Figure 5(a) and $n = 50$ in Figure 5(b)), and the value begins to decline. It is the basic RAW throughput characteristics which has been proved in several researches [9, 25]. Figures 5(a) and 5(b) further show that RO-RAW has better performance on throughput than CA-CWA. We take the simulation results in Figure 5(a) for example. No matter how the number of nodes changes, RO-RAW has better performance than CA-CWA. However, after the throughput reaches the peak value ($n > 40$), RO-RAW has a more significant performance improvement. It is because CA-CWA is a contention window-based optimization scheme, which can only adjust the contention window of the station. But it cannot adjust the distribution of the stations in each RAW period and RAW slot. It means the load distribution of the stations is perhaps not balanced, and this issue may be worse when the number of inactive nodes is large. RO-RAW overcomes this problem and thus achieves a better performance.

Figures 6(a) and 6(b) illustrate the delay performance of the two RAW optimization schemes when varying the number of RAW stations. It can be observed that when the station numbers are relatively low ($n = 40$ in Figure 6(a) and $n = 50$ in Figure 6(b)), the average delay is almost zero. The reason is that the channel competition is not very severe in these cases. But when the number of stations gets higher, there is a significant increase in the average delay due to the severe channel competition. Figures 6(a) and 6(b) further show that our proposed scheme also has better performance on average delay than CA-CWA. When the channel gets crowded, RO-RAW is able to estimate the channel status and reallocated the RAW slots. Thus, it has a better delay performance when the number of stations is relatively higher compared with CA-CWA. The same conclusion can be also drawn when analyzing the packet loss performance (Figures 7(a) and 7(b)) of the two schemes.

In the second scenario, the slot format subfield is filled with 0, and the RAW slots and C are set to 8 and 50. This configuration provides a larger number of slots in a RAW period, but a shorter time for each slot, compared with the first scenario. However, the main conclusions are similar to the conclusions obtained in the first scenario.

As shown in Figures 8(a) and 8(b), the peak value and other values are changed compared with the values in the first scenario because the number of the RAW slots has been increased and the value of C is decreased. But the general trend of the throughput curve does not change. RO-RAW still shows its performance advantages than CA-CWA, especially when the number of stations is relatively large. The same conclusion can be also drawn when analyzing the delay (Figures 9(a) and 9(b)) and packet loss performance (Figures 10(a) and 10(b)) of the two schemes in the second scenario.

5. Conclusion

In this paper, we propose a run-time RAW optimization scheme with the extended Kalman filter, namely, RO-RAW, to improve the RAW performance in IEEE 802.11ah networks. RO-RAW first estimates the current channel status and returns the estimated station numbers by the EKF method. Based on the estimated number of competing stations, RO-RAW adjusts the RAW parameters to the optimal parameter settings which are calculated in advance. To validate the performance of the proposed scheme, we compared it with another RAW optimization scheme CA-CWA in the NS-3 simulator. The simulation results show that RO-RAW substantially improves the throughput, latency, and packet loss performance compared with CA-CWA in different simulation scenarios. The results further show that, when the channel is relatively congested, RO-RAW improves the performance of RAW more significantly.

Data Availability

The data used to support the findings of this study are included in the article.

Conflicts of Interest

The authors declare that they have no conflicts of interest.

Acknowledgments

This work was supported by the Major National Science and Technology Program of China: High-Grade Numerical Control Machine Tools and Basic Manufacturing Equipment (No. 2019ZX04003001-006).

References

[1] Y. Cheng, Y. Zhang, P. Ji, W. Xu, Z. Zhou, and F. Tao, "Cyber-physical integration for moving digital factories forward towards smart manufacturing: a survey," *The International Journal of Advanced Manufacturing Technology*, vol. 97, no. 1-4, pp. 1209–1221, 2018.

[2] M. Sharp, R. Ak, and T. Hedberg Jr., "A survey of the advancing use and development of machine learning in smart

manufacturing," *Journal of Manufacturing Systems*, vol. 48, pp. 170–179, 2018.

[3] R. Masoni, F. Ferrise, M. Bordegoni et al., "Supporting remote maintenance in industry 4.0 through augmented reality," *Procedia Manufacturing*, vol. 11, pp. 1296–1302, 2017.

[4] C. Zhao, N. Kang, J. Li, and J. A. Horst, "Production control to reduce starvation in a partially flexible production-inventory system," *IEEE Transactions on Automatic Control*, vol. 63, no. 2, pp. 477–491, 2018.

[5] M. Chui, M. Miremadi, J. Bughin, K. George, P. Willmott, and M. Dewhurst, "A future that works: Ai, automation, employment, and productivity," vol. 60, McKinsey Global Institute Research, Technical Report, 2017.

[6] Y. Cheng, D. Yang, and H. Zhou, "Det-WiFi: a multihop TDMA MAC implementation for industrial deterministic applications based on commodity 802.11 hardware," *Wireless Communications and Mobile Computing*, vol. 2017, Article ID 4943691, 10 pages, 2017.

[7] Y. Cheng, D. Yang, H. Zhou, and H. Wang, "Adopting IEEE 802.11 MAC for industrial delay-sensitive wireless control and monitoring applications: a survey," *Computer Networks*, vol. 157, pp. 41–67, 2019.

[8] V. Baños-Gonzalez, M. S. Afaqui, E. Lopez-Aguilera, and E. Garcia-Villegas, "IEEE 802.11ah: a technology to face the IoT challenge," *Sensors*, vol. 16, no. 11, p. 1960, 2016.

[9] O. Raeesi, J. Pirskanen, A. Hazmi, T. Levanen, and M. Valkama, "Performance evaluation of IEEE 802.11ah and its restricted access window mechanism," in *2014 IEEE International Conference on Communications Workshops (ICC)*, pp. 460–466, Sydney, NSW, Australia, 2014.

[10] E. Khorov, A. Krotov, and A. Lyakhov, "Modelling machine type communication in IEEE 802.11ah networks," in *2015 IEEE International Conference on Communication Workshop (ICCW)*, pp. 1149–1154, London, UK, 2015.

[11] M. Z. Ali, J. Misic, and V. B. Misic, "Performance evaluation of heterogeneous IoT nodes with differentiated QoS in IEEE 802.11ah RAW mechanism," *IEEE Transactions on Vehicular Technology*, vol. 68, no. 4, pp. 3905–3918, 2019.

[12] T. Sakurai and H. L. Vu, "MAC access delay of IEEE 802.11 DCF," *IEEE Transactions on Wireless Communications*, vol. 6, no. 5, pp. 1702–1710, 2007.

[13] T. Adame, A. Bel, B. Bellalta, J. Barcelo, and M. Oliver, "IEEE 802.11AH: the wifi approach for M2M communications," *IEEE Wireless Communications*, vol. 21, no. 6, pp. 144–152, 2014.

[14] W. Sun, M. Choi, and S. Choi, "IEEE 802.11 ah: a long range 802.11 WLAN at sub 1 GHz," *Journal of ICT Standardization*, vol. 1, no. 1, pp. 83–108, 2017.

[15] E. Khorov, A. Lyakhov, A. Krotov, and A. Guschin, "A survey on IEEE 802.11ah: an enabling networking technology for smart cities," *Computer Communications*, vol. 58, pp. 53–69, 2015.

[16] T.-C. Chang, C.-H. Lin, K. C.-J. Lin, and W.-T. Chen, "Traffic-aware sensor grouping for IEEE 802.11ah networks: regression based analysis and design," *IEEE Transactions on Mobile Computing*, vol. 18, no. 3, pp. 674–687, 2019.

[17] C. W. Park, D. Hwang, and T.-J. Lee, "Enhancement of IEEE 802.11ah MAC for M2M communications," *IEEE Communications Letters*, vol. 18, no. 7, pp. 1151–1154, 2014.

[18] Y. Cheng, H. Zhou, and D. Yang, "Ca-CWA: channel-aware contention window adaption in IEEE 802.11ah for soft real-time industrial applications," *Sensors*, vol. 19, no. 13, p. 3002, 2019.

[19] G. Bianchi, "Performance analysis of the IEEE 802.11 distributed coordination function," *IEEE Journal on Selected Areas in Communications*, vol. 18, no. 3, pp. 535–547, 2000.

[20] G. Bianchi and I. Tinnirello, "Remarks on IEEE 802.11 DCF performance analysis," *IEEE Communications Letters*, vol. 9, no. 8, pp. 765–767, 2005.

[21] G. Bianchi and I. Tinnirello, "Kalman filter estimation of the number of competing terminals in an IEEE 802.11 network," in *IEEE INFOCOM 2003. Twenty-second Annual Joint Conference of the IEEE Computer and Communications Societies (IEEE Cat. No.03CH37428)*, vol. 2, pp. 844–852, San Francisco, CA, USA, 2003.

[22] I. Tinnirello and A. Sgora, "A Kalman filter approach for distinguishing channel and collision errors in IEEE 802.11 networks," in *IEEE GLOBECOM 2008-2008 IEEE Global Telecommunications Conference*, pp. 1–5, New Orleans, LO, USA, 2008.

[23] L. Tian, S. Deronne, S. Latré, and J. Famaey, "Implementation and validation of an IEEE 802.11 ah module for ns-3," in *Proceedings of the Workshop on ns-3*, pp. 49–56, Seattle WA USA, 2016.

[24] L. Tian, A. Šljivo, S. Santi, E. De Poorter, J. Hoebeke, and J. Famaey, "Extension of the IEEE 802.11 ah ns-3 simulation module," in *Proceedings of the 10th Workshop on ns-3*, pp. 53–60, Surathkal India, 2018.

[25] L. Tian, J. Famaey, and S. Latré, "Evaluation of the IEEE 802.11ah restricted access window mechanism for dense IoT networks," in *2016 IEEE 17th International Symposium on A World of Wireless, Mobile and Multimedia Networks (WoWMoM)*, pp. 1–9, Coimbra, Portugal, 2016.

Hindawi
Wireless Communications and Mobile Computing
Volume 2020, Article ID 9517840, 16 pages
https://doi.org/10.1155/2020/9517840

Research Article

Design of Improved BP Decoders and Corresponding LT Code Degree Distribution for AWGN Channels

Lei Zhang and Li Su

Information Engineering College, Capital Normal University, Beijing 100048, China

Correspondence should be addressed to Lei Zhang; 6576@cnu.edu.cn

Received 28 January 2020; Revised 16 September 2020; Accepted 3 October 2020; Published 20 October 2020

Academic Editor: Chaoyun Song

This paper presents the performance of a hard decision belief propagation (HDBP) decoder used for Luby transform (LT) codes over additive white Gaussian noise channels; subsequently, three improved HDBP decoders are proposed. We first analyze the performance improvement of the sorted ripple and delayed decoding process in a HDBP decoder; subsequently, we propose ripple-sorted belief propagation (RSBP) as well as ripple-sorted and delayed belief propagation (RSDBP) decoders to improve the bit error rate (BER). Based on the analysis of the distribution of error encoded symbols, we propose a ripple-sorted and threshold-based belief propagation (RSTBP) decoder, which deletes low-reliability encoded symbols, to further improve the BER. Degree distribution significantly affects the performance of LT codes. Therefore, we propose a method for designing optimal degree distributions for the proposed decoders. Through simulation results, we demonstrate that the proposed RSBP and RSDBP decoders provide significantly better BER performances than the HDBP decoder. RSDBP and RSTDP combined with the proposed degree distributions outperformed state-of-the-art degree distributions in terms of the number of encoded symbols required to recover an input symbol correctly (NERRIC) and the frame error rate (FER). For a hybrid decoder formulated by combining RSDBP with a soft decision belief propagation decoder, the proposed degree distribution outperforms the other degree distributions in terms of decoding complexity.

1. Introduction

The Luby transform (LT) codes proposed in [1] are the first practical fountain code that performs well on reliable communications over a binary erasure channel (BEC). Successful hard decision belief propagation (HDBP) decoding is possible when$(1+\varepsilon)k$ encoded symbols are available, where ε is the overhead of decoding. With the advantage of being rateless, LT codes have been introduced in broadcast services and noisy channels [2]. The performance of LT codes over additive white Gaussian noise (AWGN) channels has been investigated in [3]. To improve decoding performance, soft information is used in a soft decision belief propagation (SDBP) decoder, which is used as the decoding algorithm over noisy channels [4].

Different strategies have been proposed to improve the performance of LT codes over AWGN channels. A Gauss–Jordan-elimination-assisted belief propagation (BP) decoder was proposed to address the premature termination of BP decoding [5]. However, it is only practical for short LT codes. Generally, an SDBP decoder begins when all encoded symbols are available. Therefore, in greedy spreading serial decoding, encoded symbols are processed at once, and messages propagated greedily to improve the convergence speed [6]. However, the increase in decoding complexity was demonstrated in [5, 6]. A cross-level decoding scheme that combines LT codes with low-density parity check (LDPC) codes was proposed [7]. Although this method provided an effective decoding scheme, it required additional bit decoding from the LDPC, thereby increasing the decoding complexity. The piggybacking BP decoding algorithm, which decreases the decoding overhead and decoding delay, was proposed for repeated accumulated (RA) rateless codes [8]. However, it is only useful for RA rateless codes. A parallel soft iterative decoding algorithm was proposed for satellite systems [9]. Similar to the study in [7], it is only effective when combining LDPC codes with LT codes in the physical layer. A low-complexity BP decoder was proposed to improve

Pseudocode of LT encoding
Input: input symbols $X = (x_1, x_2, \cdots, x_k)$, degree distribution $\Omega(d)$
Output: an encoded symbol c
initialize an encoded symbol c=0
select a degree d from [1, k] according to $\Omega(d)$
select d different input symbols from X and add to a neighbor set V
for input symbol v in V**do**
    c=c XOR v
end for
return$c$

Algorithm 1.

performance by deleting low-reliability symbols at the cost of a slight transmission efficiency loss [10]. The BP-based algorithm is combined with the log likelihood ratio- (LLR-) based adaptive demodulation (ADM) algorithm to further reduce the decoding complexity [11]. The maximum a posteriori probability-based ADM algorithm was proposed to improve performance by discarding incorrect bits [12]. An adaptive decoding algorithm was proposed to reduce the decoding complexity by reducing the number of active check nodes [13], which degraded the performance of LT codes. In [10–13], the decoding complexity was reduced at the expense of increasing overhead because unreliable symbols were deleted. The trade-off between performance and decoding complexity was analyzed in [14]. Reducing the decoding complexity is important for the practicability of LT codes over noisy channels. However, the decoding complexity of the SDBP decoder remains high.

Several degree distributions have been proposed for LT codes over AWGN channels. An optimization process is formulated to design a new degree distribution, which improves the performance of LT codes over AWGN channels [15]. Three types of check-node degree distributions are proposed to improve the performance of systematic LT codes over AWGN channels [16]. A novel optimization model was proposed to design degree distributions over AWGN multiple access channels [17]. A ripple-based design of the degree distribution for AWGN channels was proposed in [18]. However, designing a good degree distribution and improving the performance in HDBP decoding over noisy channels remain an open problem.

Compared with SDBP decoding, HDBP decoding significantly reduced decoding complexity, which is extremely important for battery-powered equipment. The use of HDBP decoding can effectively reduce the decoding complexity of the hybrid decoding scheme, in which SDBP decoding will be invoked when HDBP decoding fails. Herein, the performance of HDBP decoding is analyzed, and improved HDBP decoders and their corresponding degree distributions are proposed. First, we investigate the ripple size throughout the decoding process and argue that sorting encoded symbols in ripple improves decoding performance; subsequently, we propose a ripple-sorted BP (RSBP) decoder. Based on the RSBP decoder, we discovered that with more encoded symbols available before decoding started, the decoding performance improved. Hence, we

Pseudocode of hard decision BP decoding
Input: encoded symbols received from channels
Output: recovered input symbols $\widehat{X}$
initialize ripple R as an empty queue
initialize recovered input symbols $\widehat{X}$ as an array
initialize waited encoded symbols Y as an array
whilesizeof$(\widehat{X}) < k$**do**
    receive an encoded symbol y from channels
    XORs$(\widehat{X}, y)$
    degree$(y) == 1$?push(R, y): push(Y, y)
    whilesizeof$(R) > 0$**do**
        dequeue an input symbol $\widehat{x}$ from R
        push$(\widehat{X}, x)$
        for encoded symbol y in Y**do**
            XOR$(y, \widehat{x})$
            degree$(y) == 1$?push(R, y): push(Y, y)
        end for
    end while
end while
return$\widehat{X}$

Algorithm 2.

propose an improved BP decoder known as a ripple-sorted and delayed BP (RSDBP) decoder. Based on the analysis of the distribution of error encoded symbols, we argue that low-reliability encoded symbols should be deleted to improve decoding performance and propose a ripple-sorted and threshold-based BP (RSTBP) decoder. Second, by analyzing the random walk model, we propose a method to generate a set of candidate ripple-size evaluations. A ripple-based design of degree distribution known as the generalised degree distribution algorithm (GDDA) is used to generate the degree distribution [19]. Based on the Monte Carlo method, the optimal degree distribution for a specific BP decoder is achieved. Simulation results demonstrated that our proposed RSBP and RSDBP decoders outperformed the BP decoder in terms of the bit error rate (BER) performance. Additionally, RSDBP and RSTDP combined with the proposed degree distributions outperformed state-of-the-art degree distributions in terms of the number of encoded symbols required to recover an input symbol correctly (NERRIC) and the frame error rate (FER). For the hybrid decoder formulated by combining

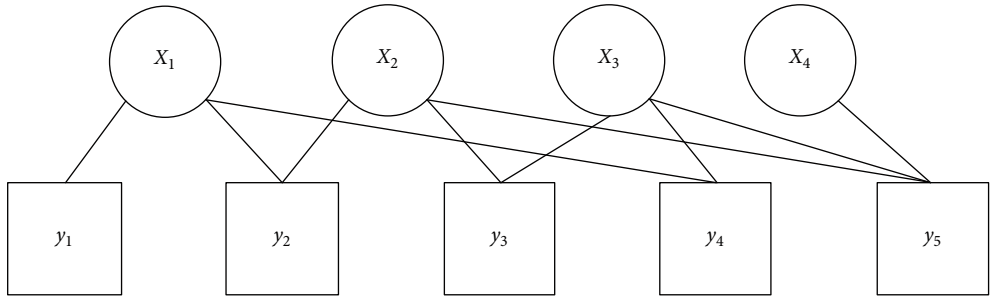

Figure 1: An example of tanner graph.

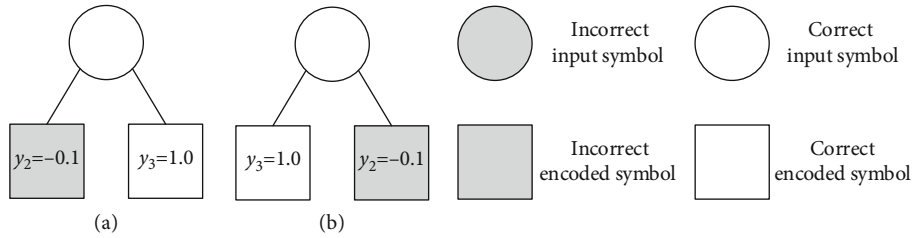

Figure 2: (a) lower-reliable encoded symbol arrived first. (b) higher-reliable encoded symbol arrived first.

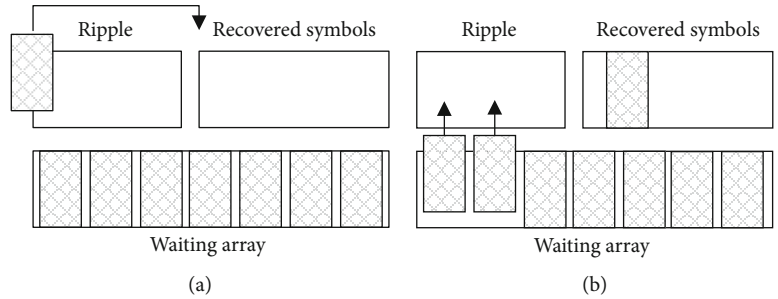

Figure 3: (a) Get a symbol from ripple and XOR with encoded symbols in waiting array. (b) Add the degree-one encoded symbols to the ripple.

RSBP with an SDBP decoder, the proposed degree distribution outperformed state-of-the-art degree distributions in terms of decoding complexity.

The remainder of this paper is organised as follows. In Section 2, a review of the system model and the encoding and decoding of LT codes are provided. In Section 3, the performance of HDBP decoding is analyzed. In Section 4, our RSBP, RSDBP, and RSTBP decoders are presented. In Section 5, the performance of the proposed decoders is analyzed. In Section 6, a method to generate the optimal degree distribution for a specific BP decoder is proposed. In Section 7, our experimental design is outlined, and the efficiency of the proposed decoders and the proposed degree distribution are demonstrated by experimental results. Finally, our study is summarised as follows.

2. Background

2.1. System Model. Information messages must be transmitted from the source to the destination over AWGN channels. Messages are partitioned into blocks, and each block is partitioned into symbols. The input symbols of the LT codes are denoted as $X = (x_1, x_2, \cdots, x_k)$, which is a combination of original symbols and a cyclic redundancy check (CRC). Typically, a single input symbol can be one bit or even a packet. For simplicity, one bit is regarded as an input symbol in this study. At the source, a stream of encoded symbols $C = (c_1, c_2, \cdots, c_N, \cdots)$ is generated from k input symbols. The encoded symbol c_j is modulated by the binary phase shift keying and transmitted to the destination independently as s_i. At the destination, the output of the AWGN channels for each symbol s_j is as follows:

$$y_j = s_j + n_j, \tag{1}$$

where $n_i \sim N(0, N_0/2)$, with $N(\cdot)$ being the normal distribution. At the destination, $(1+\varepsilon)k$encoded symbols are received to recover the k input symbol. Generally, a soft

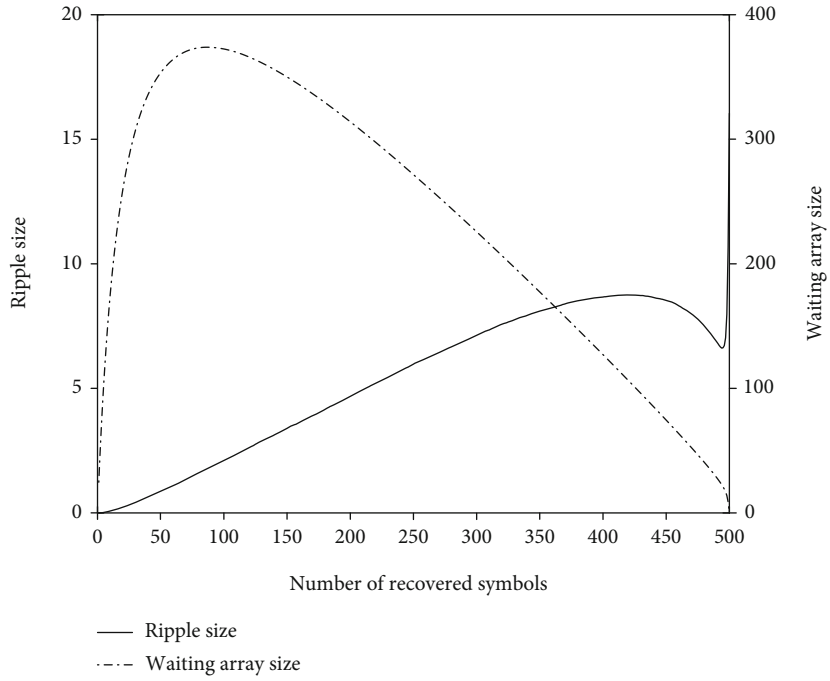

Figure 4: Ripple size and waiting array size as a function of number of recovered symbols for $k = 500$.

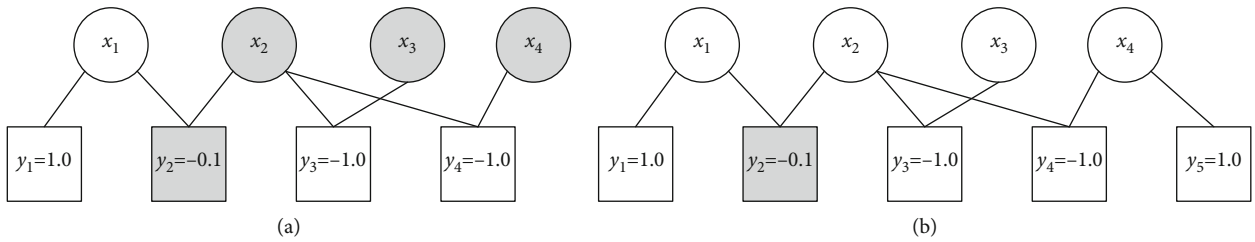

Figure 5: (a) BP decoder. (b) Delayed BP decoder.

demodulation is performed on encoded symbols. The log-likelihood ratio (LLR) of the encoded symbol is defined as

$$L\left(y_j\right) = \ln \frac{\Pr\left(s_j = 1 \middle| y_j\right)}{\Pr\left(s_j = 0 \middle| y_j\right)}. \quad (2)$$

In this study, HDBP decoding was concatenated with SDBP decoding, which can reduce decoding complexity. The encoded symbols with LLR were passed to HDBP decoding, and the output of decoding was verified by a CRC. Decoding is successful if it passes; otherwise, SDBP decoding is invoked.

2.2. BP Encoding. Given k input symbols $X = (x_1, x_2, \cdots, x_k)$ and a degree distribution$\Omega(d)$, $d = 1, 2, \cdots, k$, subsequently, an infinite number of encoded symbols are generated according to Algorithm 1.

2.3. Hard Decision BP Decoding. BP decoding is widely used for LT codes, which are implemented in different variants for different channels. HDBP decoding is used in BEC, whereas SDBP decoding is used in noisy channels. We discovered that HDBP decoding concatenated with SDBP decoding can be used in noisy channels, which will be analyzed herein. In HDBP decoding, encoded symbols participating in the decoding process are considered as correct symbols. Hence, simple inversed XOR operations are performed. The pseudocode of HDBP decoding is shown in Algorithm 2, where decoding is performed at once. Decoding is completed when sufficient encoded symbols are received.

3. Analysis of Hard Decision BP Decoding

For HDBP decoding, suppose n encoded symbols $y_1, y_2, \cdots, y_n$ are sufficient to recover k input symbols $x_1, x_2, \cdots, x_k$. The relationship between the input symbols and encoded symbols can be expressed by a Tanner graph. For example, the Tanner graph of four input symbols and five encoded symbols is shown in Figure 1.

3.1. Error Probability of Hard Decision BP Decoding. Let $\rho(y_j)$ denotes the error probability of the encoded symbol y_j.

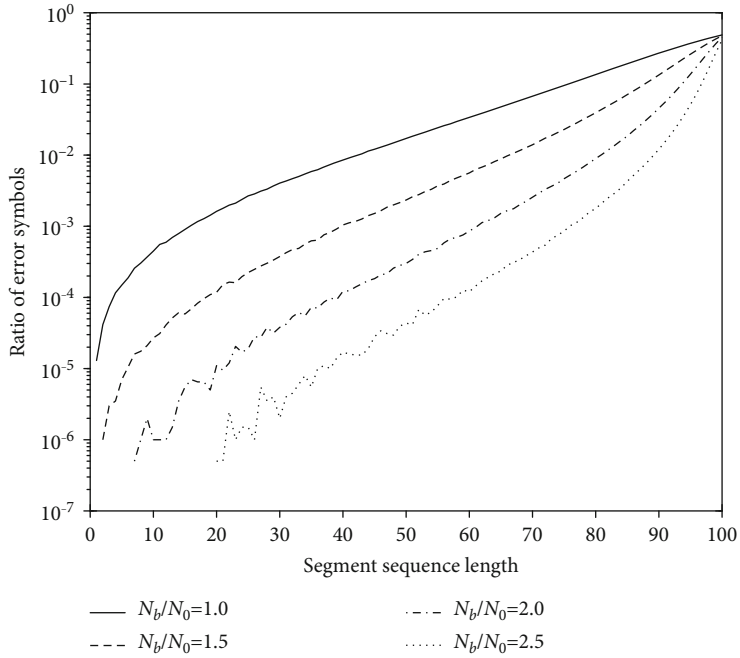

Figure 6: Ratio of error symbols as a function of segment sequence length.

```
Pseudocode of calculating threshold
Input: Probability δ
Output: Threshold t
initialize an ordered array S
initialize n=0
whilei<Mdo
    generate a packet p and add to S
    ifp is error then
        n=n+1
    end if
    i++9:  end while
e = n × δ
i=M
whilei ≥ 0do
    p=S[i]
    ifp is error then
        e=e − 1
    end if
    ife<= 0 do
        t = Abs(LLR(S[i]))
        break
    end if
    i−
end while
returnt
```

Algorithm 3.

Generally, $\rho(y_1) < \rho(y_2)$, if $|L(y_1)| > |L(y_2)|$ and vice versa. A decreasing function exists such that

$$\rho\left(y_j\right) = f\left(\left|L\left(y_j\right)\right|\right). \tag{3}$$

Let $\rho(x_i)$ denotes the error probability of the input symbol x_i if it is recovered by the encoded symbol y_j, which is shown in formula (4).

$$\rho(x_i) = \begin{cases} \rho\left(y_j\right) & d\left(y_j\right) = 1 \\ \max\left(\rho\left(y_j\right), \rho\left(N\left(y_j, x_i\right)\right)\right) & d\left(y_j\right) > 1 \end{cases}, \tag{4}$$

where $N(y_j, x_i)$ denotes the neighbors of y_j except x_i. In HDBP decoding, input symbols are recovered individually in sequence. In Figure 1, (x_1, x_2, x_3, x_4) is a reasonable sequence of input symbols recovered in decoding, and it is not the only one. For a sequence, we define $Q(x_i)$ as the set of encoded symbols that are the only neighbors of the input symbol x_i at the end of decoding. For the sequence (x_1, x_2, x_3, x_4), we have $Q(x_1) = \{y_1\}$,$Q(x_2) = \{y_2, y_3\}$, $Q(x_3) = \{y_4\}$, and $Q(x_4) = \{y_5\}$. We discovered that x_2 can be recovered by both y_2 and y_3. Let$Q'(x_i)$ denotes the set of encoded symbols supported to decode x_i. We have $Q'(x_2) = \{y_1, y_2\}$ if it is recovered by y_2; otherwise, $Q'(x_2) = \{y_1, y_4, y_3\}$. Therefore, we have

$$\rho(x_i) = \max\left(\rho\left(Q'(x_i)\right)\right). \tag{5}$$

Let $\mathbb{Q} = \{Q'(x_1), Q'(x_2), \cdots, Q'(x_k)\}$; the error probability of HDBP decoding is shown in formula (6).

$$\rho(\mathbb{Q}) = 1 - \prod_{i=1}^{k} 1 - \rho(x_i). \tag{6}$$

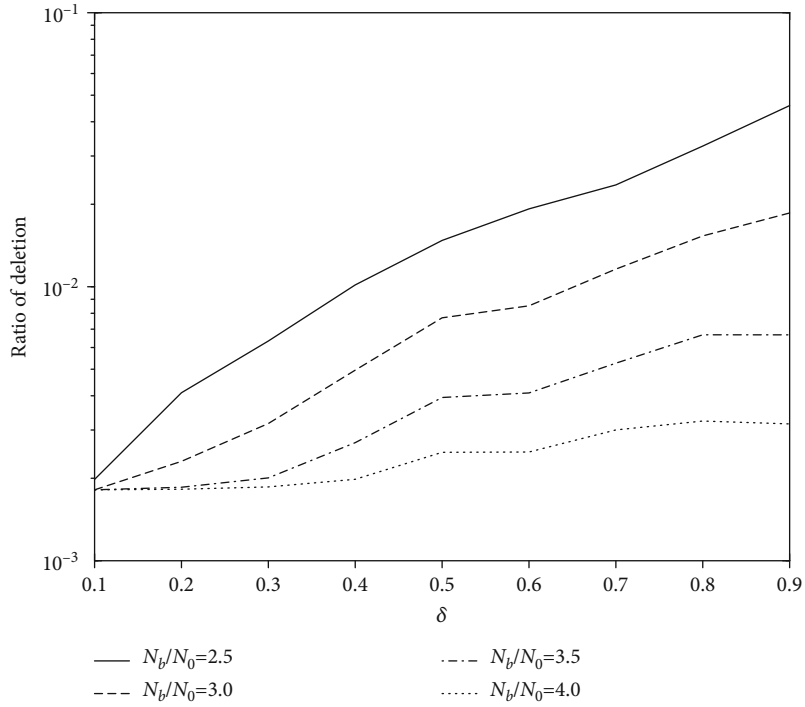

Figure 7: Ratio of deletion as a function of δ.

Table 1: Computational complexities of four decoders.

	BP	RSBP	RSDBP	RSTBP
XOR	$O(\bar{d}k)$	$O(\bar{d}k)$	$O(\bar{d}k)$	$O(\bar{d}k)$
SORT	–	$O(k \log R_{\max})$	$O(k \log R_{\max})$	$O(k \log R_{\max})$

Table 2: Numerical results of computational complexities with k=256.

	BP	RSBP	RSDBP	RSTBP
XOR	2156.27	2156.60	2157.47	2157.52
SORT	–	560.89	571.29	571.30

For a Tanner graph, several different $\mathbb{Q}$ exist. Our aim is to optimize the supported set of each input symbol to reduce the error probability of decoding. For example, x_2 should be recovered by a supported set with a lower error probability. For example, the Tanner graph with the LLR value is shown in Figure 2. The LLRs of y_2 and y_3 were set as -0.1 and 0.2, respectively. As shown in Figure 2(a), the input symbol is incorrect if it is recovered by y_2. Otherwise, it is correct if it is recovered by y_3, which is shown in Figure 2(b).

3.2. Improvement in Error Probability. In HDBP decoding, each input symbol is recovered by $1+\varepsilon$ encoded symbols on average. In other words, ε input symbols will be recovered by two encoded symbols. This is a valid assumption because the probability of an input symbol recovered by more than two encoded symbols is small. Consider the case in which both encoded symbols y_1 and y_2 have only the neighbor of the input symbol $x_i$at the end of decoding. The error probability of x_i is shown in formula (7) if it is recovered by y_1 or y_2 at random.

$$\rho(x_i) = \frac{1}{2}\sum_{j=1}^{2} \max\left(\rho\left(y_j\right), \rho\left(N\left(y_j, x_i\right)\right)\right). \tag{7}$$

Otherwise, the error probability of x_i is as shown in formula (8) if it is recovered by the encoded symbol with a lower error probability.

$$\rho(x_i) = \min\left(\max\left(\rho(y_1), \rho(N(y_1, x_i))\right), \max\left(\rho(y_2), \rho(N(y_2, x_i))\right)\right). \tag{8}$$

Therefore, the error probability of decoding is reduced if the encoded symbol with a lower error probability is selected to recover the corresponding input symbol.

4. Improved Hard Decision BP Decoders

As shown, the error probability of the input symbol can be reduced by selecting the support set with a lower error probability. In this section, we propose three improved HDBP decoders to reduce the probability of decoding.

4.1. Ripple-Sorted BP Decoder. The structure of the HDBP decoder is shown in Figure 3. First, degree-one encoded symbols are added to the ripple to start the decoding. The symbols in the ripple are processed individually until the ripple is empty. Two methods can be used to reduce the error probability of recovered symbols in the decoding process.

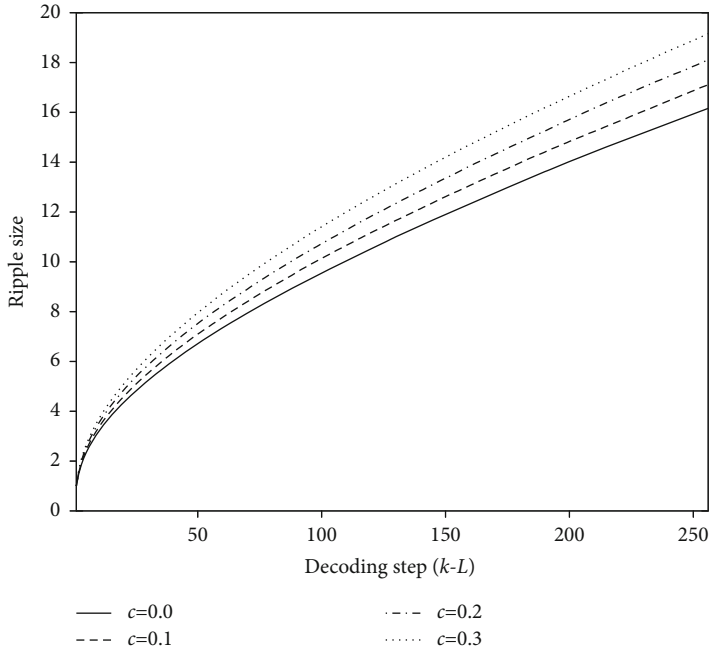

Figure 8: Ripple size as a function of decoding step for different c.

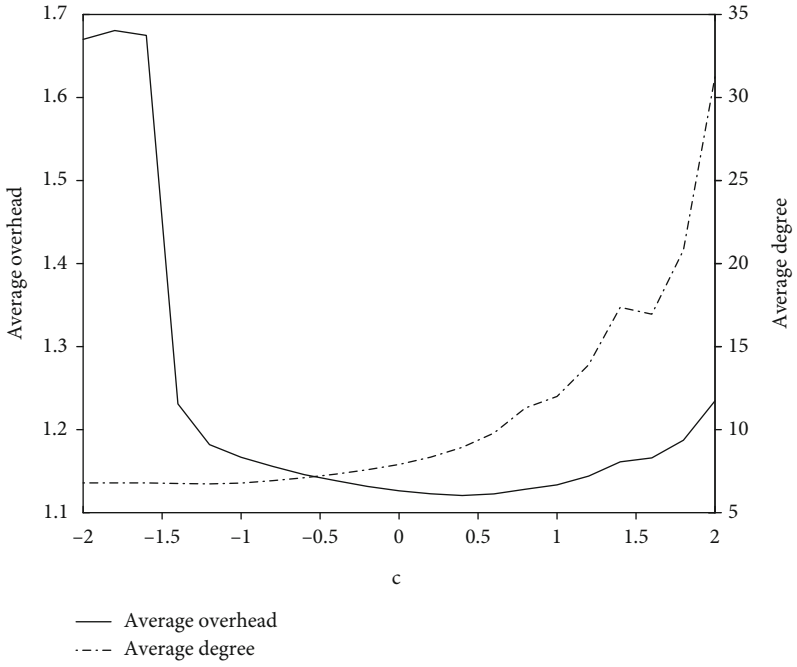

Figure 9: Average overhead and average degree as a function of c.

The first one is to sort symbols in the ripple. The second one is to sort symbols in the waiting array.

Lemma 1. *Sorting the symbols in the waiting array can be replaced by sorting the symbols in the ripple, and both the RSBP decoder and waiting-array-sorted BP (WSBP) decoder can reduce the error probability of decoding.*

Proof. The symbols released in each step depend only on the symbol being processed and the symbols in the waiting array; they are irrelevant to the order of the waiting array. The released symbols are sorted in the WSBP decoder, whereas the released symbols are sorted after being added to the ripple in the RSBP decoder. We assume that two symbols y_1 and y_2 are released simultaneously and $|L(y_1)| > |L(y_2)|$ without loss of generality. If the remaining neighbor of both y_1 and y_2 is x_1,

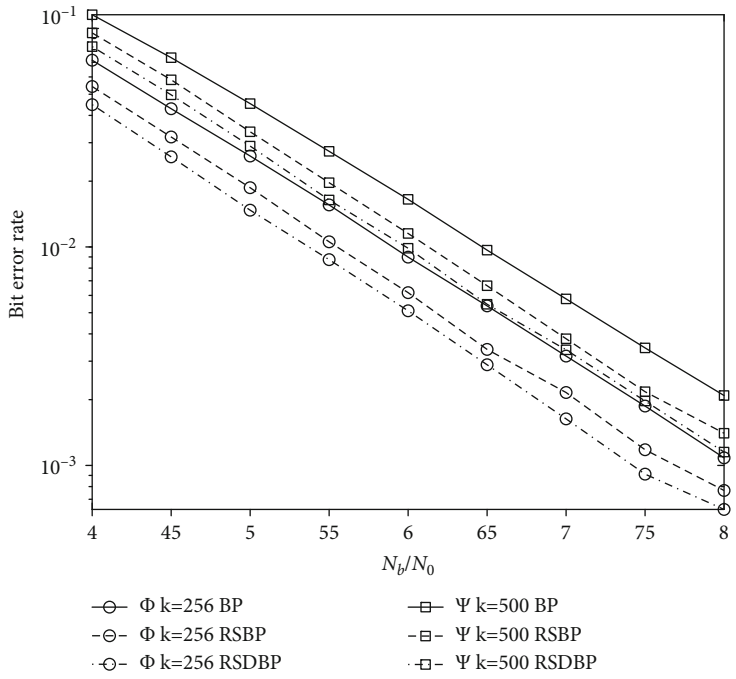

Figure 10: BER as a function of N_b/N_0.

Table 3: Computational time of three decoders.

k	BP (ms)	RSBP (ms)	RSDBP (ms)
256	0.766	0.768	0.772
500	3.069	3.081	3.088

Table 4: Optimal parameter values and average degree of the proposed degree distribution Ω.

k	$m_{\max}$	c	$\bar{d}$	ε
256	3	0.3	7.68	0.1614
500	4	0.4	9.08	0.1196

Table 5: Average degree of compared degree distributions.

	k	$\bar{d}$	ε
Φ	256	8.11	0.1636
Ψ	500	16.10	0.1381

the error probability of x_1 is reduced in both the RSBP and WSBP decoders. Hence, Lemma 1 is proven.

Lemma 2. *For HDBP decoding, sorting symbols in ripple is better than sorting symbols in the waiting array.*

Proof. We assume that two symbols y_1 and y_2 exist in the ripple and $|L(y_1)| > |L(y_2)|$. The remaining neighbors of y_1 and y_2 are x_1 and x_2, respectively. It is clear that the error probability of the symbol released in this step is equal to or greater than the error probability of y_1. Therefore, the symbol with minimal error probability should recover the corresponding input symbol in each decoding step. However, the error probability of the symbol released in the next steps may be less than the error probability of y_2. If y_3, $|L(y_3)| > |L(y_2)|$ is released and added to the ripple when y_1 is processed, the remaining neighbor of y_3 will be x_2. The input symbol x_2 should be recovered by y_3. In this case, the performance of the RSBP decoder is better than that of the WSBP decoder. Hence, Lemma 2 is proven.

he design of the ripple size evolution assumes that the ripple size should be remain more than one throughout the decoding process. Therefore, in theory, the performance of the RSBP decoder is better than that of the HDBP decoder. To analyze the performance improvement, the ripple size and waiting array size are analyzed by Monte Carlo simulations. The result is shown in Figure 4 with $k = 500$ and the degree distribution in [18], where the average ripple size and average waiting array size in each decoding step are calculated by 100000 simulations. The percentage of ripple sizes greater than one exceeds 80%, which means that symbols in the ripple can be sorted based on the absolute LLR value. As shown in Figure 4, the waiting array size is large at the beginning of decoding, which means that the probability of y_1 and y_2 released in the same decoding step is high. Additionally, we discovered that the number of symbols in the waiting array is larger than that in the ripple exception of $n_r \geq 499$. Therefore, sorting symbols in ripple is more efficient than sorting symbols in a waiting array. The proposed RSBP decoder can be implemented by replacing push (R, y) with pushAndSort (R, y) in Algorithm 2.

4.2. Ripple-Sorted and Delayed BP Decoder. For HDBP decoding, the number of symbols released in each step

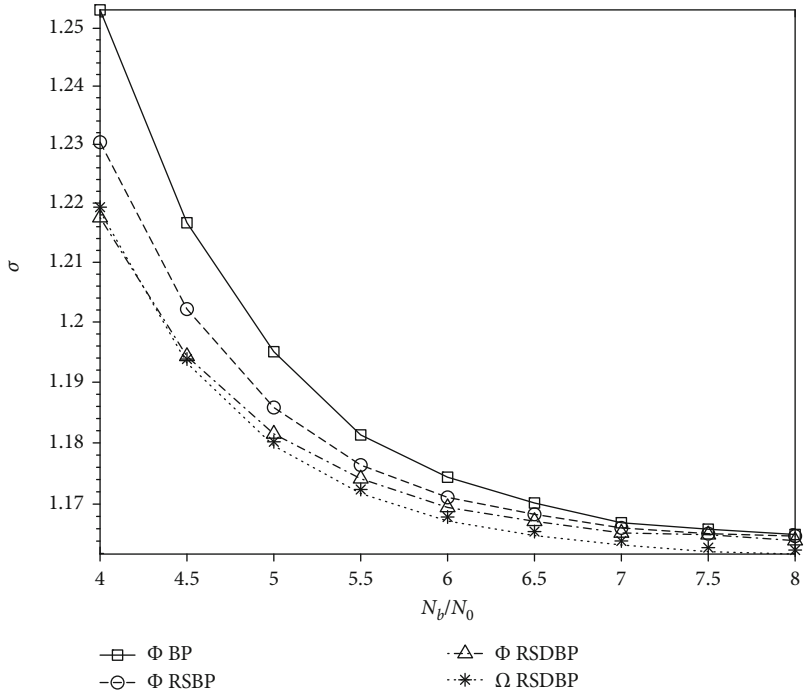

Figure 11: σ as a function of SNR for $k = 256$.

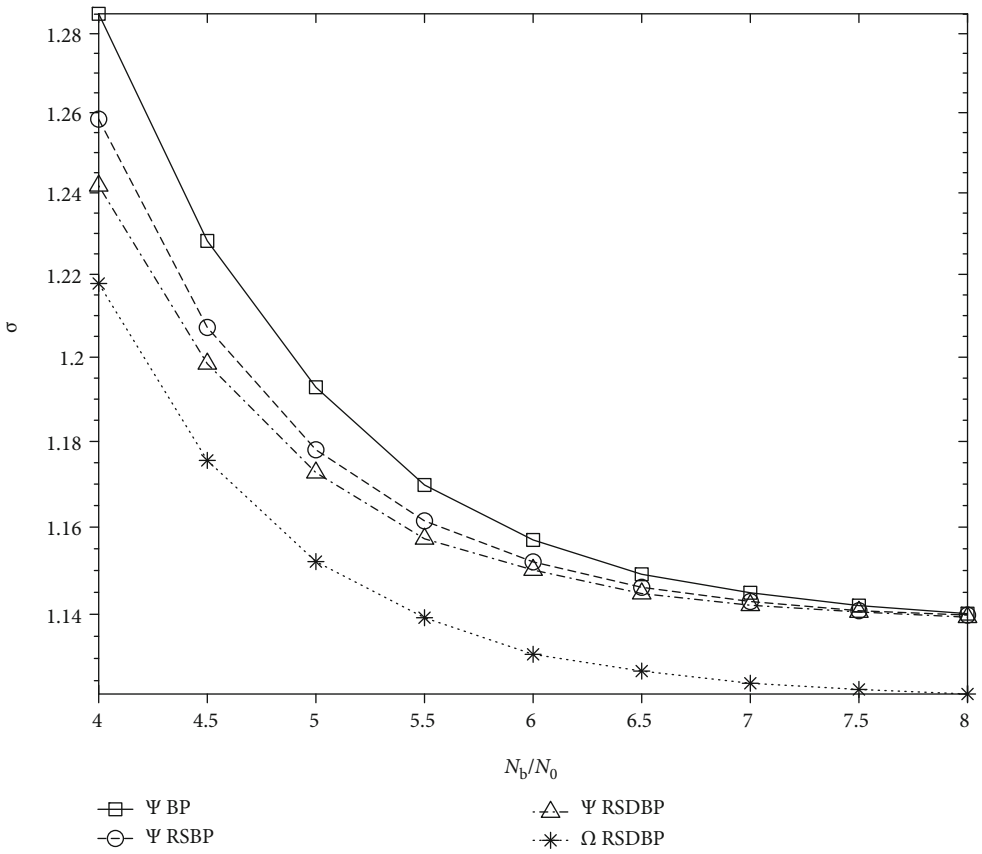

Figure 12: σ as a function of SNR for $k = 500$.

increased with the size of the waiting array. Therefore, the performance increased with the size of the waiting array. For example, as shown in Figure 5(a), the input symbol x_2 recovered by y_2 is incorrect because y_2 is incorrect. As a result of error propagation, x_3, x_4 are also incorrect. In Figure 5(b), the decoding process is delayed until sufficient encoded symbols are available. The input symbol x_4 recovered by y_5 is correct because y_5 is correct; therefore, x_3, x_4 are correct as well. Consequently, the encoded symbol y_2 with a high error probability is redundant.

Lemma 3. *The more encoded symbols are available before decoding starts, the better is the BER performance of decoding.*

Proof. We assume that the input symbol x can be recovered by one of y_1, y_2 with $|L(y_1)| < |L(y_2)|$. If y_1 is processed before y_2 is available, then the error probability of x is reduced if decoding is delayed until y_2 is available. If more encoded symbols are available before decoding starts, the error probability of more input symbols will be reduced. Hence, Lemma 3 is proven.

Based on Lemma 3, we propose our RSDBP decoder, which delays the start of the decoding until $k(1+\varepsilon)$ encoded symbols are received. The parameter ε depends on k and the degree distribution. For example, ε is set as 0.16 for $k = 256$ with a degree distribution in [20]. The proposed RSDBP decoder can be implemented by starting the RSBP decoding process until sufficient encoded symbols are added to the waiting array.

4.3. Ripple-Sorted and Threshold-Based BP Decoder. Let P denotes the ratio of error symbols, which increases as the SNR decreases. The BER performance of the RSDBP decoder decreased as P increased. To reduce the probability of incorrect encoded symbols participating in decoding, the encoded symbols with a high error probability should be deleted. The distribution of error symbols can be analyzed using Monte Carlo simulations. For example, $2k$ ($k = 500$) encoded symbols are generated and sorted by the error probability, denoted as $y_1, y_2, \cdots, y_{2k}, |L(y_1)| \geq |L(y_2)| \geq \cdots \geq |L(y_{2k})|$. We segmented $y_1, y_2, \cdots, y_{2k}$ into 100 segments. The ratio of error encoded symbols in each segment is shown in Figure 6. As shown, only a small number of error encoded symbols exist, and the ratio of error encoded symbols increased with the segment sequence. Therefore, most error encoded symbols can be deleted from decoding if the tails of the sorted encoded symbols are deleted.

For HDBP decoding, the received encoded symbol y_j will be deleted if $|L(y_j)| < t$, where t denotes the threshold. Otherwise, it will participate in decoding. Let δ denotes the probability that an error symbol will be deleted. For deletion probability δ, the threshold t can be calculated by Monte Carlo simulations, as shown in Algorithm 3.

Let ω denotes the ratio of encoded symbols deleted by decoding, which depends on δ. Figure 7 shows the ratio of deletion as a function of δ. As shown, the ratio of deletion decreased as the SNR increased, whereas it increased with δ.

Table 6: Optimal parameter values for proposed degree distribution.

k	δ	$m_{\max}$	c	$\bar{d}$
256	0.01	3	0.22	7.36
	0.90	3	0.24	7.40
500	0.01	4	0.25	8.62
	0.90	4	0.40	8.84

Therefore, the trade-off between the BER performance and overhead can be adjusted by δ.

Based on the analysis of symbol deletion, we propose a new decoder named the RSTBP decoder, in which encoded symbols with higher error probabilities are deleted from decoding. The proposed RSTBP decoder can be implemented by deleting encoded symbols that exceed the threshold.

5. Analysis of the Improved BP Decoder

Lemma 4. *The decoding complexity of the sorting ripple satisfies the constraint*

$$C \leq O((1+\varepsilon)klogR(k)). \tag{9}$$

Proof. The ripple size decreases as the decoding process proceeds. Initially, $R(k)$ symbols are released and sorted, and the decoding complexity is $O(R(k)\log R(k))$. The remaining $(1+\varepsilon)k - R(k)$ symbols will be inserted into the ripple, and the decoding complexity is less than $O(((1+\varepsilon)k - R(k))\log R(k))$. Hence, Lemma 4 is proven.

The computational complexities of the four decoders are shown in Table 1, where $\bar{d} = 1/k\sum_{d=1}^{k} d\Omega(d)$ and $R_{\max} = \max(R_k, R_{k-1}, \cdots, R_1)$, and the numerical results of computational complexities obtained by simulations are shown in Table 2. It is noteworthy that the number of XOR operations depends only on the average degree, and the number of SORT operations in RSDBP is the same as that in RSTBP. The number of SORT operations in RSBP is slightly less than that in RSDBP because small input symbols have been recovered before $(1+\varepsilon)k$ encoded symbols are available.

Lemma 5. *For a P and δ, the number of error encoded symbols participating in decoding is*

$$N_e = \frac{(1-\delta)P}{1-\delta P}(1+\varepsilon)k. \tag{10}$$

Proof. Let N denotes the number of encoded symbols received, and we have $N(1-\delta P) = (1+\varepsilon)k$. The error encoded symbols participating in decoding are $N_e = NP(1-\delta)$. Hence, Lemma 5 is proved.

Lemma 6. *The number of input symbols recovered by error encoded symbols directly satisfies the constraint*

$$N_e{}' \leq N_e - \frac{\varepsilon N_e{}^2}{2(1+\varepsilon)k}. \tag{11}$$

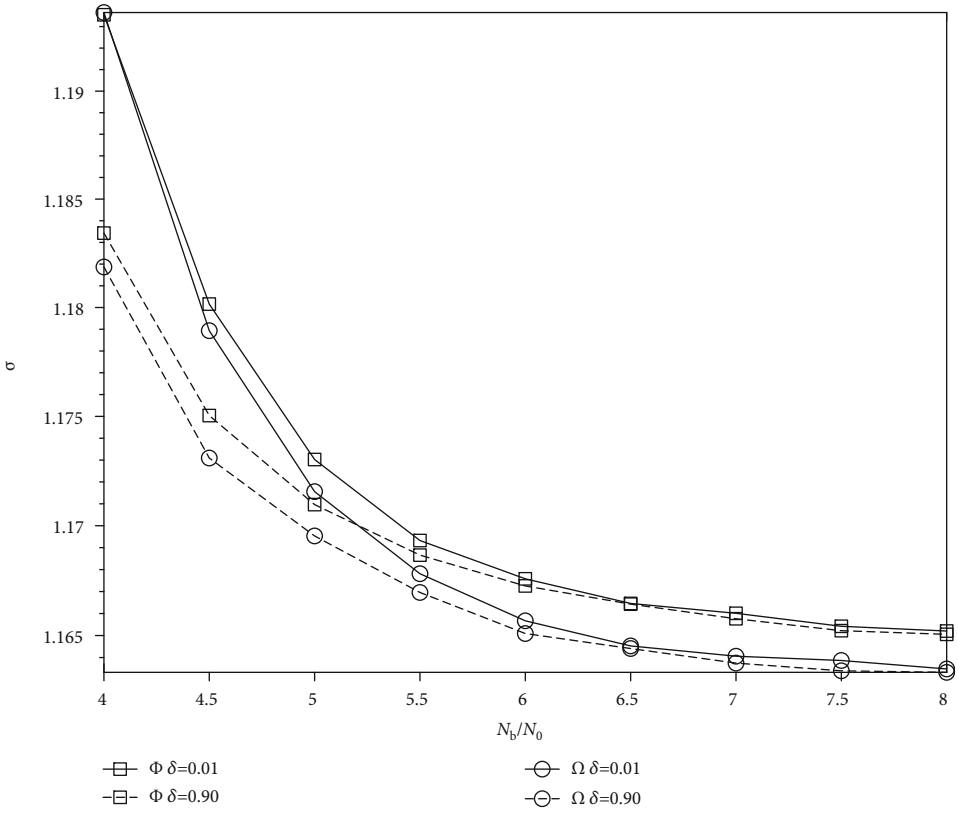

Figure 13: σ as a function of SNR for $k = 256$.

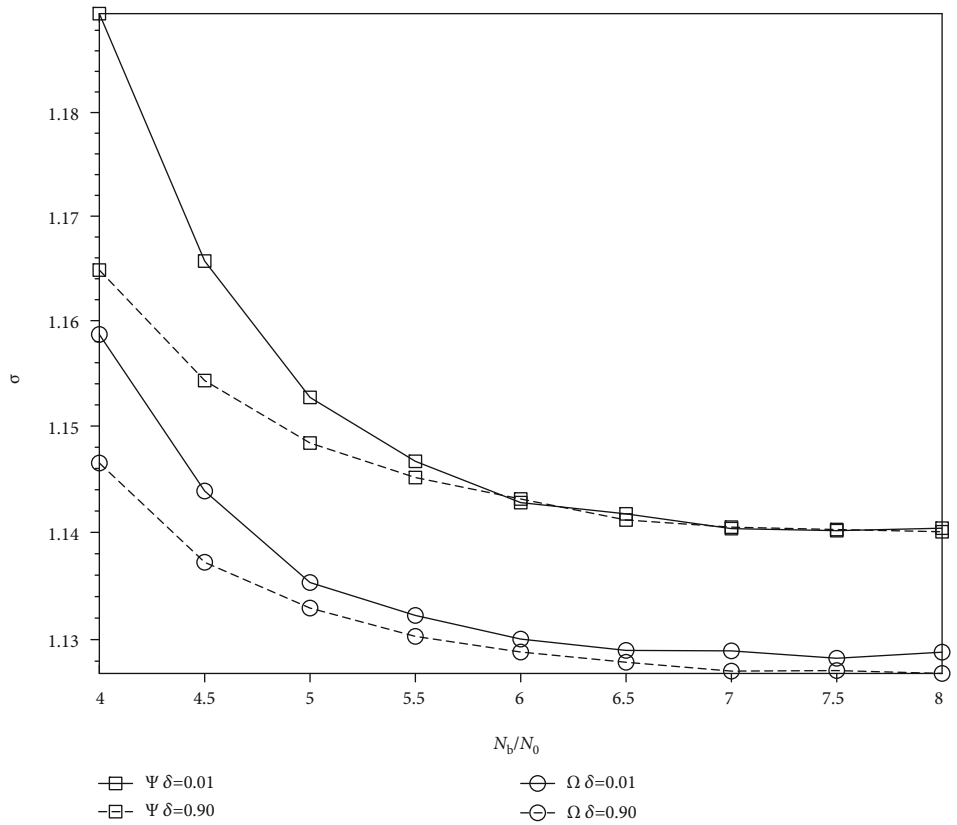

Figure 14: σ as a function of SNR for $k = 500$.

Proof. There exist ε pairs of encoded symbols. Since N_e is small compared with $(1+\varepsilon)k$, the probability of an error encoded symbol pairing with a correct encoded symbol is $\varepsilon N_e/(1+\varepsilon)k$. Let $(y_1, y_2), |y_1| \le |y_2|$ denotes a pair of encoded symbols without loss of generality. If one of y_1 and y_2 is an error encoded symbol, the probability that y_1 is the error encoded symbol exceeds 0.5. Therefore, more than $\varepsilon {N_e}^2/2(1+\varepsilon)k$ error encoded symbols will be considered as redundant symbols. Hence, Lemma 6 is proven.

Definition 7. (error propagation probability). the neighbors of the encoded symbol are selected randomly. Therefore, the probability that an encoded symbol with degree d is affected by an error input symbol that satisfies the constraint

$$\rho(d) = \frac{C_1^1 C_k^{d-1}}{C_k^d}. \tag{12}$$

We observed that the error propagation probability decreased with the average degree. For example, no error propagation was observed when the average degree was one. Hence, a trade-off occurred between the error propagation probability and overhead.

Definition 8. (number of affected encoded symbols). let $d_1, d_2, \cdots, d_L$ denote the degrees of L encoding symbols that will recover L input symbols. The number of encoded symbols affected by an error symbol in step L directly satisfies the constraint

$$N(L) = \sum_{i=1}^{L} \rho(d_i). \tag{13}$$

Lemma 9. (total number of affected encoded symbols). *let $l_1, l_2, \cdots, l_{N(L)}$ denotes the steps affected by the error symbol in steps k-L. The total number of encoded symbols affected by an error symbol satisfies the constraint*

$$\mathbb{N}(L) \approx \begin{cases} N(L) + \sum_{l=1}^{N(L)} \mathbb{N}(l) & L > 1 \\ N(L) & L = 1 \end{cases}. \tag{14}$$

Proof. Compared with k, the average degree of encoded symbols is small. Hence, $\rho(d)$ is relatively small. The number of encoded symbols that are affected by an error symbol directly and indirectly is small. Therefore, the double counting problem is disregarded; hence, the lemma is proven.

To validate the performance of LT codes in AWGN channels, we propose a new indicator known as NERRIC, which is defined as follows:

$$\sigma = (1+\varepsilon)/\tau, \tag{15}$$

where τ denotes the BER of decoding.

Table 7: Optimal parameters of the proposed degree distribution with fixed overhead.

k	ε	$m_{\max}$	c
256	0.20	3	-0.4
	0.25	3	0.4
500	0.15	6	0.4
	0.20	6	0.5

6. The Optimal Degree Distribution for a Specific BP Decoder

Studies regarding the design of an optimal degree distribution for a specific BP decoder over AWGN channels are limited, as previously discussed. Herein, a method for designing a degree distribution for a specific goal is proposed. The ripple size evolution is important for the design of a degree distribution. Random walk was used to model the number of encoded symbols released in each step. We assumed that the number of encoded symbols released in each step was a Poisson distribution.

Lemma 10. (symbol release). *let $\varphi(m)$ denotes the probability that m encoded symbols will be released in each step. It satisfies the constraint*

$$\varphi(m) = e^{-1}/m. \tag{16}$$

Proof. The number of encoded symbols released is a Poisson distribution. The expectation of this distribution is one. Therefore, Lemma 10 is proven.

Let $m_{\max}$ denotes the maximum number of encoded symbols released in a single decoding step. For a fixed $m_{\max}$, Monte Carlo simulations can be used to generate plenty of ripple size evolutions. Each ripple addition is modeled as a random walk with a probability distribution $\varphi(m)$. The ripple size evolution is modeled as follows:

$$R_L = R_L + c\sigma_L, \tag{17}$$

where $\bar{R}_L$ and σ_L denote the average ripple size and variance of the simulation results in decoding step L, respectively; c denotes a parameter to adjust the ripple size evolution. For $m_{\max} = 3$, the ripple size as a function of decoding step for different c is shown in Figure 8. It is clear that the expected ripple size evolution can be generated by carefully adjusting parameter c. Given the ripple size evolution, the degree distribution can be calculated using the GDDA. The degree distribution is obtained based on formula (18).

$$\Omega = GDDA(RSE(m_{\max}, c)), \tag{18}$$

where $RSE(m_{\max}, c)$ denotes the ripple size evaluation determined by parameters $m_{\max}, c$.

Let Ω denotes the degree distribution designed to minimize average overhead. Let Ω' denotes another well-

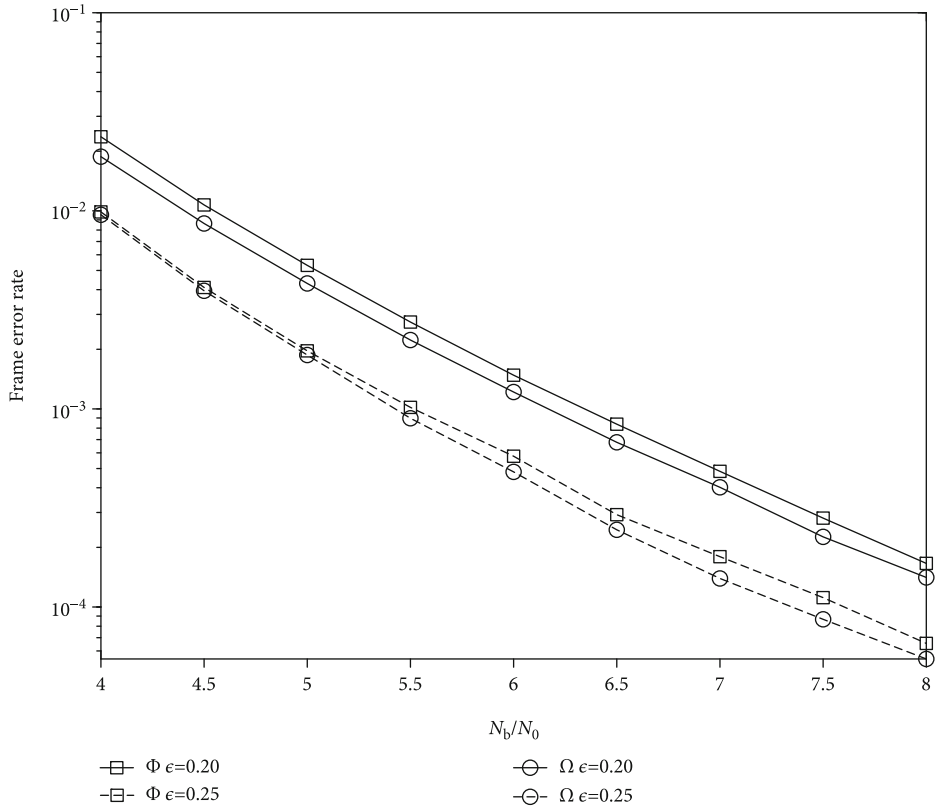

Figure 15: Frame error rate as a function of SNR for $k = 256$.

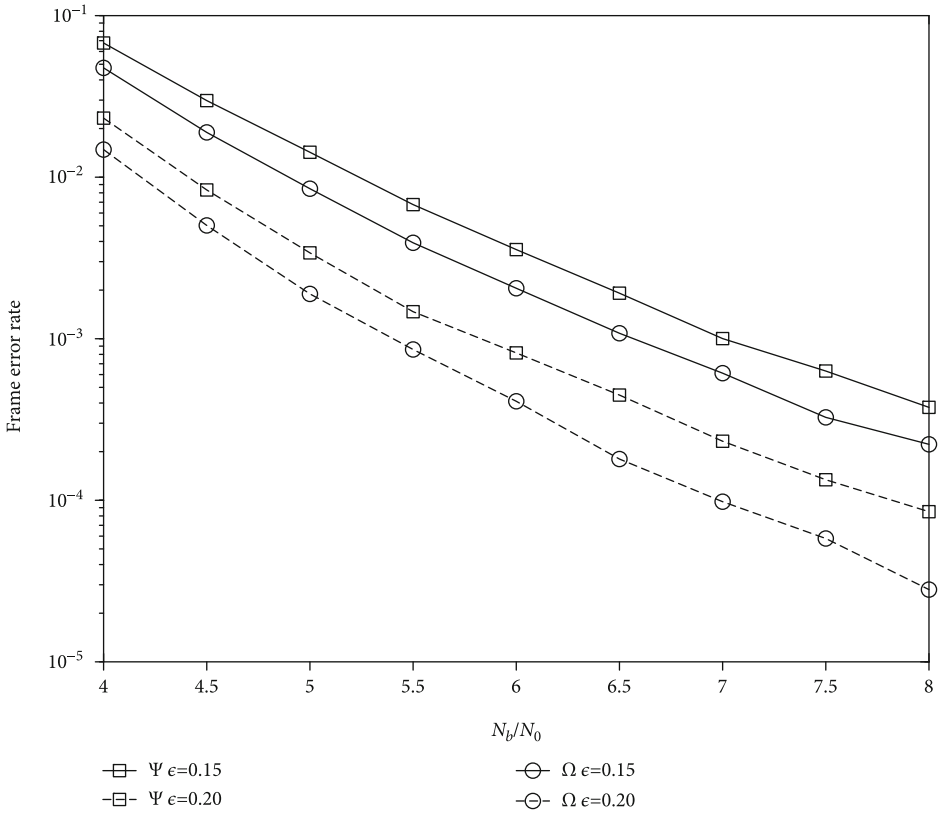

Figure 16: Frame error rate as a function of SNR for $k = 500$.

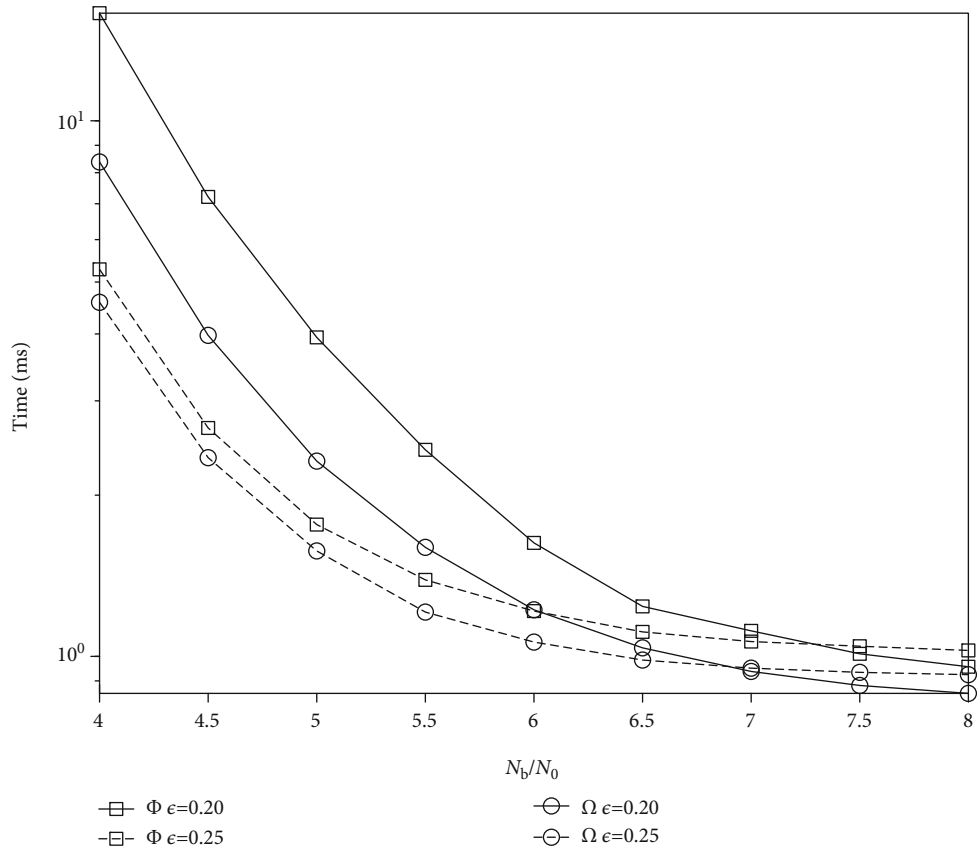

Figure 17: Decoding time as a function of SNR for $k = 256$.

designed degree distribution to decrease the average degree at the expense of increasing the average overhead. The average overhead and average degree as a function of parameter c are shown in Figure 9. The BER decreased as the average degree decreased because of two reasons. First, the more encoded symbols participated in decoding, the more encoded symbols recovered the same input symbol, resulting in a decrease error probability of decoding. Subsequently, the error propagation decreased with the average degree. Therefore, the BER is in conflict with the average overhead. Additionally, the average degree directly determines the number of operations during the encoding and decoding processes.

Let $G(\Omega)$ denotes the objective function of the degree distribution Ω. Additionally, the optimal parameters $(m_{\max}, c)$ can be converted to a pure optimization problem as follows:

$$m_{\max}, c = \arg \min_{m_{\max}, c} G(GDDA(RSE(m_{\max}, c))) \quad (19)$$

The variable c is used for the range [-1,1] and $m_{\max}$ for the range $[3, \sqrt{k}]$. Generally, for a fixed $m_{\max}$, it might appear that a lower value of c would be desirable for decreasing both the average degree and BER at the expense of increasing the average overhead.

7. Numerical Results

In this section, some simulation results are provided to validate our study. The decoding algorithms were implemented in C++ and executed on a computer with a Xeon E3-1505 M CPU and 16 GB of RAM under Windows10. The degree distributions proposed in [18, 20] were used in our simulations, which are denoted as Φ and Ψ, respectively, and our proposed degree distribution is denoted as Ω. The BER as a function of N_b/N_0 is shown in Figure 10. The BERs of the RSBP and RSDBP decoders were better than that of the BP decoder, consistent with our analyses. For example, with $k = 500$ and $N_b/N_0 = 4.0$, the BER of the BP decoder was 0.115, whereas the BER of the RSDBP decoder was 0.082. The computational times of BP, RSBP, and RSDBP are shown in Table 3. As shown, the computational times of the three decoders were similar.

The RSDBP decoder combined with the proposed degree distribution Ω was compared with the other decoders. The degree distribution Ω was designed to optimize σ by selecting the appropriate $m_{\max}$ and c; the optimal parameters and average degree of Ω are shown in Table 4, whereas the average degrees of Φ and Ψ are shown in Table 5. As shown, the average degree of Ω is smaller than those of the others.

Figures 11 and 12 illustrate the NERRIC σ achieved by different decoders and different degree distributions with $k = 256$ and $k = 500$, respectively. It is clear that the RSBP

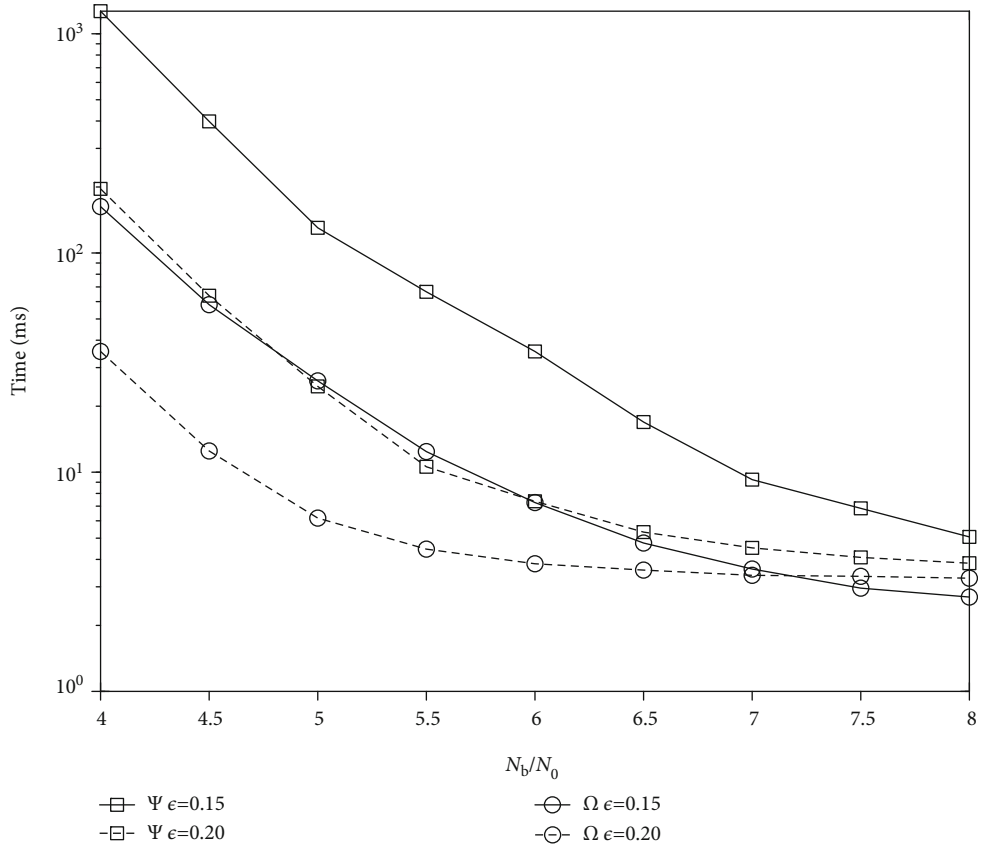

Figure 18: Decoding time as a function of SNR for $k = 500$.

and RSDBP decoders outperformed the BP decoder, which is consistent with the theoretical analysis. The improvement decreased as the SNR increased because barely any error encoded symbols were discovered in channels with higher SNRs. Furthermore, RSDBP combined with the proposed degree distribution outperformed the other methods, and the improvement increased with the SNR. For example, with $k = 500$ and $N_b/N_0 = 4.0$, the σ of the RSDBP decoder combined with Ψ was 1.241, whereas the σ of RSDBP combined with the proposed degree distribution was 1.217. This is because the optimization goal was to minimize σ, and the probability of error propagation decreased with the average degree.

The RSTBP decoder combined with the degree distribution Ω was compared with the other decoders, and the optimal parameters of Ω with different $\delta$and k are listed in Table 6.

Figures 13 and 14 show σ as a function of SNR for $k = 256$ and $k = 500$, respectively. As shown from the figures, the proposed degree distribution Ω yielded better results than the others for both $\delta = 0.01$ and $\delta = 0.90$to minimize σ for optimization. As the SNR increased, the performance of Ω was better than that of the others. This is because the average degree of Ω was smaller. Furthermore, as δincreased, σ decreased more slowly. This is because the number of error encoded symbols decreased as the SNR increased, and the number of encoded symbols deleted at $\delta = 0.01$approached that at $\delta = 0.90$.

In hybrid decoding, the decoding complexity decreased as the FER increased. For RSDBP decoder, the degree distributionΩcan be tuned to achieve a lower FER in a fixed overhead. The optimal parameters of the degree distribution Ω with different ε and k values are shown in Table 7.

Figures 15 and 16 show the FER as a function of the SNR with $k = 256$ and $k = 500$, respectively. It was observed that the proposed optimal degree distribution outperformed the others for different fixed overheads. For instance, in the case of $k = 500$, $\varepsilon = 0.2$, and $N_b/N_0 = 4.0$, the FERs of Ψ and Ω were 0.0232 and 0.0138, respectively. This is because a better trade-off between the average overhead and average degree was achieved to reduce the effect of error propagation.

A hybrid decoder can be formulated by combining the RSDBP and SDBP decoders. Figures 17 and 18 show the decoding time as a function of the SNR for $k = 256$ and $k = 500$, respectively. It was observed that Ω outperformed the others in terms of the decoding complexity, as Ω was better than the others in the HDBP decoding stage.

8. Conclusions

Herein, we first analyzed the improvement of BP decoding by introducing a sorting ripple, delaying the decoding process, and deleting low-reliable symbols. Subsequently, we proposed three improved HDBP decoders, namely, RSBP, RSDBP, and RSTBP decoders. We demonstrated that both RSBP and RSDBP outperformed BP decoding in terms of

NERRIC although the decoding complexity increased slightly. Compared with the RSDBP decoder, the RSTBP decoder further increased the NERRIC but the average overhead increased. Furthermore, a ripple size evolution-based design of the optimal degree distribution was proposed. Numerical simulations demonstrated that the proposed degree distribution outperformed the others in terms of both the NERRIC and FER. The proposed scheme was not limited to AWGN channels and LT codes. It can be readily extended to noisy channels and Raptor codes. In future work, the energy consumption of LT codes will be investigated to identify a balance among the FER, average overhead, and average degree.

Data Availability

The data used to support the findings of this study are available from the corresponding author upon request.

Conflicts of Interest

The authors declare that they have no conflicts of interest.

Acknowledgments

This study was supported by the Beijing Natural Science Foundation (4194073).

References

[1] M. Luby, "LT codes," in *Proc. IEEE Symp. Found. Comp. Sci*, pp. 271–280, Vancouver, Canada, 2002.

[2] M. Luby, T. Gasiba, T. Stockhammer, and M. Watson, "Reliable multimedia download delivery in cellular broadcast networks," *IEEE Trans. Broadcast*, vol. 53, no. 1, pp. 235–246, 2007.

[3] R. Palanki and J. S. Yedidia, "Rateless codes on noisy channels," in *International Symposium onInformation Theory, 2004. ISIT 2004. Proceedings*, p. 37, Chicago, USA, 2004.

[4] H. Jenkač, T. Mayer, T. Stockhammer, and W. Xu, "Soft decoding of LT-codes for wireless broadcast," in *Proc. IST Mobile Summit 2005*, 2005.

[5] A. Kharel and L. Cao, "Decoding of short LT codes over BIAWGN channels with Gauss-Jordan elimination-assisted belief propagation method," in *2015 Wireless Telecommunications Symposium*, pp. 1–6, 2015.

[6] L. He, J. Lei, and Y. Huang, "A greedy spreading serial decoding of LT Codes," *IEEE Access*, vol. 7, pp. 31186–31196, 2019.

[7] C. Cao, H. Li, and Z. Hu, "A new cross-level decoding scheme for LT Codes," *IEEE Communications Letters*, vol. 19, no. 6, pp. 893–896, 2015.

[8] R. Sun, M. Zhao, J. Liu, J. Sun, H. Guan, and Z. Zhao, "Piggybacking belief propagation decoding for rateless codes based on RA structure," in *2018 IEEE/CIC international conference on communications in China (ICCC)*, pp. 237–241, IEEE, 2018.

[9] M. Zhang, S. Chan, and S. Kim, "Soft iterative decoding algorithms for rateless codes in satellite systems," *Algorithms*, vol. 12, no. 8, p. 151, 2019.

[10] L. Weijia and C. Shengnan, "Performance analysis of complexity reduction BP decoding of rateless codes by deleting low reliable symbols," *The Journal of China Universities of Posts and Telecommunications*, vol. 23, no. 5, pp. 26–31, 2016.

[11] C. Albayrak and K. Turk, "Reduced-complexity decoding of LT Codes," *Wireless Personal Communications*, vol. 94, no. 3, pp. 969–975, 2017.

[12] K. Turk and P. Fan, "Adaptive demodulation using rateless codes based on maximum a posteriori Probability," *IEEE Communications Letters*, vol. 16, no. 8, pp. 1284–1287, 2012.

[13] I. Hussain, M. Xiao, and L. K. Rasmussen, "Reduced-complexity decoding of LT codes over noisy channels," in *2013 IEEE wireless communications and networking conference (WCNC)*pp. 3856–3860, IEEE, 2013.

[14] D. Park and S. Y. Chung, "Performance—complexity tradeoffs of rateless codes," in *2008 IEEE international symposium on information theory*, pp. 2056–2060, IEEE, 2008.

[15] A. Kharel and L. Cao, "Improved fountain codes for BI-AWGN channels," in *2017 IEEE wireless communications and networking conference (WCNC)*, pp. 1–6, IEEE, 2017.

[16] L. Wang and W. Tang, "Performance analysis and improvement of LT codes over AWGN channels," *Journal of Computers*, vol. 9, no. 4, pp. 974–982, 2014.

[17] D. Deng, D. Xu, and S. Xu, "Optimisation design of systematic LT codes over AWGN multiple access channel," *IET Communications*, vol. 12, no. 11, pp. 1351–1358, 2018.

[18] J. H. Sorensen, T. Koike-Akino, P. Orlik, J. Ostergaard, and P. Popovski, "Ripple design of LT codes for BIAWGN Channels," *IEEE Transactions on Communications*, vol. 62, no. 2, pp. 434–441, 2014.

[19] L. Zhang, T. Li, J. Liao, Q. Qi, and J. Wang, "Design of improved Luby transform codes with decreasing ripple size and feedback," *IET Communications*, vol. 8, no. 8, pp. 1409–1416, 2014.

[20] S. Xu and D. Xu, "Design of degree distributions for finite length LT codes," *Wireless Personal Communications*, vol. 98, no. 2, pp. 2251–2260, 2018.

Hindawi
Wireless Communications and Mobile Computing
Volume 2020, Article ID 8876705, 11 pages
https://doi.org/10.1155/2020/8876705

Research Article

The Lyapunov Optimization for Two-Tier Hierarchical-Based MAC in Cloud Robotics

Yansu Hu,[1] Ang Gao,[2,3] Changqing Wang,[4] Wen Cao,[1] and Maode Yan[1]

[1]*School of Electronic and Control Engineering, Chang'an University, Xi'an 710064, China*
[2]*Yangtze River Delta Research Institute of Northwest Polytechnic University, Taicang 215400, China*
[3]*School of Electronics and Information, Northwest Polytechnic University, Xi'an 710072, China*
[4]*School of Automation, Northwest Polytechnic University, Xi'an 710072, China*

Correspondence should be addressed to Ang Gao; gaoang@nwpu.edu.cn

Received 10 April 2020; Revised 10 June 2020; Accepted 20 July 2020; Published 28 August 2020

Academic Editor: Chaoyun Song

Cloud robotics can largely enhance the robot intelligence by offloading tasks to the cloud dynamically. However, the robots differ in their own hardware configuration such as battery and processing capacity, while the transmission frames are also a mixture of different quality of service (QoS) requirements. As the competition for limited channel resource is inevitable, how to optimize the system performance by effective resource allocation is a key problem. The paper proposes a two-tier hierarchical-based MAC (Two-Tier MAC) which means the classification exists not only in frames but also in robots. The Lyapunov optimization technique is used to maximize the time-averaged quality satisfaction. The experiments show the superior performance of the Two-Tier MAC compared with other MAC protocols especially in overloaded networks. Meanwhile, the system also presents a longer lifetime because the Two-Tier MAC takes energy balance into consideration.

1. Introduction

Robotics is evolving from a single platform to cluster collaboration for the applications with high complexity, uncertainty, and real time. Although robots share information and cooperate with each other by a decentralized wireless network, the intelligence is still limited by their own hardware configuration. Cloud robotics [1] provides a novel concept to break the individual limitation in low intelligence and processing capacity. By means of the offloading task to cloud dynamically, robots get rid of the huge storage and intensive computing bottleneck.

As shown in Figure 1, the offloading task is divided into a series of flows and is processed on cloud hosts in parallel by virtualization technology. Task flows are then repacked by upper layers with header information and finally encapsulated into MAC frames in the data link. For enhancing the survival ability in complex environment, robots adopt a decentralized ad hoc network and contend for communication channel in the carrier sense multiple access/collision avoidance (CSMA/CA) mode.

As the competition is inevitable, how to allocate the limited resource to guarantee the QoS performance and maximize the total system utility is a big challenge for the offloading scenario. Frame differentiation is easily thought of. For example, simultaneous localization and mapping (SLAM) should enjoy a better real-time than environment monitoring application. However, robots themselves also differ in processing capacity, hardware configuration, task emergency, and so on which is often overlooked. Meanwhile, the network condition is time varying which is hard to predict. When the network is overloading, the system cannot support the QoS for all robots. The data arrival rate should be adjusted to avoid blocking.

For the problems above, the paper proposes a two-tier hierarchical-based MAC (Two-Tier MAC) to realize the

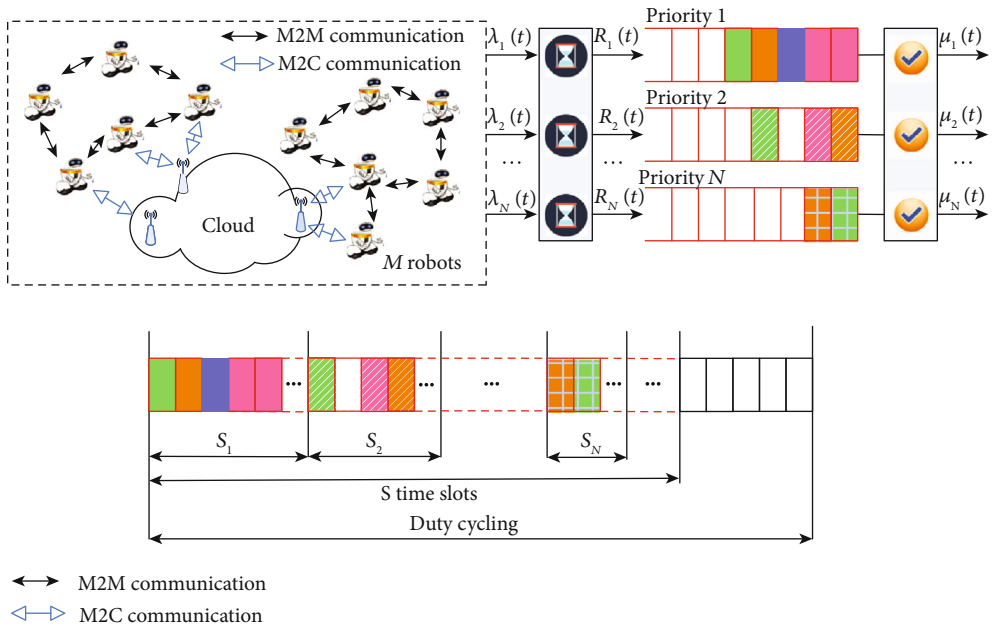

Figure 1: Two-Tier MAC architecture of cloud robotics.

classification on both frames and robots. The Lyapunov optimization technique as well as isolated time slots and admission control is adopted to maximize the system utility even in poor network condition. The main contributions are as follows:

(i) The classification on both frames and robots is considered. All frames are divided into different priorities waiting in corresponding queues with isolated time slots to reduce collision consumption. Frames in the same queue but from different robots are allocated diverse accessing probability to ensure the energy balance

(ii) The system optimization can be decoupled into two independent issues by the Lyapunov method. One is admission control (AC) in which the frames will be rejected when the network is overloading. The other is resource allocation (RA) to adjust the accessing probability to maximize the system utility function

The rest of the paper is organized as follows. Chapter II reviews related works. In Chapter III, the scheme of the Two-Tier MAC is detailed. The Lyapunov optimization method is described in Chapter IV. In Chapter V, a series of experiments are operated to test the effectiveness of the Two-Tier MAC. The conclusion and future work are illustrated in Chapter VI.

2. Related Works

Since the widespread of heterogeneous, crosslayered "thin robots," it is the best way to control the network transmission in the MAC layer or transceivers in the physics layer.

Some researches based on multiqueuing architecture have realized QoS support by assigning different queues with different resource or CSMA/CA parameters, such as contention window size, interframe space, active time, transmission power, TCP congestion window, and data rate [2, 3]. In specific, QoS-based MAC [2] adjusts the contention window for diverse QoS requirements and duty cycle to preserve sensory energy. PRIN-MAC [4] can minimize energy consumption and increase system throughput by varying the interarrival time according to the packets priorities. ASMAC [5] avoids overhearing and reduces contention and delay by asynchronously scheduling the wake-up time of neighboring nodes. RF-MAC [6] focuses on how the placement, chosen frequency, and number of RF energy transmitters impact the sensor charging time. CACC-MAC [7] is proposed for crosslayer congestion control by the dynamic TCP congestion window and MAC contention window scheme. The mechanism proposed in [3] operates QoS provisioning at the MAC layer for urgent traffic and provides data rate adjustment at the application layer. Each algorithm can improve QoS performance in certain scenarios. However, they are verified from the view of system realization or protocol design without theory analysis such as system stability and dynamic performance.

Based on this problem, we have tried to apply control theory in this area in recent years. FD-MAC [8] designs a less-step controller to provide proportional delay differentiated (PDD) QoS support. It adopts a linear model for system identification which is not precisely enough and without taking energy consumption into consideration. On this basis, CSFD-MAC [9] proposes a cascade self-tuning architecture as well as active power management, and MQEB-MAC [10] adopts a back propagating (BP) neural network to develop an all-in-one mixed QoS

insurance and energy-balanced scheme. Although the algorithms above are verified to be valid by experiments, they still have the following limitations: Firstly, they only focus on the difference in frames but neglect the heterogeneity of the robots themselves. Secondly, channel condition is time varying, but few papers notice the system performance under poor channel conditions which is actually a common scenario in the wireless network. Thirdly, the mathematical model above is either too simple such as the linear system or low in real time such as the BP neural network.

3. System Model

3.1. Two-Tier Hierarchical Architecture. Figure 1 shows the Two-Tier MAC architecture for cloud robotics, and Table 1 exhibits all the variables present in the paper. There are M robots, and all frames are divided into N types waiting in the isolated queues without interference. Note that blocks with the same color come from the same robot, while blocks fulfilled with the same shape have the same frame priority.

To avoid blocking, the arrival rate should be adjusted according to the channel condition. For example, if one queue is fulfilled, the robot should reject new corresponding arrived frames. Queues will be allocated different time slots according to the frame priority, and frames in the same queue are allocated diverse accessing probability according to robot classification.

3.2. Time Slot Isolation. Actually, the robots are power driven related to system lifetime. Isolated time slots are adopted to reduce the collision energy consumption. Frames contend for communication channel by the CSMA/CA mode, with the key algorithm that once the collision is detected, the node will wait for a random back off in the range of $[0, \mathrm{CW}](\mathrm{CW}_{\min} \le \mathrm{CW} \le \mathrm{CW}_{\max})$ where CW is called the contention window. The more intensive a robot attempts to transmit frames, the higher the probability collision and retransmission occur, which will not only cause the unnecessary energy wasting but also induce a large end-to-end delay. Define ρ to be the accessing probability, then

$$\rho = \frac{2}{\mathrm{CW} + 1}. \tag{1}$$

Figure 1 also shows a dynamic time slot isolation framework. There are S time slots in total, and s_n means the number of time slots allocated to the n^{th} queue $(\sum s_n \le S, n = 1, 2, \cdots N)$. Frames with the same priority content for channel medium in specified time slots are actually a kind of resource reservation mechanism to avoid the across-class contention. Data arrival rate of robots is independently and identically distributed (i.i.d). Without loss of generality, assume the data priority is prefixed or dynamically negotiated by high level protocol, and robots are classified by battery capacity.

3.3. Utility Function. In the n^{th} queue, suppose that the arrival rate and the admission rate are $\lambda_n(t)$ and $R_n(t)$, respectively. Although each frame expects a higher admission rate, it is still limited by data arrival rate, i.e.,

$$0 \le R_n(t) \le \lambda_n(t), \quad \forall n, t. \tag{2}$$

It is known that user experience and satisfaction follow logarithmic laws [11]. Since the normalized positive weight vector $[w_1, w_2, \cdots w_n]^T (0 \le w_n \le 1, \sum w_n = 1)$ is prefixed by a high level protocol, the utility function for the n^{th} queue can be written as

$$u_n(t) = w_n \log_2[R_n(t)], \quad n = 1, 2, \cdots N. \tag{3}$$

3.4. Queuing Model. Define $Q_n(t)$ to be the data backlog (number of frames waiting in the queue) for the n^{th} queue at time t. The queue grows with the admission rate $R_n(t)$ and gets short with the service rate $\mu_n(t)$. According to the queue theory [12], the recursive formula of queue length is

$$Q_n(t+1) = \max\left[Q_n(t) - \mu_n(t), 0\right] + R_n(t). \tag{4}$$

As mentioned before, frames are with the same priority content for the channel medium in specified time slots in the manner of CSMA/CA. So the service rate mainly depends on both the time slots and accessing probability.

Table 1: Nomenclature.

M	Number of robots
N	Number of frame types
CW	Size of contention window
$\rho_{m,n}$	Accessing probability of n^{th} frame type in robot m
S	Total number of time slots in a duty-cycling
s_n	Number of time slots allocated to n^{th} frame
$\lambda_n(t)$	Arrival rate for n^{th} queue
$R_n(t)$	Admission rate for n^{th} queue
w_n	Positive weight n^{th} queue
$u_n(t)$	Utility function for n^{th} queue
$\mu_n(t)$	Service rate for n^{th} queue
$Q_n(t)$	Data backlog for n^{th} queue
ν_m	PHY transmission ratio for m^{th} robot
τ_m	Class factor for m^{th} robot
$E(.)$	Mathematical expectation
Γ	Fitness function
s_n'	Normalized value of s_n
I^{binary}	Binary chromosome vector
F_{code}	Coding function
F_{decode}	Decoding function

For every robot, supposing PHY transmission ratio is v_m $(n = 1, 2, \cdots M)$, the class factor is τ_m, then the service rate is

$$\mu_n(t) = \tau_m v_m \rho_{mn} \frac{s_n}{S}, \tag{5}$$

where ρ_{mn} is the accessing probability of the n^{th} frame type in robot m. So there is

$$0 \le \rho_{mn} \le 1, \ \sum_{n=1}^{N} \rho_{mn} = 1, \quad \forall m. \tag{6}$$

According to paper [13], an individual queue $Q_n(t)$ is the mean-rate-stable if

$$\lim_{T\to\infty} \frac{E\{Q_n(t)\}}{T} = 0, \tag{7}$$

and a network is stable if all individual queues in the network are stable. In a real system, the mean rate stability implies that the long-term average departure rate from the queue is greater than or equal to the long-term average input rate injected into the queue, i.e., $\lim_{T\to\infty}(1/T)$ $\sum_{t=0}^{T-1}\mu_n(t) \ge \lim_{T\to\infty}(1/T)\sum_{t=0}^{T-1}R_n(t)$. Thus, all frames placed in the queue will be finally transmitted when the data queue is mean-rate-stable.

3.5. Problem Formulation. In summary, the utility function can be optimized by adjusting the time slots s_n and accessing the probability ρ_{mn} dynamically. The problem can be described as

$$\text{P1}: \max_{\mathbf{R}(t),\mathbf{s}(t),\rho(t)} \lim_{T\to\infty} \frac{1}{T}\sum_{t=1}^{T-1} E\left\{\sum_{n=1}^{N} u_n(\text{t})\right\}, \tag{8}$$

s.t.

$$0 \le R_n(t) \le \lambda_n, \quad \forall n, t, \tag{C1}$$

$$0 \le \rho_{mn}(t) \le 1, \ \sum_{n=1}^{N} \rho_{mn}(t) = 1, \quad \forall m, \tag{C2}$$

$$0 \le s_n(t) \le S, \ \sum_{n=1}^{N} s_n(t) \le S, \tag{C3}$$

$$\lim_{T\to\infty} \frac{E\{Q_n(t)\}}{T} = 0, \tag{C4}$$

where $\mathbf{R}(t) = \{R_n(t)\}$, $\mathbf{s}(t) = \{s_n(t)\}$, and $\rho(t) = \{\rho_{mn}(t)\}$ are the optimized parameter vector/matrix to be solved. C1 constrains the admission rate which cannot exceed the arrival rate. C2 constrains the accessing probability which is in the range of [0,1], and the total value of different frame priorities in one robot at a time should equal to 1. C3 constrains the time slots which are limited by an upper bound for energy consumption, and C4 constrains the queue which is mean-rate-stable.

4. Lyapunov Optimization

4.1. Problem Transformation. The queue system should be stable, so the Lyapunov method is used to ensure the stability in the long term. Define the Lyapunov function as

$$L[\mathbf{G}(t)] = \frac{1}{2}\sum_{n=1}^{N} Q_n^2(t). \tag{9}$$

Without loss of generality, assume all queues are empty when $t = 0$, i.e., $L[\mathbf{G}(0)] = 0$. Lyapunov function drift is

$$\Delta\mathbf{L}(t) \triangleq \Xi\{L[\mathbf{G}(t+1)] - L[\mathbf{G}(t)]\}. \tag{10}$$

The drift-minus-reward term has an upper bound according to Lemma 1.

Lemma 1 (see [14]). *For any nonnegative real number Q, b, and a, there holds that*

$$[\max(Q - b, 0) + A]^2 \le Q^2 + b^2 + A^2 + 2Q(A - b), \tag{11}$$

$$\begin{aligned}\Delta\mathbf{L}(t) - V\sum_{n=1}^{N} u_n(t) &\le B + E\left\{\sum_{n=1}^{N} Q_n(t)[R_n(t) - \mu_n(t)]\right\} \\ &= B + E\left\{\sum_{n=1}^{N}[Q_n(t)R_n(t) - Vw_n\log_2(R_n(t))]\right\} \\ &\quad - E\left\{\sum_{n=1}^{N}[Q_n(t)\mu_n(t)]\right\},\end{aligned} \tag{12}$$

where $B = E\{\sum_{n=1}^{N}[R_n^2(t) + \mu_n^2(t)/2]\}$ *is defined as a finite constant to simplify the inequation above, and V is a nonnegative constant parameter that controls the trade-off between drift* $\Delta\mathbf{L}(t)$ *and satisfaction function. By the Lyapunov optimization technique, problem P1 can be transformed into minimizing the right-hand side (RHS) of (12) subjected to constraints C1-C4.*

Furthermore, according to Equation (12), P1 can be decoupled into two subproblems: the first one is the admission control (AC) related to $\mathbf{R}(t)$, which means the new frames will be rejected if the queue is full. The second one is the resource allocation (RA) related to $\mathbf{s}(t)$ and $\rho(t)$ to guarantee the higher priority could enjoy a better QoS performance.

4.2. Admission Control. Due to the resource limitation, admission control is adopted to ensure that the QoS performance will not degrade below an acceptable level even in

Input: size of the population T, maximum generation G, crossover probability p_c, mutation probability p_m.
Output:arg $\max_{\rho,s'} \Gamma$.

Initialization
Randomly initialize sets T of optimization's variables $[\rho, s']_t (t = 1, \cdots T)$ as the initial population with constrains C2 and C3'
Coding $[\rho, s']_t$ into I^{binary} by function F_{code}, i.e., $I^{g=1} = [I_1^{\text{binary}}, \cdots I_T^{\text{binary}}]$
While $g \le G$ **do**
Calculate the individual fitness Γ_t^g according F_{decode}
Calculate the selection probability $p_t^g = \Gamma_t^g / \sum_t^T \Gamma_i^g$
Save the best fitness Γ_*^g and the corresponding individual I_*^{binary}
If $\|\Gamma_*^g - \Gamma_*^{g-1}\| \le \delta$, **then**
Return $F_{\text{decode}}(I_*^{\text{binary}})$
End
Selection: randomly choose T chromosomes as a new population by Roulette Wheel selection
Crossover: for every two pair of individuals in $I \wedge^g$, take multi-point crossover at every gene position with probability p_c
Mutation: for every individual in $I \wedge^g$, take binary-reverse at every gene position with the probability p_m
$I_g \leftarrow I \wedge^g \cap I_*^{\text{binary}}$
$g = g + 1$
End
Return $F_{\text{decode}}(I_*^{\text{binary}})$

Algorithm 1: GA algorithm.

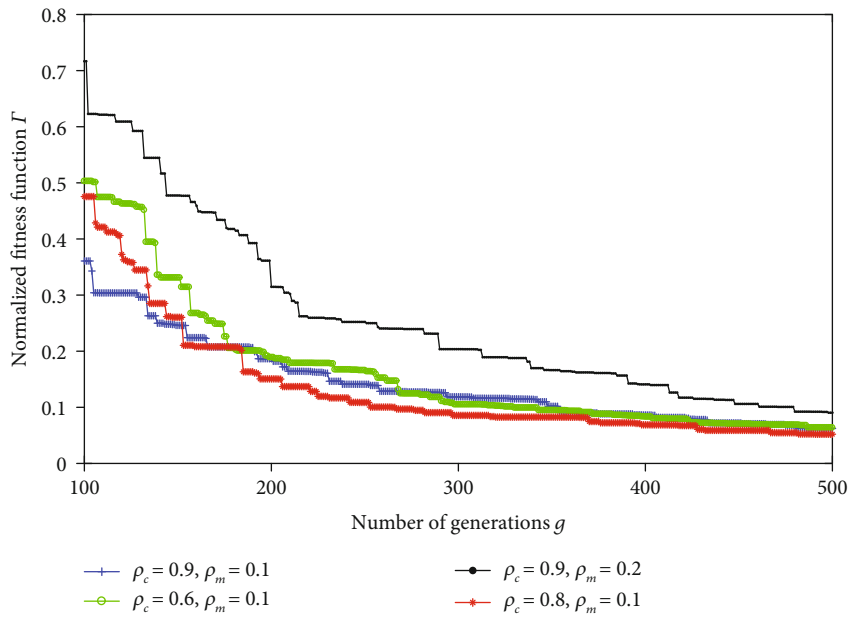

Figure 2: Convergence of GA with different p_c and p_m.

the overloading case. Based on Equation (12), the AC problem is formulated as

$$\text{P2}: \min_{R_n(t)} \sum_{n=1}^{N} [Q_n(t) R_n(t) - V w_n \log_2(R_n(t))], \tag{13}$$

s.t.

$$0 \le R_n(t) \le \lambda_n, \quad \forall n, t. \tag{14}$$

Easily verify that P2 is a convex optimization problem. Set the derivative of $Q_n(t)R_n(t) - V w_n \log_2 [R_n(t)]$ with respect to $R_n(t)$ to be 0 to solve the service rate:

$$\begin{aligned} Q_n(t) - \frac{V w_n}{R_n(t) \ln 2} &= 0, \\ R_n(t) = \frac{V w_n}{Q_n(t) \ln 2} &= 0. \end{aligned} \tag{15}$$

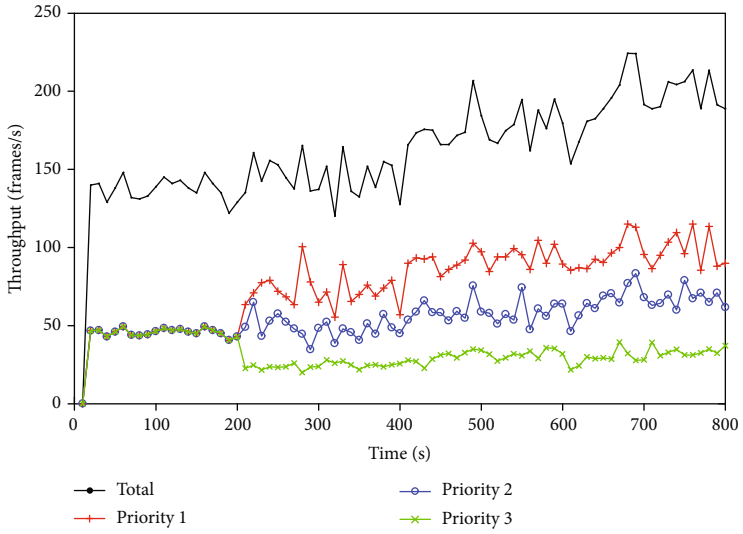

(a) Throughput

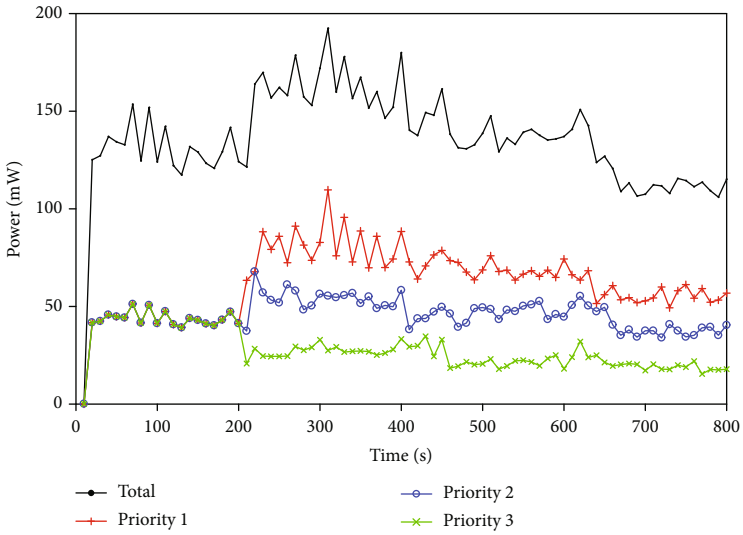

(b) Power

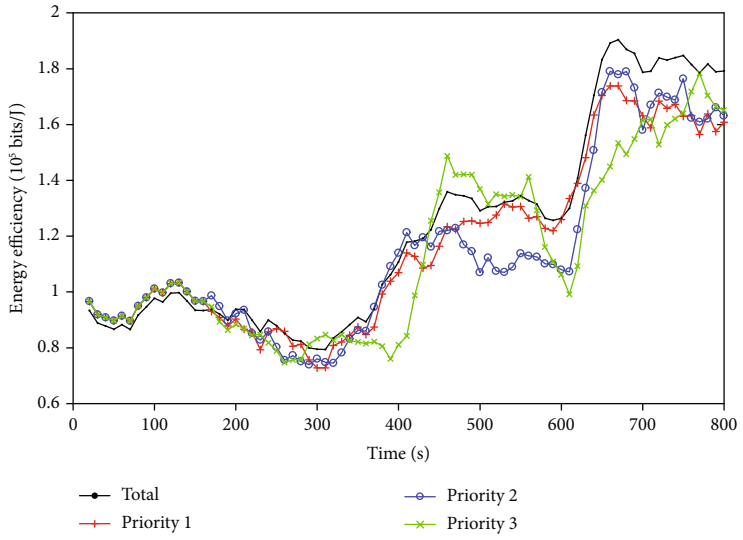

(c) Energy efficiency

Figure 3: Static performance along with time.

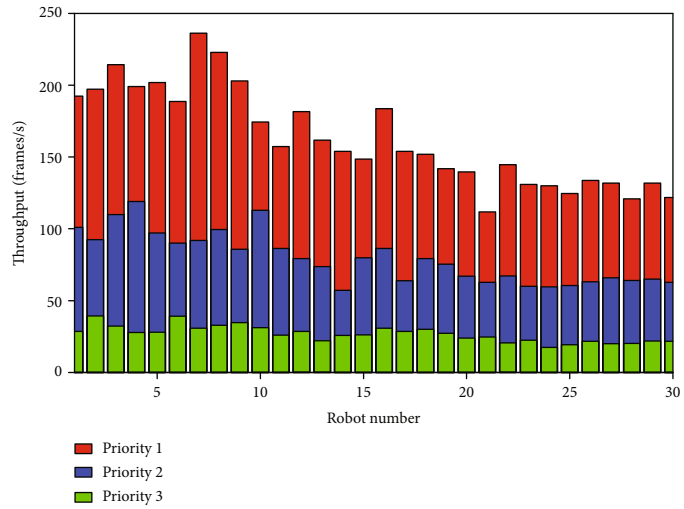

(a) Throughput

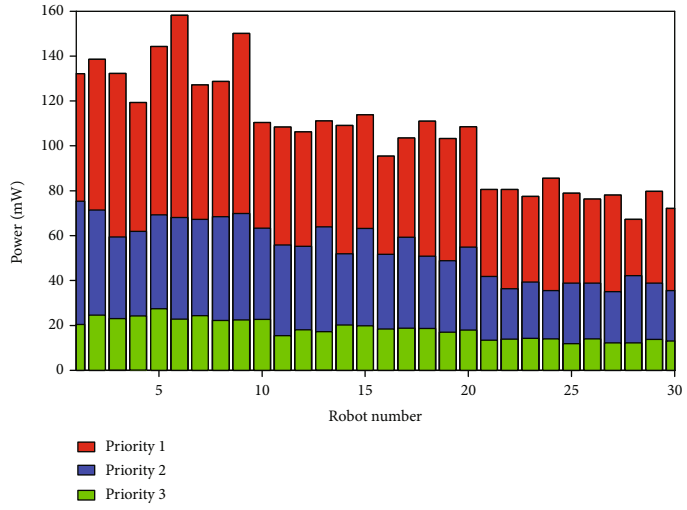

(b) Power

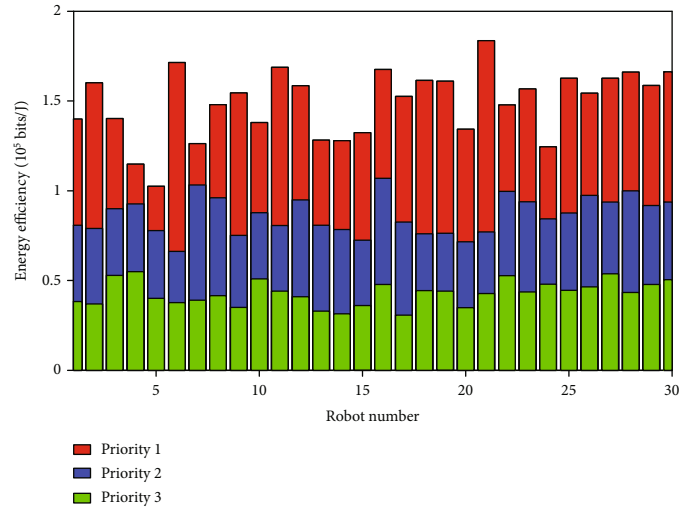

(c) Energy efficiency

Figure 4: Statistic performance of Two-Tier MAC.

Since the admission rate is also limited by arrival rate, the optimal AC decision is

$$R_n^*(t) = \min\left\{\frac{Vw_n}{Q_n(t)\ln 2}, \lambda_n\right\}. \quad (16)$$

4.3. Resource Allocation. For the RA problem, both the time slots and accessing probability should be optimized to maximize P3:

$$\text{P3}: \max_{s_n(t),\rho_{mn}(t)} E\left\{\sum_{n=1}^{N} Q_n(t)\nu_m\rho_{mn}\frac{s_n}{S}\right\}, \quad (17)$$

s.t.

$$0 \le \rho_{mn}(t) \le 1, \ \sum_{n=1}^{N}\rho_{mn}(t) = 1, \quad \forall m, \quad (18)$$

$$0 \le s_n(t) \le S, \ \sum_{n=1}^{N} s_n(t) \le S. \quad (19)$$

P3 is nonconvex and may have several local minima, which make it different to find the closed-form solution. In recent years, some heuristic algorithms have been applied and proven to be valid. In this paper, the genetic algorithm (GA) as shown in Algorithm 1 is used for it can jump out of local minimal points and obtain the global optimization by finding a better artificial population iteratively.

For the unified value range of variables, take $s_n' = s_n/S$ to replace original s_n:

$$0 \le s_n' \le 1, 0 \le \sum s_n' \le 1. \quad (\text{C3'})$$

The fitness function is denoted as $\Gamma = E\{\sum_{n=1}^{N} Q_n(t)\nu_m \rho_{mn}s_n'\}$. Since $\rho \in R^{M\times N}$, $s' \in R^N$ are interpreted into a binary chromosome by a 16-bit Gray code, each individual can be represented by a $(16MN + 16N)$-bit-long binary vector, i.e., $I^{\text{binary}} = [\rho_{16\times M\times N}^{\text{binary}}, s'^{\text{binary}}_{16\times N}]$. The coding and decoding functions used in Algorithm 1 are defined as $I^{\text{binary}} = F_{\text{code}}(\rho, s')$ and $(\rho, s') = F_{\text{decode}}(I^{\text{binary}})$, respectively. The superscript g denotes the number of generations. The output of GA is $[\rho, s']$, and ρ can be adjusted by CW according to Equation (1).

Since P3 is nonconvex, it is hard to prove the convergence in a mathematical way. However, as shown in Figure 2, the GA algorithm can converge with a finite number of generations by simulation with different crossover probability p_c and mutation probability p_m.

5. Experiments and Results

The experiments are operated by ZigBit TM 900 hardware module with Atmel R AVR2025 software package. Specifically, ZigBit TM 900 is a 784/868/915 MHz IEEE 802.15.4 OEM module, while AVR2025 is a configurable MAC stack for ZigBit 900, which provides the fundamental abstract methods for hardware operation and a secondary development supported the MAC stack.

Table 2: Battery configuration.

Classification	Robot number	Battery configuration
Class 1	No.01-no.10	2000 mAh/3.7 V
Class 2	No.11-no.20	1800 mAh/3.7 V
Class 3	No.21-no.30	1500 mAh/3.7 V

Table 3: System lifetime in different MAC protocols.

MAC protocols	Lifetime (min)
IEEE 802.15.4	102
FD-MAC	96
MQEB-MAC	109
Two-Tier MAC	117

30 robots classified into 3 groups according to their battery configuration are deployed in the radius of 100 m. Every node randomly sends data packets to the other. Packets are encapsulated into MAC frames with 3 different priorities which are preset by upper layers as $\omega_1 : \omega_2 : \omega_3 = 3 : 2 : 1$. A larger value means a better service.

The interval of frames obeys the normal distribution with the average of $-\bar{T}_t/\log(1-K)$, where $K(0 < K < 1)$ is the offered traffic normalized by service data rate. The frame length follows the Pareto distribution with the shape parameter of 1.1 and average of 105×8 bits. The transmitted power is 1 mW, $\text{CW}_{\min} = 23$, $\text{CW}_{\max} = 28$. The average frame length is 105 bytes and the symbol rate is 256 kbps.

5.1. Static Performance. Static performance concerns the throughput, power consumption, and energy efficiency changing with time, which are related to system utility, lifetime, and data transmission efficiency, respectively. Energy efficiency is defines as

$$\text{Eff} = \frac{\sum \text{len}_i}{\text{energy}} = \frac{\sum \text{len}_i/t}{\text{energy}/t} = \frac{\Xi_{\text{len}}N/t}{\text{power}} = \frac{\Xi_{\text{len}}\text{throughput}}{\text{power}}. \quad (20)$$

The experiments last 800 s, and 4 different MAC protocols (IEEE 802.15.4, FD-MAC, MQEB-MAC, and Two-Tier MAC) are compared.

(1) During 0-200 s, it runs the original IEEE 802.15.4 MAC without any classification scheme

(2) During 200-400 s, FD-MAC operates for frame differentiation. However, the throughput remains nearly the same, and the presented energy efficiency drops slightly. That is because in channel contention, energy is consumed once a node transmits whether or not the data is correctly received. FDMAC which makes a small CW size with high priority increases

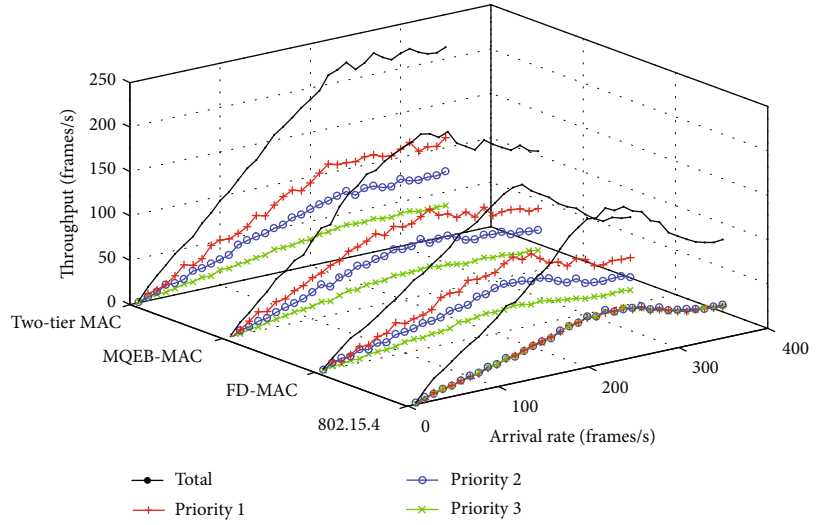

(a) Throughput

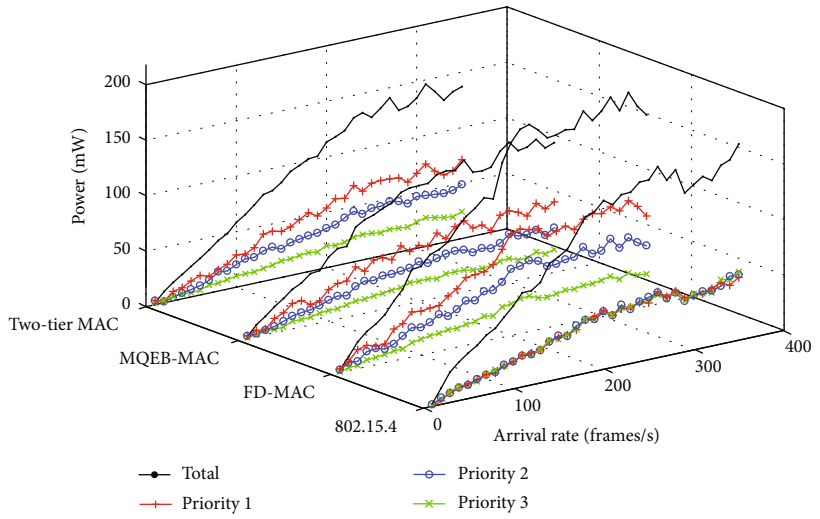

(b) Power

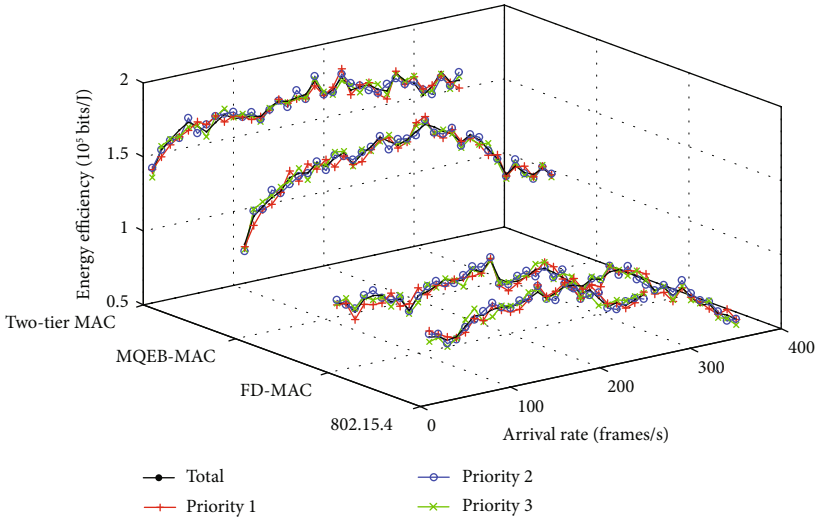

(c) Energy efficiency

FIGURE 5: Dynamic performance along with arrival rate.

the collision probability, which will induce unwanted re-transmission and energy wasting

(3) During 400-600 s, MQEB-MAC presents its advance in both throughput and energy efficiency because of the time slot isolation and BP self-tuning control. However, energy saving by only reducing the time slots allocated to soft QoS traffic limits further performance improvement

(4) During 600-800 s, Two-Tier MAC takes over to maximize the system utility. Throughput is increased because of Lyapunov optimization, and the power consumption is reduced because of the time slot isolation scheme for avoiding across-class collision. As a result, the energy efficiency is largely improved compared with the other three MAC protocols, specifically, about 50.1%, 55.4%, and 23.8% enhancement compared with IEEE 802.15.4, FD-MAC, and MQEBMAC, respectively

Notice that for a specific MAC protocol, frames with high priority enjoy a large throughput but at the same time will lead to more power consumption. So no matter which frame priority, there is no big difference in energy efficiency of the same protocol (Figure 3(c)). The phenomenon will also be present in Section 5.2.

5.2. Statistic Performance. Figure 4 shows the statistic performance of the Two-Tier MAC on each robot. 30 robots are classified into 3 groups according to their battery configuration as shown in Table 2, and the factor is $\tau_1 : \tau_2 : \tau_3 = 4 : 3 : 2$.

For one robot itself, the frames with different priorities are distinguished. Frames with a higher priority enjoy a better throughput which is in accordance with the results shown in Figure 3.

Among different robots, the ones in the higher class still have a better throughput statistically (Figure 3(a)) but lead to more power consumption (Figure 3(b)). As a result, no matter which frame priority or robot class, the energy efficiency is always approximately equal (Figure 3(c)). This conclusion is greatly meaningful to the system lifetime discussed below.

Define the system lifetime as the moment when the first robot is out of battery. The lifetime in different protocols is shown in Table 3. Obviously, the lifetime in the Two-Tier MAC will be extended to take energy balance into consideration.

5.3. Dynamic Performance. The experiments above only consider the normal load scene. However, traffic burst is more common in cloud robotics. Here, we focus on the effect of varying arrival rates to the system performance, i.e., dynamic performance, especially in the overloading situation. The parameter setting is the same as the former except that the arrival rate changes in the range of 50-350 frame/s.

As shown in Figure 5, when the system capacity is unsaturated (50-250 frame/s), the throughput is proportional to the growth of the arrival rate for all protocols. The features of power consumption and energy efficiency present similar characteristic with Section 5.1. After that, robots suffer from traffic bursting which leads to distinct performance in the four protocols.

For 802.15.4, FD-MAC, and MQEB-MAC, network congestion occurs, and the system performance is reduced because of the noncongesting protection mechanism. Data loss will consume extra energy and lead to the degradation of throughput and energy efficiency. On the contrary, thanks to the admission control, the Two-Tier MAC could reject new frames when the network is overloading to avoid network congestion. So the energy efficiency can be maintained even in this severe network environment.

6. Conclusion

Considering the heterogeneity on both robots and frames, a two-tier hierarchical-based MAC is proposed to guarantee the differentiated QoS performance and maximize the system throughput. Experiments show that compared with IEEE 802.15.4, FD-MAC, and MQEB-MAC, the Two-Tier MAC can improve the overall throughput by the Lyapunov theory, reduce power consumption by the time slot isolation scheme, and expend system lifetime by the energy balance. Even in the overloading condition, the QoS performance can be guaranteed thanks to the admission control.

In the future, we would like to do more work to find the close-formed solution for the optimized problem instead of the heuristic algorithm. In addition, in this paper, all robots operate task offloading to the central cloud which suffers from large end-to-end delay. Along the development of 5G, offloading in the distributed mobile edge computing (MEC) scenario should be studied in the future.

Data Availability

The data used to support the findings of this study are included within the article.

Conflicts of Interest

The authors declare that there is no conflict of interests regarding the publication of this paper.

Acknowledgments

This work is supported by the Fundamental Research Funds for the Central Universities (nos. 300102328105 and 300102320203), Xi'an Technology Plan (no. GXYD21.1), China Postdoctoral Science Foundation (no. 2017M623243), Shaanxi Province Postdoctoral Science Foundation (no. 2018BSHYDZZ26), Shaanxi and Guangxi Keypoint Research and Invention Program (nos. 2019ZDLGY13-02-02, 2017ZDXMGY-101, and AB19110036), Taicang Keypoint Science and Technology Plan (nos. TC2018SF03 and TC2019SF03), National Natural Science Foundation of China (nos. 61803042 and 61803040), National Natural Science Foundation of Shaanxi Province (no. 2019JLZ-06), and IoT

Innovation and Fusion Application Project of MIIT (no. [2018]470).

References

[1] H. Liu, S. Liu, and K. Zheng, "A Reinforcement Learning-Based Resource Allocation Scheme for Cloud Robotics," *IEEE Access*, vol. 6, pp. 17215–17222, 2018.

[2] N. Saxena, A. Roy, and J. Shin, "Dynamic duty cycle and adaptive contention window based QoS-MAC protocol for wireless multimedia sensor networks," *Computer Networks*, vol. 52, no. 13, pp. 2532–2542, 2008.

[3] N. B. Yunus Ozen and C. Bayilmis, "Two tiered service differentiation mechanism for wireless multimedia sensor network MAC layers," in *2015 23nd Signal Processing and Communications Applications Conference (SIU)*, pp. 2318–2321, Malatya, Turkey, 2015.

[4] A. K. Subramanian and I. Paramasivam, "PRIN: A Priority-Based Energy Efficient MAC Protocol for Wireless Sensor Networks Varying the Sample Inter-Arrival Time," *Wireless Personal Communications*, vol. 92, no. 3, pp. 863–881, 2017.

[5] B. Jang, J. B. Lim, and M. L. Sichitiu, "An asynchronous scheduled MAC protocol for wireless sensor networks," *Computer Networks*, vol. 57, no. 1, pp. 85–98, 2013.

[6] M. Y. Naderi, P. Nintanavongsa, and K. R. Chowdhury, "RF-MAC: A Medium Access Control Protocol for Re-Chargeable Sensor Networks Powered by Wireless Energy Harvesting," *IEEE Transactions on Wireless Communications*, vol. 13, no. 7, pp. 3926–3937, 2014.

[7] B. J. Chang and S. P. Chen, "Cross-layer-based adaptive congestion and contention controls for accessing cloud services in 5G IEEE 802.11 family wireless networks," *Computer Communications*, vol. 106, pp. 33–45, 2017.

[8] A. Gao and Y. Hu, "A Feedback Approach for QoS-Enhanced MAC in Wireless Sensor Network," *Journal of Sensors*, vol. 2016, Article ID 8365217, 12 pages, 2016.

[9] Y. Hu, A. Gao, T. Xu, and L. Li, "Cascade self-tuning control architecture for QoS-aware MAC in WSN," *IET Wireless Sensor Systems*, vol. 7, no. 5, pp. 146–154, 2017.

[10] A. Gao, Y. Hu, L. Li, and X. Li, "BP Network Control for Resource Allocation and QoS Ensurance in UAV Cloud," *Journal of Sensors*, vol. 2018, Article ID 1419843, 14 pages, 2018.

[11] P. Reichl, B. Tuffin, and R. Schatz, "Logarithmic laws in service quality perception: where microeconomics meets psychophysics and quality of experience," *Telecommunication Systems*, vol. 52, no. 2, pp. 587–600, 2013.

[12] S. Lakshminarayana, M. Assaad, and M. Debbah, "Transmit Power Minimization in Small Cell Networks Under Time Average QoS Constraints," *IEEE Journal on Selected Areas in Communications*, vol. 33, no. 10, pp. 2087–2103, 2015.

[13] M. J. Neely, "Stochastic network optimization with application to communication and queueing systems," *Synthesis Lectures on Communication Networks*, vol. 3, no. 1, pp. 1–211, 2010.

[14] Y. Guo, Q. Yang, and K. S. Kwak, "Quality-oriented Rate Control and Resource Allocation in Time-Varying OFDMA Networks," *IEEE Transactions on Vehicular Technology*, vol. 66, no. 3, pp. 2324–2338, 2017.